

Ministry of Education and Science of the Russian Federation  
Saint Petersburg National Research University of Information  
Technologies, Mechanics, and Optics

***NANOSYSTEMS:***  
***PHYSICS, CHEMISTRY, MATHEMATICS***

**2018, volume 9(4)**

**Наносистемы: физика, химия, математика**

**2018, том 9, № 4**



# NANOSYSTEMS:

**PHYSICS, CHEMISTRY, MATHEMATICS**

## ADVISORY BOARD MEMBERS

**Chairman:** V.N. Vasiliev (*St. Petersburg, Russia*),  
V.M. Buznik (*Moscow, Russia*); V.M. Ievlev (*Voronezh, Russia*), P.S. Kop'ev (*St. Petersburg, Russia*), N.F. Morozov (*St. Petersburg, Russia*), V.N. Parmon (*Novosibirsk, Russia*),  
A.I. Rusanov (*St. Petersburg, Russia*),

## EDITORIAL BOARD

**Editor-in-Chief:** I.Yu. Popov (*St. Petersburg, Russia*)

### Section Co-Editors:

Physics – V.M. Uzdin (*St. Petersburg, Russia*),  
Chemistry, material science – V.V. Gusarov (*St. Petersburg, Russia*),  
Mathematics – I.Yu. Popov (*St. Petersburg, Russia*).

### Editorial Board Members:

V.M. Adamyan (*Odessa, Ukraine*); O.V. Al'myasheva (*St. Petersburg, Russia*);  
A.P. Alodjants (*Vladimir, Russia*); S. Bechta (*Stockholm, Sweden*); J. Behrndt (*Graz, Austria*);  
M.B. Belonenko (*Volgograd, Russia*); V.G. Bepalov (*St. Petersburg, Russia*); J. Brasche (*Clausthal, Germany*);  
A. Chatterjee (*Hyderabad, India*); S.A. Chivilikhin (*St. Petersburg, Russia*); A.V. Chizhov (*Dubna, Russia*);  
A.N. Enyashin (*Ekaterinburg, Russia*), P.P. Fedorov (*Moscow, Russia*); E.A. Gudilin (*Moscow, Russia*);  
V.K. Ivanov (*Moscow, Russia*), H. Jónsson (*Reykjavik, Iceland*); A.A. Kiselev (*Durham, USA*); Yu.S. Kivshar (*Canberra, Australia*);  
S.A. Kozlov (*St. Petersburg, Russia*); P.A. Kurasov (*Stockholm, Sweden*); A.V. Lukashin (*Moscow, Russia*);  
V.A. Margulis (*Saransk, Russia*); I.V. Melikhov (*Moscow, Russia*); G.P. Mirosnichenko (*St. Petersburg, Russia*);  
I.Ya. Mittova (*Voronezh, Russia*); H. Neidhardt (*Berlin, Germany*); V.V. Pankov (*Minsk, Belarus*); K. Pankrashkin (*Orsay, France*);  
A.V. Ragulya (*Kiev, Ukraine*); V. Rajendran (*Tamil Nadu, India*); A.A. Rempel (*Ekaterinburg, Russia*);  
V.Ya. Rudyak (*Novosibirsk, Russia*); D. Shoikhet (*Karmiel, Israel*); P. Stovicek (*Prague, Czech Republic*);  
V.M. Talanov (*Novocherkassk, Russia*); A.Ya. Vul' (*St. Petersburg, Russia*); A.V. Yakimansky (*St. Petersburg, Russia*), V.A. Zagrebnoy (*Marseille, France*).

### Editors:

I.V. Blinova; A.I. Popov; A.I. Trifanov; E.S. Trifanova (*St. Petersburg, Russia*),  
R. Simoneaux (*Philadelphia, Pennsylvania, USA*).

**Address:** University ITMO, Kronverkskiy pr., 49, St. Petersburg 197101, Russia.

**Phone:** +7(812)312-61-31, **Journal site:** <http://nanojournal.ifmo.ru/>,

**E-mail:** [popov1955@gmail.com](mailto:popov1955@gmail.com).

## AIM AND SCOPE

The scope of the journal includes all areas of nano-sciences. Papers devoted to basic problems of physics, chemistry, material science and mathematics inspired by nanosystems investigations are welcomed. Both theoretical and experimental works concerning the properties and behavior of nanosystems, problems of its creation and application, mathematical methods of nanosystem studies are considered.

The journal publishes scientific reviews (up to 30 journal pages), research papers (up to 15 pages) and letters (up to 5 pages). All manuscripts are peer-reviewed. Authors are informed about the referee opinion and the Editorial decision.

# CONTENT

## MATHEMATICS

- I. F. Melikhov, I.Y. Popov  
**Asymptotic analysis of thin viscous plate model** 447
- D.A. Eremin, E.N. Grishanov, D.S. Nikiforov, I.Y. Popov  
**Wave dynamics on time-depending graph with Aharonov-Bohm ring** 457

## PHYSICS

- A.I. Mikhailov, V.F. Kabanov, E.G. Glukhovskoy, M.I. Shishkin, M.V. Gavrikov  
**Methodology of analyzing the CdSe semiconductor quantum dots parameters** 464
- S.V. Kovalevskii, I.A. Moshnikov, V.V. Kovalevski  
**Heat-treated nano-structured shungite rocks and electrophysical properties associated** 468
- Md. Tajul Islam, Golam Sarwar Jahan, Ali Newaz Bahar, Kawsar Ahmed, Md. Abdullah-Al-Shafi  
**A new efficient non-reversible 4 bit binary to gray and 4 bit gray to binary converter in QCA** 473
- V.O. Sheremetev, A. S. Rudenko, A. I. Trifanov  
**Testing Bell inequalities for multi-partite systems with frequency-encoded photonic qubits** 484

## CHEMISTRY AND MATERIAL SCIENCE

- A.A. Efimov, P.V. Arsenov, V.V. Ivanov  
**Investigation of the possibility for reducing agglomeration of aerosol nanoparticles by using the needle-plate corona charger** 491
- M.N. Nikolaeva, A.N. Bugrov, T.D. Anan'eva, E.V. Gushchina, M.S. Dunaevskii, A.T. Dideikin  
**Resistance of reduced graphene oxide on polystyrene surface** 496
- A.I. Zaitsev, A.V. Koldaev, N.A. Arutyunyan  
**Promising directions of increasing the properties of steel** 500
- K.A. Sergeeva, A.A. Sergeev, A.A. Rempel  
**An effective nanostructured green phosphor  $Zn_2SiO_4:Mn^{2+}$  prepared by sol-gel method** 507

I.V. Beketov, A.P. Safronov, A.I. Medvedev, A.M. Murzakaev, O.R. Timoshenkova, T.M. Demina <b>In-situ formation of carbon shells on the surface of Ni nanoparticles synthesized by the electric explosion of wire</b>	<b>513</b>
E.A. Anumol, F.L. Deepak, A.N. Enyashin <b>Capillary filling of carbon nanotubes by BiCl<sub>3</sub>: TEM and MD insight</b>	<b>521</b>
A.I. Izotov, G.V. Kilman, R.V. Shalaev, A.M. Prudnikov <b>Laboratory facility for working with supercritical fluids</b>	<b>532</b>
O. Shydlovska, E. Kharchenko, N. Zholobak, A. Shcherbakov, A. Marynin, O. Ivanova, A. Baranchikov, V. Ivanov <b>Cerium oxide nanoparticles increase the cytotoxicity of TNF-alpha <i>in vitro</i></b>	<b>537</b>
A.A. Valeeva, M.G. Kostenko, A. Pfitzner, A.A. Rempel <b>Effect of high pressures and high temperatures on the structure of nanostructured titanium monoxide</b>	<b>544</b>
S.V. Rempel, K.A. Sergeeva, H. Schroettner, A.A. Valeeva <b>Effect of nonstoichiometry and amount of additives on the structure of HAp-TiO<sub>y</sub> mixtures produced by high-energy fragmentation</b>	<b>549</b>
A.M. Volodin, A.F. Bedilo, V.O. Stoyanovskii, V.I. Zaikovskii <b>High-temperature synthesis of finely dispersed oxide materials and C12A7:e electrides in carbon nanoreactor conditions</b>	<b>558</b>
O.V. Almjasheva, A.A. Krasilin, V.V. Gusarov <b>Formation mechanism of core-shell nanocrystals obtained via dehydration of coprecipitated hydroxides at hydrothermal conditions</b>	<b>568</b>
<b>Information for authors</b>	<b>573</b>

## Asymptotic analysis of thin viscous plate model

I. F. Melikhov, I. Yu. Popov

ITMO University, Kronverkskiy, 49, St. Petersburg, 197101, Russia

ivan.melikhov@gmail.com; popov1955@gmail.com

PACS 47.15.G-,02.30.Jr

DOI 10.17586/2220-8054-2018-9-4-447-456

A cell membrane is a very complex medium, which is difficult to study. One of the simplest approaches is to assume it purely elastic or purely viscous. In this paper, we follow the second assumption and derive mathematical model of nearly-planar viscous plate evolving under action of applied forces. The obtained model is non-linear and covers both stretching and bending of the membrane. In contrast to analogous works on viscous sheets, we use a unique scale for velocity components and take a few first terms in asymptotic expansion. The developed approach can be used for description of the cell membrane with nanoparticles inserted.

**Keywords:** viscous plate, asymptotics.

*Received:* 15 June 2018

*Revised:* 5 July 2018

### 1. Introduction

Interest for flows in layers of narrow thickness (nanolayers or microlayers) is due to the rapid development of fluid-based transport processes using in nanotechnologies (see, e.g., [1] and references therein). A special interest in the field is caused by the relation to power systems, medicine, the development of advanced filter elements, etc. For example, the authors of [2] proposed and fabricated a multilayer lateral-flow nanoparticle filtration and separation device. Results of [3] are relevant for water desalination applications. Paper [4] describes a system for ultra-fast mixing of solvents with aqueous fluids and subsequent precipitation of poorly water soluble drug nanoparticles or colloidal carrier particles. Work [5] describes various applications of carbon nanotubes in nanofluidic-based devices. There are great medical challenges in the field. For example, paper [6] studies selective killing of cancer cells by nanoparticle-assisted ultrasound. The author discovered that if the cell membrane contains gold nanoparticles then cancer cell membranes are destroyed by ultrasound with essentially greater probability than that for the corresponding normal cell. To give a theoretical explanation of the phenomenon, one needs a mathematical model. A way to its creation lies through an assumption that the cell membrane is a viscous fluid. Models of such type exist (see, e.g., [7]) but there is no rigorous mathematical background. The aim of this paper is mathematical (more precisely, asymptotic) analysis of viscous plate model. This creates a basis for the following construction of a thin viscous layer containing nanoparticles. One can obtain a solvable model by considering the nanoparticle as a point-like obstacle, so-called stokeslet (see, e.g., [8,9]). The mathematical background of the approach is given by the operator extensions theory (see, e.g., [10,11]). We will describe the nanoparticle inclusions in the following paper.

Asymptotic analysis is made with respect to small parameter, ratio of the transversal and longitudinal sizes of the viscous layer. Scaling analysis allows us to reveal the orders of terms. We obtained equations describing terms of different orders. Finally, we come back to dimensional form of these equations.

### 2. Problem description

We consider a viscous layer of thickness  $h(t, x, y)$ , which is bounded by two surfaces  $z = H(t, x, y) - h(t, x, y)/2$  and  $z = H(t, x, y) + h(t, x, y)/2$ . Here the center-surface is denoted by  $z = H(t, x, y)$ . This configuration is illustrated in Fig. 1.

We will study layer's behavior under action of arbitrary volumetric and surface forces. The fluid dynamics is described by Navier-Stokes equations [12]:

$$\rho(\partial_t \mathbf{v} + (\mathbf{v} \cdot \nabla) \mathbf{v}) = \nabla \cdot \sigma + \mathbf{f}, \quad (1)$$

$$\nabla \cdot \mathbf{v} = 0, \quad (2)$$

where  $\rho$  is the fluid density,  $\mathbf{v} = (u, v, w)$  is the velocity vector,  $\mathbf{f} = (f_x, f_y, f_z)^T$  is the volumetric force vector,  $\sigma$  is the stress tensor defined as

$$\sigma = -p\mathbf{I} + \mu(\nabla \mathbf{v} + (\nabla \mathbf{v})^T), \quad (3)$$

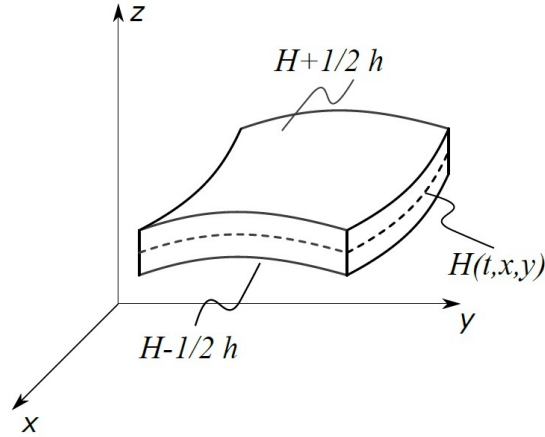


FIG. 1. A viscous layer

where  $\mathbf{I}$  is the unit tensor,  $p$  is the pressure,  $\mu = \mu(x, y)$  is the fluid's dynamic viscosity.

In addition, we set the boundary conditions on the free surfaces. They include the conditions on stress:

$$\mathbf{n}^{\pm} \cdot \boldsymbol{\sigma}^{\pm} \cdot \mathbf{e}_x = F_x^{\pm}, \quad (4)$$

$$\mathbf{n}^{\pm} \cdot \boldsymbol{\sigma}^{\pm} \cdot \mathbf{e}_y = F_y^{\pm}, \quad (5)$$

$$\mathbf{n}^{\pm} \cdot \boldsymbol{\sigma}^{\pm} \cdot \mathbf{e}_z = F_z^{\pm}, \quad (6)$$

where  $\mathbf{n}^{\pm}$  are normal vectors to the top and bottom surfaces,  $\boldsymbol{\sigma}^{\pm}$  are values of the stress tensor on the free surfaces,  $\mathbf{e}_x, \mathbf{e}_y, \mathbf{e}_z$  are Cartesian basis vectors,  $F_x^{\pm}, F_y^{\pm}, F_z^{\pm}$  are applied surface stresses.

Finally, the kinematic conditions take the form:

$$\partial_t H \pm \frac{1}{2} \partial_t h + u \left( \partial_x H \pm \frac{1}{2} \partial_x h \right) + v \left( \partial_y H \pm \frac{1}{2} \partial_y h \right) - w = 0. \quad (7)$$

Here the sign “+” is related to the top free surface, and “-” – to the bottom surface.

### 3. Scaling analysis

The governing equations (1)–(7) describes dynamics of the layer, but they are highly nonlinear and difficult to solve. And the main challenge is that due to free surfaces the computation domain is unknown and should be resolved along with velocity and pressure fields. However, we can employ the fact that the considered layer has a small thickness comparing to characteristic length and carry out asymptotic analysis. The first step is scaling analysis.

We define the longitudinal and transversal spatial scales as  $L$  and  $H_0$  correspondingly and introduce parameter  $\varepsilon = H_0/L$ , which we will exploit as a small parameter. As for the velocity scale, we will not vary the longitudinal and transversal directions, as done in the works [13–15]. Instead, we choose a universal scale  $U$ , which will be discussed later. The viscosity scale is denoted by  $\mu_0$  and the pressure scale is chosen in the way to meet the scale of viscous stresses.

The dimensionless variables are introduced in the following way:

$$\begin{aligned} \tilde{x} &= \frac{x}{L}, & \tilde{y} &= \frac{y}{L}, & \tilde{z} &= \frac{z}{H_0}, & \tilde{H} &= \frac{H}{H_0}, & \tilde{h} &= \frac{h}{H_0}, & \tilde{t} &= \frac{H_0}{U} t, \\ \tilde{\mu} &= \frac{\mu}{\mu_0}, & \tilde{u} &= \frac{u}{U}, & \tilde{v} &= \frac{v}{U}, & \tilde{w} &= \frac{w}{U}, & \tilde{p} &= \frac{H_0}{\mu_0 U} p, \\ \tilde{f}_x &= \frac{f_x}{\mathcal{F}_{\parallel}}, & \tilde{f}_y &= \frac{f_y}{\mathcal{F}_{\parallel}}, & \tilde{f}_z &= \frac{f_z}{\mathcal{F}_{\perp}}, & \tilde{F}_x &= \frac{F_x}{\mathfrak{F}_{\parallel}}, & \tilde{F}_y &= \frac{F_y}{\mathfrak{F}_{\parallel}}, & \tilde{F}_z &= \frac{F_z}{\mathfrak{F}_{\perp}}, \end{aligned}$$

where the scales of volumetric forces  $\mathcal{F}_{\parallel}, \mathcal{F}_{\perp}$  and surface stresses  $\mathfrak{F}_{\parallel}, \mathfrak{F}_{\perp}$  will be discussed further. The introduced dimensionless variables imply scales for the stress tensor components.

The introduced scales imply scaling of the stress tensor  $\sigma$ :

$$\begin{aligned}\tilde{\sigma}_{xx} &= \frac{H_0}{\mu_0 U} \sigma_{xx}, & \tilde{\sigma}_{xy} &= \varepsilon \frac{H_0}{\mu_0 U} \sigma_{xy}, & \tilde{\sigma}_{yy} &= \frac{H_0}{\mu_0 U} \sigma_{yy}, \\ \tilde{\sigma}_{xz} &= \frac{H_0}{\mu_0 U} \sigma_{xz}, & \tilde{\sigma}_{yz} &= \frac{H_0}{\mu_0 U} \sigma_{yz}, & \tilde{\sigma}_{zz} &= \frac{H_0}{\mu_0 U} \sigma_{zz}.\end{aligned}$$

Further we will omit the sign  $\tilde{\phantom{\sigma}}$  over dimensionless variables in the sake of simplicity.

Components of the stress tensor are expressed as:

$$\begin{aligned}\sigma_{xx} &= -p + 2\varepsilon\mu\partial_x u, & \sigma_{yy} &= -p + 2\varepsilon\mu\partial_y v, & \sigma_{zz} &= -p + 2\mu\partial_z w, \\ \sigma_{xy} &= \sigma_{yx} = \mu(\partial_y u + \partial_x v), & \sigma_{xz} &= \sigma_{zx} = \mu(\partial_z u + \varepsilon\partial_x w), & \sigma_{yz} &= \sigma_{zy} = \mu(\partial_z v + \varepsilon\partial_y w).\end{aligned}\quad (8)$$

The equations (1)–(2) takes the dimensional form:

$$ReI_u = \varepsilon\partial_x\sigma_{xx} + \varepsilon^2\partial_y\sigma_{xy} + \partial_z\sigma_{xz} + \frac{H_0^2\mathcal{F}_{\parallel}}{\mu_0 U} f_x, \quad (9)$$

$$ReI_v = \varepsilon^2\partial_x\sigma_{yx} + \varepsilon\partial_y\sigma_{yy} + \partial_z\sigma_{yz} + \frac{H_0^2\mathcal{F}_{\parallel}}{\mu_0 U} f_y, \quad (10)$$

$$ReI_w = \varepsilon\partial_x\sigma_{zx} + \varepsilon\partial_y\sigma_{zy} + \partial_z\sigma_{zz} + \frac{H_0^2\mathcal{F}_{\perp}}{\mu_0 U} f_z, \quad (11)$$

$$\varepsilon\partial_x u + \varepsilon\partial_y v + \partial_z w = 0, \quad (12)$$

where Reynold number  $Re$  is defined as:

$$Re = \frac{\rho U H_0}{\mu_0},$$

and the inertial terms are denoted as:

$$I_u = (\partial_t u + \varepsilon u \partial_x u + \varepsilon v \partial_y u + w \partial_z u), \quad (13)$$

$$I_v = (\partial_t v + \varepsilon u \partial_x v + \varepsilon v \partial_y v + w \partial_z v), \quad (14)$$

$$I_w = (\partial_t w + \varepsilon u \partial_x w + \varepsilon v \partial_y w + w \partial_z w). \quad (15)$$

The boundary conditions (4)–(6) takes the form:

$$\sigma_{xz} - \varepsilon\sigma_{xx} \left( \partial_x H \pm \frac{1}{2} \partial_x h \right) - \varepsilon^2\sigma_{xy} \left( \partial_y H \pm \frac{1}{2} \partial_y h \right) = \mp \frac{H_0 \mathfrak{F}_{\parallel}}{\mu_0 U} \frac{F_x^{\pm}}{N^{\pm}}, \quad (16)$$

$$\sigma_{yz} - \varepsilon^2\sigma_{yx} \left( \partial_x H \pm \frac{1}{2} \partial_x h \right) - \varepsilon\sigma_{yy} \left( \partial_y H \pm \frac{1}{2} \partial_y h \right) = \mp \frac{H_0 \mathfrak{F}_{\parallel}}{\mu_0 U} \frac{F_y^{\pm}}{N^{\pm}}, \quad (17)$$

$$\sigma_{zz} - \varepsilon\sigma_{zx} \left( \partial_x H \pm \frac{1}{2} \partial_x h \right) - \varepsilon\sigma_{zy} \left( \partial_y H \pm \frac{1}{2} \partial_y h \right) = \mp \frac{H_0 \mathfrak{F}_{\perp}}{\mu_0 U} \frac{F_z^{\pm}}{N^{\pm}}, \quad (18)$$

where:

$$N^{\pm} = \left( 1 + \varepsilon^2 \left( \partial_x H + \frac{1}{2} \partial_x h \right)^2 + \varepsilon^2 \left( \partial_y H + \frac{1}{2} \partial_y h \right)^2 \right)^{-1/2}. \quad (19)$$

Kinematic condition (7) is rewritten as:

$$w = \partial_t H \pm \frac{1}{2} \partial_t h + \varepsilon \left[ u \left( \partial_x H \pm \frac{1}{2} \partial_x h \right) + v \left( \partial_y H \pm \frac{1}{2} \partial_y h \right) \right]. \quad (20)$$

#### 4. Viscous plate equations

The equation (9) can be treated as a first order equation on  $\sigma_{xz}$ , which can be solved, giving:

$$\sigma_{xz} = \sigma_{xz}|_{-} + \int_{-}^z \left[ ReI_u - \varepsilon\partial_x\sigma_{xx} - \varepsilon^2\partial_y\sigma_{xy} - \frac{H_0^2\mathcal{F}_{\parallel}}{\mu_0 U} f_x \right] dz', \quad (21)$$

where  $\sigma_{xz}|_-$  is the value of  $\sigma_{xz}$  at the bottom surface  $H - h/2$  taken from the boundary conditions, and the lower integration limit  $z|_-$  is denoted to the surface  $H - h/2$ . In addition, this solution should satisfy the boundary conditions on the top surface  $H + h/2$ . It leads to the solvability condition of the equation (9):

$$\sigma_{xz}|_+ = \sigma_{xz}|_- + \int_{-}^{+} \left[ ReI_u - \varepsilon \partial_x \sigma_{xx} - \varepsilon^2 \partial_y \sigma_{xy} - \frac{H_0^2 \mathcal{F}_{\parallel}}{\mu_0 U} f_x \right] dz,$$

where the integrals are taken over the interval from  $H - h/2$  to  $H + h/2$ .

Using the rule of integral differentiation and accounting for boundary conditions (16), we come to the following form of the solvability condition:

$$\varepsilon \partial_x \left[ \int_{-}^{+} \sigma_{xx} dz \right] + \varepsilon^2 \partial_y \left[ \int_{-}^{+} \sigma_{xy} dz \right] = Re \bar{I}_u - \frac{H_0^2 \mathcal{F}_{\parallel}}{\mu_0 U} \bar{f}_x + \frac{H_0 \mathfrak{F}_{\parallel}}{\mu_0 U} \left( \frac{F_x^+}{N^+} + \frac{F_x^-}{N^-} \right), \quad (22)$$

where  $\bar{I}_u$ ,  $\bar{f}_x$  are thickness-averaged inertia terms and volumetric force:

$$\bar{I}_u = \int_{-}^{+} I_u dz, \quad \bar{f}_x = \int_{-}^{+} f_x dz.$$

Treating two other components of equation (9) in the same way we get the expressions of  $\sigma_{yz}$ ,  $\sigma_{zz}$ :

$$\sigma_{yz} = \sigma_{yz}|_- + \int_{-}^{z} \left[ ReI_v - \varepsilon^2 \partial_x \sigma_{yx} - \varepsilon \partial_y \sigma_{yy} - \frac{H_0^2 \mathcal{F}_{\parallel}}{\mu_0 U} f_y \right] dz', \quad (23)$$

$$\sigma_{zz} = \sigma_{zz}|_- + \int_{-}^{z} \left[ ReI_w - \varepsilon \partial_x \sigma_{zx} - \varepsilon \partial_y \sigma_{zy} - \frac{H_0^2 \mathcal{F}_{\perp}}{\mu_0 U} f_z \right] dz' \quad (24)$$

and solvability conditions for (10)–(11):

$$\varepsilon^2 \partial_x \left[ \int_{-}^{+} \sigma_{yx} dz \right] + \varepsilon \partial_y \left[ \int_{-}^{+} \sigma_{yy} dz \right] = Re \bar{I}_v - \frac{H_0^2 \mathcal{F}_{\parallel}}{\mu_0 U} \bar{f}_y + \frac{H_0 \mathfrak{F}_{\parallel}}{\mu_0 U} \left( \frac{F_y^+}{N^+} + \frac{F_y^-}{N^-} \right), \quad (25)$$

$$\varepsilon \partial_x \left[ \int_{-}^{+} \sigma_{zx} dz \right] + \varepsilon \partial_y \left[ \int_{-}^{+} \sigma_{zy} dz \right] = Re \bar{I}_w - \frac{H_0^2 \mathcal{F}_{\perp}}{\mu_0 U} \bar{f}_z + \frac{H_0 \mathfrak{F}_{\perp}}{\mu_0 U} \left( \frac{F_z^+}{N^+} + \frac{F_z^-}{N^-} \right). \quad (26)$$

Consider the integral  $\int_{-}^{+} \sigma_{zx} dz$ , which after differentiation by parts and accounting for (9) can be written as:

$$\begin{aligned} \int_{-}^{+} \sigma_{zx} dz &= (z - H) \sigma_{zx}|_{-}^{+} - \int_{-}^{+} (z - H) \partial_z \sigma_{zx} dz = \\ &= (z - H) \sigma_{zx}|_{-}^{+} + \varepsilon \int_{-}^{+} (z - H) \partial_x \sigma_{xx} dz + \varepsilon^2 \int_{-}^{+} (z - H) \partial_y \sigma_{xy} dz + \\ &\quad + \frac{H_0^2 \mathcal{F}_{\parallel}}{\mu_0 U} \int_{-}^{+} (z - H) f_x dz - Re \int_{-}^{+} (z - H) I_u dz. \end{aligned}$$

Applying integral differentiation rule we get:

$$\begin{aligned} \int_{-}^{+} \sigma_{zx} dz = & \\ = \varepsilon \partial_x \left[ \int_{-}^{+} (z-H) \sigma_{xx} dz \right] & + \varepsilon^2 \partial_y \left[ \int_{-}^{+} (z-H) \sigma_{xy} dz \right] + \varepsilon \partial_x H \int_{-}^{+} \sigma_{xx} dz + \varepsilon^2 \partial_y H \int_{-}^{+} \sigma_{xy} dz + \\ & + \frac{H_0^2 \mathcal{F}_{\parallel}}{\mu_0 U} \int_{-}^{+} (z-H) f_x dz - Re \int_{-}^{+} (z-H) I_u dz - \frac{H_0 \mathfrak{F}_{\parallel}}{\mu_0 U} h \left( \frac{F_x^+}{N^+} - \frac{F_x^-}{N^-} \right). \end{aligned} \quad (27)$$

Calculating  $\int_{-}^{+} \sigma_{zy} dz$  in the same way and substituting the obtained expressions in (26), we get the final form of the third solvability condition:

$$\begin{aligned} \varepsilon \partial_x \left\{ \varepsilon \partial_x \left[ \int_{-}^{+} (z-H) \sigma_{xx} dz \right] + \varepsilon^2 \partial_y \left[ \int_{-}^{+} (z-H) \sigma_{xy} dz \right] + \right. & \\ \left. + \varepsilon \partial_x H \int_{-}^{+} \sigma_{xx} dz + \varepsilon^2 \partial_y H \int_{-}^{+} \sigma_{xy} dz \right\} + & \\ + \varepsilon \partial_y \left\{ \varepsilon^2 \partial_x \left[ \int_{-}^{+} (z-H) \sigma_{yx} dz \right] + \varepsilon \partial_y \left[ \int_{-}^{+} (z-H) \sigma_{yy} dz \right] + \right. & \\ \left. + \varepsilon^2 \partial_x H \int_{-}^{+} \sigma_{yx} dz + \varepsilon \partial_y H \int_{-}^{+} \sigma_{yy} dz \right\} = & \\ = -\frac{H_0^2 \mathcal{F}_{\perp}}{\mu_0 U} \bar{f}_z - \varepsilon \frac{H_0^2 \mathcal{F}_{\parallel}}{\mu_0 U} \left[ \partial_x \left( \int_{-}^{+} (z-H) f_x dz \right) + \partial_y \left( \int_{-}^{+} (z-H) f_y dz \right) \right] + & \\ + \frac{H_0 \mathfrak{F}_{\perp}}{\mu_0 U} \left( \frac{F_z^+}{N^+} + \frac{F_z^-}{N^-} \right) + \varepsilon \frac{H_0 \mathfrak{F}_{\parallel}}{\mu_0 U} \left[ \partial_x \left( \frac{h}{2} \left( \frac{F_x^+}{N^+} - \frac{F_x^-}{N^-} \right) \right) + \partial_y \left( \frac{h}{2} \left( \frac{F_y^+}{N^+} - \frac{F_y^-}{N^-} \right) \right) \right] + & \\ + Re \left\{ \bar{I}_w + \varepsilon \partial_x \left[ \int_{-}^{+} (z-H) I_u dz \right] + \varepsilon \partial_y \left[ \int_{-}^{+} (z-H) I_v dz \right] \right\}. \end{aligned} \quad (28)$$

Further, we will consider systems with  $Re = O(\varepsilon^4)$ . The force scales  $\mathcal{F}_{\parallel}$ ,  $\mathcal{F}_{\perp}$ ,  $\mathfrak{F}_{\parallel}$ ,  $\mathfrak{F}_{\perp}$  we define from (22), (25), (28). We focus on the cases, when external forces are balanced by viscous stresses, which implies:

$$\begin{aligned} \mathcal{F}_{\parallel} &= \varepsilon^2 \frac{\mu_0 U}{H_0^2}, & \mathfrak{F}_{\parallel} &= \varepsilon^2 \frac{\mu_0 U}{H_0}, \\ \mathcal{F}_{\perp} &= \varepsilon^3 \frac{\mu_0 U}{H_0^2}, & \mathfrak{F}_{\perp} &= \varepsilon^3 \frac{\mu_0 U}{H_0}. \end{aligned}$$

In addition to the equations of dynamics (9)–(11), we consider continuity equation (12). Integrating it with respect to  $z$ -coordinate, we find:

$$w = w|_{-} - \varepsilon \int_{-}^z \partial_x u + \partial_y v dz. \quad (29)$$

As before, applying boundary conditions on the top surface leads to the solvability condition:

$$\partial_t h + \varepsilon \partial_x (h \bar{u}) + \varepsilon \partial_y (h \bar{v}) = 0, \quad (30)$$

where thickness-averaged velocities  $\bar{u}$ ,  $\bar{v}$  are found as:

$$\bar{u} = \frac{1}{h} \int_{-}^{+} u dz, \quad \bar{v} = \frac{1}{h} \int_{-}^{+} v dz.$$

Finally, we find the form of average vertical velocity  $\bar{w}$ . Integrating the expression (29), employing the equation (12) and using the boundary conditions we get:

$$\bar{w} = \partial_t H + \varepsilon h^{-1} \left[ \partial_x \left( \int_{-}^{+} (z - H) u dz \right) + \partial_x H \int_{-}^{+} u dz + \partial_y \left( \int_{-}^{+} (z - H) v dz \right) + \partial_y H \int_{-}^{+} v dz \right]. \quad (31)$$

Note that, in general, the average velocity  $\bar{w}$  is not equal to the velocity of the center surface  $\partial_t H$ .

In the subsequent analysis, we will focus on the cases, when  $F_x^{\pm} = F_y^{\pm} = 0$ ,  $\partial_z f_x = \partial_z f_y = 0$ . Then the equations (22), (25), (28) can be written in simpler form, similar to elastic plate equations:

$$\varepsilon^{-1} \partial_x N_{xx} + \partial_y N_{xy} = \varepsilon^2 Re^* \bar{I}_u - \bar{f}_x, \quad (32)$$

$$\partial_x N_{yx} + \varepsilon^{-1} \partial_y N_{yy} = \varepsilon^2 Re^* \bar{I}_v - \bar{f}_y, \quad (33)$$

$$\partial_x Q_x + \partial_y Q_y = \varepsilon Re^* \left[ \bar{I}_w + \varepsilon \left( \partial_x \bar{I}_u + \partial_y \bar{I}_v \right) \right] - \bar{f}_z + \left( \frac{F_z^+}{N^+} + \frac{F_z^-}{N^-} \right), \quad (34)$$

where the effective in-plane stresses are defined as:

$$N_{xx} = \int_{-}^{+} \sigma_{xx} dz, \quad N_{yy} = \int_{-}^{+} \sigma_{yy} dz, \quad N_{xy} = N_{yx} = \int_{-}^{+} \sigma_{xy} dz, \quad (35)$$

the residual forces are:

$$Q_x = \varepsilon^{-1} \partial_x M_{xx} + \varepsilon^{-1} N_{xx} \partial_x H + \partial_y M_{xy} + N_{xy} \partial_y H, \quad (36)$$

$$Q_y = \partial_x M_{yx} + N_{yx} \partial_x H + \varepsilon^{-1} \partial_y M_{yy} + \varepsilon^{-1} N_{yy} \partial_y H \quad (37)$$

and bending moments are:

$$M_{xx} = \int_{-}^{+} (z - H) \sigma_{xx} dz, \quad (38)$$

$$M_{xy} = M_{yx} = \int_{-}^{+} (z - H) \sigma_{xy} dz, \quad (39)$$

$$M_{yy} = \int_{-}^{+} (z - H) \sigma_{yy} dz, \quad (40)$$

symbols  $\bar{I}_u$ ,  $\bar{I}_v$ ,  $\bar{I}_w$  are denoted to the moments of inertial forces:

$$\bar{I}_u = \int_{-}^{+} (z - H) I_u dz, \quad \bar{I}_v = \int_{-}^{+} (z - H) I_v dz, \quad \bar{I}_w = \int_{-}^{+} (z - H) I_w dz. \quad (41)$$

## 5. Asymptotic solution

Up to now we just rearranged non-dimensional Navier-Stokes equations without using the small parameter expansion. Now we are going to find velocity distribution through thickness, expanding the variables on small parameter:

$$A = A^{(0)} + \varepsilon A^{(1)} + \varepsilon^2 A^{(2)} + o(\varepsilon^2).$$

From the equations (21), (23) we have in zero order

$$\sigma_{xz}^{(0)} = 0, \quad (42)$$

$$\sigma_{yz}^{(0)} = 0, \quad (43)$$

or

$$\begin{aligned}\mu\partial_z u^{(0)} &= 0, \\ \mu\partial_z v^{(0)} &= 0,\end{aligned}$$

which has the following solution:

$$u^{(0)} = \bar{u}^{(0)}(t, x, y), \tag{44}$$

$$v^{(0)} = \bar{v}^{(0)}(t, x, y). \tag{45}$$

The continuity equation (12) implies:

$$\partial_z w^{(0)} = 0,$$

thus

$$w^{(0)} = \bar{w}^{(0)}(t, x, y). \tag{46}$$

Finally, for  $zz$ -stress in zero order, we have:

$$\sigma_{zz}^{(0)} = 0, \tag{47}$$

therefore

$$-p^{(0)} + 2\mu\partial_z w^{(0)} = 0$$

or, taking into account (46),

$$p^{(0)} = 0. \tag{48}$$

Note that:

$$\sigma_{xx}^{(0)} = \sigma_{yy}^{(0)} = -p^{(0)} = 0.$$

Since the equations (32)–(34) include terms of the order  $\varepsilon^{-1}$ , the obtained expressions are not enough. We have to continue with analysis of the first order.

Due to (21) the stress  $\sigma_{xz}$  in the first order is equal to

$$\sigma_{xz}^{(1)} = \sigma_{xx}^{(0)} \Big|_- \left( \partial_x H - \frac{1}{2} \partial_x h \right) - \int_-^+ \partial_x \sigma_{xx}^{(0)} dz, \tag{49}$$

where the right-hand side is zero. Thus:

$$\mu \left( \partial_z u^{(1)} + \partial_x \bar{w}^{(0)} \right) = 0.$$

And we get that:

$$u^{(1)} = \partial_x \bar{w}^{(0)}(H - z) + \bar{u}^{(1)}. \tag{50}$$

In the same way, we obtain that:

$$\sigma_{xz}^{(1)} = 0, \tag{51}$$

$$v^{(1)} = \partial_y \bar{w}^{(0)}(H - z) + \bar{v}^{(1)}. \tag{52}$$

The continuity equation (12) in the first order is written as:

$$\partial_z w^{(1)} = -\partial_x u^{(0)} - \partial_y v^{(0)}. \tag{53}$$

The value of  $\partial_z w^{(1)}$  will be used for calculating the stress  $\sigma_{zz}^{(1)}$ , which is equal to:

$$\sigma_{zz}^{(1)} = \sigma_{zx}^{(0)} \Big|_- \left( \partial_x H - \frac{1}{2} \partial_x h \right) + \sigma_{zy}^{(0)} \Big|_- \left( \partial_y H - \frac{1}{2} \partial_y h \right) - \int_-^+ \left( \partial_x \sigma_{zx}^{(0)} + \partial_y \sigma_{zy}^{(0)} \right) dz, \tag{54}$$

where the right-hand side vanishes. Therefore:

$$-p^{(1)} + 2\mu\partial_z w^{(1)} = 0$$

and taking into account (53) we get

$$p^{(1)} = -2\mu \left( \partial_x u^{(0)} + \partial_y v^{(0)} \right). \tag{55}$$

As for the next order,  $\varepsilon^2$ , we consider only the continuity equation:

$$\partial_z w^{(2)} = -\partial_x u^{(1)} - \partial_y v^{(1)} \tag{56}$$

and equation (24):

$$\sigma_{zz}^{(2)} = \sigma_{zx}^{(1)} \Big|_{-} \left( \partial_x H - \frac{1}{2} \partial_x h \right) + \sigma_{zy}^{(1)} \Big|_{-} \left( \partial_y H - \frac{1}{2} \partial_y h \right) - \int_{-}^{+} \left( \partial_x \sigma_{zx}^{(1)} + \partial_y \sigma_{zy}^{(1)} \right) dz, \quad (57)$$

where the right-hand side is zero again. Therefore, we get:

$$p^{(2)} = -2\mu \left( \partial_x u^{(1)} + \partial_y v^{(1)} \right). \quad (58)$$

Finally, using the expression for longitudinal velocity  $u$  (44), (50) and  $v$  (45), (52), pressure  $p$  (48), (55), (58) we obtain stress distributions across thickness

$$\sigma_{xx} = 2\varepsilon\mu \left\{ 2\partial_x \left[ \bar{u}^{(0)} + \varepsilon \left( \partial_x \left( \bar{w}^{(0)}(H-z) \right) + \bar{u}^{(1)} \right) \right] + \partial_y \left[ \bar{v}^{(0)} + \varepsilon \left( \partial_y \left( \bar{w}^{(0)}(H-z) \right) + \bar{v}^{(1)} \right) \right] \right\} + O(\varepsilon^3), \quad (59)$$

$$\sigma_{xy} = \mu \left\{ \partial_y \left[ \bar{u}^{(0)} + \varepsilon \left( \partial_x \left( \bar{w}^{(0)}(H-z) \right) + \bar{u}^{(1)} \right) \right] + \partial_x \left[ \bar{v}^{(0)} + \varepsilon \left( \partial_y \left( \bar{w}^{(0)}(H-z) \right) + \bar{v}^{(1)} \right) \right] \right\} + O(\varepsilon^2), \quad (60)$$

$$\sigma_{yy} = 2\varepsilon\mu \left\{ \partial_x \left[ \bar{u}^{(0)} + \varepsilon \left( \partial_x \left( \bar{w}^{(0)}(H-z) \right) + \bar{u}^{(1)} \right) \right] + 2\partial_y \left[ \bar{v}^{(0)} + \varepsilon \left( \partial_y \left( \bar{w}^{(0)}(H-z) \right) + \bar{v}^{(1)} \right) \right] \right\} + O(\varepsilon^3). \quad (61)$$

Integrating it through thickness, we find effective stresses:

$$N_{xx} = 2\varepsilon\mu h \left\{ 2 \left[ \partial_x \left( \bar{u}^{(0)} + \varepsilon \bar{u}^{(1)} \right) + \varepsilon \partial_x \bar{w}^{(0)} \partial_x H \right] + \left[ \partial_y \left( \bar{v}^{(0)} + \varepsilon \bar{v}^{(1)} \right) + \varepsilon \partial_y \bar{w}^{(0)} \partial_y H \right] \right\} + O(\varepsilon^3), \quad (62)$$

$$N_{xy} = \mu h \left[ \partial_y \left( \bar{u}^{(0)} + \varepsilon \bar{u}^{(1)} \right) + \partial_x \left( \bar{v}^{(0)} + \varepsilon \bar{v}^{(1)} \right) + \varepsilon \left( \partial_x \bar{w}^{(0)} \partial_y H + \partial_y \bar{w}^{(0)} \partial_x H \right) \right] + O(\varepsilon^2), \quad (63)$$

$$N_{yy} = 2\varepsilon\mu h \left\{ \left[ \partial_x \left( \bar{u}^{(0)} + \varepsilon \bar{u}^{(1)} \right) + \varepsilon \partial_x \bar{w}^{(0)} \partial_x H \right] + 2 \left[ \partial_y \left( \bar{v}^{(0)} + \varepsilon \bar{v}^{(1)} \right) + \varepsilon \partial_y \bar{w}^{(0)} \partial_y H \right] \right\} + O(\varepsilon^3). \quad (64)$$

and bending moments:

$$M_{xx} = -\varepsilon^2 \frac{\mu h^3}{6} \left( 2\partial_{xx}^2 \bar{w}^{(0)} + \partial_{yy}^2 \bar{w}^{(0)} \right) + O(\varepsilon^3), \quad (65)$$

$$M_{xy} = -\varepsilon \frac{\mu h^3}{6} \partial_{xy}^2 \bar{w}^{(0)} + O(\varepsilon^2), \quad (66)$$

$$M_{yy} = -\varepsilon^2 \frac{\mu h^3}{6} \left( \partial_{xx}^2 \bar{w}^{(0)} + 2\partial_{yy}^2 \bar{w}^{(0)} \right) + O(\varepsilon^3). \quad (67)$$

Substituting (62)–(67) in equations (32)–(34), we obtain with accuracy of  $O(\varepsilon^2)$

$$\varepsilon^{-1} \partial_x N_{xx} + \partial_y N_{xy} = -\bar{f}_x, \quad (68)$$

$$\partial_x N_{yx} + \varepsilon^{-1} \partial_y N_{yy} = -\bar{f}_y, \quad (69)$$

$$\partial_x Q_x + \partial_y Q_y = \varepsilon R e^* \partial_t w^{(0)} - \bar{f}_z + (F_z^+ + F_z^-). \quad (70)$$

Then, the continuity equation (30) takes the form:

$$\partial_t h + \varepsilon \partial_x (h \bar{u}^{(0)}) + \varepsilon \partial_y (h \bar{v}^{(0)}) = 0, \quad (71)$$

and the average vertical velocity is equal to the center surface velocity:

$$\bar{w}^{(0)} = \partial_t H. \quad (72)$$

## 6. Dimensional equations

In this section, we come back to dimensional variables. First, we collect the expansion for average velocities:

$$\bar{u} = \bar{u}^{(0)} + \varepsilon \bar{u}^{(1)} + O(\varepsilon^2),$$

$$\bar{v} = \bar{v}^{(0)} + \varepsilon \bar{v}^{(1)} + O(\varepsilon^2),$$

$$\bar{w} = \bar{w}^{(0)} + O(\varepsilon).$$

Then we can rearrange the equation and rewrite them in dimensional form:

$$\partial_t h + \partial_x(h\bar{u}) + \partial_y(h\bar{v}) = 0, \quad (73)$$

$$\partial_x N_{xx} + \partial_y N_{xy} = -\bar{f}_x, \quad (74)$$

$$\partial_x N_{yx} + \partial_y N_{yy} = -\bar{f}_y, \quad (75)$$

$$\partial_x Q_x + \partial_y Q_y = \rho h \partial_t \bar{w} - \bar{f}_z + (F_z^+ + F_z^-), \quad (76)$$

where the membrane stresses are defined as:

$$N_{xx} = 2\mu h [2(\partial_x \bar{u} + \partial_x \bar{w} \partial_x H) + (\partial_y \bar{v} + \partial_y \bar{w} \partial_y H)], \quad (77)$$

$$N_{xy} = \mu h (\partial_y \bar{u} + \partial_x \bar{w} \partial_y H + \partial_x \bar{v} + \partial_y \bar{w} \partial_x H), \quad (78)$$

$$N_{yy} = 2\mu h [(\partial_x \bar{u} + \partial_x \bar{w} \partial_x H) + 2(\partial_y \bar{v} + \partial_y \bar{w} \partial_y H)]. \quad (79)$$

the residual forces depend on bending moments and membrane stresses:

$$Q_x = \partial_x M_{xx} + \partial_y M_{xy} + N_{xx} \partial_x H + N_{xy} \partial_y H, \quad (80)$$

$$Q_y = \partial_x M_{yx} + \partial_y M_{yy} + N_{yx} \partial_x H + N_{yy} \partial_y H, \quad (81)$$

and the bending moments are calculated as:

$$M_{xx} = -\frac{\mu h^3}{6} (2\partial_{xx}^2 \bar{w} + \partial_{yy}^2 \bar{w}), \quad (82)$$

$$M_{xy} = -\frac{\mu h^3}{6} \partial_{xy}^2 \bar{w}, \quad (83)$$

$$M_{yy} = -\frac{\mu h^3}{6} (\partial_{xx}^2 \bar{w} + 2\partial_{yy}^2 \bar{w}). \quad (84)$$

The average vertical velocity is expressed as:

$$\bar{w} = \partial_t H. \quad (85)$$

Finally, the average volumetric forces are calculated in the following way:

$$\bar{f}_x = \int_{-}^{+} f_x dz, \quad \bar{f}_y = \int_{-}^{+} f_y dz, \quad \bar{f}_z = \int_{-}^{+} f_z dz. \quad (86)$$

Equations (73)–(86) form the viscous plate model. They include terms up to the order of  $O(\varepsilon)$ . The variables to solve for are the averaged velocities  $\bar{u}$ ,  $\bar{v}$ , the deflection  $H$  and the thickness  $h$ . However, from computational point of view it is convenient to keep the unknown variable  $\bar{w}$ .

For the finite plate, the equations should be accompanied by boundary conditions along the plate's perimeter. It can be clamped, hinged or free conditions similar to those for elastic plates.

## 7. Discussion

During the model derivation we made the assumption that both deflection  $H$  and thickness  $h$  are of the same scale  $H_0$ , which is much smaller than plate's length. However, we didn't impose any restrictions on the ratio  $H/h$ . In contrast, classical elastic plate linear theory is applicable only in the cases  $H/h \ll 1$ . Indeed, the derived equations are analogous to non-linear elastic plate theory (see, e.g., [16]). It is worth noting that inertial effects appears even for quite small Reynolds numbers  $Re \sim \varepsilon^4$ .

As we mentioned before, there are two classical problems regarding viscous plate: stretching and bending. These two effects are described by different scales for velocities. In order to cover them within one model, these problems were solved separately and then matching asymptotic series was done [13–15]. Our approach has the benefit of the unique velocity scale.

Let's consider the system with no transversal forces  $f_z$ ,  $F_z^\pm$ . In this case, it is enough to consider only  $\bar{u}^{(0)}$ ,  $\bar{v}^{(0)}$  for calculation of (59)–(61). Then non-linear terms in (62)–(64), which include  $\bar{w}^{(0)}$ , are of higher order

and can be neglected. The bending moments (65)–(67) vanishes, and equation (70) implies  $H = 0$ . Thus, plate's stretching is described by continuity equation (73) and stress balance equations (74)–(75).

Pure bending can be considered when applied longitudinal forces are zero. Then zero-order equations (32)–(32) have the only solution  $\bar{u}^{(0)} = \bar{v}^{(0)} = 0$ , which together with (71) imply constant-in-time thickness  $\partial_t h = 0$ . The corresponding longitudinal velocities becomes of order  $\varepsilon$ .

In more involved cases bending and stretching occurs simultaneously. In particular, it happens in the cases of large deflections, when bending implies stretching. The latter effectively makes the system stiffer.

Different external influences can be treated as applied forces. For example, nanoparticles can be seen as pointwise forces, applied at the surface.

### Acknowledgements

This work was partially financially supported by the Government of the Russian Federation (grant 08-08), by grant 16-11-10330 of Russian Science Foundation.

### References

- [1] Rudyak V., Belkin A. Molecular dynamics simulation of fluid viscosity in nanochannels. *Nanosystems: Phys. Chem. Math.*, 2018, **9**(3), P. 349–355.
- [2] Jiang Y., Yu Z., Huang X., Chen R., Chen W., Zeng Y., Xu Ch., Min H., Zheng N., Cheng X. A multilayer lateral-flow microfluidic device for particle separation. *Microfluid Nanofluid*, 2018, **22**, P. 40.
- [3] Celebi A.T., Barisik M., Beskok A. Surface charge-dependent transport of water in graphene nano-channels. *Microfluid Nanofluid*, 2018, **22**, P. 7.
- [4] Erfle P., Riewe J., Bunjes H., Dietzel A. Optically monitored segmented flow for controlled ultra-fast mixing and nanoparticle precipitation. *Microfluid Nanofluid*, 2017, **21**, P. 179.
- [5] Ghasemi A., Amiri H., Zare H., Masroor M., Hasanzadeh A., Beyzavi A., Aref A.R., Karimi M., Hamblin M.R. Carbon nanotubes in microfluidic lab-on-a-chip technology: current trends and future perspectives. *Microfluid Nanofluid*, 2017, **21**, P. 151.
- [6] Kosheleva O.K., Lai T.C., Chen N.G., Hsiao V., Chen Ch.H. Selective killing of cancer cells by nanoparticle-assisted ultrasound. *J. Nanobiotechnol.*, 2016, **14**, P. 46.
- [7] Okamoto R., Kanemori Y., Komura Sh., Fournier J.-B. Relaxation dynamics of two-component fluid bilayer membranes. *Eur. Phys. J. E*, 2016, **39**, P. 52.
- [8] Hackborn W.W. Asymmetric Stokes flow between parallel planes due to a rotlet. *J. Fluid Mech.*, 1990, **218**, P. 631–646.
- [9] Pozrikidis C. Computation of periodic Green's functions of Stokes flow. *J. Engineering Math.*, 1996, **30**, P. 79–96.
- [10] Gugel Yu.V., Popov I.Yu., Popova S.L. Hydrotron: creep and slip. *Fluid. Dyn. Res.*, 1996, **18**(4), P. 199–210.
- [11] Popov I.Y., Blinova I.V., Kyz'yurova K.N. Stokes flow driven by a Stokeslet in a cone. *Acta Mechanica*, 2014, **225**, P. 3115–3121.
- [12] Landau L.D., Lifshitz E.M. *Fluid Mechanics*, 2nd ed., Vol. 6. Pergamon Press, Oxford.: 1993. 532 p.
- [13] Ribe, N.M. Bending and stretching of thin viscous sheets. *Journal of Fluid Mechanics*, 2001, **433**, P. 135–160.
- [14] Ribe, N.M. A general theory for the dynamics of thin viscous sheets. *Journal of Fluid Mechanics*, 2002, **457**, P. 255–283.
- [15] Pflingst, G., Audoly, B., Boudaoud, A. Linear and nonlinear stability of floating viscous sheets. *Journal of Fluid Mechanics*, 2011, **683**, P. 112–148.
- [16] Timoshenko, S., Woinowsky-Krieger, S. *Theory of plates and shells*. McGraw-Hill, New York.: 1959, P. 595 p.

## Wave dynamics on time-dependent graph with Aharonov–Bohm ring

D. A. Eremin<sup>1</sup>, E. N. Grishanov<sup>1</sup>, D. S. Nikiforov<sup>2</sup>, I. Y. Popov<sup>2</sup>

<sup>1</sup>Department of Mathematics and IT, Ogarev Mordovia State University  
Bolshevistskaya Str. 68, Saransk, Russia

<sup>2</sup>Department of Higher Mathematics, ITMO University,  
Kroverkskiy pr. 49, St. Petersburg, 197101, Russia

ereminda@mail.ru, evgenyg@mail.ru, dmitrii.nikiforov@gmail.com, popov1955@gmail.com

PACS 03.65.-w, 02.30.Tb, 02.10.Db, 73.63.Nm

DOI 10.17586/2220-8054-2018-9-4-457-463

Aharonov–Bohm ring (AB ring) is an element frequently used in nanosystems. The paper deals with wave dynamics on quantum graph consisting of AB ring coupled to a segment. It is assumed that the lengths of the edges vary in time. Variable replacement is made to come to the problem for stationary geometric graph. The obtained equation is solved using the expansion with respect to a complete system of eigenfunctions of the unperturbed self-adjoint operator for the stationary graph. The coefficients of the expansion are found as solutions of a system of differential equations numerically. The influence of the magnetic field is studied. The comparison with the case of stable geometric graph is made.

**Keywords:** quantum graph, Aharonov–Bohm ring.

*Received:* 15 June 2018

*Revised:* 18 July 2018

### 1. Introduction

Nanostructures in a magnetic field attract great attention of physicists due to its interesting behavior. Many of these properties, e.g., giant magnetoresistance, have found wide range of applications in nanotechnology, computer hardware, etc. One of the basic elements for nanostructures in a magnetic field is Aharonov–Bohm ring [1], i.e. a nano-sized conducting ring in a magnetic field orthogonal to the ring plane. The Aharonov–Bohm effect was observed and studied in many physical situations (see, e.g., [2–6]). For such structures, quantum graph model is actively used [7–10]. It is a rather effective mathematical model allowing one to describe the spectral and transport properties of many complex physical systems [11–15]. We consider a quantum graph with edge lengths varying in time. Although this model is very interesting from a physical point of view (see, e.g., [16]), there are only a few works devoted to this problem. One can mention papers concerning the time-dependent boundary conditions [17] or time dependent point-like interactions [18], but consideration of time-dependent graphs began recently [19–23]. Wave dynamics for time-dependent quantum graphs in a magnetic field was not studied previously. There are only works concerning Aharonov–Bohm rings in fluctuating magnetic field (see, e.g., [24]). In the present paper, we construct and study a model of time-dependent quantum graph with loop in magnetic field. We investigate the dependence of the dynamics on a magnetic field.

### 2. Model

#### 2.1. Graph description

We consider quantum graph  $\Gamma$  with a loop (ring) shown in Fig. 1. It is assumed that the magnetic field acts at the ring. Lengths of graph edges, ring ( $L_r(t)$ ) and segment ( $L_\ell(t)$ ), vary in time in accordance with the following relations:

$$\begin{cases} L_r(t) = 2\pi rL(t), \\ L_\ell(t) = lL(t), \end{cases} \quad (1)$$

where  $r, l$  are constants,  $L(t)$  is some twice continuously differentiable function. Obviously,  $L_r(t)$  and  $L_\ell(t)$  should be positive.

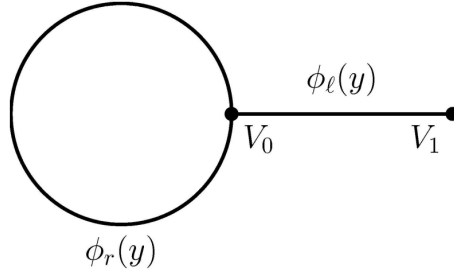


FIG. 1. Geometrical structure of the graph

## 2.2. Schrödinger operator on the graph

We start with the problem corresponding to the absence of a magnetic field. It means free Schrödinger operator acts on edges of the graph:

$$\begin{cases} i\hbar \frac{\partial}{\partial t} \Psi_r(x, t) = -\frac{\hbar^2}{2m} \frac{\partial^2}{\partial x^2} \Psi_r(x, t), & 0 \leq x \leq L_r(t), \\ i\hbar \frac{\partial}{\partial t} \Psi_\ell(x, t) = -\frac{\hbar^2}{2m} \frac{\partial^2}{\partial x^2} \Psi_\ell(x, t), & 0 \leq x \leq L_\ell(t). \end{cases} \quad (2)$$

We look for continuous solution satisfying the Kirchhoff conditions at the central vertex  $V_0$  and the Dirichlet conditions at the boundary one  $V_1$ :

$$\begin{cases} \Psi_\ell(0, t) = \Psi_r(0, t) = \Psi_r(L_r(t), t), \\ \Psi_\ell(L_\ell(t), t) = 0, \\ \frac{\partial}{\partial x} \Psi_\ell(0, t) + \frac{\partial}{\partial x} \Psi_r(0, t) - \frac{\partial}{\partial x} \Psi_r(L_r(t), t) = 0. \end{cases} \quad (3)$$

We replace variables in (2), (3) to obtain a problem with non-varying edges:

$$\begin{cases} y = \frac{x}{L(t)}, \\ t_1 = t, \end{cases} \quad (4)$$

Further,  $t_1$  is mentioned as  $t$  for simplicity. After the replacement, we come to the following equations:

$$\begin{cases} i \frac{\partial}{\partial t} \Psi_r = -\frac{1}{L^2} \frac{\partial^2}{\partial y^2} \Psi_r + i \frac{\dot{L}}{L} y \frac{\partial}{\partial y} \Psi_r, & 0 \leq x \leq 2\pi r, \\ i \frac{\partial}{\partial t} \Psi_\ell = -\frac{1}{L^2} \frac{\partial^2}{\partial y^2} \Psi_\ell + i \frac{\dot{L}}{L} y \frac{\partial}{\partial y} \Psi_\ell, & 0 \leq x \leq l. \end{cases} \quad (5)$$

Here  $\dot{L} = dL/dt$ . The boundary conditions remain the same as (3). The appearing factor  $L(t)$  in the last condition can be omitted due to its positivity.

Thus, we obtained the problem for stable geometric graph. To solve it, we will use eigenfunctions of the stationary Schrödinger operator. The corresponding problem for such quantum graph (with the length of segment equals  $l$  and the radius of the ring equals  $r$ ) has the form:

$$\begin{aligned} -\frac{d^2}{dy^2} \phi_\ell(y) &= k^2 \phi_\ell(y), 0 \leq y \leq l, \\ -\frac{d^2}{dy^2} \phi_r(y) &= k^2 \phi_r(y), 0 \leq y \leq 2\pi r, \\ \begin{cases} \phi_\ell(0) = \phi_r(0) = \phi_r(2\pi r), \\ \phi_\ell(l) = 0, \\ \frac{d}{y} \phi_l|_{y=0} + \frac{d}{dy} \phi_r|_{y=0} - \frac{d}{dy} \phi_r|_{y=2\pi r} = 0. \end{cases} \end{aligned}$$

The eigenfunctions are as follows

$$\begin{aligned}\phi_\ell^{(n)}(y) &= \frac{\sin(k_n(l-y))}{B_n \sin(k_n)}, \\ \phi_r^{(n)}(y) &= \frac{\cos(k_n(y-\pi r))}{B_n \cos(k_n \pi r)},\end{aligned}$$

the normalizing coefficient is

$$B_n^2 = \frac{1}{2 \sin^2(k_n l)} + \frac{\pi r}{\cos^2(\pi k_n r)},$$

and  $k_n$  is  $n$ -th root of characteristic equation

$$2 \tan(\pi k r) = \cot k l.$$

Dealing with stationary geometric graph, we can expand solution into a series of the eigenfunctions which form a complete set as eigenfunctions of self-adjoint operator:

$$\begin{pmatrix} \psi_\ell(y, t) \\ \psi_r(y, t) \end{pmatrix} = \sum_n c_n(t) \begin{pmatrix} \phi_\ell^{(n)}(y) \\ \phi_r^{(n)}(y) \end{pmatrix}. \tag{6}$$

After the substitution of expansion (6) into equations (5), multiplication by  $\phi_r^{(m)}$  and  $\phi_\ell^{(m)}$ , correspondingly, summation of the both equations and integration of the obtained expression over graph  $\Gamma$ , we come to a system of ordinary differential equations for coefficients  $c_n(t)$  of the expansion:

$$\dot{c}_m(t) + i \frac{k_m^2}{L^2} c_m - \sum_n c_n \frac{\dot{L}}{L} \int_\Gamma y \frac{\partial \phi^{(n)}}{\partial y} \phi^{(m)} dy = 0. \tag{7}$$

The system is truncated and solved numerically. We will discuss it in the next section, where the analogous procedure will be applied to the graph in a magnetic field.

### 2.3. Quantum graph in magnetic field

In the model, it is assumed that we have different operators acting at the loop and at the segment. While at the segment, we deal with the free Schrödinger operator, at the loop we consider the Landau operator, i.e. the Schrödinger operator with a magnetic field:

$$\begin{cases} i\hbar \frac{\partial}{\partial t} \Psi_r(x, t) = \frac{\hbar^2}{2m} \left( -i \frac{\partial}{\partial x} + \frac{\Phi(t)}{L(t)\Phi_0} \right)^2 \Psi_r(x, t), & 0 \leq x \leq L_r(t), \\ i\hbar \frac{\partial}{\partial t} \Psi_\ell(x, t) = -\frac{\hbar^2}{2m} \frac{\partial^2}{\partial x^2} \Psi_\ell(x, t), & 0 \leq x \leq L_\ell(t), \end{cases} \tag{8}$$

where the magnetic flux is  $\Phi(t) = \pi r^2 L^2(t) B$ ,  $\Phi_0$  is the magnetic flux quantum and  $B$  is constant magnetic field.

After variables replacement (4), one obtains:

$$\begin{cases} i\hbar \left( -\frac{\dot{L}}{L} y \frac{\partial}{\partial y} \Psi_r(y, t) + \frac{\partial}{\partial t} \Psi_r(y, t) \right) = \\ -\frac{\hbar^2}{2m} \frac{1}{L^2} \frac{\partial^2}{\partial y^2} \Psi_r(y, t) - i \frac{\hbar^2}{m} \frac{\Phi}{L\Phi_0} \frac{1}{L} \frac{\partial}{\partial y} \Psi_r(y, t) + i \frac{\hbar^2}{m} \frac{\Phi^2}{L^2 \Phi_0^2} \Psi_r(y, t), & 0 \leq y \leq l_0, \\ i\hbar \left( -\frac{\dot{L}}{L} y \frac{\partial}{\partial y} \Psi_\ell(y, t) + \frac{\partial}{\partial t} \Psi_\ell(y, t) \right) = -\frac{\hbar^2}{2m} \frac{1}{L^2} \frac{\partial^2}{\partial y^2} \Psi_\ell(y, t). \end{cases} \tag{9}$$

To solve the equations, we use the expansion with respect to the complete system of eigenfunctions of the free stationary Schrödinger operator on the stationary graph:

$$\begin{pmatrix} \Psi_\ell(y, t) \\ \Psi_r(y, t) \end{pmatrix} = \sum_n C_n(t) \begin{pmatrix} \phi_\ell^{(n)}(y) \\ \phi_r^{(n)}(y) \end{pmatrix}. \tag{10}$$

We put expansion (10) into equations (9) and multiply the both sides by  $\phi_r^{(m)}$  and  $\phi_\ell^{(m)}$ , correspondingly. Then, we summarize both equations and integrate the expression over graph  $\Gamma$ . Finally, we come to a system of ordinary

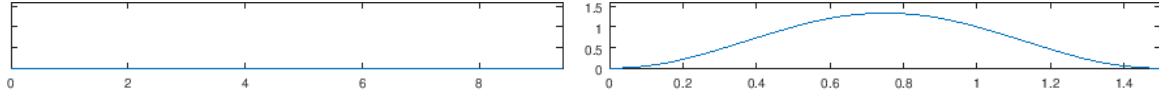


FIG. 2. Wave function modulo. Left – at the ring, right – at the segment;  $t = 0.0$  (Initial function) (arbitrary units)

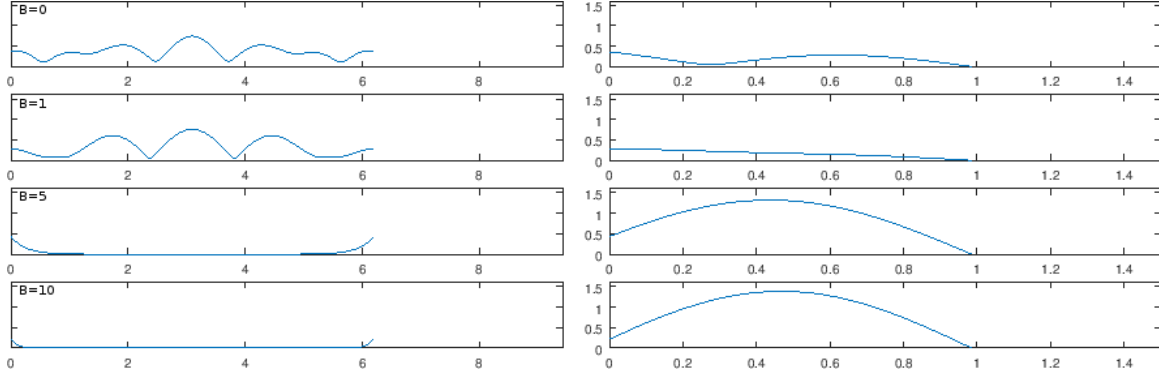


FIG. 3. Wave function modulo for different values of  $B$ . Left – at the ring, right – at the segment;  $t = 1.6$  (arbitrary units)

differential equations for coefficients  $C_n(t)$  of expansion (10):

$$\begin{aligned} \dot{C}_m + i \frac{\hbar}{2m} \frac{k_m^2}{L^2} C_m - \sum_n C_n \frac{\dot{L}}{L} \left( \int_0^{2\pi r} y \frac{\partial \phi_r^{(n)}}{\partial y} \phi_r^{(m)} dy + \int_0^l y \frac{\partial \phi_\ell^{(n)}}{\partial y} \phi_\ell^{(m)} dy \right) \\ + \frac{\hbar}{m} \frac{\pi r B}{\Phi_0} \sum_n C_n \int_0^{2\pi r} \frac{\partial \phi_r^{(n)}}{\partial y} \phi_r^{(m)} dy + i \frac{\hbar}{2m} \frac{\pi^2 r^2 L^2 B^2}{\Phi_0^2} \sum_n C_n \int_0^{2\pi r} \phi_\ell^{(n)} \phi_\ell^{(m)} dy = 0. \end{aligned} \quad (11)$$

### 3. Results and discussion

The initial conditions for system (11) are obtained from the initial condition for the wave function:

$$C_n(0) = \int_0^{2\pi r} \Psi_r(y, 0) \phi_r^{(n)} dy + \int_0^l \Psi_\ell(y, 0) \phi_\ell^{(n)} dy. \quad (12)$$

We choose the initial value of the wave function in the following form:

$$\begin{aligned} \Psi_r(y, 0) &= 0, \\ \Psi_\ell(y, 0) &= (1 - \cos 2\pi y) \sqrt{\frac{2}{3}}. \end{aligned}$$

Other parameters are chosen in the following way:

$$\begin{aligned} L(t) &= a + b \cos \omega t, \quad a = 1, \quad b = 0.5, \quad \omega = 1, \\ \hbar &= 2m = 1, \quad l = r = 1. \end{aligned}$$

System (11) is infinite. To solve it numerically, we make a truncation. We increase the number of equations up to the moment when the result becomes stable.

Results for  $B = 0, 1, 5, 10$  are shown in Fig. 2–6. One can see that an increase of the magnetic field lead to greater localization of the solution at the segment and to stabilization of the wave function.

The stabilization of the wave function is observed. Comparing results for the graph having constant lengths of edges ( $L = 1$ ) and for the time-dependent graph, one can see that in the stationary case, the magnetic field can stabilize the solution more quickly. Results for  $B = 5$  are shown in Fig. 7–9.

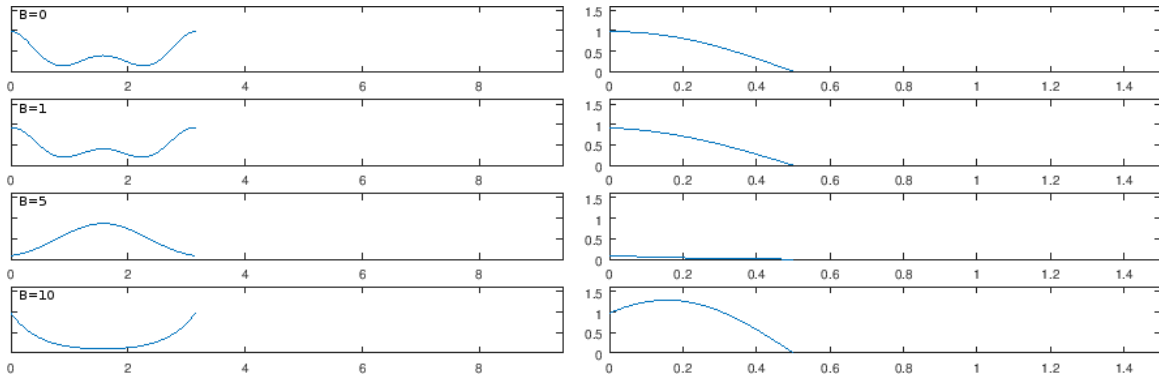


FIG. 4. Wave function modulo for different values of  $B$ . Left – at the ring, right – at the segment;  $t = 3.24$  (arbitrary units)

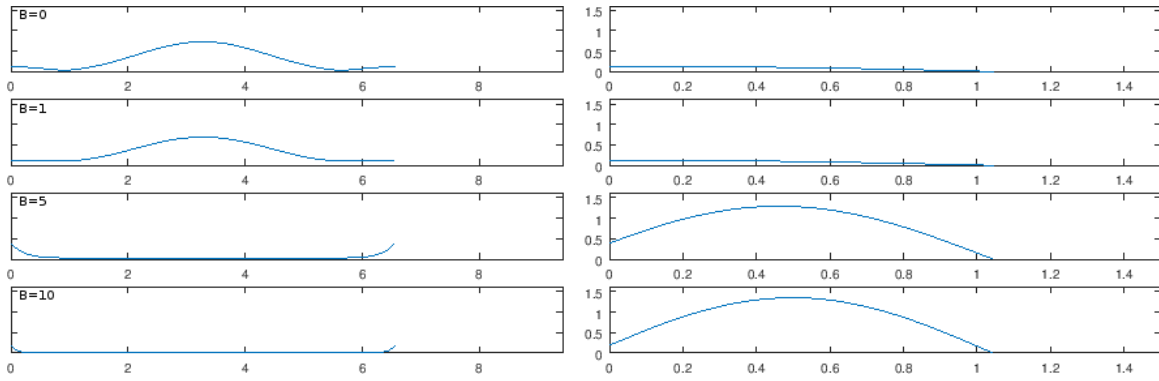


FIG. 5. Wave function modulo for different values of  $B$ . Left – at the ring, right – at the segment;  $t = 4.8$  (arbitrary units)

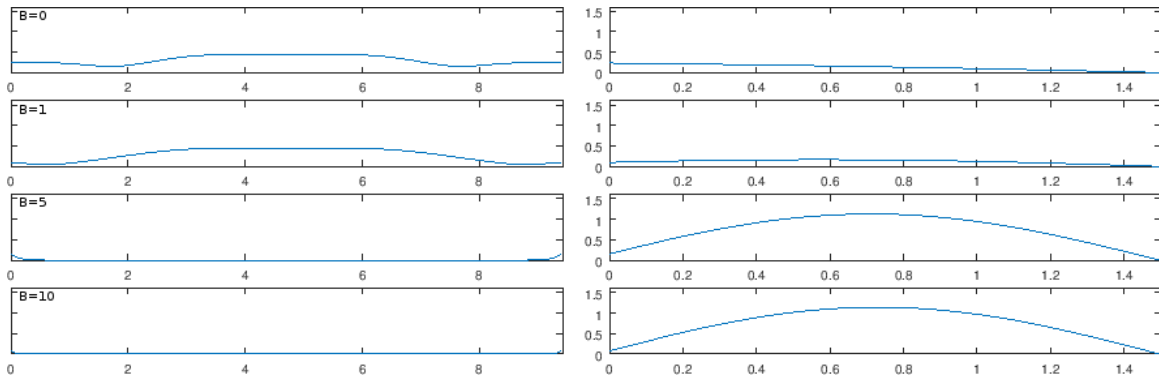


FIG. 6. Wave function modulo for different values of  $B$ . Left – at the ring, right – at the segment;  $t = 6.4$  (arbitrary units)

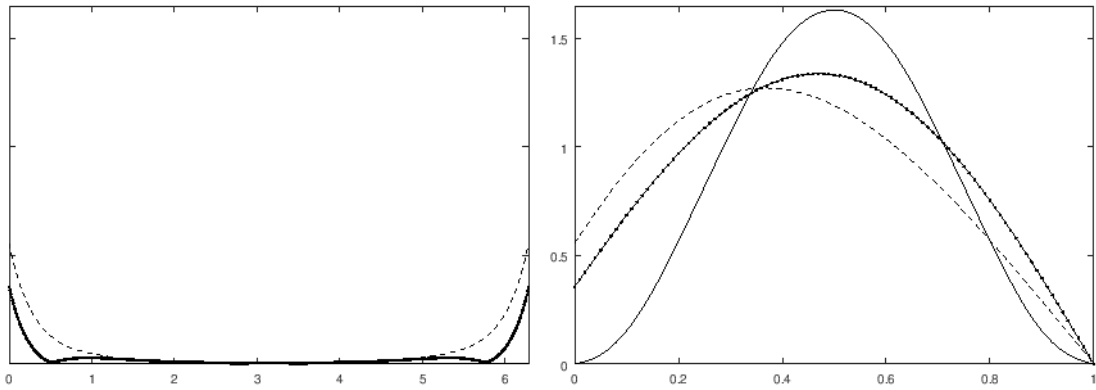


FIG. 7. Wave function modulo for  $B = 5$ . Left – at the ring, right – at the segment; thin curve –  $t = 0.0$ , dotted curve –  $t = 0.2$ , solid curve –  $t = 0.4$  (arbitrary units)

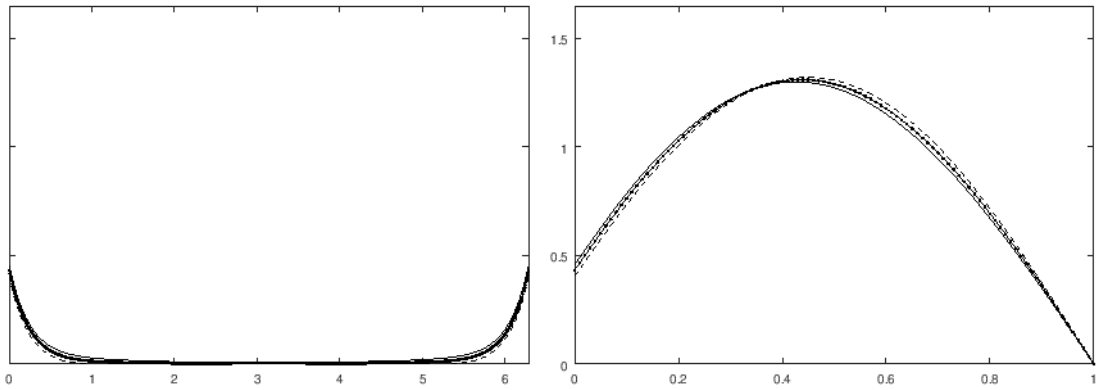


FIG. 8. Wave function modulo for  $B = 5$ . Left – at the ring, right – at the segment; thin curve –  $t = 0.6$ , dotted curve –  $t = 0.8$ , solid curve –  $t = 1.0$  (arbitrary units)

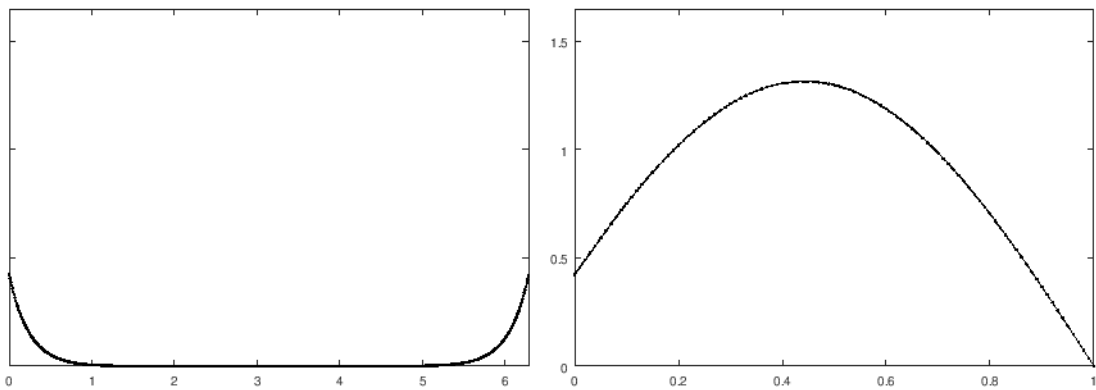


FIG. 9. Wave function modulo for  $B = 5$ . Left – at the ring, right – at the segment; thin curve –  $t = 1.2$ , dotted curve –  $t = 1.4$ , solid curve –  $t = 1.6 \dots$  (arbitrary units)

## Acknowledgements

This work was partially financially supported by the Government of the Russian Federation (grant 08-08), by grant 16-11-10330 of Russian Science Foundation.

## References

- [1] Aharonov Y., Bohm D. Significance of electromagnetic potentials in the quantum theory. *Phys. Rev.*, 1959, **115**, P. 485–491.
- [2] Léna C. Eigenvalues variations for Aharonov-Bohm operators. *J. Math. Phys.*, 2015, **56**, P. 011502.
- [3] Fischer A.M., CampoV.L., Jr., Portnoi M.E., Romer R.A. Exciton Storage in a Nanoscale AharonovBohm Ring with Electric Field Tuning. *Phys. Rev. Lett.*, 2009, **102**, P. 096405.
- [4] Entin-Wohlman O., Imry Y., Aharony A. Effects of external radiation on biased Aharonov-Bohm rings. *Phys. Rev. B*, 2004, **70**, P. 075301.
- [5] Shelykh I. A., Galkin N. G., Bagraev N. T. Conductance of a gated AharonovBohm ring touching a quantum wire, *Phys. Rev. B*, 2006, **74**, P. 165331.
- [6] Nichele F., Komijani Y., Hennel S., Ger C., Wegscheider W., Reuter D., Wieck A. D., Ihn T., Ensslin K. AharonovBohm rings with strong spinorbit interaction: the role of sample-specific properties. *New J. Phys.*, 2013, **15**, P. 033029
- [7] Kurasov P., Enerbäck. Aharonov-Bohm ring touching a quantum wire: ow to model it and to solve the inverse problem. *Rep. Math. Phys.*, 2011, **68**, P. 271–287.
- [8] Kokoreva M. A., Margulis V. A., Pyataev M. A. Electron transport in a two-terminal AharonovBohm ring with impurities. *Physica E*, 2011, **43**, P. 1610–1634.
- [9] Kokoreva M. A., Pyataev M. A. Spectral and transport properties of one-dimensional nanoring superlattice. *Int. J. Mod. Phys. B*, 2013, **27**(20), P. 1350103.
- [10] Grishanov E.N., Eremin D.A., Ivanov D.A., Popov I.Y., Smirnov P.I. Periodic chain of disks in a magnetic field: bulk states and edge states. *Nanosystems: Physics, Chemistry, Mathematics.*, 2015, **6**(5), P. 637–643.
- [11] N. I. Gerasimenko, B. S. Pavlov, Scattering problems on noncompact graphs. *Theoret. Math. Phys.*, 1988, **74**, P. 230–240.
- [12] P. Exner, P. Keating, P. Kuchment, T. Sumada, A. Teplyaev, *Analysis on graph and its applications. Proc. Symp. Pure Math.* Providence, RI, 2008, **77**.
- [13] P. Duclos, P. Exner, O. Turek. On the spectrum of a bent chain graph. *J. Phys. A: Math. Theor.*, 2008, **41**, P. 415206/1-18.
- [14] I.Y.Popov, A.N.Skorynina, I.V.Blinova. On the existence of point spectrum for branching strips quantum graph. *J. Math. Phys.*, 2014, **55**, P. 033504/1-20.
- [15] I. Y. Popov, P. I. Smirnov, Spectral problem for branching chain quantum graph. *Phys. Lett.*, 2013, **A 377**, P. 439–442.
- [16] J.V. Jose, R. Gordery. Study of a quantum Fermi-acceleration model. *Phys. Rev. Lett.*, 1986, **56**, P. 290.
- [17] A.J. Makowski, S.T. Dembinski. Exactly solvable models with time-dependent boundary conditions. *Phys. Lett.*, 1991, **A,154**(5-6), P. 217–220.
- [18] C. Cacciapuoti, A. Mantile, A. Posilicano. Time dependent delta-prime interactions in dimension one. *Nanosystems: Phys. Chem. Math.*, 2016, **7**(2), P. 303–314.
- [19] Z.A. Sobirov, D.U. Matrasulov, Sh. Ataev and H. Yusupov In *Complex Phenomena in Nanoscale Systems. Eds. G. Casati, D. Matrasulov.* Berlin, Springer, 2009.
- [20] D.U. Matrasulov, J.R. Yusupov, K.K. Sabirov, Z.A. Sobirov. Time-dependent quantum graph. *Nanosystems: Phys. Chem. Math.*, 2015, **6**(2), P. 173–181.
- [21] O. Karpova, K. Sabirov, D. Otajanov, A. Ruzmetov, A.A. Saidov. Absorbing boundary conditions for Schrödinger equation in a time-dependent interval. *Nanosystems: Phys. Chem. Math.*, 2017, **8**(1), P. 13–19.
- [22] Eremin D.A., Grishanov E.N., Kostrov O.G., Nikiforov D.S., Popov I.Y. Time dependent quantum graph with loop. *Nanosystems: Physics, Chemistry, Mathematics*, 2017, **8**, P. 420–425.
- [23] Popov I.Y., Nikiforov D.S. Classical and quantum wave dynamics on time-dependent geometric graph. *Chinese Journal of Physics*. 2018, **56**(2), P. 747–753.
- [24] Marquardt F., Bruder C. Aharonov-Bohm ring with fluctuating flux. *Phys. Rev. B*, 2002, **65**, P. 125315.

## Methodology of analyzing the CdSe semiconductor quantum dots parameters

A. I. Mikhailov, V. F. Kabanov, E. G. Glukhovskoy, M. I. Shishkin, M. V. Gavrikov

Saratov State University, Department of Nanoand Biomedical Technologies,  
Astrakhanskaya 83, Saratov, 410012, Russia  
glukhovskoy@gmail.com

PACS 73.22.Dj, 73.21.La

DOI 10.17586/2220-8054-2018-9-4-464-467

Direct methods (using a laser particle size analyzer) and indirect (from the analysis of spectral characteristics and differential normalized tunnel CVC) methods of CdSe QD size estimation allowed determination of the size (4 – 5 nm) and shown good qualitative and quantitative agreement of the results with an error of less than 10 %. It is concluded that the tunnel differential CVC analysis is an effective method for express measurement that can be used in quantum-size object investigations.

**Keywords:** quantum dots, cadmium selenide, differential tunneling current-voltage characteristics, energy spectrum.

*Received:* 5 February 2018

*Revised:* 14 June 2018

### 1. Introduction

Semiconductor structures, used in solid-state electronic devices, can contain single or multiple and associated quantum-size objects. Quantum dots (QD) are one of the most interesting quantum-size structures in terms of application in optoelectronics and nanoelectronics.

Semiconductor compounds  $A^2B^6$  are among the most promising and interesting semiconductor materials from a practical point of view, and have been so for many years. These materials have a high luminescence quantum yield, photostability and are widely used in optoelectronics [1–4].

The purpose of this paper is to develop and substantiate a methodology for studying the electrophysical properties of a monolayer film structure of semiconductor quantum dots of the  $A^2B^6$  group (e.g. CdSe).

### 2. Samples obtaining technologies

CdSe quantum dots monolayers, formed on the water surface and transferred to solid substrates with an indium-tin oxide (ITO) conductive layer by using Langmuir–Blodgett technology, were investigated. The quantum dots were synthesized according to previously-described methodologies [5–7].

### 3. Research methods

The obtained samples were investigated by scanning tunneling microscopy (STM), laser particle size analyzer and optical spectroscopy methods.

In the optical spectroscopy method, a standard violet LED with 500 mCd luminous intensity and a spectrum maximum wavelength 380 nm was used as the primary excitation light source. Light from this source fell on a sample that was placed in a diffuse reflection attachment ( $0 - 45^\circ$ ), which allowed collection of light that was diffusely reflected from the sample and emitted by the sample (secondary). Then, the light passed through a band-pass filter, and in the long-wavelength part of the spectrum, a filter with a 360 – 600 nm transmission was automatically replaced by filter with a 600 – 1000 nm transmission. The measurement process was carried out in an automatic mode, the rate of the spectrum acquisition was 70 nm/min, and the sampling interval was 1 nm.

Scanning electron microscope (SEM) and optical spectroscopy methods may not always provide unambiguous interpretation of the experimental data, e.g. in situations when the quantum-size particle has an inhomogeneous structure or when the several particles form a conglomerate. In this case, for more complete analysis of the electrophysical properties of the obtained QD film samples, in particular, the electronic spectrum, we used STM. This method was realized by using a scanning probe microscope NANOEDUCATOR-2. Before the investigation of nanoparticles tunnel CVC, the film surface was scanned by STM methods in a constant current mode. After analysis of the obtained STM image of the sample's surface, 10 points on the surface were selected for the obtaining of CVC. At each point, not less than 10 CVC were obtained in automatic mode. Measurements were carried out for current values ranging from  $10^{-11}$  to  $10^{-7}$  A and voltage ranging from 0 to 5 V. By reproducibility of the measurement results, we selected points with stable characteristics, and after that, we averaged the obtained

CVC. The measurements results were processed according to the generally accepted methods for scanning probe microscopy of semiconductor nanostructures.

For the experimental tunnel CVC analysis, we used the differential CVC method – dependence  $(dI/dV)/(I/V)$  on the voltage  $V$  [8,9]. Additionally, as shown in [10,11], this method can be used for analyzing the investigated structures' conductivity mechanisms, parameter calculation and a number of other important electronic processes.

#### 4. Model and numerical estimates

The model of electrons tunneling through the energy levels of the discrete spectrum of the QD was considered in [12].

When QD model of a cubic shape with an edge  $a$ , the position of QD energy spectrum levels:

$$\varepsilon_i = \frac{(\pi \hbar)^2}{2 m^*} \cdot \frac{1}{a^2} \cdot (l^2 + m^2 + n^2), \quad (1)$$

where  $l, m, n = 1, 2, 3, \dots$  – are positive natural numbers corresponding to the level numbers;  $m^*$  – effective mass of the electron;  $a$  – characteristic size of the QD.

In the case of a spherical QD with radius  $a$  in the one-electron spectrum in a parabolic well approximation:

$$\varepsilon_i = \frac{(\pi \hbar)^2}{2 m^*} \cdot \frac{1}{a^2} \cdot (4n + 2l + 3), \quad (2)$$

where  $n$  – radial quantum number ( $n = 0, 1, 2, \dots$ );  $l$  – orbital quantum number ( $l = 0, 1, 2, \dots$ ).

The calculated electron energy values for the first three allowed energy levels (1, 2, 3) in accordance with (1), (2) for CdSe are shown in Fig. 1(b). The electron's effective mass value in the CdSe conduction band, used in calculations  $m^* = 0.13m_0$ , where  $m_0$  – is the free electron mass. In accordance with this model it is possible to estimate the QD characteristic size.

We considered and analyzed normalized differential tunneling CVC with a negative bias potential on the substrate relative to the probe (Fig. 1a). In this case, electrons tunnel from the ITO electrode through the discrete levels of a quantum-size object to the tunneling microscope probe. The conduction electron discrete energy spectrum of a quantum-size object determines the peaks on the normalized differential CVC (arrows in Fig. 1). The black solid line in Fig. 1a is a trend line constructed using linear filtering (by MS Excel tools).

The obtained values on the axis of the bias potential were put in correspondence with the energy values on the calculated energy spectrum dependence for the models used. For example, in Fig. 1, the peak values corresponded to 0.40 V; 0.62 V; 0.81 V. On the graphs of the energy spectra (Fig. 1b), this corresponds to a range of QD values of 4.4 – 4.8 nm for the “spherical” model and 4.3 – 5.4 nm for the “cubic” model.

Analysis of the peak's position on differential normalized tunnel CVC on the basis of averaging over a group of samples allowed us to estimate the linear size of quantum-size objects, which ranged from 4 – 5 nm (with an error in the peak's position measurement not more than  $2kT$ ). The use of a “spherical” QD model for the samples makes it possible to obtain more accurate size determination than the “cubic” QD model: the range of values on the “size” axis compared with the corresponding ranges of energy values is defined much more accurately (Fig. 1b).

To clarify the validity of this method based on the analysis of the peaks position on differential normalized tunnel CVC, in addition, we estimated the QD size by analyzing the spectral characteristics of the samples (Fig. 2). In Fig. 2, samples with different QD formation time (from 15 to 300 sec) are presented.

The QD size estimation, when considering Eqs. (1) and (2), the energy of the width of the material band gap  $\varepsilon_g = 1.74$  eV, and assuming that the change in the position of the QD first energy level  $\varepsilon_{c1}$  relative to the conduction band bottom of bulk material  $\varepsilon_c$  is several times greater than the corresponding change the valence band top energy  $\varepsilon_{v1}$  relatively  $\varepsilon_v$  (because  $m_n^* \ll m_p^*$ ), gave the result 4.1 – 5.1 nm.

The results of CdSe QD investigations using the Malvern ZetaSizer Nano ZS laser particle size analyzer are shown in Fig. 3.

The obtained results, with an assumed QD shell thickness of  $\sim 1$  nm, showed the characteristic QD size of 3.9 – 4.9 nm.

The processing of the investigated samples made it possible to conclude that the calculated QD sizes obtained by experimental differential tunnel CVC analysis, spectral characteristic analysis and measurement with a laser particle size analyzer are in good qualitative and quantitative agreement.

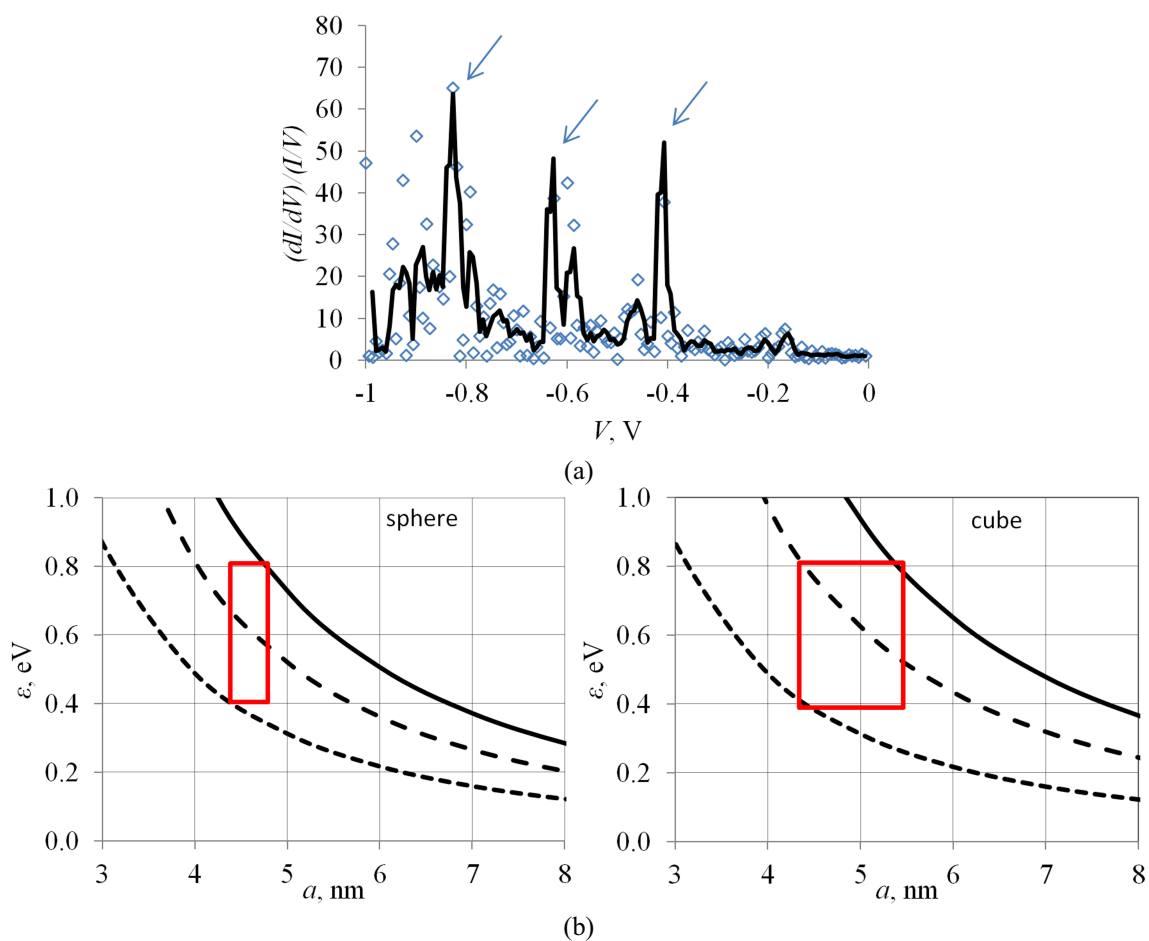


FIG. 1. Typical differential current-voltage characteristics of CdSe QD (a), (b) – accordance with the calculated levels of the energy spectrum according to the spherical QD model and according to the cubic QD model

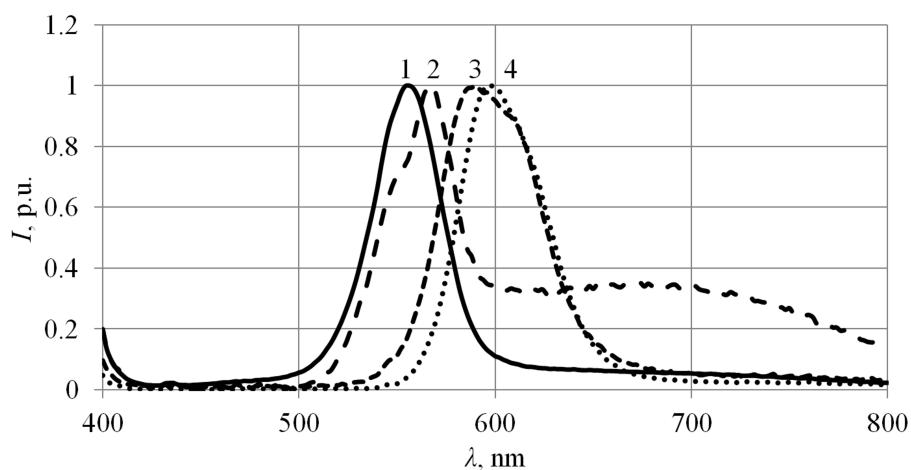


FIG. 2. Spectral characteristics of CdSe QD: 1, 2, 3, 4 – different samples

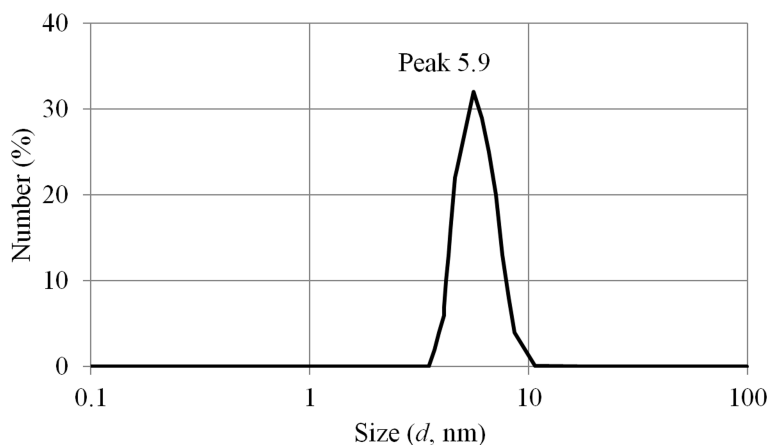


FIG. 3. CdSe QD size estimating using a laser particle size analyzer

## 5. Conclusions

Thus, based on the CdSe QD size estimate analysis, we can conclude that both direct (using a laser particle size analyzer) and indirect (from the analysis of spectral characteristics and differential normalized tunnel CVC) methods of QD size determination have shown good qualitative and quantitative agreement of the results with an error less than 10 %. Additionally, the differential normalized tunnel CVC analysis method made it possible to determine a more suitable model for determining the energy spectrum of the investigated samples – the spherical QD model. Moreover, this method can be used to analyze the conductivity mechanisms of investigated structures, as well as calculate parameters for many other important electronic processes. All this allows us to consider, that the differential normalized tunnel CVC method is an effective method for rapid quantification, which can be used in studies involving quantum-size objects.

## Acknowledgements

The authors are sincerely grateful to Prof. I. Goryacheva for provided samples of quantum dots. This work was supported by grants from the Russian Foundation for Basic Research Projects No. 16-07-00093 and No. 16-07-00185.

## References

- [1] Karpovich I.A. Quantum engineering: self-assembled quantum dots. *Soros educational journal*, 2001, **7** (11), P. 102–108 (in Russian).
- [2] Karpov S.V., Mikushev S.V. Electron-hole excitations in CdSe quantum dots under strong and intermediate confinement conditions. *Physics of the Solid State*, 2010, **52** (8), P. 1750–1756.
- [3] Boichuk V.I., Leshko. R.Ya., Holskyi V.B., Karpyn D.S. Optical spectra of small CdS nanocrystals. *Semiconductor Physics, Quantum Electronics & Optoelectronics*, 2016, **19** (4), P. 384–390.
- [4] Vitukhnovskii A.G., Vashchenko, A.A., Lebedev V.S., et al. Organic light-emitting diode with an emitter based on a planar layer of CdSe semiconductor nanoplatelets. *JETP Letters*, 2014, **100** (2), P. 86–90.
- [5] Reiss P., Protiere M., Li L. Core/shell semiconductor nanocrystals. *Small*, 2009, **5** (2), P. 154–168.
- [6] Speranskaya E.S., Gofman V.V., Goryacheva I.Yu. Preparation of water soluble zinc-blende CdSe/ZnS quantum dots. *Nanotechnologies in Russia*, 2013, **8** (1–2), P. 129–135.
- [7] Kosolapova K.I., Al-Alwani A.J.K., Gorbachev I.A., Glukhovskoy E.G. Purification non-aqueous solution of quantum dots CdSe-CdS-ZnS from excess organic substance-stabilizer by use PE-HD membrane. *J. Phys.: Conf. Ser.*, 2015, **643**, P. 012084(1–5).
- [8] Troyan V.I., Pushkin M.A., Borman V.D., Tronin V.N. *Physical basis of techniques for studying nanostructures and surface of solids*, Ed. by V.D. Borman, MEPhI, Moscow, 2008, 260 p. (in Russian).
- [9] Demikhovskii V.Ya., Filatov D.O. *Scanning probe microscopy study of electronic states in low-dimensional structures: learning guide on physicochemical fundamentals of nanotechnology*, Nizhny Novgorod, 2007, 77 p. (in Russian).
- [10] Mikhailov A.I., Kabanov V.F., Zhukov N.D. Peculiarities of field electron emission from submicron protrusions on a rough InSb surface. *Technical Physics Letters*, 2015, **41** (11), P. 1065–1067.
- [11] Mikhailov A.I., Kabanov V.F., et al. Electronic properties of A2B6 quantum dots incorporated into Langmuir-Blodgett films. *Bulletin of the Russian Academy of Sciences: Physics*, 2017, **81** (12), P. 1472–1475.
- [12] Mikhailov A.I., Kabanov V.F., Zhukov N.D., Glukhovskoy E.G. Features of the energy spectrum of quantum dots indium antimonide. *Nanosystems: Physics, Chemistry, Mathematics*, 2017, **8** (5), P. 596–599.

## Heat-treated nano-structured shungite rocks and electrophysical properties associated

S. V. Kovalevskii<sup>1</sup>, I. A. Moshnikov<sup>2</sup>, V. V. Kovalevski<sup>2</sup>

<sup>1</sup>“Shungiton” Ltd Company, Petrozavodsk, Russia

<sup>2</sup>Institute of Geology, Karelian Research Center, RAS, Petrozavodsk, Russia

semen.tlg@bk.ru , igorm@krc.karelia.ru, kovalevs@krc.karelia.ru

PACS 68.37.Og, 61.48.-c

DOI 10.17586/2220-8054-2018-9-4-468-472

Shungite rocks of two different types were treated at  $\sim 1400$  °C and a set of nanomaterials have been obtained. Among the different materials obtained were: carbon hollow fibers; spherical or ellipsoid particles; silicon carbide amorphous; crystalline nanofibers and nanoparticles having different morphologies; iron and iron silicide nanoparticles encapsulated into carbon shells. Measurements were performed for shielding effectiveness (SE) and the electrical conductivity ( $\sigma$ ) of untreated and heat-treated shungite rocks. The shungite rock with dominated hyperfullerene carbon is remarkable for a two-fold increase in the  $\sigma$  and a 10 dB increase in SE with a slight decrease of the carbon content by 1.5 % in relation to the untreated sample. In contrast, the treated shungite rock with high SiC nanofiber content is characterized by a halving of the  $\sigma$  and a 10 dB decrease in SE with a decrease of the carbon content by 6 % relative to the original sample.

**Keywords:** shungite rocks, carbon, carbon nano-sized shells and fibers, SiC nano-sized fibers, shielding effectiveness, electrical conductivity.

*Received:* 6 March 2018

*Revised:* 13 June 2018

### 1. Introduction

The shungite rocks of Karelia (Russia) form a large, diverse group of Precambrian carbon-bearing rocks with poorly-crystallized carbon (shungite) that can be characterized as natural composite materials. Shungite rocks have variable carbon content and mineral composition, which may contain quartz, mica, carbonates and traces of other minerals. Shungite has chemical composition consisting of C with traces of N, O, H and S. All types of these rocks have very variable physico-chemical properties, depending on the shungite structure, C content, the composition and characteristics of minerals and distribution of carbon and minerals in the shungite rocks. For example, type I rocks have a relatively low specific gravity ( $1.8 - 2.0$  g/cm<sup>3</sup>), high electric conductivity (about 100 S/cm), and some types have unusually high specific surface areas (up to 500 m<sup>2</sup>/g) as measured by the (BET) adsorption of gaseous nitrogen [1]. Shungite is remarkable for the noted occurrence of globules, 3-dimensional closed shells but, more commonly, fractions of such shells that are highly disordered into short bent stacks. Shungite demonstrates fullerene-like signs of the atomic, molecular and band structures [2].

In recent years, it becomes very relevant issue of improving the quality shungite natural raw materials by modification of carbon and mineral component under the influence of a relatively soft – biogenic, or an extreme physical and chemical treatment both in laboratory and natural environment. Practically important indicators of the transformations are the electrical conductivity and shielding effectiveness [3].

### 2. Experimental

Two shungite rocks with different mineral contents (Table 1) were treated at  $\sim 1400$  °C. The calculation of the content of the amorphous component (carbon) and crystalline phases were determined using the procedure provided with the software Siroquant on the diffractometer ARL X TRA and using zinc oxide (ZnO) as a standard (Fig. 1). The EM-125 electron microscope was used for transmission electron microscopy and selected area electron diffraction study. Trace element compositions of shungites were determined using the UP 266 laser system connected to an X-Series 2 Thermo Fisher Scientific ICP-MS in the Analytical Centre of Institute of Geology of the Karelian Research Centre of RAS (Table 2) [4].

Processes, which consisted of solid phase reactions, including catalytically initiated reactions, between micro- and nanominerals (quartz, mica) and noncrystalline carbon of shungite rocks, occurred at reaction temperature. As a result, a set of nanomaterials have been obtained, primarily, carbon in the form of hyperfullerene structures, hollow fibers (Fig. 2a) and hollow spherical or ellipsoid particles (Fig. 2b) formed by smoothly bent packets of carbon layers. Some were similar to onion-like or fullerene-like carbon spheres with promising electrophysical properties [5, 6]. Additionally, similar C-hollow particles have been found in the untreated shungite rocks and the rocks subjected to heating resulted from contact metamorphism [7]. The interaction between carbon and minerals

TABLE 1. Mineral composition and electrophysical properties of untreated and nano-structured shungite rocks

Mineral composition and properties	Shungite No. 1		Shungite No. 2	
	untreated	heat-treated	untreated	heat-treated
C %	55	56	46	40
Quartz	6	3	37	15
Muscovite	3	–	16	–
Pyrite	–	–	2	–
Chlorite	32	–	–	–
Albite	4	<2	–	–
Cristobalite	–	3	–	2
SiC	–	21	–	33
FeSi <sub>x</sub>	–	15	–	10
$\sigma$ (1 kHz), S/m	715	1530	340	140
SE (10/100/750 MHz), dB	53/54.5/71.5	61/67.5/–	46.5/47/55.5	38.5/38.6/41.5

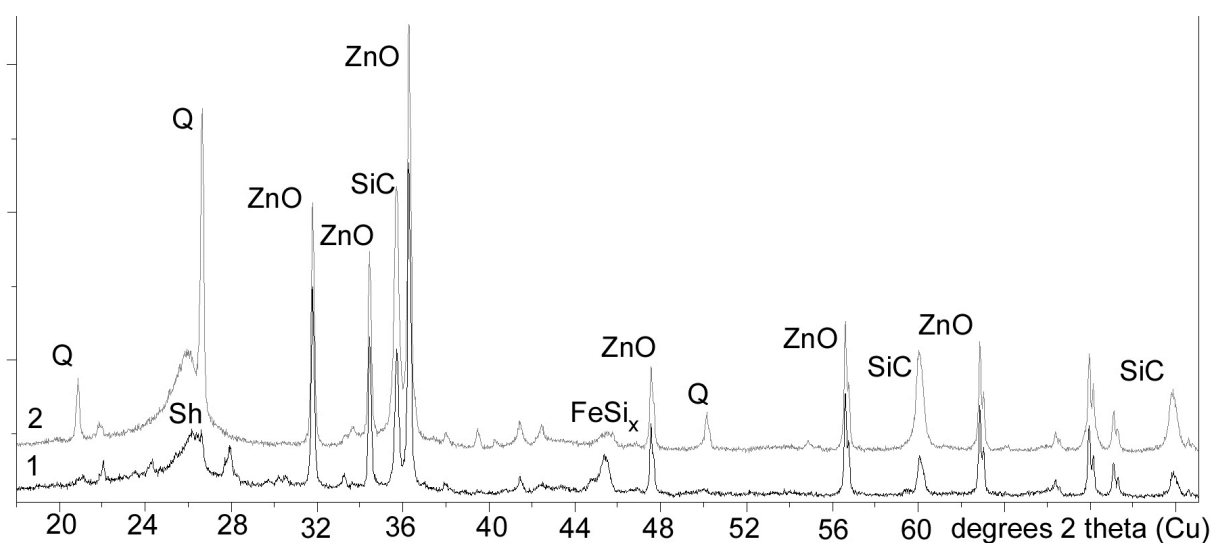


FIG. 1. X-ray diffractograms of nano-structured shungite rocks (No. 1 and 2) with zinc oxide (ZnO) as a standard, where, Q is quartz and Sh is shungite carbon

TABLE 2. Trace element compositions of the untreated shungite rocks

Shungite rocks	Some catalytically active and heavy trace elements (ppm)								
	Ti	V	Cr	Mn	Ni	Cu	Mo	Ba	Pb
Sh 1	2717	223	108	439	101	59	11	195	4
Sh 2	1839	222	74	41	72	21	9	373	14

leads to the formation of silicon carbide nanofibers and nanoparticles with different morphologies and structures (amorphous and crystalline) (Fig. 3a,b), and iron and iron silicide nanoparticles encapsulated into carbon shells grow. The processes of nanostructure formation are very sensitive to the type of shungite rocks and experimental conditions. The obtained nanomaterials possess unique properties, for example, encapsulated  $\text{FeC}_x$  particles are in the superparamagnetic state [8], similar to the nanoparticles encapsulated separately by the polymer [9]. A compound of this type can be used as fillers of new composite materials [10].

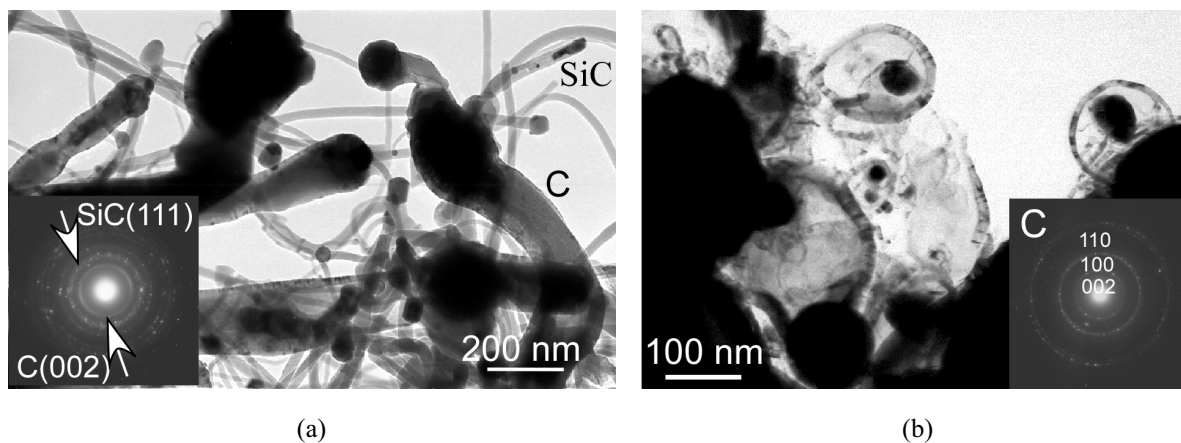


FIG. 2. Transmission electron microscopy images and selected area electron diffraction (inserts) of hollow carbon fibers (a) and hollow carbon particles (b) of nano-structured shungite rocks

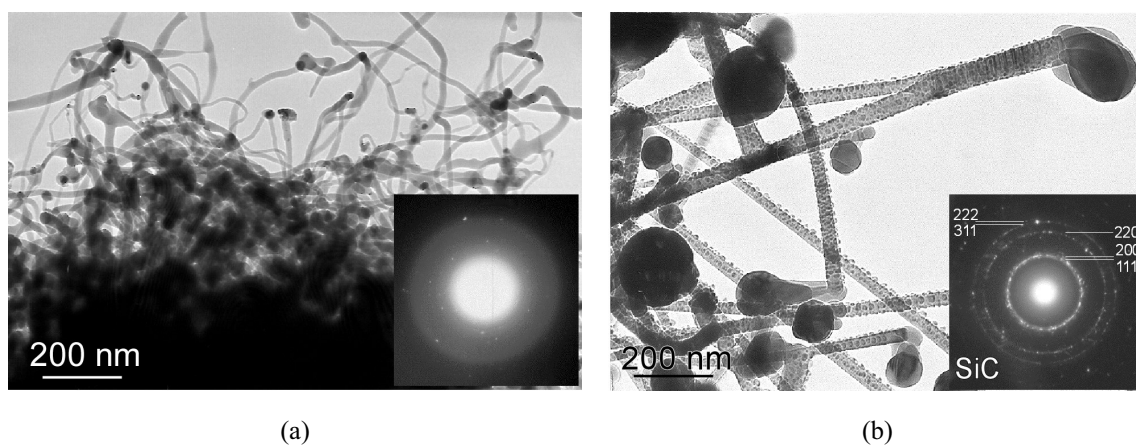


FIG. 3. Transmission electron microscopy images and selected area electron diffraction of amorphous (a) and crystalline (b) SiC fibers of nano-structured shungite rocks

To enrich the nanostructured shungite rocks with specified components for use as a filler and modifier of composites, we investigated the processes of dispersion in liquids of different density, such as alcohol, water and tribromomethane [11]. However, despite the dispersion, it was impossible to obtain narrow fractions of components present in the nanostructured shungite rock. This circumstance is caused by both complex composition of samples and critical processes of dispersion, that requires further research on the selection of modes and processing schemes. Therefore, at this stage, the initial nanostructured rocks were used for manufacturing the composites.

The shielding effectiveness (SE) measurements were carried out using the coaxial transmission line method in the frequency range of 0.01 – 1000 MHz. The electrical conductivity ( $\sigma$ ) was measured at a frequency of 1 kHz. The two different shungite samples were powdered and electrophysical parameters, such as the conductivity and the shielding effectiveness were measured. Measurements of shielding effectiveness (SE) and the electrical conductivity ( $\sigma$ ) of untreated and heat-treated different shungite rocks were carried out as reported elsewhere [12]. For the heat-treated nano-structured shungite rock with dominated hyperfullerene carbon, the  $\sigma$  doubled in magnitude and SE increased by 10 dB with an increase of carbon content by 1.5 % over the untreated sample. In contrast, for

the heat-treated nano-structured shungite rock with a high SiC nanofiber content, there was a decrease of carbon content by 6 % after treatment, the  $\sigma$  value was halved and the SE was decreased by 10 dB (Table 1, Fig. 4).

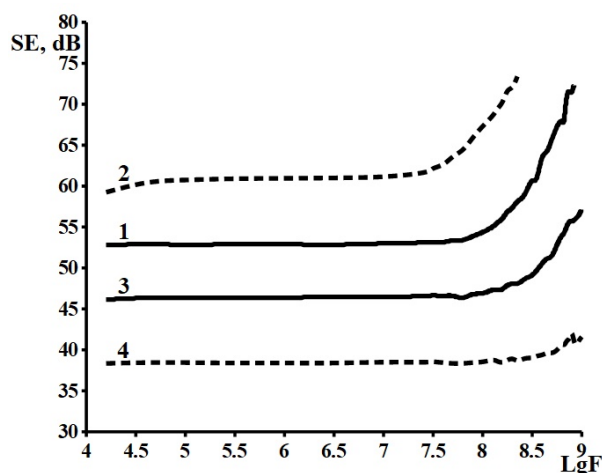


FIG. 4. Dependence of shielding effectiveness of shungite rocks on electromagnetic field frequency. Shungite 1: 1 – untreated, 2 – heat-treated; Shungite 2: 3 – untreated, 4 – heat-treated

### 3. Discussion of the results

Shungite is non-graphitized carbon and very resistant to heat treatment. Significant changes of those are observed only at temperatures above 2100 °C, and are associated with increasing of coherent scattering regions and reducing the carbon layer distortion. The band structure and electrophysical properties of those change consequently. On the contrary, shungite rocks are characterized by the fine nature of the mineral distribution and the large contact area of the carbon and mineral components that provide a high content of carbon and silicon, determine the possibility of their mutual crystallogenesis, including formation carbides and silicides, not at such high temperatures, since 1400 – 1600 °C. The difference of shungite rocks by the rock-forming minerals and trace element composition leads to the synthesis of different morphologies and the structural state of carbon and composite components (see Tables 1 and 2). In particular, carbides of silicon, having a microcrystalline structure and a well-defined crystallographic form can be obtained. However, the most interesting and promising in the technological aspect are the micro- and nano- fibrous carbides of silicon. In shungite rocks with the different rock-forming minerals and trace element compositions, the synthesis of mono- or polycrystalline, and amorphous nano-sized fibrous silicon carbides, having different morphological structure, length, and diameter occur. The diversity of morphological and structural forms of silicon carbide indicates different mechanisms of their growth, which can be determined by the change in the kinetic crystallogenesis processes influenced by the distribution and morphologies of carbon and minerals as well as trace elements.

Due to the formation hyperfullerene structures during the heat treatment for the shungite No.1, higher shielding effectiveness values than the untreated shungite have been obtained. In addition, according to electron microscopy, some hyperfullerene structures, presumably filled with iron and/or iron carbide, which can also contribute to the shielding of electromagnetic energy. Therefore, we can assume that the presence of hyperfullerene structures make a special contribution to the shielding ability of the modified shungite rocks. But as their number and sizes depend on the structural characteristics of the shungite rocks, then it becomes important to pre-selection of the type of shungites for modifications and future use in the creation of radio-shielding materials. The presence of various nanostructured rocks with fundamentally different physical properties makes it possible to predict the creation of new composite materials on their basis.

### Acknowledgements

The work is performed in the framework of the research, PFNI GAN “Geology and Genesis of deposits, Mineralogy and Technology of Shungite rocks of Onega structure” (number of state registration of AAAA-A18-118020690238-0).

## References

- [1] Buseck P.R., Galdobina L.P., et al. Shungites: the C-rich rocks of Karelia, Russia. *Can Mineralog.*, 1997, **35**, P. 1363–1378.
- [2] Kovalevski V.V., Prikhodko A.V., Buseck P.R. Diamagnetism of natural fullerene-like carbon. *Carbon*, 2005, **43** (2), P. 401–405.
- [3] Golubev Ye.. Electrophysical properties and structural features of shungite. *Physics of the Solid State*, 2013, **55** (5), P. 995–1002.
- [4] Svetov S. A., Stepanova A. V., et al. Precision geochemical (ICP-MS, LA-ICP-MS) analysis of rock and mineral composition: the method and accuracy estimation in the case study of Early Precambrian mafic complexes. *Proceedings of the Karelian Research Centre RAS, Precambrian Geology Series*, 2015, **7**, P. 54–73.
- [5] Tkachev E.N., Romanenko A.I., et al. Electrophysical Properties of Onion-Like Carbon. *Russian Physics Journal*, 2016, **59** (2), P. 171–176.
- [6] Yang Shikuan, Zeng Haibo, et al. Luminescent hollow carbon shells and fullerene-like carbon spheres produced by laser ablation with toluene. *Journal of Materials Chemistry*, 2011, **21** (12), P. 4432–4436.
- [7] Chazhengina S.Y., Kovalevski V.V. Structural characteristics of shungite carbon subjected to contact metamorphism overprinted by greenschist-facies regional metamorphism. *European Journal of Mineralogy*, 2013, **25** (5), P. 835–843.
- [8] Zyryanov V.V., Kovalevski V.V., Petrov S.A., Matvienko A.A. Nanosized materials from shungite rocks. *Inorganic materials*, 2012, **48** (11), P. 1234–1242.
- [9] Andersson R.L., Cabedo L., et al. Superparamagnetic [sic] nanofibers by electrospinning. *RSC Advances*, 2016, **6** (26), P. 21413–21422.
- [10] Kalashnikov I.E., Kovalevski V.V., Chernyshova T.A., Bolotova L.K. Aluminum-matrix composite materials with shungite rock fillers. *Russian Metallurgy*, 2010, **11**, P. 1063–1071.
- [11] Kovalevskii S.V., Kalashnikov I.E. Study of dispersion phenomena of a nanostructured shungite rock. *Physical and chemical aspects of the study of clusters, nanostructures and nanomaterials*, 2014, **6**, P. 178–185.
- [12] Moshnikov I.A., Kovalevski V.V. Electrophysical properties of shungites at low temperatures. *Nanosystems: Physics, Chemistry, Mathematics*, 2016, **7** (1), P. 214–219.

## A new efficient non-reversible 4 bit binary to gray and 4 bit gray to binary converter in QCA

Md. Tajul Islam<sup>1</sup>, Golam Sarwar Jahan<sup>1</sup>, Ali Newaz Bahar<sup>1</sup>, Kawsar Ahmed<sup>1</sup>, Md. Abdullah-Al-Shafi<sup>2</sup>

<sup>1</sup>Department of Information and Communication Technology, Mawlana Bhashani Science and Technology University, Santosh, Tangail-1902, Bangladesh

<sup>2</sup>Institute of Information Technology (IIT), University of Dhaka, Dhaka-1000, Bangladesh

tajulmbstu@gmail.com, sarwar13040@gmail.com, bahar\_mitdu@yahoo.com, kawsar.ict@mbstu.ac.bd, alshafi08@gmail.com

**DOI 10.17586/2220-8054-2018-9-4-473-483**

The present Very Large Scale Integration (VLSI) technology is based on Complementary Metal-oxide-Semiconductor (CMOS) technology. The development of the VLSI technology has reached its peak due to the fundamental physical limits of CMOS technology. The recent challenges, as well as the physical limitation of the traditional CMOS technology, has overcome by the Quantum-dot Cellular Automata (QCA) which is first introduced by C. S. Lent. The nanoscale size quantum cell is a feature of QCA technology. In this paper, we propose a new QCA structure for 4-bit binary to 4-bit gray and 4-bit gray to 4-bit binary using two input XOR gate. These structures are designed and simulated with QCA designer and compared with previous structure.

**Keywords:** quantum-dot cellular automata (QCA), binary code, gray code, converter, QCA cell, QCA designer.

*Received: 1 June 2018*

*Revised: 6 July 2018*

### 1. Introduction

Quantum Dot Cellular Automata (QCA) is one of the new and fledgling technology at the nanoscale [1] has been used widely in digital circuits and systems, also an innovative access towards the present age of nanotechnology, a substitution of contemporary CMOS technology [2] and proposes a novel designing technique which is appropriate for logic circuits. Presently, CMOS technology has faced many problems such as delay, power consumption, size of circuits, the area [1, 3–5], deteriorating supply voltage, power dissipation; hinder the microelectronics momentum using regular circuit scaling [1]. By using this technology, these problems are generated and different new technologies have recently been proposed to overcome these problems [6, 7]; QCA is one of them. Electron transformation in IC technology is known as current flow in the device, but in QCA. there is no current flow only charge transformation, which is why this technology requires exceedingly low power for computing. Logic state representation is the main characteristic of this technology, not in terms of voltage levels but alternately represented in terms of logic cells. In QCA, coulombic interaction is caused to create the necessary computing logic states of 1 and 0; this technology uses less device to perform the calculation. This computing of logical states is created by the position of the electrons inside the QCA cells. These cells are the group of basic parts. QCA logic gates and circuits are carried out by these cells. In QCA, these cells have been replaced in lieu of hardware components [8]. In recent years, several QCA based logic circuits have been proposed [9–16].

### 2. Quantum DOT Cellular Automata (QCA)

#### 2.1. Basic QCA gate

A basic QCA cell comprises four quantum dots in a square shape coupled with tunnel barriers. To represent the information, quantum dot cellular automata use a binary logic. In a QCA logic device, two types of arrangements are normally seen denoted as cell polarization;  $P = +1$  and  $P = -1$ , which represent “1” and “0” respectively are shown in Fig. 1. Through the charge configuration of the QCA cell, binary information is encoded. In any traditional logic circuit, data is exchanged by the electrical current but QCA works by the Columbic communication that associates the condition of one cell to the condition of its neighbors, which results in data change. All cell in a line with same polarization is known as QCA wire, shown in Fig. 2.

In QCA, majority voter gate and inverter act as the basic gate. The majority voter (MV) gate generates an output 1 if the majority of inputs are 1, as shown in Fig. 3(a). The logical operation of majority voter gate is shown in eq. (1):

$$MV(A, B, C) = AB + BC + AC. \quad (1)$$

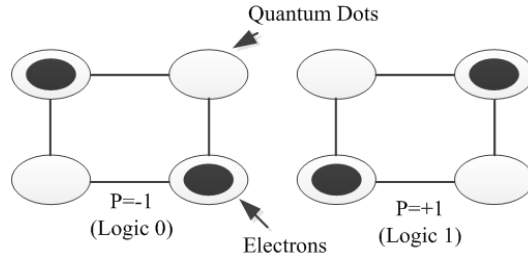


FIG. 1. Two different polarization

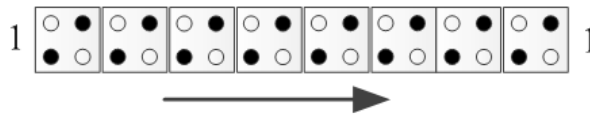


FIG. 2. QCA wire

We can implement the AND gate and OR gate from the majority voter by fixing the input (control input) permanently to a 0 or 1. The logical operation of AND gate and OR gate from the majority voter gate is shown in eq. (2) and eq. (3) respectively. If the control input is permanently set to 1, then it will work as an AND gate, shown in Fig. 3(b). Similarly, if the control input is 0 then it is an OR gate is shown in Fig. 3(c).

$$MV(A, B, 1) = A + B, \tag{2}$$

$$MV(A, B, 0) = AB. \tag{3}$$

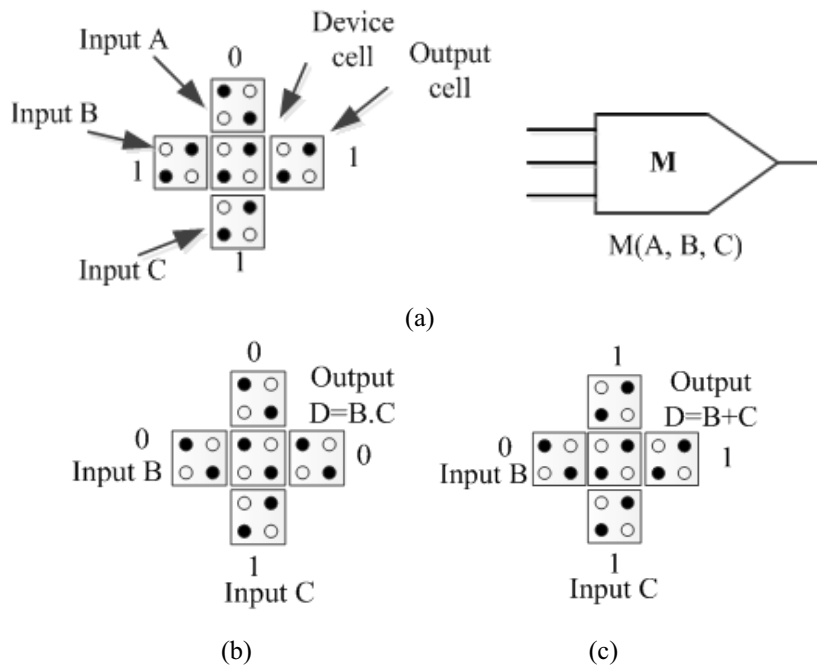


FIG. 3. (a) Majority voter gate; (b) AND gate; (c) OR gate

### 2.2. XOR gate

Quantum Logical Circuit has several logical gates, among which XOR Gate is one [17, 18]. XOR gate is used in many circuits, so it is very important. There are several structures for this gate, one of which is shown in Fig. 5.

The basic operation of XOR gate is  $(A \text{ xor } B)$  or  $F(A, B) = A\bar{B} + \bar{A}B$ . The above structure can be implemented as QCA design shown in Fig. 6(a). The result of simulation of this design is shown in Fig. 6(b).

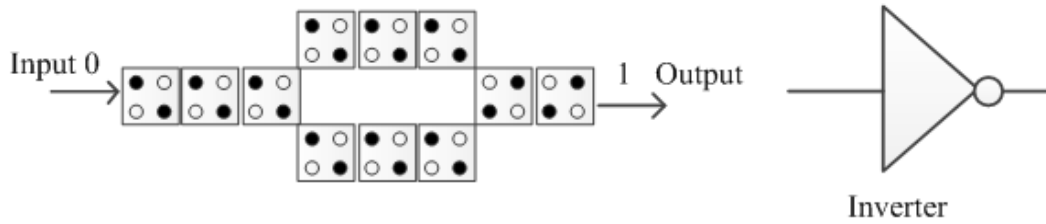


FIG. 4. Inverter

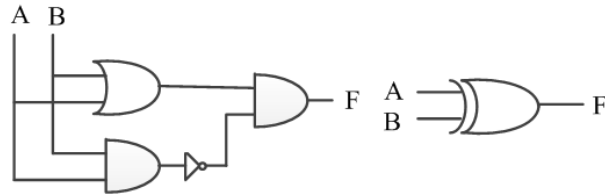


FIG. 5. Schematic of XOR gate

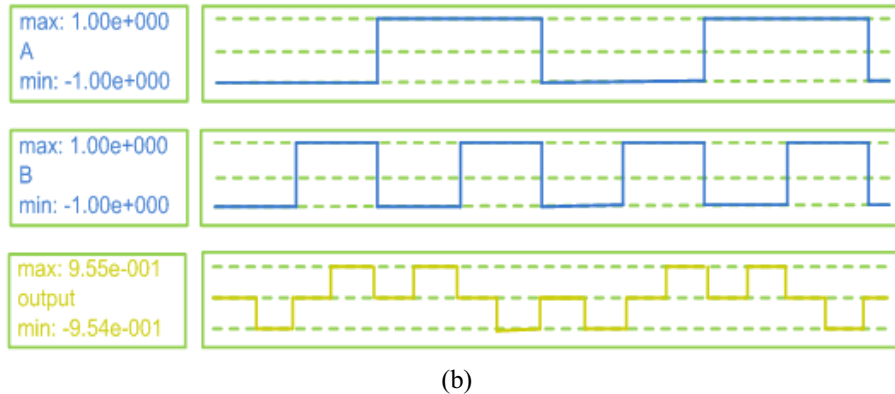
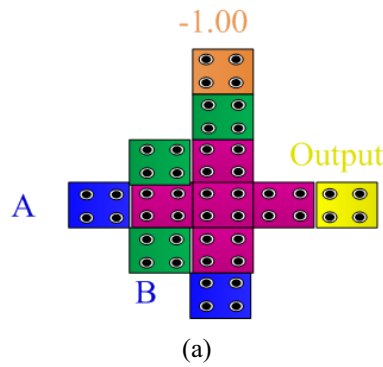


FIG. 6. XOR gate: (a) QCA layout; (b) Simulation result

### 3. Non-reversible 4-bit binary to 4-bit gray code converter

A circuit is said to be non-reversible if it does not contain an equal number of inputs and an equal number of outputs. On the other hand, the non-reversible circuit is a circuit whose inputs cannot be reconstructed from its outputs.

The simplest form of computer code or programming data is called Binary code which is represented entirely by a binary system of digits consisting of a string of consecutive zeros and ones. In binary to gray code conversion, the Most Significant Bit (MSB) of the gray code is always equal to the MSB of the given binary code and by doing XOR operation between binary code bit at that index and previous index, the other bits of the output gray code can be obtained.

In this section, we have proposed the non-reversible 4-bit binary to 4-bit gray code converter structure using two-input XOR gate. For non-reversible 4-bit binary to 4-bit gray code converter, inputs are described as B0, B1, B2, and B3 where corresponding outputs are G0, G1, G2, and G3. It is observed that three two-input XOR gates are needed to design non-reversible 4-bit binary to 4-bit gray code converter. The first XOR gate generates G0 and XOR of B0, B1. The second XOR gate generates G1 and XOR of B1, B2, while the third XOR gate generates G2 and XOR of B2, B3. The output G3 is calculated directly from input B3, so  $G3 = B3$ . Here, the polarization is set to  $-1$  which is used as fixed polarization. Gray code outputs equation has shown in eq. (4):

$$G0 = B0 \oplus B1, \quad G1 = B1 \oplus B2, \quad G2 = B2 \oplus B3, \quad G3 = B3. \quad (4)$$

In Fig. 7(a), we have shown the logical circuit of this converter as well as QCA design of this structure in Fig. 7(b). A truth table of this converter has shown on Table 2. The outcomes of the simulation of this converter have shown in Fig. 8.

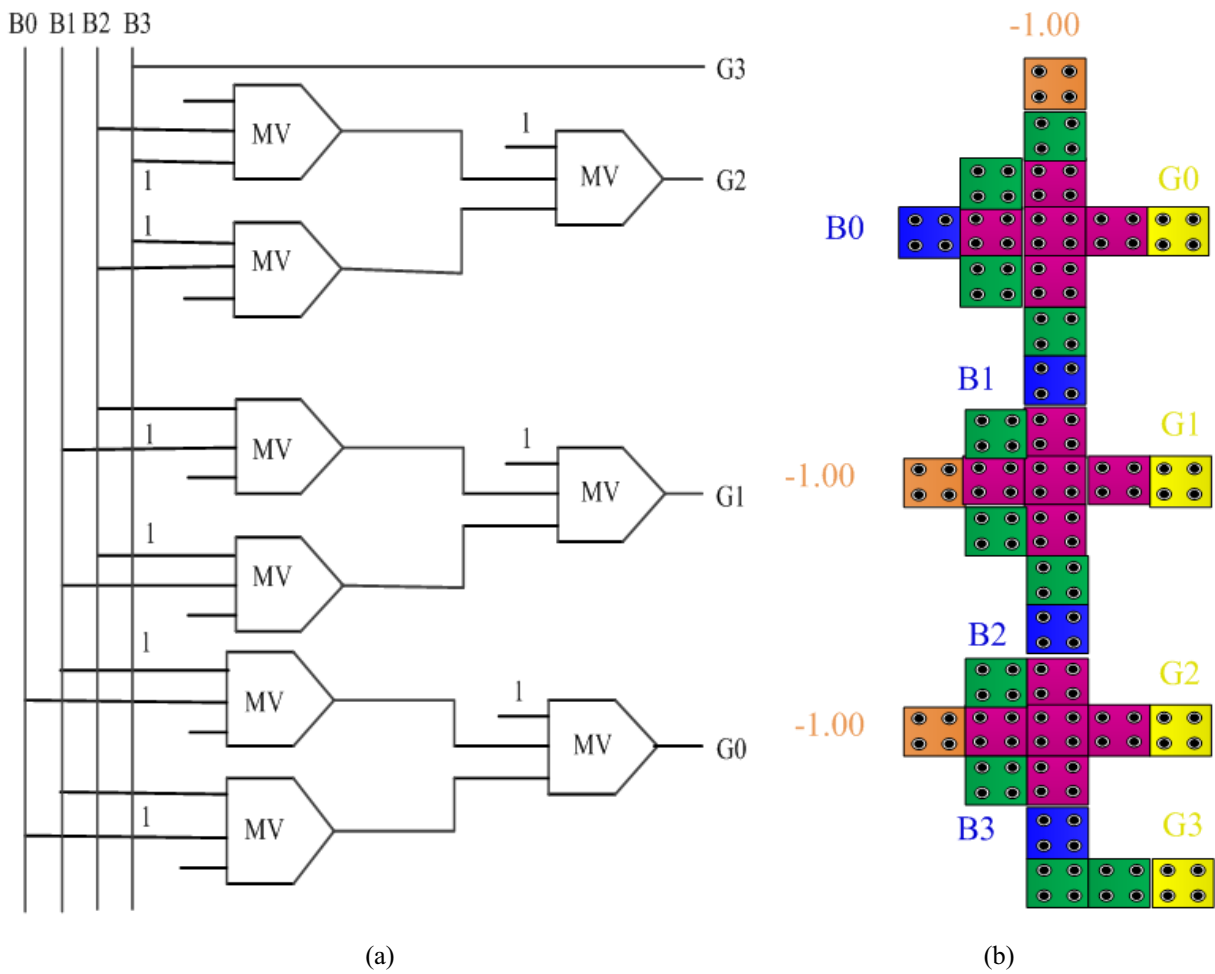


FIG. 7. Non-reversible 4-bit binary to 4-bit gray code converter: (a) Logical circuit; (b) QCA layout

For the proposed structure of non-reversible 4-bit binary to 4-bit gray code converter, the simulation factors values are shown in Table 3. The proposed work compared to previous works has a good improvement, especially in cell numbers and occupied areas. By comparing the previous works in [19] and [20], our proposed circuit has 37 cells which have improved 70.87 % and 80.73 %. Besides comparing the previous works in [19–22], the occupied area 90.24 %, 88.24 %, 55.56 % and 77.78 % have been reduced. The work is better than [19] because our proposed structure has no crossover. In our work, the clock cycle latency is 0.50 which is better than [19] and [20].

TABLE 1. Design factors for XOR gate

Design factor	Value
Cell count	12
Area	0.02 $\mu\text{m}^2$
Crossover	Zero
Latency	0.50

TABLE 2. Truth table of 4-bit binary to 4-bit gray code converter

Input				Output			
B0	B1	B2	B3	G0	G1	G2	G3
0	0	0	0	0	0	0	0
0	0	0	1	0	0	1	1
0	0	1	0	0	1	1	0
0	0	1	1	0	1	0	1
0	1	0	0	1	1	0	0
0	1	0	1	1	1	1	1
0	1	1	0	1	0	1	0
0	1	1	1	1	0	0	1
1	0	0	0	1	0	0	0
1	0	0	1	1	0	1	1
1	0	1	0	1	1	1	0
1	0	1	1	1	1	0	1
1	1	0	0	0	1	0	0
1	1	0	1	0	1	1	1
1	1	1	0	0	0	1	0
1	1	1	1	0	0	0	1

TABLE 3. Simulation factor for non-reversible 4-bit binary to 4-bit gray code converter

Design factor	Proposed work	Previous work in [19]	Previous work in [20]	Previous work in [21]	Previous work in [22]
Cell count	37	127	192	105	131
Area ( $\mu\text{m}^2$ )	0.04	0.41	0.34	0.09	0.18
Crossover	Zero	Three	Zero	Zero	–
Latency	0.50	0.75	2	–	–

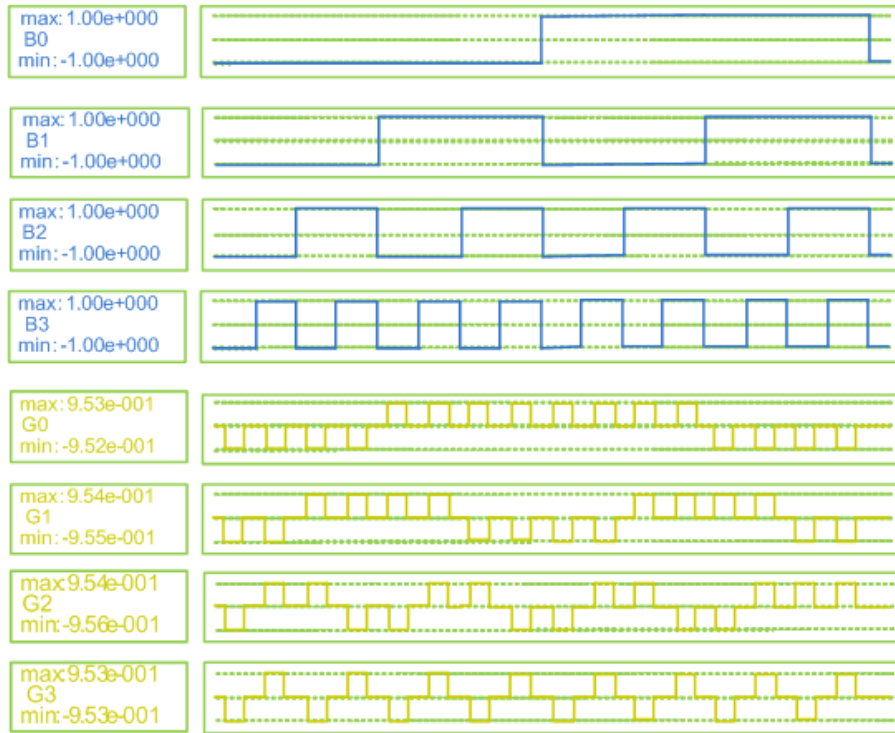


FIG. 8. Simulation result of 4-bit binary to 4-bit gray code converter

#### 4. Non-reversible 4-bit gray to 4-bit binary code converter

Gray code is a reflected code where an ordering of  $2n$  binary numbers such that only one bit changes from one entry to the next. In gray to binary code conversion, the Most Significant Bit (MSB) of the binary code is always equal to the MSB of the given gray code and by checking gray code bit at that index, other bits of the output binary code can be obtained. If current gray code bit is 0, then copy previous binary code bit. Otherwise, copy invert of previous binary code bit.

In this section, based on the XOR gate, we have also proposed a QCA circuit to convert the 4-bit gray code to 4-bit binary code. For non-reversible 4-bit gray to 4-bit binary code converter, inputs are described as G3, G2, G1 and G0 where corresponding outputs are B3, B2, B1, and B0. It is observed that three two-input XOR gates are needed to design non-reversible 4-bit binary to 4-bit gray code converter. The output B3 is calculated directly from input G3, so  $B3 = G3$ . First XOR gate generates B2 and XOR of B3, G2. Second XOR gate generates B1 and XOR of B2, G1. Third XOR gate generates B0 and XOR of B1, G0. Here, polarization is set to  $-1$  which is used as fixed polarization. Binary code outputs equation has shown in eq. (5):

$$B0 = B1 \oplus G0, \quad B1 = B2 \oplus G1, \quad B2 = B3 \oplus G2, \quad B3 = G3. \quad (5)$$

In Fig. 9(a) we have shown the logical circuit of this converter as well as QCA design of this structure in Fig. 9(b). A truth table of this converter has shown on Table. 4. The outcomes of the simulation of this converter are shown in Fig. 10.

For the proposed structure of non-reversible 4-bit gray to 4-bit binary code converter the simulation factors values have shown in Table. 4. The Proposed work compared to previous works shows good improvement, especially in cell numbers and occupied areas. By comparing the previous works in [19] and [20] respectively, our proposed circuit has 47 cells which have improved 52.53 % and 82.53 %, as well as the occupied area. In our work, the clock cycle latency is 1.00 which is also better than [20].

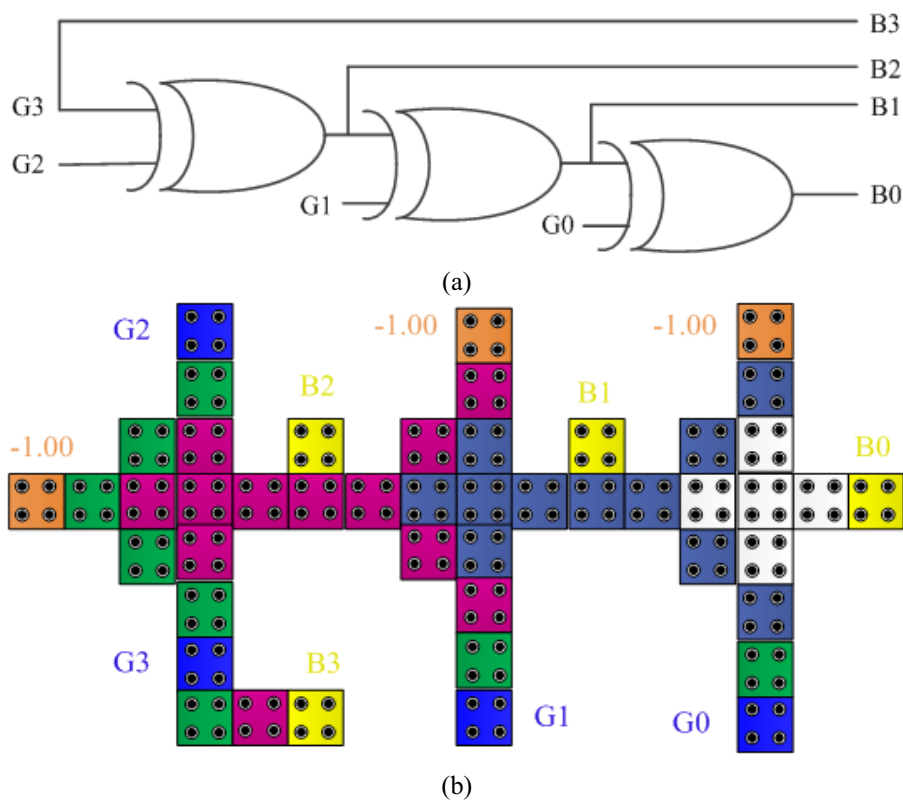


FIG. 9. Non-reversible 4-bit gray to 4-bit binary code converter: (a) Logical circuit; (b) QCA layout

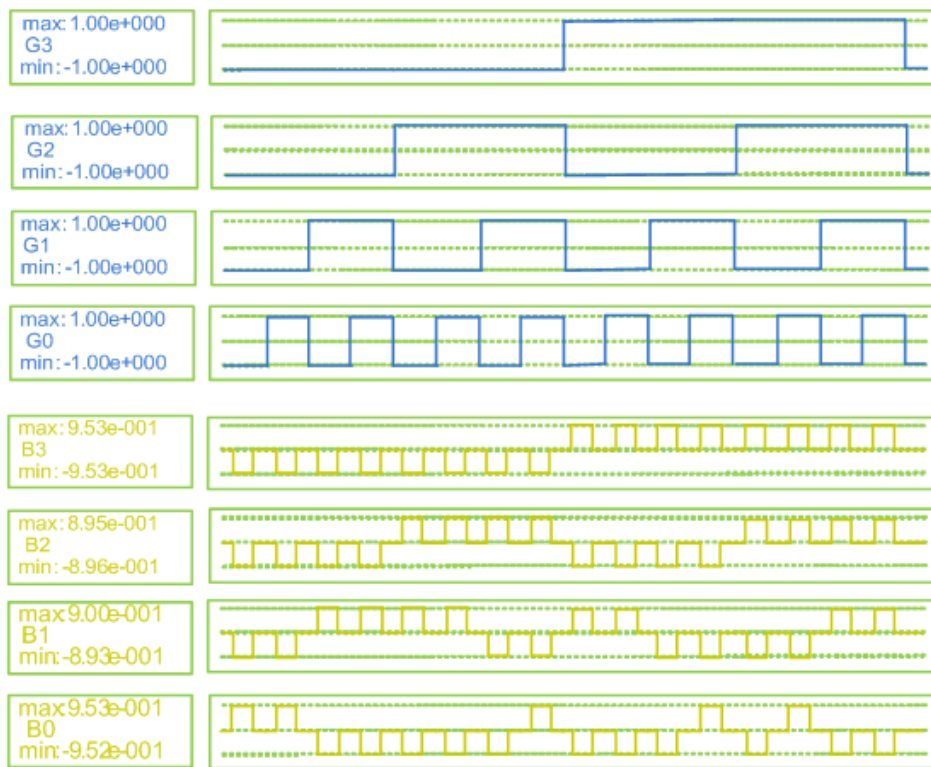


FIG. 10. Simulation result of non-reversible 4-bit gray to 4-bit binary code converter

TABLE 4. Truth table of 4-bit gray to 4-bit binary code converter

Input				Output			
G3	G2	G1	G0	B3	B2	B1	B0
0	0	0	0	0	0	0	0
0	0	0	1	0	0	0	1
0	0	1	0	0	0	1	1
0	0	1	1	0	0	1	0
0	1	0	0	0	1	1	1
0	1	0	1	0	1	1	0
0	1	1	0	0	1	0	0
0	1	1	1	0	1	0	1
1	0	0	0	1	1	1	1
1	0	0	1	1	1	1	0
1	0	1	0	1	1	0	0
1	0	1	1	1	1	0	1
1	1	0	0	1	0	0	0
1	1	0	1	1	0	0	1
1	1	1	0	1	0	1	1
1	1	1	1	1	0	1	0

TABLE 5. Simulation factors for the non-reversible 4-bit gray code to 4-bit binary code converter

Design factor	Proposed work	Previous work in [19]	Previous work in [20]
Cell count	47	99	269
Area ( $\mu\text{m}^2$ )	0.05	–	0.69
Crossover	Zero	Zero	Zero
Latency	1	0.75	6

### 5. Power depletion of the proposed layout

The power dissipation by a QCA cell is calculated using the Hartree–Fock approximation [23–25]. The Hamiltonian matrix of a mean-field approach is illustrated as the eq. (6):

$$\mathbf{H} = \begin{bmatrix} \frac{-E_k}{2} \sum_i C_i f_{i,j} & -\gamma \\ -\gamma & \frac{E_k}{2} \sum_i C_i f_{i,j} \end{bmatrix} = \begin{bmatrix} \frac{-E_k}{2} (C_{j-1} + C_{j+1}) & -\gamma \\ -\gamma & \frac{E_k}{2} (C_{j-1} + C_{j+1}) \end{bmatrix}. \quad (6)$$

The energy cost of two neighboring cells ( $i$  and  $j$ ) with opposite polarizations is derived as follows in eq. (7):

$$E_{i,j} = \frac{1}{4 \prod_{\epsilon_0 \in r} \epsilon_r} \sum_{n=1}^4 \sum_{m=1}^4 \frac{q_{i,n} q_{j,m}}{|r_{i,n} - r_{j,m}|}. \quad (7)$$

For a single QCA cell the instantaneous total power equation can be calculated as:

$$P_t = \frac{dE}{dt} = \frac{\hbar}{2} \left[ \frac{d\vec{\Gamma}}{dt} \cdot \vec{\lambda} \right] + \frac{\hbar}{2} \left[ \vec{\Gamma} \cdot \frac{d\vec{\lambda}}{dt} \right] = P_1 + P_2. \quad (8)$$

In eq. (8), the term  $P_1$  includes two main components: first, the power gain achieved from the difference of the input and output signal powers ( $P_{in} - P_{out}$ ) and second, the transferred clocking power to the cell ( $P_{clock}$ ) and the term  $P_2$  represents dissipated power ( $P_{diss}$ ) [24]. The upper bound power dissipation model [26] of a QCA cell can be given as eq. (9):

$$P_{diss} = \frac{E_{diss}}{T_{cc}} \frac{\hbar}{2T_{cc}} \vec{\Gamma}_+ \times \left[ -\frac{\vec{\Gamma}_+}{|\vec{\Gamma}_+|} \tanh\left(\frac{\hbar|\vec{\Gamma}_+|}{k_B T}\right) + \frac{\vec{\Gamma}_-}{|\vec{\Gamma}_-|} \tanh\left(\frac{\hbar|\vec{\Gamma}_-|}{k_B T}\right) \right]. \quad (9)$$

Finally, in one clock cycle, the energy dissipation of a QCA cell is estimated as follows in eq. (10):

$$E_{diss} = \frac{\hbar}{2} \int_{-T}^T \vec{\Gamma} \cdot \frac{d\vec{\lambda}}{dt} dt = \frac{\hbar}{2} \left( \left[ \vec{\Gamma} \cdot \vec{\lambda} \right]_{-T}^T - \int_{-T}^T \vec{\lambda} \cdot \frac{d\vec{\Gamma}}{dt} dt \right). \quad (10)$$

Power estimation tool known as QCAPro [25,27–29] is used to calculate the dissipated power. Combination of leakage and switching power [24] known as the total power loss in a QCA circuit is evaluated by the QCAPro. The power dissipation map of our proposed designs is obtained at 2 K temperature with  $0.5E_k$ . In the following figures, high power dissipating cells are indicated using thermal hotspots with darker colors. The thermal hotspot map or power map of the proposed non-reversible 4-bit binary to gray and 4-bit gray to binary converter under energy level of  $0.5E_k$  are shown in Fig. 11(a) and (b) respectively.

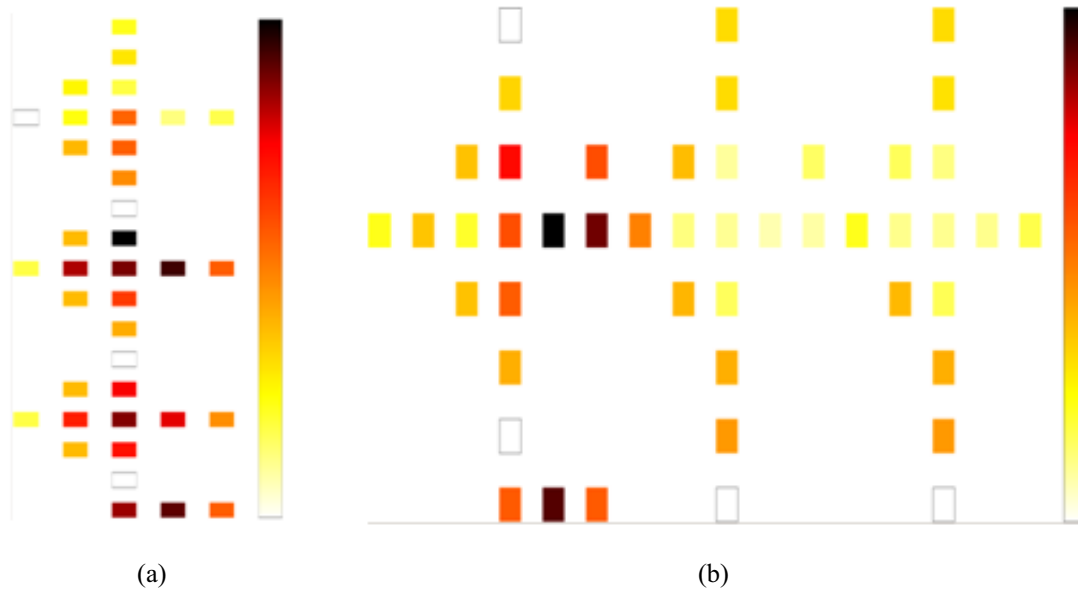


FIG. 11. Power dissipation map for the proposed non-reversible (a) 4-bit Binary to Gray converter (b) 4-bit Gray to Binary converter at 2K temperature and tunneling energy of  $0.5 E_k$

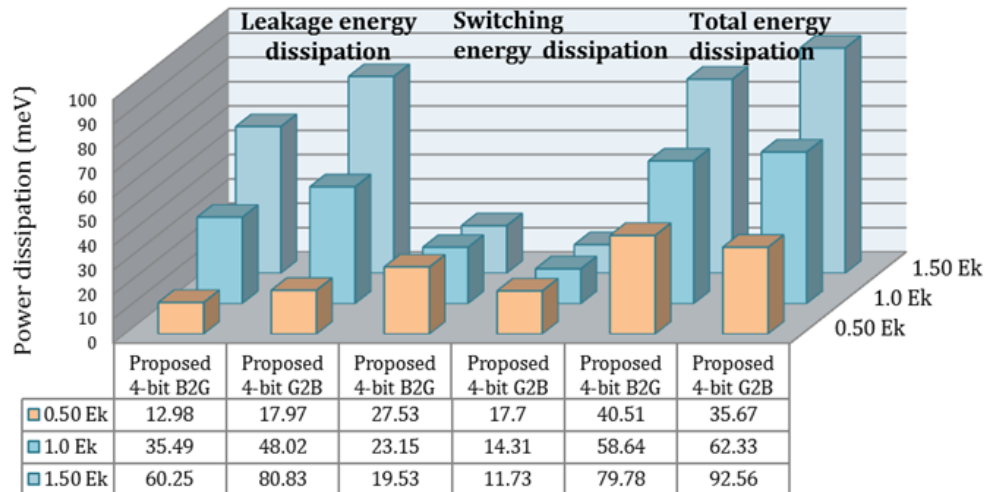
In addition, the leakage, switching and total energy dissipation of proposed designs at three different tunneling energy levels ( $0.5E_k$ ,  $1.0E_k$ ,  $1.5E_k$ ) at 2 K temperature is given in Table 6.

The dissipated leakage energy by the proposed non-reversible 4-bit binary to gray code converter are 12.98 meV, 35.49 meV and 60.25 meV at  $\gamma = 0.5E_k$ ,  $\gamma = 1.0E_k$  and  $\gamma = 1.5E_k$  respectively and by proposed non-reversible 4-bit binary to gray code converter are 17.97 meV, 48.02 meV and 80.83 meV at  $\gamma = 0.50E_k$ ,  $\gamma = 1.0E_k$  and  $\gamma = 1.5E_k$  respectively. The dissipated switching energy by the proposed non-reversible 4-bit binary to gray code converter are 27.53 meV, 23.15 meV and 19.53 meV at  $\gamma = 0.50E_k$ ,  $\gamma = 1.0E_k$  and  $\gamma = 1.50E_k$  respectively and by proposed non-reversible 4-bit binary to gray code converter are 17.7 meV, 14.31 meV and 11.73 meV at  $\gamma = 0.50E_k$ ,  $\gamma = 1.0E_k$  and  $\gamma = 1.50E_k$  respectively.

TABLE 6. Energy dissipation analysis of proposed non-reversible gate

Circuit	Power dissipated at $T = 2$ K								
	Avg. leakage energy dissipation (meV)			Avg. switching energy dissipation (meV)			Total energy dissipation (meV)		
	$0.5 E_k$	$1.0 E_k$	$1.5 E_k$	$0.5 E_k$	$1.0 E_k$	$1.5 E_k$	$0.5 E_k$	$1.0 E_k$	$1.5 E_k$
B2G Converter	12.98	5.49	0.25	7.53	3.15	9.53	0.51	8.64	9.78
G2B Converter	7.97	8.02	0.83	7.70	4.31	1.73	5.67	2.33	2.56

Finally, the total dissipated energy by the proposed non-reversible 4-bit binary to gray code converter are 40.51 meV, 58.64 meV and 79.78 meV at  $\gamma = 0.50E_k$ ,  $\gamma = 1.0E_k$  and  $\gamma = 1.50E_k$  respectively and by proposed non-reversible 4-bit binary to gray code converter are 35.67 meV, 62.33 meV and 92.56 meV at  $\gamma = 0.50E_k$ ,  $\gamma = 1.0E_k$  and  $\gamma = 1.50E_k$  respectively. The leakage energy, switching energy and the total energy dissipation of proposed designs are presented graphically in Fig. 12 respectively.

FIG. 12. Energy dissipation graph of proposed B2G and G2B at three different tunneling energy levels at temperature ( $T = 2$  K)

## 6. Conclusion

In this paper, we have presented a 4-bit non-reversible binary to gray and vice versa converter with a new QCA design. We designed our circuits in non-reversible mode. These structures come up with improvements compared to the previous works. These proposed circuits are fit in the manner that they enclose fewer cells, clock phases, logic gate count, overall size, and area as well as distinguish them from earlier reported designs. The proposed circuits can be considered as a promising step to design highly area efficient and low power consuming complex logic circuits as well as input-output devices.

## References

- [1] Lent C.S., Tougaw P.D., Porod W., Bernstein G.H. Quantum cellular automata. *Nanotechnology*, 1993, **4** (1), P. 49–57.
- [2] Cho H., Swartzlander Jr. E.E. Adder and multiplier design in quantum-dot cellular automata. *IEEE Transactions on Computers*, 2009, **58** (6), P. 721–727.
- [3] Schaller R.R. Moore's law: past, present and future. *IEEE spectrum*, 1997, **34** (6), P. 52–59.
- [4] Niemier M.T. Designing digital systems in quantum cellular automata. PhD diss., University of Notre Dame, 2000.
- [5] Orlov A.O., Amlani I., et al. Realization of a functional cell for quantum-dot cellular automata. *Science*, 1997, **277** (5328), P. 928–930.
- [6] Tahoori M.B., Momenzadeh M., Huang J., Lombardi F. Defects and faults in quantum cellular automata at nano scale. *IEEE*, 2004, P. 291.
- [7] Snider G.L., Orlov A.O., et al. Quantum-dot cellular automata. *Journal of Vacuum Science & Technology A*, 1999, **17** (4), P. 1394–1398.

- [8] Thapliyal H., Ranganathan N., Kotiyal S. Design of testable reversible sequential circuits. *IEEE Transactions on Very Large Scale Integration Systems*, 2013, **21** (7), P. 1201–1209.
- [9] Mallaiah A., Swamy G.N., Padmapriya K. 1 bit and 2 bit comparator designs and analysis for quantum-dot cellular automata. *Nanosystems: Physics, Chemistry, Mathematics*, 2017, **8** (6), P. 709–716.
- [10] Bahar A.N., Waheed S., Habib M.A. A novel presentation of reversible logic gate in Quantum-dot Cellular Automata (QCA). *International Conference on Electrical Engineering and Information Communication Technology*, 2014, 14651168.
- [11] Islam S.S., Farzana S., Bahar A.N. Area efficient layout design of Multiply Complements Logic (MCL) gate using QCA Technology. *Global Journal of Research In Engineering*, 2014, **14** (4), P. 7–10.
- [12] Bahar A.N., Waheed S., Hossain N. A new approach of presenting reversible logic gate in nanoscale. *Springer Plus*, 2015, **4** (1), P. 153.
- [13] Abdullah-Al-Shafi M., Bahar A.N. QCA: An effective approach to implement logic circuit in nanoscale. *International Conference on Informatics, Electronics and Vision*, 2016, P. 620–624.
- [14] Bahar A.N., Waheed S. Design and implementation of an efficient single layer five input majority voter gate in quantum-dot cellular automata. *Springer Plus*, 2016, **5** (1), P. 636.
- [15] Abdullah-Al-Shafi M., Bahar A.N. Optimized design and performance analysis of novel comparator and full adder in nanoscale. *Cogent Engineering*, 2016, **3** (1), 1237864.
- [16] Biswas P.K., Bahar A.N., et al. An Efficient Design of Reversible Subtractor in Quantum-Dot Cellular Automata. *International Journal of Grid and Distributed Computing*, 2017, **10** (5), P. 13–24.
- [17] Heikalabad S.R., Navin A.H., Hosseinzadeh M. Content addressable memory cell in quantum-dot cellular automata. *Microelectronic Engineering*, 2016, **163**, P. 140–150.
- [18] Heikalabad S.R., Navin A.H., Hosseinzadeh M., Oladghaffari T. Midpoint memory: a special memory structure for data-oriented models implementation. *Journal of Circuits, Systems and Computers*, 2015, **24** (05), 1550063.
- [19] Rao N.G., Srikanth P.C., Sharan P. A novel quantum-dot cellular automata for 4-bit code converters. *Optik – International Journal for Light and Electron Optics*, 2016, **127** (10), P. 4246–4249.
- [20] Beigh M.R., Mustafa M. Design and simulation of efficient code converter circuits for Quantum-Dot cellular automata. *Journal of Computational and Theoretical Nanoscience*, 2014, **11** (12), P. 2564–2569.
- [21] Chaithanya P., Ramesh B., Srujana V., Vikram V. Implementation of Efficient Binary To Gray Code Converter Using Quantum Dot Cellular Automata. *International Journal for Research in Applied Science and Engineering Technology*, 2017, **5** (9), P. 522–529.
- [22] Islam S., Abdullah-Al-Shafi M.O.H.A.M.M.A.D., Bahar A.N. Implementation of Binary to Gray code Converters in Quantum Dot Cellular Automata. *Journal of Today's Ideas – Tomorrow's Technologies*, 2015, **3** (2), P. 145–160.
- [23] Timler J., Lent C.S. Power gain and dissipation in quantum-dot cellular automata. *Journal of applied physics*, 2002, **91** (2), P. 823–831.
- [24] Srivastava S., Sarkar S., Bhanja S. Estimation of upper bound of power dissipation in QCA circuits. *IEEE transactions on nanotechnology*, 2009, **8** (1), P. 116–127.
- [25] Srivastava S., Asthana A., Bhanja S., Sarkar S. QCAPro-an error-power estimation tool for QCA circuit design. *Circuits and Systems, IEEE International Symposium*, 2011, P. 2377–2380.
- [26] Reshi J.I., Bandy M.T. Efficient design of nano scale adder and subtractor circuits using quantum dot cellular automata. *International Conference on Electrical, Electronics, Engineering Trends, Communication, Optimization and Sciences*, 2016, 17693881.
- [27] Abdullah-Al-Shafi M., Bahar A.N. Novel binary to gray code converters in QCA with power dissipation analysis. *International Journal of Multimedia and Ubiquitous Engineering*, 2016, **11** (8), P. 379–396.
- [28] Bahar A.N., Rahman M.M., Nahid N.M., Hassan M.K. Energy dissipation dataset for reversible logic gates in quantum dot-cellular automata. *Data in Brief*, 2017, **10**, P. 557–560.
- [29] Bahar A.N., Uddin M.S., et al. Designing efficient QCA even parity generator circuits with power dissipation analysis. *Alexandria Engineering Journal*, 2017, In Press, <https://doi.org/10.1016/j.aej.2017.02.002>.

## Testing Bell inequalities for multi-partite systems with frequency-encoded photonic qubits

V. O. Sheremetev, A. S. Rudenko, A. I. Trifanov

ITMO University, Kronverkskiy, 49, St. Petersburg, 197101, Russia

vlad.sheremetiev@gmail.com, plane2393@gmail.com, alextrifanov@gmail.com

DOI 10.17586/2220-8054-2018-9-4-484-490

Generalizing the problem of state nonlocality measurement, we suggest a multi-partite Bell test for multi-photon frequency-entangled quantum state in a quantum network. Each side of this network is equipped with a generalized detector, consisting of an electro-optic phase modulator, frequency filter and photo-counter. In our paper, we develop a theory of Bell nonlocality measurement in frequency domain, using generalized Svetlichny inequalities. Solving the optimization problem for detectors inputs, we obtain optimal measurement parameters which allow strong violation of considered inequalities. As a particular case, we consider bi- and tripartite cases for EPR, GHZ and Wigner states correspondingly.

**Keywords:** Quantum nano-technologies, Bell nonlocality, spectral-entangled photons, phase modulation.

*Received: 12 July 2018*

### 1. Introduction

One of the most crucial experiment testing the validity of quantum mechanics is examination of nonlocal nature of quantum correlations [1]. Quantum entanglement [2], which is usually used as a basic resource for communication and information processing appears to be an echo of this quantum phenomenon [3–5]. In 1964, Bell [6] approved his famous theorem which states incompatibility between predictions of quantum theory and any physical theory satisfying notion of locality and hidden variable assumption. The Bell parameter  $S$  being the function of detector's local settings and state of monitored composite system violates certain inequality in the case of nonlocal correlation existence. For the bipartite system, this may take the form of Clauser–Horne–Shimony–Holt [8] (CHSH) inequality  $|S^{(2)}| \leq 2$ , whereas in the tripartite case, we have Mermin  $|S^{(3)}| \leq 2$  and Svetlichny  $|S^{(3)}| \leq 4$  counterparts [9, 10].

From the perspective of application in quantum nano-technologies and quantum communication protocols [11] it is very attractive to realize Bell test on photonic quantum states, which are widely used in quantum cryptography and information processing [12, 13]. Current experimental methods in quantum optics allow generation of entanglement in many-photon systems as soon as manipulating by single- and multi-photon states in integral silica devices [14, 15]. With these techniques, Bell inequalities were tested for bipartite and tripartite systems in the case of polarization and time-bin coding [16, 17]. Frequency-bin coding is another attractive way for representation of quantum information units due to relatively simple technique of manipulating collective state of frequency-encoded qubits by phase shifters and electro-optical modulators [18, 19]. By analogy, with linear optical quantum computation (LOQC), this branch of quantum information science was titled Spectral-LOQC (S-LOQC) [20]. Recently [21] it was reported about testing CHSH inequality in frequency domain for biphotons generated in spontaneous-down-conversion process by choosing optimal parameters of modulation. In [22], the Bell inequality was tested on frequency-bin entangled photon pairs using time-resolved detection.

Here, we deal with generalization of the problem solved for bipartite case in [21, 23]. In our model,  $N$  communicating parts of quantum network realize Bell test on common multi-photon state. Each part of the network is equipped with a phase modulator, filter and photo-detector and receive only one photon. We estimate modulation parameters, which allow us to register nonlocal property of shared state and violate of some inequality (CHSH, Mermin, Svetlichny, etc.) using Bell theorem. For these, we use the full-quantum model of electro-optical phase modulation process including finite number of interacting modes [24]. This model asymptotically approaches the semi-classical one, which was considered in [23], when number of interacting modes goes to infinity. Testing a number of cases with different shared entangled states, we solve the optimization problem obtain corresponding modulation parameters, which prove state nonlocality for each case. Additionally, we estimate the region of detection settings, which reveals Bell nonlocality.

Our paper has the following structure. Section 2 is devoted to main definitions and mathematical model of multi-partite Bell test. In Section 3, we introduce the notion of frequency bin and derive multi-photon frequency-entangled quantum state, shared between all parties of quantum network. In Section 4, we describe generalized

measurement procedure at each size of the network and formulate Svetlichny inequality for the case under investigation. Numerical modelling and solution of optimization problem for particular cases of entangled two (EPR) and three (GHZ and Wigner) states are in Section 5. Section 6 is devoted to discussion and conclude the paper.

### 2. Modelling of multi-partite Bell test

In a model of our theoretical Bell experiment, we will use notations following [1]. We set A (Alice), B (Bob), C (Charlie), ... as communicating parts of considered quantum network (see fig. 1). At each side of this network, there is a measurement device  $D_A, D_B, D_C, \dots$  with a definite input:  $x^{(A)} \in \{x_i\}_{i=1}^{n_A}$  for  $D_A$ ,  $y^{(B)} \in \{y_j\}_{j=1}^{n_B}$  for  $D_B$ ,  $z^{(C)} \in \{z_k\}_{k=1}^{n_C}$  for  $D_C$ , ... . Possible outcomes of measurement procedure on each detector is denoted by  $a \in \{a_\alpha\}_{\alpha=1}^{m_A}$  for Alice side,  $b \in \{b_\beta\}_{\beta=1}^{m_B}$  for Bob side,  $c \in \{c_\gamma\}_{\gamma=1}^{m_C}$  for Charlie, etc. The object of our interest will be a set  $P$  of joint probabilities  $p(a_\alpha, b_\beta, c_\gamma \dots | x_i, y_j, z_k \dots)$  to detect results  $a_\alpha, b_\beta, c_\gamma, \dots$  setting parameters  $x_i, y_j, z_k, \dots$  which usually called *behaviour*. For instance, *local behavior*  $P_L$  of distributed detection system is supposed to satisfy the following condition for each join probability  $p \in P_L$ :

$$p(a_\alpha, b_\beta, c_\gamma \dots | x_i, y_j, z_k \dots) = \int_{\Lambda} d\lambda q(\lambda) p(a_\alpha | x_i, \lambda) p(b_\beta | y_j, \lambda) p(c_\gamma | z_k, \lambda) \dots \quad (1)$$

Here,  $\lambda \in \Lambda$  is “hidden” variable taking value in space  $\Lambda$  and distributed according to the probability density  $q(\lambda)$ . Quantum mechanics gives the following rule for calculating probabilities:

$$p(a_\alpha, b_\beta, c_\gamma \dots | x_i, y_j, z_k \dots) = \text{tr}(\rho_{ABC\dots} M_{a_\alpha | x_i} \otimes M_{b_\beta | y_j} \otimes M_{c_\gamma | z_k} \otimes \dots), \quad (2)$$

that form *quantum behaviour*  $P_Q$  of measurement apparatus. Here,  $\rho_{ABC\dots}$  is quantum state on common Hilbert space  $H_A \otimes H_B \otimes H_C \otimes \dots$ , and  $M$  are measurement operators (positive operator-valued measures) on corresponded subspace. Due to the fact that  $P_L \subset P_Q$ , there exist quantum states (nonlocal) with statistics different from that of correspondent to local behavior. This means that probability distribution of the form (1) for any quantum state  $\rho_{ABC\dots}$  does not exist. Inequality for detecting genuine multi-partite nonlocality was introduced [25] and generalized [26] by Svetlichny. It has the form:

$$S_N = \langle S_{N-1} r'_N \rangle + \langle S'_{N-1} r_N \rangle \leq 2^{N-1}, \quad (3)$$

obtained from repeating the procedure which allowed us to build Svetlichny’s inequality from CHSH:

$$S_3 = \langle r'_1 r_2 r_3 \rangle + \langle r_1 r'_2 r_3 \rangle + \langle r_1 r_2 r'_3 \rangle - \langle r'_1 r'_2 r'_3 \rangle + \langle r'_1 r'_2 r_3 \rangle + \langle r'_1 r_2 r'_3 \rangle + \langle r_1 r'_2 r'_3 \rangle - \langle r_1 r_2 r_3 \rangle \equiv \langle S r'_3 \rangle + \langle S' r_3 \rangle \leq 4. \quad (4)$$

Here it is supposed that all measurements are dichotomic and their results are denoted by  $r_j = \pm 1$  and  $r'_j = \pm 1$ , where  $r_1 = a, r_2 = b, r_3 = c, \dots$

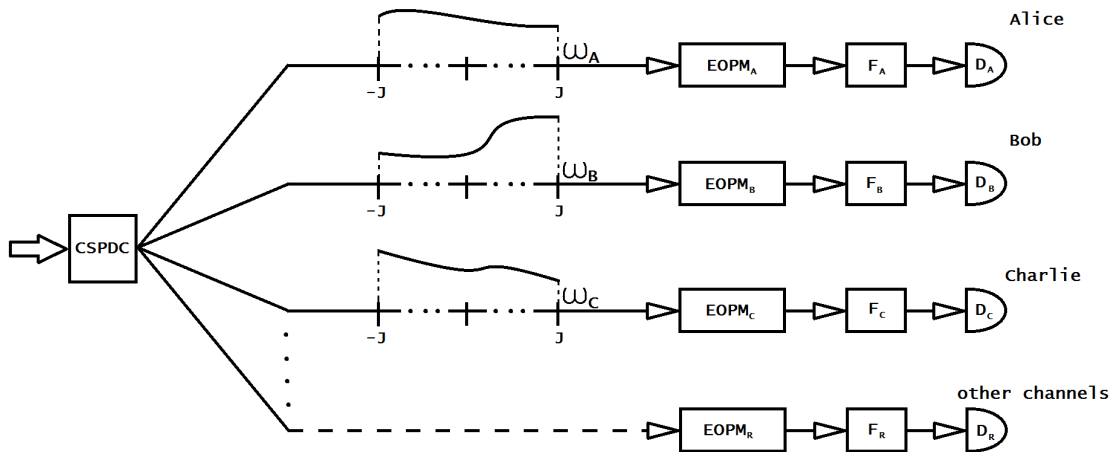


FIG. 1. Quantum network for  $N$ -photon experiment. The source is a pump laser that generates frequency-entangled photons resulting from cascade spontaneous parametric down-conversion process. In each channel, tuned EOPMs are located. Photons phases are modulated by EOPMs driven by signals at certain frequencies with respective pairs of parameters.  $F_R$  for drop filters,  $D_R$  for detectors (SSPDs)

In the next section we will define common  $N$ -photon quantum multi-mode state shared between all  $N$  parties of the quantum optical network and describe procedure revealing it's nonlocal properties using formalism presented in this section.

### 3. Frequency-bin coding and multi-mode quantum states

We will consider a process of entangled  $N$ -photon quantum state generation resulting, for example, from cascade spontaneous down conversion scheme. This process produce photons in frequency-entangled state of the form  $\rho_{ABC\dots} = |\chi\rangle\langle\chi|$ , where:

$$|\chi\rangle \equiv |\chi\rangle_{ABC\dots} = \int_{-\infty}^{\infty} d\omega_a d\omega_b d\omega_c \dots F(\omega_a, \omega_b, \omega_c, \dots) |1_{\omega_a}\rangle_A |1_{\omega_b}\rangle_B |1_{\omega_c}\rangle_C \dots \quad (5)$$

Here,  $F(\omega_a, \omega_b, \omega_c, \dots)$  is spectral density distribution and  $|1_{\omega_r}\rangle_R$  is denoted single photon state with frequency  $\omega_r$ ,  $r \in \{a, b, c, \dots\}$  transmitted to channel  $R \in \{A, B, C, \dots\}$ . Each channel  $R$  is equipped with electro-optical phase modulator  $EOPM_R$ , frequency filter  $F_R$  and photo-counter  $D_R$ . Modulation frequency  $\Omega_{MW}$  for all  $EOPM_R$  is assumed to be the same, while other parameters may be different. The action of EOPMs on arriving state can only change the frequencies by integer multiples of  $\Omega_{MW}$ . For the next, following [21] we introduce the notion of frequency bin: all photons whose frequencies are contained in an interval  $[\omega_0 - \Omega/2, \omega_0 + \Omega/2]$  are grouped into a single frequency bin centred on frequency  $\omega_0$ . Assuming  $\Omega \ll \Omega_{MW}$  we can write our initial state in the discretized form:

$$|\chi\rangle_{ABC\dots} = \sum_{a,b,c,\dots \in Z} F_{a,b,c,\dots} |1_a\rangle_A |1_b\rangle_B |1_c\rangle_C \dots, \quad (6)$$

where we introduced  $\omega_r \equiv \omega_0 + r\Omega_{MW}$  and dropped leaving only index  $r$ . Considering photon creation operator  $a_{r,R}^\dagger$  on frequency  $\omega_r$  in channel  $R$  and fixing order for  $R$  (to drop  $R$ ), we finally obtain:

$$|\chi\rangle_{ABC\dots} = \sum_{a,b,c,\dots \in Z} F_{a,b,c,\dots} a_a^\dagger a_b^\dagger a_c^\dagger \dots |0\rangle. \quad (7)$$

The state of this form will be the subject of our investigation of it's nonlocal properties with the help of inequalities (3) and (4).

### 4. Detection procedure and inequality derivation

As it was mentioned above, each side of our quantum network is equipped with EOPM, filter and photo-counter. To realize the procedure of state nonlocality detection using inequality (3) we consider these three devices as generalized measurement apparatus, whose input is parametrized by modulator parameters  $(\varphi, \tilde{\alpha}, \tilde{\beta})$  and filter properties. The next question is: what agreement should reach all parties about the inputs and outputs of their measurement devices to reveal nonlocal properties of state (7). We restrict ourselves by two sets of modulation parameters as to different inputs for each generalized detector. And our goal now is to obtain optimal values of these parameters to maximize functional (3) solving corresponding optimization problem. To do this, we consider full quantum model of EOPM, investigated in [24] and write the modulator action as:

$$U |\chi\rangle_{ABC\dots} = \sum_{a',b',c',\dots \in Z} F_{a',b',c',\dots} \tilde{a}_{a'}^\dagger \tilde{a}_{b'}^\dagger \tilde{a}_{c'}^\dagger \dots |0\rangle, \quad (8)$$

where evolution operator  $U \equiv U(\varphi, \tilde{\alpha}, \tilde{\beta})$  and output operators  $\tilde{a}_r^\dagger$  are expressed through input ones with use of the formula:

$$\tilde{a}_r^\dagger = U^\dagger a_r^\dagger U = e^{-i(\omega_0 + r'\Omega_{MW})T} \sum_{r=-J}^J (-1)^r e^{-i(r+r')\tilde{\alpha}} d_{r',r}^J(\tilde{\beta}) e^{i(r'-r)\varphi} a_r^\dagger \equiv \sum_{r=-J}^J M_{r'r}^{(J)} a_r^\dagger, \quad (9)$$

where  $T$  is modulation time,  $(2J+1)$  is number of interacted modes in modulator and  $d_{\mu\nu}^J(\tilde{\beta})$  is the Wigner  $d$ -function. Using (9), Eq. (8) may be written as:

$$U |\chi\rangle_{ABC\dots} = \sum_{a,b,c,\dots \in Z} \tilde{F}_{a,b,c,\dots} a_a^\dagger a_b^\dagger a_c^\dagger \dots |0\rangle, \quad (10)$$

and

$$\tilde{F}_{a,b,c,\dots} = \sum_{a',b',c',\dots \in Z} F_{a',b',c',\dots} M_{a'a}^{(J)} M_{b'b}^{(J)} M_{c'c}^{(J)} \dots \quad (11)$$

For physical reasons and from the fact that evolution operator  $U$  is unitary, we have  $\|F\|_2 = \|\tilde{F}\|_2 = 1$ , where

$$\|F\|_2 = \sum_{a,b,c,\dots \in Z} |F_{a,b,c,\dots}|^2.$$

After determination of two inputs  $(\tilde{\alpha}_i, \tilde{\beta}_i)$ ,  $i = 1, 2$  for each measurement device, we characterize measurement result in channel  $R$  by random variable  $\theta_R = \pm 1$ , that takes value  $\theta_{r,R} = 1$  then there was a photo-count at bin  $\omega_r$  in channel  $R$  and  $\theta_R = -1$  otherwise. Joint probability for the events when all photons are detected at frequency  $\omega_{a_\alpha}$  in channel  $A$ ,  $\omega_{b_\beta}$  in channel  $B$ ,  $\omega_{c_\gamma}$  in channel  $C, \dots$  under input parameters  $x_i = (\tilde{\alpha}_i, \tilde{\beta}_i)_A$ ,  $y_j = (\tilde{\alpha}_j, \tilde{\beta}_j)_B$ ,  $z_k = (\tilde{\alpha}_k, \tilde{\beta}_k)_C$ , etc. is

$$p(a_\alpha, b_\beta, c_\gamma, \dots | x_i, y_j, z_k, \dots) = \left| \langle 1_{a_\alpha} 1_{b_\beta} 1_{c_\gamma} | U | \chi \rangle_{ABC\dots} \right|^2 = \left| \tilde{F}_{a_\alpha b_\beta c_\gamma \dots} \right|^2. \quad (12)$$

To estimate the “true” statistics of initial state before modulation process, we use Bayes’ theorem, which gives conditional probability:

$$p_B(a, b, c, \dots | a', b', c', \dots) = \frac{\left| F_{a',b',c',\dots} M_{a'a}^{(J)} M_{b'b}^{(J)} M_{c'c}^{(J)} \dots \right|^2}{\sum_{a',b',c',\dots \in Z} \left| F_{a',b',c',\dots} M_{a'a}^{(J)} M_{b'b}^{(J)} M_{c'c}^{(J)} \dots \right|^2}. \quad (13)$$

Taking into account the possible values of random variables  $\theta_{r,R} \in \{\pm 1\}$ , we can write:

$$\langle \theta_{r_1,A}, \theta_{r_2,B}, \theta_{r_3,C}, \dots \rangle \equiv \langle \theta_{a,A}, \theta_{b,B}, \theta_{c,C}, \dots \rangle = \text{sgn}(\theta_{a,A} \theta_{b,B} \theta_{c,C} \dots) p_B(a, b, c, \dots | a', b', c', \dots). \quad (14)$$

Thus, we arrive to Svetlichny inequality for frequency-encoded multi-mode quantum states. The next section will be devoted to optimization problem for modulator parameters which maximize Bell functional and reveal nonlocality of shared multi-photon entangled quantum state.

## 5. Numerical modelling: bipartite and tripartite cases

In this section, we will represent the results of some numerical analysis.

Let us choose the system to have 6 interacted modes (this means  $J = 2.5$ ) in every channel. Photons in every channel could have their own spectrum, but without loss of generality let us make them all to be equal. We have there only 6 frequencies from  $\omega_0 - 2.5 \cdot \Omega_{MW}$  to  $\omega_0 + 2.5 \cdot \Omega_{MW}$ .

### 5.1. Bipartite case

In the section, we investigate two-particle case in a specific scheme, which approve Bell results and in particular CH74 (Clauser–Horne, [7]) inequality in a frequency domain. This setup was initially proposed in [21] to test CH74 inequality using phase modulated photons generated in spontaneous down conversion (SPDC) process. Using the approach presented above, we now can determine  $S$  in CH74 inequality and formulate optimization problem, which has a solution. We got the maximum value for  $S$  of 2.389. This result corresponds with [21], but in our approach we can operate with any frequency spectrum. We show plots in order to get understanding of nonlocality domain pattern in Fig. 2.

### 5.2. Tripartite case

Here, we are going to modelling a priory entangled tripartite states in order to verify whether they are nonlocal.

*5.2.1. Wigner-state.* We start with Wigner state expressed in terms of frequency entangled photon triplet:

$$|W\rangle = |-0.5_A, 1.5_B, 2.5_C\rangle + |-0.5_A, 2.5_B, -1.5_C\rangle + |2.5_A, -0.5_B, -1.5_C\rangle, \quad (15)$$

where i.e.  $|-0.5\rangle$  means  $|\omega_0 - 0.5\hat{\Omega}_{RF}\rangle$  and  $A, B, C$  represent Alice’s, Bob’s and Charlie’s channels respectively.

We show the spectrum probability density of the state before modulation in the Fig. 3(a).

Every channel has its own EOM [24]. In Fig. 4(a) the spectrum probability density of the Wigner state after modulation is shown.

For this state we build Svetlichy inequality  $S(\alpha_{11}, \beta_{11}, \alpha_{21}, \beta_{21}, \alpha_{31}, \beta_{31}, \alpha_{12}, \beta_{12}, \alpha_{22}, \beta_{22}, \alpha_{32}, \beta_{32})$ . We found the maximum of the functional in this case as 4.914 at point

$$\{1.946, 4.444, 5.094, 3.691, 6.161, 0.445, 2.371, 5.121, 0.094, 5.482, 3.799, 6.224\}. \quad (16)$$

Now, we can describe domain of nonlocality for our state varying any parameters in 18. For clarity we vary the second EOM parameter of first channel  $\beta_{11}$  and the same second EOM parameter of the second channel  $\beta_{21}$ .

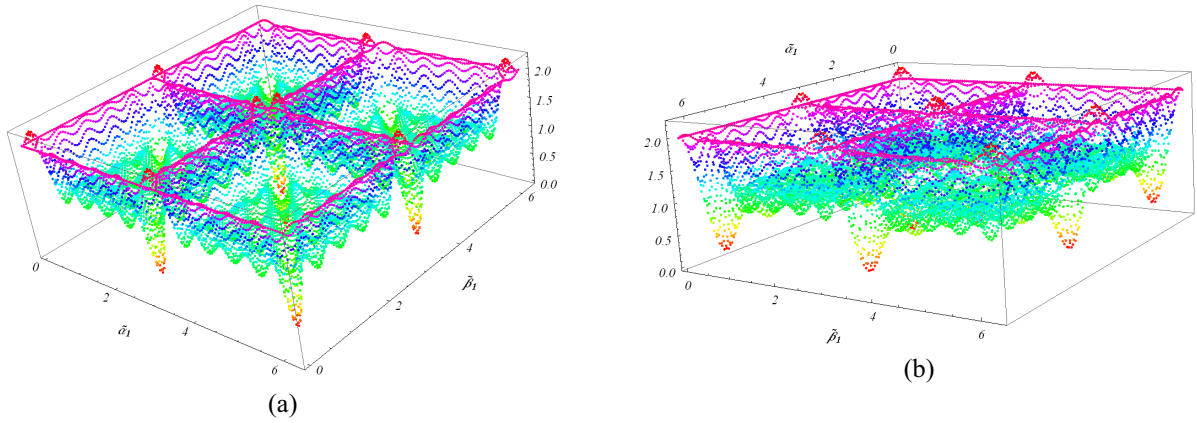


FIG. 2. We build 3d-surface of Bell functional, varying two of the parameters. All the parameters are in  $[0; 2\pi]$ . The surface is projection the Bell inequality onto pair of parameters  $\tilde{\alpha}_1$  and  $\tilde{\beta}_1$  given fixed other parameters  $(S(0, 0, 0, 0, 0, \tilde{\alpha}_1, 0.3, \tilde{\beta}_1))$ . There are extremes at points of  $(x; y)$  where  $x, y \in 0, \pi, 2\pi$ . (a) and (b) displays  $S$

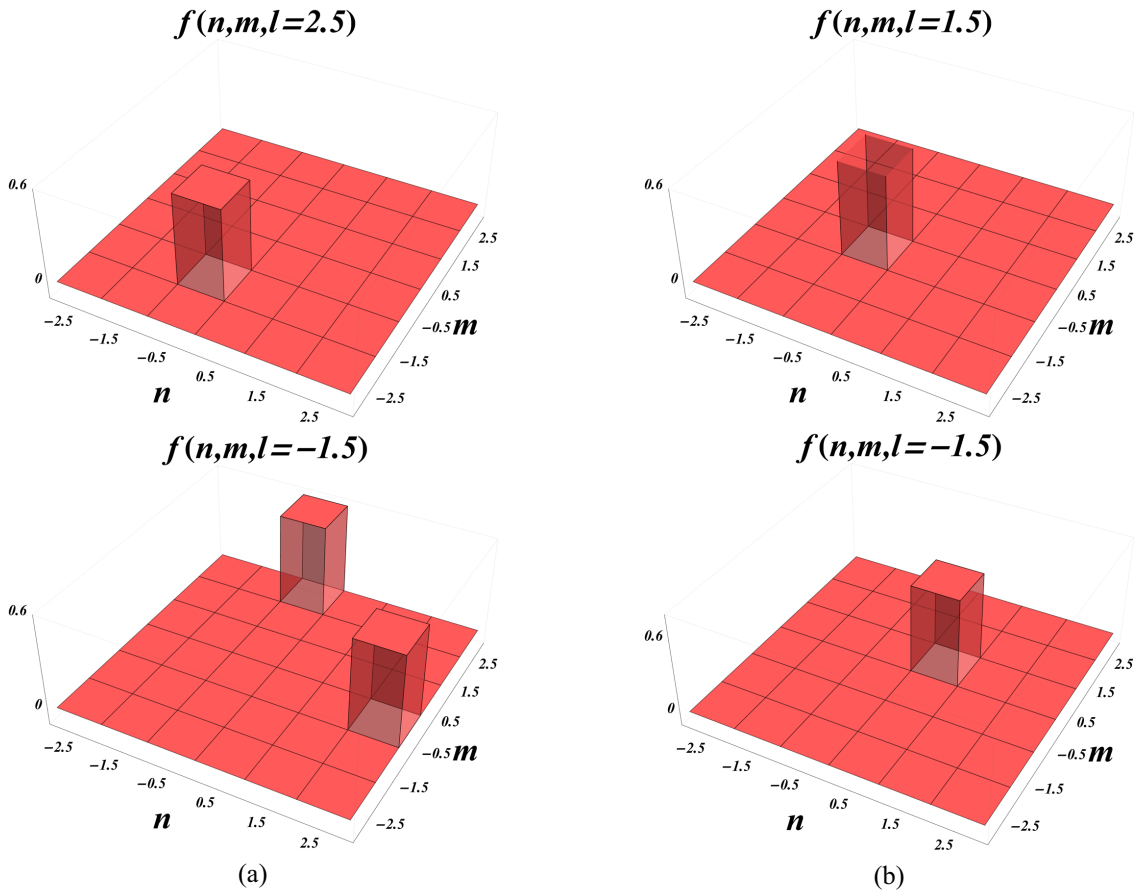


FIG. 3. (a) The spectrum probability density of the Wigner state before modulation for certain third frequency  $l$ .  $m$  denotes the first channel frequency,  $n$  denotes the second. For other  $l$  the probability function is equal to zero. (b) The spectrum probability density of the GHZ state before modulation for certain third frequency  $l$ . As before for other  $l$  the probability function is equals to zero

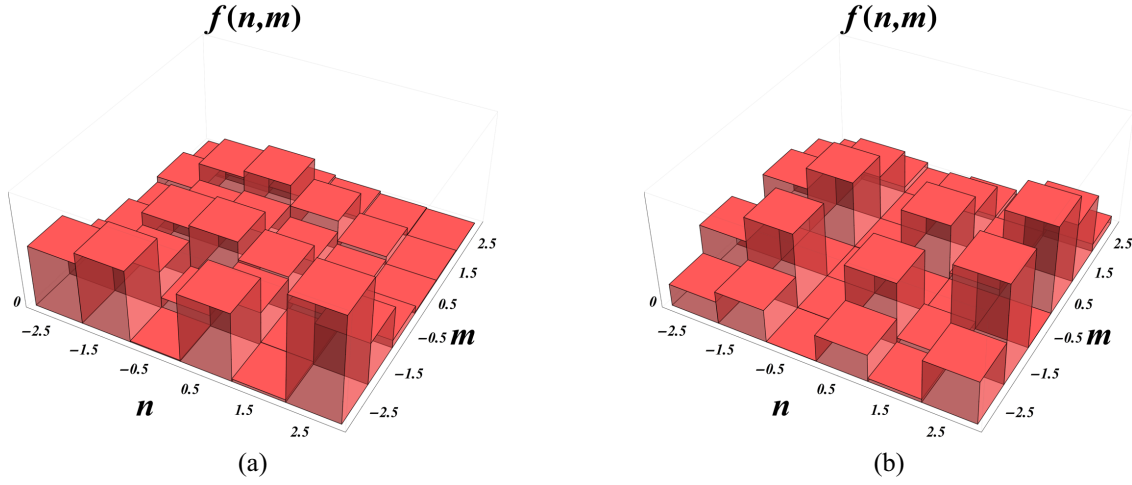


FIG. 4. (a) The spectrum probability density of the Wigner state after modulation for any third frequency  $l$ .  $m$  denotes the first channel frequency,  $n$  denotes the second. (b) The spectrum probability density of the GHZ state after modulation for any third frequency  $l$ .  $m$  denotes the first channel frequency,  $n$  denotes the second

Domains violating the Svetlichny inequality are shown in Fig.5(a) (as was said before the local boundary of the inequality is 4).

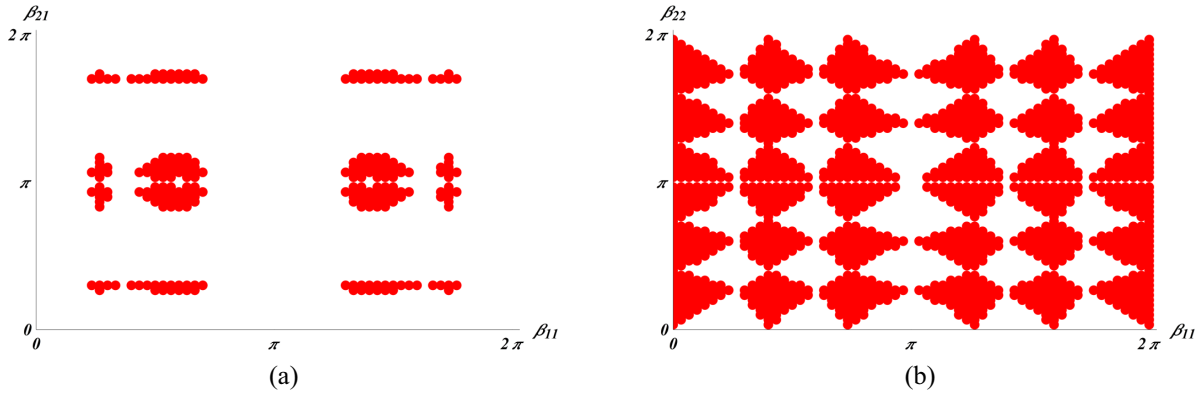


FIG. 5. (a) The nonlocal domains of Wigner state in 2d-projection. (b) The nonlocal domains of GHZ state in 2d-projection

5.2.2. *GHZ-state.* We designed the method that allows us to check any state for nonlocality. For this purpose, we need to have only spectrum probability density for a state. We show this with the example of another entangled state, such as GHZ-state. The spectrum density of GHZ-state is

$$|GHZ\rangle = |-0.5_A, -0.5_B, 1.5_C\rangle + |0.5_A, 0.5_B, -1.5_C\rangle \tag{17}$$

and is shown before modulation in Fig.3(b) and after modulation in Fig. 4(b).

For the current state, we obtained a violation 4.994 at the point

$$\{4.61, 1.25, 3.095, 3.948, 0.055, 6.213, 0.69, 5.499, 4.129, 0.517, 4.787, 2.15\}. \tag{18}$$

Now we vary  $\beta_{11}$  and  $\beta_{22}$  in order to get nonlocality domain of GHZ state in Fig.5(b).

### 6. Conclusion

The current work is devoted to Bell inequalities in multi-partite systems. We presented Bell formalism applicable to our problem and formulated CHSH inequality in case of N-dimension problem. Following [21] we formulate common state which could be modulated in our approach. Also, we derive joint probabilities to construct genuine spectral density distribution. Using the approach presented in [24], we build the method which

allows us to test any state of nonlocality and show the operation of this method on different states. We checked a priori entangled bipartite state and find the point violated CH74 inequality  $S$  maximally. The result corresponding with [21]. We presented violating of  $W$  and  $GHZ$  states and obtained domains of nonlocality in all. We can generalize the approach to any-dimensional quantum nanosystem system for any entangled or not entangled state.

### Acknowledgements

This work was partially financially supported by the Government of the Russian Federation (grant 08-08), by grant 16-11-10330 of Russian Science Foundation.

### References

- [1] Bruner N., et al. Bell nonlocality. *Review of Modern Physics*, 2014, **86** (2), P. 419–478.
- [2] Horodecki R. Quantum entanglement. *Reviews of Modern Physics*, 2009, **81** (2), P. 865–942.
- [3] Gisin N. Bell's inequality holds for all non-product states. *Physics Letters A*, 1991, **154** (5–6), P. 201–202.
- [4] Barret J. Nonsequential POVM's on entangled mixed states do not always violate a Bell inequality. *Physical Review A*, 2002, **65** (4), 042302.
- [5] Masanes L., Liang Y.-C., Doherty A.C. All Bipartite Entangled States Display Some Hidden Nonlocality. *Physical Review Letters*, 2008, **100** (9), 090403.
- [6] Bell J.S. On the Einstein Podolsky Rosen Paradox. *Physics*, 1964, **1** (3), P. 195–200.
- [7] Clauser J.F., Horne M.A. Experimental consequences of objective local theories. *Phys. Rev. D*, 1974, **10**, P. 526.
- [8] Clauser J.F., Horne M.A., Shimony A., Holt R.A. On the Einstein Podolsky Rosen Paradox. *Physical Review Letters*, 1969, **23** (15), P. 880.
- [9] Mermin N.D. Extreme quantum entanglement in a superposition of macroscopically distinct states. *Physical Review Letters*, 1990, **65** (15), P. 1838.
- [10] Belinskii A., Klyshko D. Interference of light and Bell's theorem. *Physics-Uspokhi*, 1993, **36** (8), P. 653.
- [11] Lodahl P., Mahmoodian S., Stobbe S. Interfacing single photons and single quantum dots with photonic nanostructures. *Reviews of Modern Physics*, 2015, **87** (2), P. 347.
- [12] Gisin N., et al. Quantum cryptography. *Reviews of Modern Physics*, 2002, **74** (1), P. 145–195.
- [13] Soorat R., Madhuri K., Vudayagiri A. Random number generator for cryptography. *Nanosystems: Physics, Chemistry, Mathematics*, 2017, **8** (5), P. 600–605.
- [14] Ivanova A.E., Chivilikhin S.A., Gleim A.V. The use of beam and fiber splitters in quantum random number generators based on vacuum fluctuations. *Nanosystems: Physics, Chemistry, Mathematics*, 2016, **7** (2), P. 378–383.
- [15] Kues M., et al. On-chip generation of high-dimensional entangled quantum states and their coherent control. *Nature*, 2017, **546**, P. 622.
- [16] Zeilinger A., et al. Significant-loophole-free test of Bell's theorem with entangled photons. *Physical Review Letters*, 2015, **115** (25), 250401.
- [17] Knill E., et al. Strong loophole-free test of local realism. *Physical Review Letters*, 2015, **115** (25), 250402.
- [18] Capmany J., Fernandez-Pousa C.R. Realization of Single-Photon Frequency-Domain Qubit Channels Using Phase Modulators. *IEEE Photonics Journal*, 2012, **4** (6), P. 2074–2084.
- [19] Lukens J.M., Lougovsky P. Frequency-encoded photonic qubits for scalable quantum information processing. *Optica*, 2017, **4** (1), 010008.
- [20] Lu H.-H., et al. Electro-Optic Frequency Beam Splitters and Tritters for High-Fidelity Photonic Quantum Information Processing. *Physical Review Letters*, 2018, **120** (3), 030502(6).
- [21] Olislager L., et al. Implementing two-photon interference in the frequency domain with electro-optic phase modulators. *New Journal of Physics*, 2012, **14**, 043015.
- [22] Guo X., Mey Y., Du S. Testing the Bell inequality on frequency-bin entangled photon pairs using time-resolved detection. *Optica*, 2017, **4** (4), 040388.
- [23] Capmany J., Fernandez-Pousa C.R. Quantum modelling of electro-optic modulators. *Laser Photonics Review*, 2011, **5** (6), P. 750–772.
- [24] Miroshnichenko G.P., et al. Algebraic approach to electro-optic modulation of light: exactly solvable multimode quantum model. *Journal of the Optical Society of America B*, 2017, **34** (6), 061177.
- [25] Svetlichny G. Distinguishing three-body from two-body nonseparability by a Bell-type inequality. *Physical Review D*, 1987, **35** (10), 3066.
- [26] Seevinck M., Svetlichny G. Bell-Type Inequalities for Partial Separability in  $N$ -Particle Systems and Quantum Mechanical Violations. *Physical Review Letters*, 2002, **89** (6), 060401.

## Investigation of the possibility for reducing agglomeration of aerosol nanoparticles by using the needle-plate corona charger

A. A. Efimov, P. V. Arsenov, V. V. Ivanov

Moscow Institute of Physics and Technology, Russia, 141700 Dolgoprudny, Institutskiy per., 9  
newaldan@gmail.com

PACS 92.60.Mt, 82.70.Rr, 61.46.+w

DOI 10.17586/2220-8054-2018-9-4-491-495

The results of the research are given to show the possibility of reducing the agglomeration of aerosol nanoparticles using the needle-plate corona charger. It has been found that the charger fulfills the functions of an electrofilter-separator, precipitating large particles of agglomerates at a size more than 250 nm, leaving smaller non-agglomerated particles in the flow. Using the developed charger allows us to significantly reduce the agglomeration of particles at sufficiently low aerosol flow rates. As a result of changing the parameters of the charger (corona discharge current from 35 to 215  $\mu\text{A}$ , aerosol flow through the charger from 33 to 250 l/min and the corona polarity), the mean particle size decreases more than in 1.5-fold.

**Keywords:** the needle-plate charger, agglomeration, aerosol nanoparticles, aerosol, the multi-spark discharge generator.

*Received: 27 November 2017*

### 1. Introduction

Recent years have seen an increase in the use of aerosol nano-particles to create new materials and devices [1]. It is known that the size of aerosol nanoparticles affects the characteristics of the materials and devices in which they are used. In this context, controlling the size of aerosol nanoparticles is a significant task. It is also a known fact that the size of the aerosol nanoparticles increases as a result of the agglomeration process, to be more precise as a result of the collision of particles during their movement in the gas stream.

In this regard, researchers are developing various methods to reduce the agglomeration of nanoparticles. The most effective and simple method for reducing the agglomeration of nanoparticles is diluting the aerosol flow with clean gas [2]. However, this method is not always applicable in practice because there are physical limitations to increasing the dilution ratio of the aerosol.

Charging nanoparticles is an alternative method for reducing the agglomeration process. Therefore, the corona discharge has been one of the most common methods for charging aerosol nanoparticles. There are many works devoted to the study of charging the aerosol nanoparticles in the corona discharge [3,4]. However, most of them have a disadvantage related to the complexity of the design and the high cost of chargers, which limits their various applications. Bearing all this in mind, in this work a relatively simple and cheap unipolar needle-plate charger was designed and investigated to reduce the agglomeration of aerosol nanoparticles. In particular, in this paper, we investigated the effect of the parameters of the charger (the value and polarity of the corona discharge current and gas flow) on the agglomeration of nanoparticles, namely on the mean particle size and the particle size distribution.

### 2. Experiment

In the experiments we used aerosol nanoparticles of  $\text{Al}_2\text{O}_3$ , which were obtained by a multi-spark discharge generator (m-SDG), as a result of electric erosion of the electrode material from Al in air [5,6], see Fig. 1. Then the received nanoparticles were sent to a charger (NPC). The charger was an asymmetric needle-plate discharge gap located in a dielectric tube with an internal diameter of 45 mm. A steel needle with a radius of curvature of about 40  $\mu\text{m}$  was used as the corona electrode and was located at a distance of 10 mm from the opposite electrode, which was made in the form of a plate of 100 mm long and 30 mm wide. When a high voltage was applied between the needle and the plate, a region of high electric field intensity appeared at the tip of the needle, resulting in ionization of the gas molecules and ignition of the corona discharge. As a high-voltage source, the VIDN-30 source was used, and the corona discharge current was measured with an Agilent U1253B multimeter.

Aerosol nanoparticles entering the corona discharge region acquired a unipolar charge due to the adsorption of ions or electrons on their surfaces, depending on the polarity of the corona electrode. As a result of the collection of unipolar charge their further agglomeration was prevented due to Coulomb repulsion [7].

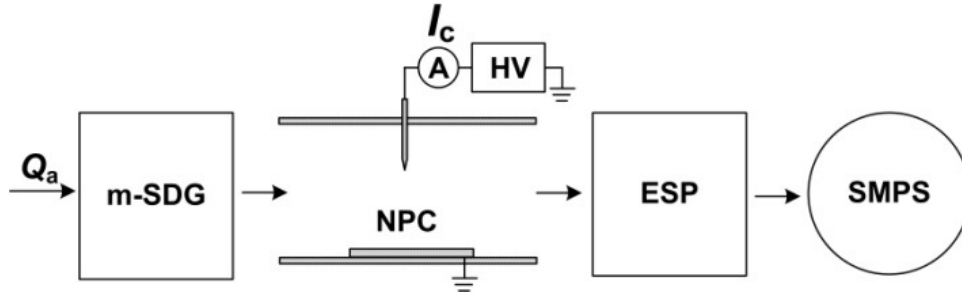


FIG. 1. Conditional scheme of the experiment to study the possibilities of reducing the agglomeration of aerosol nanoparticles using a needle-plate charger. The following abbreviations are used: m-SDG – multi-spark discharge generator, NPC – needle-plate charger, ESP – electrostatic precipitator, SMPS – aerosol spectrometer

At the output of the charger an electrostatic precipitator (ESP) was placed, where all charged particles were captured in order to determine the fraction of charged particles in the aerosol. The capture efficiency of aerosol nanoparticles  $E_{eff}$  in the charger was defined by the following formula:

$$E_{eff} = \left(1 - \frac{n_{out}}{n_{in}}\right) \cdot 100\%, \quad (1)$$

where  $n_{in}$  is the number concentration of particles in the initial aerosol,  $n_{out}$  is the number concentration of particles after passing through the charger.

Using the aerosol spectrometer (SMPS) model TSI 3936, the particle size distribution was measured and from its analysis the degree of agglomeration of the particles was determined. The agglomeration of particles was investigated by varying the basic parameters of the charger. Specifically, we researched the influence of corona discharge current from 35 to 215  $\mu\text{A}$ , charging polarity (negative and positive) and aerosol flow rate through the charger from 33 to 250 l/min.

### 3. Results and discussion

When studying the influence of the corona discharge current on the agglomeration, it was found that an increase in current from 35 to 215  $\mu\text{A}$  promotes a decrease in the agglomeration of nanoparticles, namely a decrease in their mean particle size  $d_m$  from  $117 \pm 8$  to  $87 \pm 6$  nm, respectively (Fig. 2a). Along with this, there is also a decrease in the width of the particle size distribution, namely the geometric standard deviation (GSD) is reduced from  $1.61 \pm 0.01$  to  $1.58 \pm 0.01$ , respectively. It should be noted that the initial aerosol without charge had a broader particle size distribution of  $\text{GSD} = 1.65 \pm 0.01$  and the mean particle size  $158 \pm 11$  nm. The obtained result can be explained as follows: in accordance with the theory of charging, it is known that large particles are charged more efficiently and acquire a larger number of charges than the small ones [8]. Therefore, it follows that larger particles in the electric field will have a higher electrical mobility  $Z_p$  in accordance with the following formula:

$$Z_p = \frac{n_p e C}{3\pi\mu d_p}, \quad (2)$$

where  $n_p$  is the charge per particle,  $e$  is the elementary unit of charge,  $\mu$  is the viscosity of the gas,  $d_p$  is the particle diameter,  $C$  is the Cunningham correction.

As a result, in the corona discharge field, large agglomerates will precipitate more efficiently while small agglomerates will leave the charger without depositing on the electrodes. This explanation is confirmed by the graph in Fig. 2b, which shows the dependence of the capture efficiency of the charged particles in an electric field on the particle size for different values of the corona discharge current.

In Fig. 2b, we can see that most efficiently captured particles are of the submicron range with dimensions of more than 250 nm, the filtration efficiency of which approaches 80 %. However, for particles with sizes less than 250 nm, a noticeable decrease in the efficiency of their capture is observed.

A qualitative model that clearly demonstrates the process of reducing agglomeration of particles after passing through the charger is shown in Fig. 3. The model is constructed using experimental data for corona discharge current  $I_c = 35 \mu\text{A}$ , negative polarity and aerosol flow rate  $Q_a = 33$  l/min through the charger.

This model shows the deposition and charging of particles of three size fractions – small (15 % of all particles), medium (70 % of all particles) and large (15 % of all particles). For each of the particle fractions, the part of

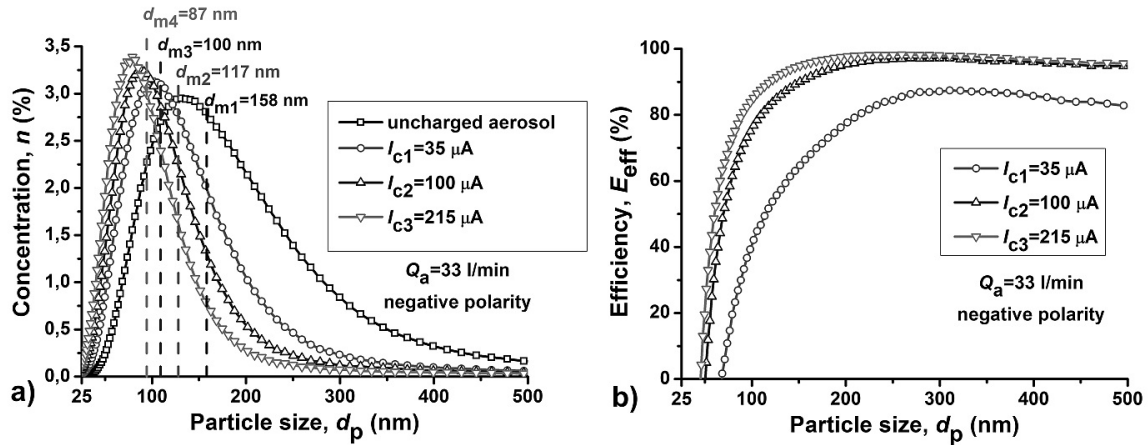


FIG. 2. Influence of the corona discharge current  $I_c$  in the needle-plate charger on (a) the particle size distribution and (b) the particle capture efficiency in the charger

charged particles  $E_{char}$  and the capture efficiency  $E_{eff}$  in the charger are determined by formulas (3, 4 and 1), respectively. The proportion of charged particles in the initial aerosol and after passing through the charger  $E_{char}^{out}$ :

$$E_{char}^{out} = \left(1 - \frac{n_{esp}}{n_{out}}\right) \cdot 100\%, \quad (3)$$

$$E_{char}^{in} = \left(1 - \frac{n_{esp}}{n_{in}}\right) \cdot 100\%, \quad (4)$$

where  $n_{esp}$  is the number concentration of neutral particles measured at the output of the electrostatic precipitator.

In Fig. 3, charged particles are shaded in gray. From Fig. 3, it can be seen that at the output of the charger there are more medium (63 % of all particles) and small particles (33 % of all particles) than larger particles (4 % of all particles). This redistribution of the proportions of small, medium and large particles in comparison with the initial aerosol was mainly due to the precipitation of the large particles. Fig. 3 shows that the fraction of charged particles after passing of the aerosol through the charger increases from  $45 \pm 3$  % to  $67 \pm 4$  % in comparison with the initial aerosol, which also contributes to the reduction of agglomeration as a result of Coulomb repulsion.

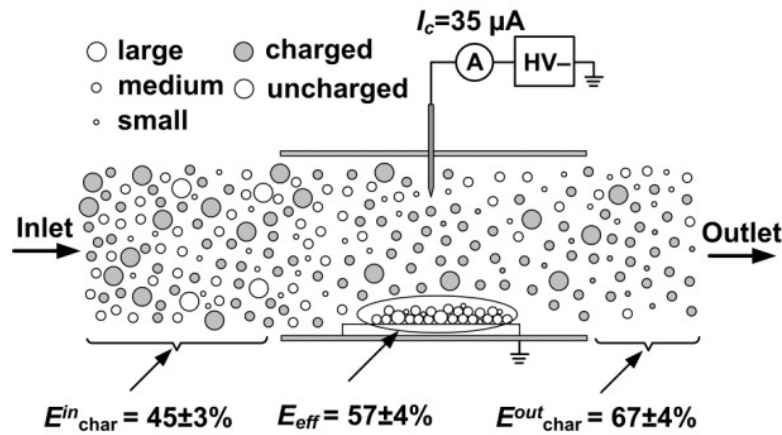


FIG. 3. Qualitative model of the experiment demonstrating the process of reducing the agglomeration of particles after passing through the needle-plate charger

While investigating the influence of corona discharge polarity at a current of  $35 \mu A$ , it was established that negative polarity shows a greater effect on reducing the agglomeration of nanoparticles compared with the positive one (Fig. 4). In particular, when using a negative corona discharge, the mean particle size  $d_m$  is 0.7 times smaller than with a positive corona discharge,  $135 \pm 10$  and  $100 \pm 8$  nm, respectively, while the original uncharged aerosol had a mean particle size of  $161 \pm 11$  nm (Fig. 4a).

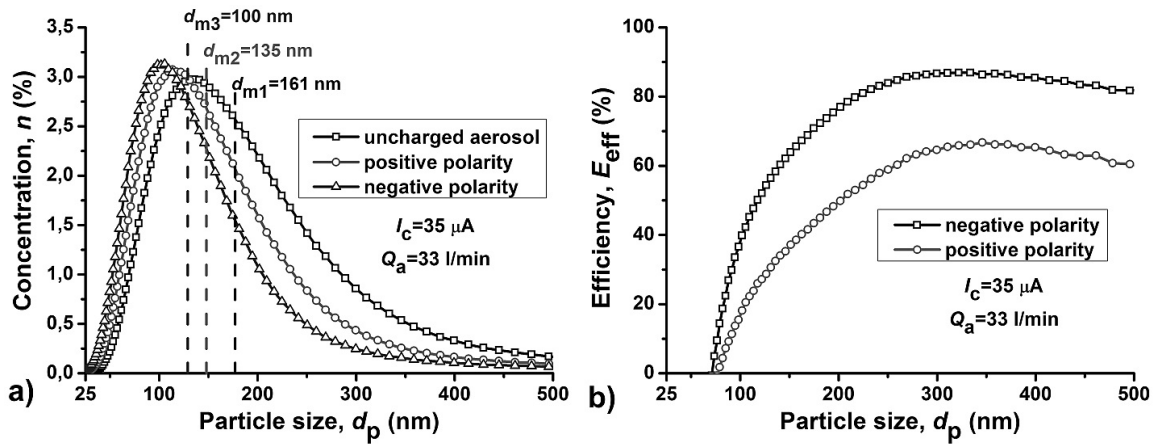


FIG. 4. The influence of polarity of corona discharge in the charger on (a) particle size distribution and (b) capture efficiency

A more effective reduction in the agglomeration of particles with the use of a negative corona discharge is explained by the fact that a higher efficiency of charging aerosol nanoparticles is achieved due to the higher electrical mobility of electrons in comparison with the mobility of positive ions,  $\sim 4 \cdot 10^2 \text{ cm}^2/\text{V}\cdot\text{s}$  and  $\sim 2 \text{ cm}^2/\text{V}\cdot\text{s}$ , respectively. This assumption is qualitatively confirmed in Fig. 4b, which shows that the capture efficiency of particle with negative charging is higher than with positive charging over the whole range of sizes from 75 to 500 nm.

The influence of the aerosol flow through the charger on its agglomeration was also investigated. Fig. 5 shows the particle size distributions throughout the charger depending on the aerosol flow rate.

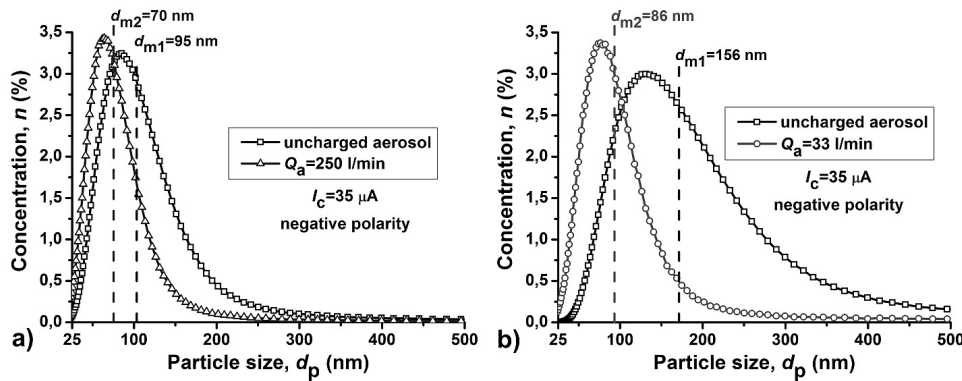


FIG. 5. Particle size distribution of uncharged and charged aerosol in the conditions of the aerosol flow rate at (a) 250 l/min and (b) 33 l/min

In Fig. 5 we can see that at the aerosol flow rate of 250 l/min (Fig. 5a), the mean particle size  $d_m$  of the initial aerosol is less than at the aerosol flow rate of 33 l/min (Fig. 5b),  $95 \pm 8$  and  $156 \pm 14$  nm, respectively. This is mainly due to a decrease in the numerical concentration of aerosol particles as a result of their dilution with a clean gas stream. It should also be noted that when the aerosol passes through the charger, there is an additional reduction in the agglomeration of particles, which manifests itself in a decrease in their mean particle size  $d_m$  from  $95 \pm 8$  to  $70 \pm 7$  nm and from  $156 \pm 14$  to  $86 \pm 7$  nm, at 250 l/min and 33 l/min, respectively. It is worth mentioning that with lower gas flow rate through the charger, more efficient charging of particles is achieved, and as a consequence, the mean particle size changes drastically. Thus, the use of a charger can significantly reduce the agglomeration of particles at fairly low aerosol flow rate.

#### 4. Conclusions

According to the results of the experiments, it has been established that the use of a corona needle-plate charger leads to a significant reduction in the agglomeration of particles: that is in a number of performed experiments, it was possible to reduce the mean particle size  $d_m$  more than in 1.5-fold.

It was found that the charger fulfills the functions of an electrofilter-separator, precipitating large particles of agglomerates at sizes more than 250 nm, leaving smaller non-agglomerated particles in the flow.

It was determined that the efficiency of large agglomerate precipitation from the aerosol flow increased with an increase in corona discharge current  $I_c$  from 35 to 215  $\mu\text{A}$ , with changing corona current from a positive to a negative polarity and a decrease in the aerosol flow rate  $Q_a$  from 250 to 33 l/min through the charger.

In the framework of this study, a model of the process of precipitation of large agglomerates is presented and the possibility of reducing agglomeration of particles at relatively low aerosol flow rate is shown.

### Acknowledgement

This work in the experimental part of this study was supported by the Russian Science Foundation (project No. 15-19-00190) and in the theoretical part was supported by the grant of the President of Russian Federation for young scientists MK-2302.2017.8.

### References

- [1] Kortshagen U.R., Sankaran R.M., Pereira R.N., et al. Nonthermal plasma synthesis of nanocrystals: Fundamental principles, materials, and applications. *Chem. Rev.*, 2016, **116**(18), P. 11061–11127.
- [2] Fissan H., Ristig S., Kaminski H., Asbach C., Epple M. Comparison of different characterization methods for nanoparticle dispersions before and after aerosolization. *Anal. Methods*, 2014, **6**(18), P. 7324–7334.
- [3] Intra P. An Overview of Unipolar Charger Developments for Nanoparticle Charging. *Aerosol Air Qual. Res.*, 2011.
- [4] M. Alonso Gámez, A. Hernández Sierra, F.J. Alguacil. Electrical charging of aerosol nanoparticles and some practical applications. *Cargado eléctrico de partículas de aerosol en régimen cinético y algunas aplicaciones prácticas*, 2003.
- [5] Efimov A.A., Ivanov V.V., Bagazeev A.V., et al. Generation of aerosol nanoparticles by the multi-spark discharge generator. *Tech. Phys. Lett.*, 2013, **39**(12), P. 1053–1056.
- [6] Efimov A., Lizunova A., Sukharev V., Ivanov V. Synthesis and Characterization of  $\text{TiO}_2$ ,  $\text{Cu}_2\text{O}$  and  $\text{Al}_2\text{O}_3$  Aerosol Nanoparticles Produced by the Multi-Spark Discharge Generator. *Korean J. Mater. Res.*, 2016, **26**(3), P. 123–129.
- [7] Qi C., Asbach C., Shin W.G., Fissan H., Pui D.Y.H. The Effect of Particle Pre-Existing Charge on Unipolar Charging and Its Implication on Electrical Aerosol Measurements. *Aerosol Sci. Technol.*, 2009, **43**(3), P. 232–240.
- [8] Pfafflin J.R., Ziegler E.N. *Encyclopedia of Environmental Science and Engineering: A-L*. CRC Press, 2006.

## Resistance of reduced graphene oxide on polystyrene surface

M. N. Nikolaeva<sup>1</sup>, A. N. Bugrov<sup>1,2</sup>, T. D. Anan'eva<sup>1</sup>,  
E. V. Gushchina<sup>3</sup>, M. S. Dunaevskii<sup>3</sup>, A. T. Dideikin<sup>3</sup>

<sup>1</sup>Institute of macromolecular compounds RAS, Bolshoy pr. 31, 199004 St. Petersburg, Russia

<sup>2</sup>Saint Petersburg Electrotechnical University "LETI",  
ul. Professora Popova 5, 197376 St. Petersburg, Russia

<sup>3</sup>Ioffe Institute, Politekhnikeskaya ul. 26, 194021 St. Petersburg, Russia

marianna\_n@mail.ru, alexander.n.bugrov@gmail.com, anthracene@hq.macro.ru  
katgushch@yandex.ru, Mike.Dunaeffsky@mail.ioffe.ru, dideikin@mail.ioffe.ru

PACS 36.20.-r; 68.65.Pq; 71.20.Rv; 72.80. Tm; 74.78.-w

DOI 10.17586/2220-8054-2018-9-4-496-499

Reduced graphene oxide flakes of large area, some of which are more than 100 micrometers in diameter, have been produced on polystyrene surface. These flakes were formed during precipitation of composite based on polystyrene with reduced graphene oxide from the benzene by petroleum ether. Extremely low resistances were obtained for these flakes in planar dimension at room temperature. The measured resistance absolute values turned out to be 2 orders of magnitude lower than the resistance of copper. This result is explained by existence of superconducting component in the reduced graphene oxide inclusions.

**Keywords:** reduced graphene oxide, polystyrene, composite, resistance.

*Received: 13 April 2018*

### 1. Introduction

There are many theoretical and some current experimental studies devoted to the superconductivity of graphene [1–13]. However, until recently, zero or very low resistance of neat graphene has not been fixed. Only manifestations of superconductivity in doped graphene [1,2] or its indirect signs in graphene and graphite have been established. The latter include the external magnetic flux trapping by pyrolytic graphite powder which indicates its superconducting state [3], superconductivity of single-layer graphene deposited on superconductor [4,5], as well as the appearance of Josephson oscillations and Shapiro steps in polymer structures containing reduced graphene oxide (RGO) [12].

It is known that RGO contributes to the appearance of high conductivity [14,15] and superconductivity in sandwich structures when placed between two macroscopic electrodes [12]. In our case, the object of study is the composite based on polystyrene with RGO combining graphene fragments and oxidized groups. In the present work, we revealed the highly conducting state of graphene flakes in planar structures at the room temperature.

It is worth noting that the RGO under consideration was functionalized by 3-(trimethoxysilyl)propyl methacrylate and can participate in radical polymerization with styrene [15]. As a result, covalent bonds between RGO and polystyrene chains are formed, similar to those in work [16]. Previously, it was shown that RGO localization near the surface of the polymer films contributes to high conductivity in the case of styrene copolymerization with functionalized RGO [17]. Beside this, it has been demonstrated by conductive atomic force microscopy method that highly conductive regions of polystyrene/RGO thin films exhibit ohmic current-voltage characteristics [18].

Maximum length dimensions of RGO under consideration revealed by SEM method are only up to 8  $\mu\text{m}$  as it was shown in [15]. The chemical precipitation of the RGO composite upon tightening the polymer coils probably promotes the aggregation of the RGO inclusions. Thus, this process can lead to enlargement of areas of RGO inclusions. Thus, the planar RGO conglomerates with sufficient areas for electrical measurements were obtained using the chemical precipitation method of RGO composite from benzene.

### 2. Experimental

Synthetic details for the RGO composite based on polystyrene as well as surface modification technique of natural crystalline graphite can be found in [14,15,17,19]. Composite content in the solvents mixture was 5 wt.%. Benzene/petroleum ether in different ratios, of 1:1, 1:3, 1:2 and 3:2 were used for RGO composite precipitation. The largest areas of graphene inclusions on the polystyrene surface were observed at a 1:1 ratio of benzene/petroleum ether. So, this solvent ratio (1:1) was chosen for production of sufficient RGO planar structures. Films of the polymer composite were deposited on glass substrate by casting through the dispenser. Scanning

probe microscope (SPM) Solver P47-Pro (NTMDT) was used for surface roughness measurements. Since RGO flakes were formed on the polystyrene surface, it was possible to evaluate its thickness by SPM. Thicknesses of RGO flakes measured by SPM did not exceed 50 nm. Thus, the objects of our investigation had turned out to be the multilayered RGO flakes obtained in the result of its self-organization during precipitation process.

Areas of obtained RGO flakes were assessed for resistance using the two-probe method. These measurements were planned only to be qualitative relative to copper resistance. Two kinds of electrodes, the diamond SPM tip doped by nitrogen and steel needles with different curvature radii were used. The curvature radii of electrodes were approximately 50 nm and 15  $\mu\text{m}$  correspondingly. Resistance values of RGO flakes were compared with macroscopic copper substrate ones. Pressure on electrodes during measurements did not exceed 0.5  $\text{g}/\mu\text{m}^2$ . Applying larger pressures caused the breaking of thin SPM electrodes and RGO flakes splitting. After all, at the excess pressure the full separation of RGO flakes from polystyrene surface can be observed.

### 3. Results and discussion

The RGO flake distribution with various shapes and areas on the polystyrene surface after precipitation was irregular and sizes of flakes differed from each other in many times (Fig. 1). This distribution drastically differs from dispersion degree and homogeneity of the filler in the polymer matrix without applying precipitation (Fig. 2). As we can suppose in the precipitation process, polymer coils became tightened. These appearing tensions between RGO planes and polymer coils create conditions for RGO releasing from polymer matrix. In this way, separate RGO particles are getting together into large RGO flakes.

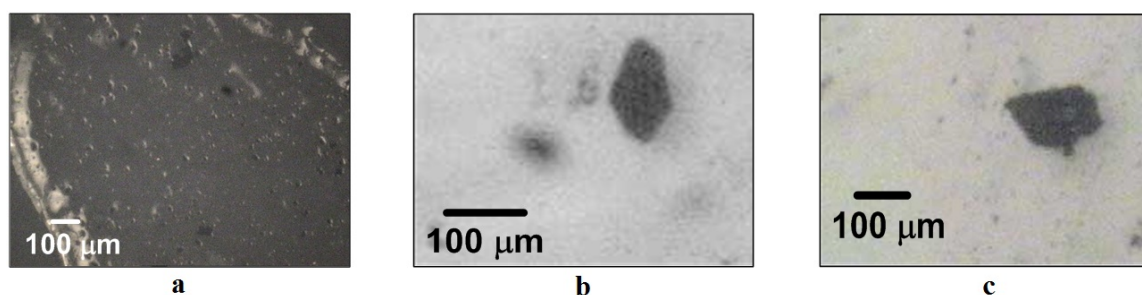


FIG. 1. Optical images of some RGO flakes on polystyrene matrix formed after precipitation. Black inclusions are RGO flakes

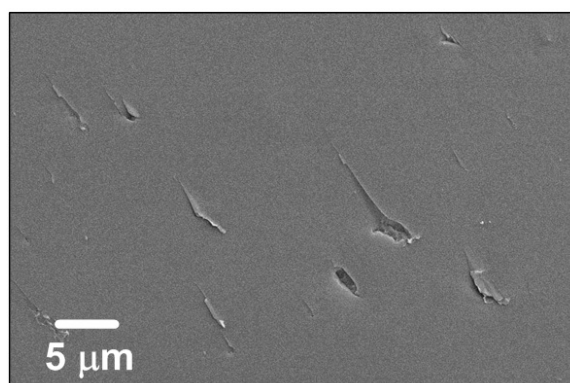


FIG. 2. SEM image of RGO distribution in polystyrene matrix without using precipitation [15]

Sufficiently large and round-shaped RGO flakes (Fig. 1b,c) were used for resistance measurements. In the case of steel electrodes with 15  $\mu\text{m}$  curvature radii, the resistances were measured for the large RGO flakes with diameter of 150 – 200  $\mu\text{m}$ . Resistance of RGO flakes was dependent on the distance between measuring electrodes. The distance increase caused sharp resistance amplification. Resistances were evaluated from current-voltage characteristics (Fig. 3,4). The resistance of RGO flakes was approximately 23  $\text{k}\Omega$  when distance between SPM tip electrodes was 10  $\mu\text{m}$  and 26  $\text{M}\Omega$  already for 30  $\mu\text{m}$  distance (Fig. 3). Resistance was 2  $\Omega$  when measured by steel electrodes with larger curvature radii for 10  $\mu\text{m}$  gap and 5  $\text{k}\Omega$  for 30  $\mu\text{m}$  gap (Fig. 4). RGO

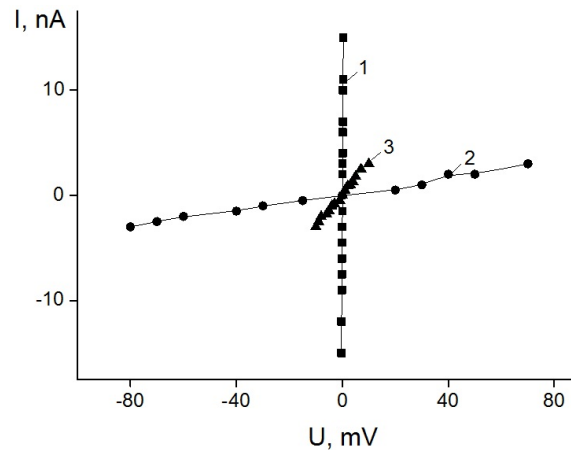


FIG. 3. Current-voltage characteristics of RGO flakes on polystyrene matrix using electrodes with 50 nm curvature radii (1 – distance between electrodes 10  $\mu\text{m}$ , 2 – distance between electrodes 30  $\mu\text{m}$ ), and copper (3)

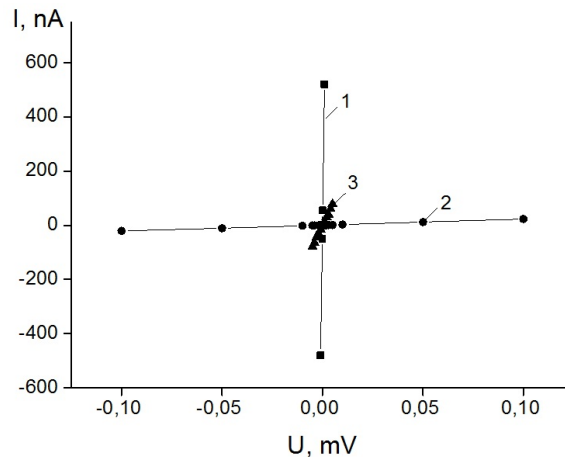


FIG. 4. Current-voltage characteristics of RGO flakes on polystyrene matrix using electrodes with 15  $\mu\text{m}$  curvature radii (1 – distance between electrodes 10  $\mu\text{m}$ , 2 – distance between electrodes 30  $\mu\text{m}$ ), and copper (3)

flakes demonstrated non-conductive state for every kind of electrodes at a distance of 40  $\mu\text{m}$  and larger. It can be explained by defects number accumulation at the RGO surface with distance increase. The resistance of copper substrate was approximately 3.3 M $\Omega$  for tip and 63  $\Omega$  for needle electrodes correspondingly (curve 3 on Fig. 3 and Fig. 4).

Ohm's nature of obtained current-voltage characteristics exclude the presence of a breakdown in films which have been investigated.

It should be noted that current values without voltage applying for 10  $\mu\text{m}$  distances between electrodes were approximately 1.5 – 2 nA. This fact is additional evidence of persistent currents in the RGO flakes. At larger distances between electrodes, the superconducting state disappears, so lines of current-voltage characteristics cross the zero point directly.

The obtained results of persistent currents observed at zero voltage can be explained by existence of superconducting phase in the RGO flakes at room temperature. Therefore the superconducting contribution in the resistance values is preserved in planar RGO structures at distances not exceeding 10  $\mu\text{m}$ . We can suppose these multilayered RGO flakes obtained as a result of self-organization during precipitation process of RGO/polystyrene composite are similar to finely dispersed pyrolytic graphite with superconducting inclusions [3]. All obtained results are in agreement with work [12], where it was shown for this RGO/polystyrene composite that Josephson oscillations and Shapiro steps still exist up to room temperature.

#### 4. Conclusions

Large areas of planar structures from RGO flakes up to 100 – 200  $\mu\text{m}$  were obtained on polystyrene surface. For this purpose, precipitation of reduced graphene oxide composite on base of polystyrene from benzene was used. Precipitation was performed in 1:1 petroleum ether-benzene. The resistance of such planar inclusions, which was measured by diamond SPM tips with curvature of radii 50 nm, turned out to be 2 orders of magnitude lower than the resistance measured for the copper substrate. A similar dependence for resistance was obtained using steel electrodes having curvature radii 15  $\mu\text{m}$ .

#### References

- [1] Ludbrook B.M., Levy G., Nigge P., et al. Evidence for superconductivity in Li-decorated monolayer graphene. *Proc. Natl Acad. Sci. USA*, 2015, **112**(38), P. 11795–11799.
- [2] Chapman J., Su Y., Howard C.A., et al. Superconductivity in Ca-doped graphene laminates. *Sci. Rep.*, 2016, **6**, P. 23254.
- [3] Saad M., Gilmudtinov I.F., Kiiamov A.G., et al. Observation of Persistent Currents in Finely Dispersed Pyrolytic Graphite. *JETP Letters*, 2018, **107**(1), P. 37–41.
- [4] Tonnoir C., Kimouche A., Coraux J., et al. Induced superconductivity in graphene grown on Rhenium. *Phys. Rev. Lett.*, 2013, **111**(24), P. 246805.
- [5] Di Bernardo A., Millo O., Barbone M., et al. Corrigendum: p-wave triggered superconductivity in single-layer graphene on an electron-doped oxide superconductor. *Nature Communications*, 2017, **8**, P. 14024.
- [6] Esquinazi P., Heikkilä T.T., Lysogorskiy Y.V., et al. On the superconductivity of graphite interfaces. *JETP Letters*, 2014, **100**(5), P. 336–339.
- [7] Uchoa B., Castro Neto A.H. Superconducting states of pure and doped graphene. *Phys Rev Letters*, 2007, **98**, P. 146801.
- [8] Lebedev S.G. Evidence of Josephson-like behaviour of thin granular carbon films. *International Review of Physics*, 2008, **2**(5), P. 312–328.
- [9] Scheike T., Böhlmann W., Esquinazi P., et al. Can doping graphite trigger room temperature superconductivity? Evidence for granular high-temperature superconductivity in water-treated graphite powder. *Advanced Materials*, 2012, **24**(43), P. 5826–5831.
- [10] Felner I., Kopelevich Y. Magnetization measurement of a possible high-temperature superconducting state in amorphous carbon doped with sulfur. *Phys. Rev. B*, 2009, **79**(23), P. 233409.
- [11] Ballestar A., Barzola-Quiquia J., Scheike T., et al. Josephson-coupled superconducting regions embedded at the interfaces of highly oriented pyrolytic graphite. *New J. Phys.*, 2013, **15**(5), P. 023024.
- [12] Ionov A.N. Josephson-Like Behaviour of the Current-Voltage Characteristics of Multi-graphene Flakes Embedded in Polystyrene. *J. Low Temp. Phys.*, 2016, **185**(5-6), P. 515–521.
- [13] Volovik G.E., Pudalov V.M. Graphite on graphite. *JETP Letters*, 2016, **104**(12), P. 880–882.
- [14] Khairullin A.R., Nikolaeva M.N., Bugrov A.N. Resistance of the composite films based on polystyrene and graphene oxide. *Nanosystems: physics, chemistry, mathematics*, 2016, **7**(6), P. 1055–1058.
- [15] Nikolaeva M.N., Bugrov A.N., Anan'eva T.D., et al. Conductive properties of the composite films of graphene oxide based on polystyrene in a metal-polymer-metal structure. *Russ. J. Appl. Chem.*, 2014, **87**(8), P. 1151–1155.
- [16] Yevlampieva N., Bugrov A., Anan'eva T., et al. Soluble poly (methyl methacrylate) composites containing covalently associated zirconium dioxide nanocrystals. *Am. J. Nano Res. and Appl.*, 2014, **2**(2), P. 1–8.
- [17] Nikolaeva M.N., Anan'eva T.D., Bugrov A.N. et al. Correlation between structure and resistance of composites based on polystyrene and multilayered graphene oxide. *Nanosystems: physics, chemistry, mathematics*, 2017, **8**(2), P. 266–271.
- [18] Nikolaeva M.N., Gushchina E V., Dunaevskii M.S., et al. The influence of substrate material on the resistance of composite films based on reduced graphene oxide and polystyrene. *Nanosystems: physics, chemistry, mathematics*, 2017, **8**(5), P. 665–669.
- [19] Bugrov A.N., Zavialova A.Yu., Smyslov R.Yu., et al. Luminescence of  $\text{Eu}^{3+}$  ions in hybrid polymer-inorganic composites based on poly(methyl methacrylate) and zirconia nanoparticles. *Journal of bioluminescence and chemiluminescence*, 2018, P. 1–13.

## Promising directions of increasing the properties of steel

A. I. Zaitsev<sup>1</sup>, A. V. Koldaev<sup>1</sup>, N. A. Arutyunyan<sup>2</sup>

<sup>1</sup>Bardin Central Research Institute of Ferrous Metallurgy,  
Radio str., 23/9, build.2, Moscow, 105005, Russia

<sup>2</sup>Department of Chemistry, Lomonosov Moscow State  
University, Leninskie Gory 1-3, GSP-1, Moscow, 119991, Russia

aizaitsev1@yandex.ru, koldaevanton@gmail.com, naarutyunyan@gmail.com

PACS 64.30.Ef

DOI 10.17586/2220-8054-2018-9-4-500-506

The study of regularities of the formation and evolution of nonmetallic inclusions and phase precipitates in modern structural steels has been carried out. It has been shown that the formation of several types of complex nonmetallic inclusions results in a substantial increase in the complex of steel properties and neutralizing the negative influence of impurities while a reduction in costs. An even more significant improvement in the properties of steel can be achieved by controlling the characteristics of carbide, carbonitride, and other types of phase precipitates. Herewith, ferritic steels are the most promising. The previously unreachable complex of indicators of difficult to combine service properties of these steels has been achieved by the formation of a homogeneous fine-dispersed microstructure and a volumetric system of primarily interphase precipitates. Based on established principles, effective technologies for the production of a wide range of various types of steels have been developed.

**Keywords:** structural steels, nonmetallic inclusions of complex composition, nanoscale phase precipitates, interphase precipitates, structure, service properties, production technology.

*Received: 31 May 2018*

### 1. Introduction

At present, steels find an ever expanding sphere of application and are becoming increasingly unique and high-technology materials. This is reflected in the rapid growth in requirements for the composition, nonmetallic inclusions, macro- and microstructural state, a complex of indicators of the level and stability of their technological, service properties, and qualitative characteristics when the legislative striving to reduce the material and energy costs of production, the intensification of the end-to-end technological process and work equipment takes place. In particular, over the last 5 – 10 years, the indicators of most properties of steels have increased several times, and the task for developing a wide range of new types is to achieve extremely high following parameters: strength (up to 2000 – 2200 MPa), plasticity (elongation to 55 – 60 %), cold resistance ( $KCV_{-60^{\circ}C}$  up to 300 – 400 J/cm<sup>2</sup>), stamping, corrosion resistance, qualitative characteristics (the content of nonmetallic inclusions is not more than 1.0 – 1.5 ball according to GOST 1778-70, some unfavorable types – not more than 2 inclusion/mm<sup>2</sup> regardless of their size, sulfur – no more than 0.001 %, the number of surface defects - no more than 1 – 2 per ton of rolled metal) [1]. An important fact is that in most cases it is necessary to ensure high values of not only one of these parameters, but of the whole complex, as a rule, of difficult to combine properties, for example, strength and plasticity; stamping, cold resistance, fatigue, and corrosion resistance, etc.

The solution of this problem lies only in the way of developing fundamentally new scientific, technical methods of research and solutions. According to the results of a large volume of studies [1–3], they are primarily related to the development and use of adequate predicting methods and effective technological strategies of controlling a number of characteristics. They include type, composition, quantity, size, morphology, and distribution by volume of metal of nonmetallic inclusions, phase precipitates, forms of presence of impurities controlling the resulting structural state and complex properties of steel. Moreover, in order to achieve fundamental progress in the direction under consideration, it is necessary to take an adequate account of the kinetics of processes occurring during metal treatment, deviations from equilibrium, and the possibility of forming nanoscale and complex objects of the structural state of steel.

### 2. Regularities of changes in the characteristics of nonmetallic inclusions in modern steels

As a result of the rapid development of metallurgical technology, the use of new materials, technological methods, the intensification of treatment processes, and the production of steel, the characteristics of nonmetallic inclusions and other elements of the structure present in the metal have fundamentally changed. First of all,

the variety of types of existing nonmetallic inclusions (precipitates) has significantly increased. In many cases they have a complex chemical and phase composition, which regularly changes during the processing of steel. In particular, the need to reduce the sulfur content to low values (often less than 0.001 %) to increase the cold resistance, viscosity, and resistance to hydrogen sulfide stress cracking have required a reduction in the dissolved oxygen content in the metal to 0.0005 – 0.0008 %, and FeO in the slag – to 0.5 – 1 %. As a result, the deoxidizing interaction with lining and slag becomes possible, and the formation of inclusions based on alumomagnesium spinel and other MgO–Al<sub>2</sub>O<sub>3</sub>, MgO–Al<sub>2</sub>O<sub>3</sub>–CaO compositions takes place [4]. This type of inclusions often dominates in modern steels, despite the fact that less than 10 years ago they were practically absent.

According to the results of the most recent detailed studies [5, 6], it has been established that under certain modes of ladle treatment and continuous casting of modern structural steels oxide inclusions are formed based on SiO<sub>2</sub>–Al<sub>2</sub>O<sub>3</sub>, SiO<sub>2</sub>–Al<sub>2</sub>O<sub>3</sub>–CaO, MnO–SiO<sub>2</sub>, and SiO<sub>2</sub>–Al<sub>2</sub>O<sub>3</sub>–MnO compositions and others, which in many respects determine the resulting structural state and complex of metal properties. Among them are vitreous inclusions. The presence of vitreous silicate based inclusions essentially improves the macro- and microstructure of the metal of continuously cast billets (CCB), inhibits the development of liquation processes. Rolled products made from such CCB are characterized by extremely high impact strength values (KCV<sub>-40°C</sub> up to 420 – 445 J/cm<sup>2</sup>), resistance to hydrogen cracking, and a number of other service properties. The presence of this type of non-metallic inclusions in low-alloyed aluminum deoxidized structural steels is a rather unexpected fact, both from the theoretical and from the practical point of view. It became possible only due to the addition of large masses of manganese and silicon containing ferroalloys in the final stages of ladle treatment of steel and the presence of significant kinetic limitations for the transformation of silicate inclusions into more stable aluminate inclusions. Thus, kinetic reasons led to a significant expansion of the types of existing inclusions in modern steels.

The change in the size of nonmetallic inclusions is also significant. The intensification of metal melt treatment processes has created favorable conditions for nucleation but not for the growth of inclusions (precipitates) already present. Thus, it promotes the regular decrease in their size, which, often, is on the order of nanometers in magnitude. As a result, when modern metallurgical technologies are implemented, the formation and evolution of nanoscale objects in the steels takes place already at the stage of processing the metallic melt [7]. There are all the prerequisites for using them instead of or in addition to phase precipitates and structural components formed due to the use of costly alloying and microalloying components, which play a key role in achieving the structural state and high complex of steel properties [1, 4, 6, 7].

A second, no less important consequence of intensification of metal treatment processes is the creation of favorable conditions not for the independent nucleation and growth of phase precipitates, but for the deposition of phases on the surface of already present particles. This leads to the formation of a large variety of inclusions (precipitates) of complex composition. In particular, in Ti microalloyed structural steels complex inclusions, which consist of titanium nitride with corundum, with calcium and manganese sulfides, and alumomagnesium spinel, were detected [1]. In a wide range of structural steels, the formation of calcium and manganese sulfides on the surface of inclusions based on alumomagnesium spinel and calcium aluminates was registered [4, 8]. During the thermo-deformation treatment of metal, cementite deposition on the surface of complex and a number of simpler inclusions (precipitates) is possible. To date, there are no adequate physico-chemical, kinetic, and structural-geometric principles and methods for predicting the conditions of formation and the composition of complex inclusions [1].

### 3. Specifics of the influence of nonmetallic inclusions on the properties of modern steels

Depending on their characteristics, the inclusions present have significantly different effects on the structural state and properties of the steel. For example, the large sized titanium nitride precipitates (more than 8 – 10 microns) facilitate the initiation of metal defects, reducing the cold resistance and resistance against various types of corrosion-mechanical destruction of rolled metal [9]. The formation of complex TiN precipitates on corundum of intermediate sizes (as a rule up to 3 – 4 μm) inhibits the formation of its independent coarse precipitates. In addition, their ability to restrain the growth of austenitic grain when heating blanks for rolling, austenization, welding, and recrystallization during rolling is important [4]. Inclusions based on alumomagnesium spinel and a number of other oxide compositions do not adversely affect corrosion resistance and service properties; on the contrary, they can restrain grain growth during austenitization and recrystallization of steel that is associated with a certain positive effect. The deposition of sulfides of calcium and, mainly, manganese on their surface gives the resulting complex oxide-sulfide inclusions an unfavorable ability to catastrophically accelerate the local corrosion of steel [10].

In the presence of additional cementite (Fig. 1) and other carbide phase deposition, which have higher strength and hardness in comparison with the metal matrix, on the surface of sulfide, oxide-sulfide, and other complex

inclusions, the formed complex precipitations can play the role of a strengthening phase. They can lead to a multiple (more than 2-3-fold) increase in the strength properties of steel while maintaining high plasticity [11]. Thus, the presented results indicate a fundamental change in the nature of the effect of nonmetallic inclusions on the properties of the metal, depending on the parameters of their formation and evolution during the processing of steel. The presented information reflects the regularities of influence for only a small number of possible types of complex nonmetallic inclusions (precipitates) on the quality and properties of steel. This stipulates the necessity of creating a database and adequate physico-chemical and kinetic methods for predicting the formation and evolution of complex nonmetallic inclusions (precipitates) at all stages of steel production (processing) that will be the basis for development of effective techniques for obtaining an unattainable complex of properties and qualitative indicators of metal. This approach opens up wide opportunities for the creation of new high-quality steels while a significant reduction in material and energy production costs, since the composition of obtained complex inclusions consists of widely distributed elements, which are usually present in steel and slag, e.g. Ca, Al, Mn, Si, C, and, even, the so-called harmful impurities – O, N, S [3,4,12]. No less significant effect is achieved due to the neutralization of the impurities' negative influence on technological and service properties of steel, and expansion of raw materials base.

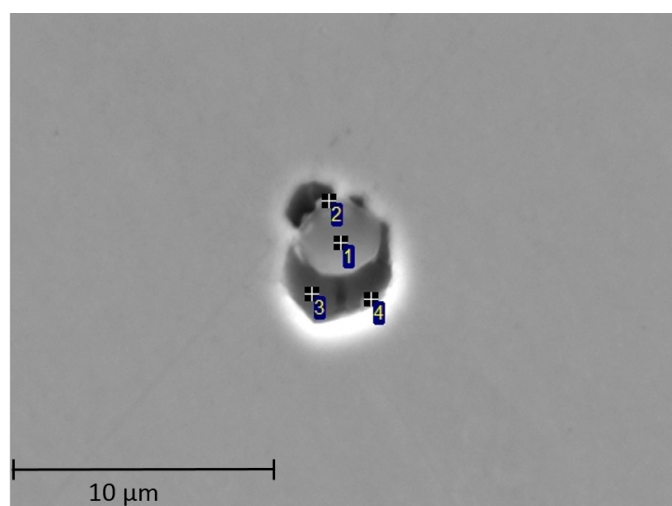


FIG. 1. Cementite precipitation on the surface of complex MnS and alumomagnesium spinel inclusion: 1 – MnS, 2 – alumomagnesium spinel, 3,4 – cementite

#### 4. Promising directions of using phase precipitates for the principal enhancement of the complex of properties of modern steels

A greatly more significant increase in the complex properties of structural steels can be achieved by controlling the characteristics of carbide, carbonitride, and other types of phase precipitates, including complex composition, and structural constituents, formed during the treatment of solid metal. Nevertheless, in spite of the fundamental importance of this problem, as a rule, a number of traditional extremely simplistic approaches are used, which to some extent differ, depending on the requirements and the type of produced and developed steels. This can be clearly illustrated by the methods of formation and enhancement of the properties of high-strength automobile body sheet steels. It is one of the most important directions for the development of domestic and world science and technology. Up to the present time, low-alloyed high-strength steels with a yield strength of up to 600 – 700 MPa occupy the leading position (production and consumption volume is more than ten times higher than the total volume for all other high-strength automobile body sheet steels) [12]. The principle of their construction is based on the implementation of traditional strengthening mechanisms (grain-boundary, solid-solution, dispersion hardening) that leads to a catastrophic decrease in ductility and other service properties of steel. In view of this problem, progressive automobile body sheet steels have been developed, which include two-phase ferritic-martensitic, and multiphase steels, and steels with ductility induced by phase transformation (TRIP and TWIP steel) [13]. Their necessary strength is provided by the presence of a certain content of hard structural constituents (martensite, bainite, etc.) in the ferrite matrix.

To enhance the strength of progressive automobile body sheet steels, it is necessary to increase the content of these hard structural constituents that leads to a catastrophic decrease in stamping, corrosion resistance, and a

number of other properties. These steels are characterized by a large difference in hardness between the ferrite matrix (soft polygonal ferrite) and hard structural components (martensite, bainite, etc.). Therefore, it is not possible to achieve high values for the hole expansion ratio, which is associated with the formation of cavities at the interface between the ferrite matrix and the hard structural components during stamping [14]. As a result, in spite of satisfactory values of the relative elongation, steels are characterized by an extremely low or even complete lack of stamping. In addition, the presence of distinct microstructure heterogeneity leads to a significant decrease in the corrosion resistance of the steel, makes it difficult to apply protective coatings, weldability, etc.

The currently used approaches for increasing the strength of traditional high-strength low-alloyed automobile body sheet steels up to 800 – 900 MPa are mainly aimed at obtaining a bainite microstructure [15]. It is assumed that carbide and carbonitride precipitates play, in the main, only a secondary role in increasing the indicators of its dispersion. This leads to a sharp decrease in ductility and other functional properties of steel. It is important, that by obtaining a homogeneous bainitic microstructure, the hole expansion ratio remains satisfactory while a sharp decrease in the ductility of the steel. Thus, for all common types of automobile body sheet steels, especially of high strength grades, the problem of simultaneously obtaining difficult to combine high indicators of plasticity, stamping, corrosion resistance, operational reliability, and other service properties is not solved.

The most promising direction for the solution of the formulated task is the creation of new steels with a homogeneous plastic ferrite matrix strengthened by a system of thermally stable (up to 700 °C) system of nanoscale, especially interphase (formed during the fcc-bcc phase transformation of steel), precipitates and refinement of ferrite grains up to 2 – 3  $\mu\text{m}$ . Because of the formulated principles, nanostructured steels such as NANO HITEN [16] have been created to date and JFE Steel (Japan) and China have produced industrial batches of hot-rolled products. Ferrite microstructure of steel has a high strength up to 700 – 800 MPa, yet, at the same time, provides high plasticity (relative elongation up to 20 – 25 %), stamping (hole expansion ratio about 100 %), stiffness, durability, and fatigue and corrosion resistance.

The steel has an extremely economical composition, (mass.%): C – 0.04 – 0.06, Mn – up to 1.5, Ti + Mo – up to 0.3 and simple production technology with high temperatures of finishing of rolling (900 – 920 °C) and coiling (650 °C). The strengthening of the steel takes place, to a large extent, due to the formation of nanoscale complex (Ti, Mo)C carbide precipitates after coiling. This greatly simplifies the production of rolled products and allows it to be produced in thicknesses of 1.8 mm. Due to the absence of silicon in the composition, the rolled products are well suited to hot-dip galvanizing and have shown excellent results in the manufacture of chassis, frame, and strength members of the automobile [17].

In the following years, the hot-rolled ferritic steels of the XPF type of XPF650, XPF800 and XPF1000 strength grades have been developed and produced on Tata Steel. They have various microalloying systems, including V, Nb, Ni, Mo, and, in some cases, B [18, 19], which differ from NANO HITEN. Hot-rolled steels of the XPF type have a unique single-phase ferrite microstructure strengthened by nanoscale precipitates and excellent characteristics, which allow manufacturers to produce parts that are 15 percent lighter than those, made from similar brands of other types, including progressive automobile body sheet steels, in particular HR CP800.

However, despite the excellent array of properties, the widespread development and expansion of such steels has not occurred to date. The possibility and principles of further increase and the limiting values of their strength are not clearly substantiated. This is mainly due to a number of unresolved fundamentally important scientific problems. First of all, there is a lack of clear scientific ideas about the regularities in the formation of a thermally stable system of nanoscale interphase precipitates playing a key role in providing an array of properties of steel. Few investigations have been devoted to a theoretical investigation of this problem [20–25]. On the other hand, the results of experimental studies [26–28] indicate the possibility of a significant increase in the indicators of strength, plasticity, and stamping of steel of this type while using an extremely economical alloying system. In addition, the problem of the possible superposition of phase precipitates of various types (formed in austenite, ferrite, and during fcc-bcc transformation) for the principal enhancement of the complex of properties of steel, including the difficult to combine characteristics, has not yet been practically studied. Nevertheless, the results of the experimental and theoretical estimates carried out testify to the possibility of implementing additional mechanisms for improving the complex properties of rolled products [2], especially when the sizes of various types of phase precipitates decrease.

However, this is currently restrained by the lack of accurate information about the regularities of the influence of the nonmetallic inclusion characteristics and phase precipitates on the implementation of various mechanisms of the formation of the structural state, mechanical and other service properties of structural steels, and adequate predictive methods and effective techniques for controlling these characteristics. It connects with a number of objective difficulties due to the complexity and interconnectedness of modern metal treatment processes, which take place under conditions far from equilibrium. The determination of their direction and degree of implementation with the required accuracy is, in many cases, hindered or even impossible. As a result, the choice of the composition and

parameters of steel treatment, in many ways is done by the method of trial and error using extremely simplified empirical relationships. Only recently, methods of thermodynamic modeling and calculation of steel treatment processes have been intensively developed [4, 14, 29]. Herewith, assuming the achievement of global or local equilibrium without taking into account deformation, only the total content of the formed phase is calculated. On the other hand, it is well known that the nature of the effect of phase precipitates on the structural state and properties of steel depends to a large extent on their characteristics. In addition, as shown by the results of the most recent detailed studies, even in the presence of deformation, the formation of carbide, carbonitride, and other phase precipitates has large kinetic limitations [30] and requires a considerable period of time, often much longer than the duration of hot rolling, for its realization. Thus, the actual task in the development of a new generation of steels is to create a fundamental database on the dependence of the characteristics of phase precipitates on the parameters of steel treatment, and the regularities governing their influence on the resulting structural state and properties of the metal.

In particular, the results of detailed experimental studies have shown that the fraction of molybdenum in the complex carbide (Ti,Mo)C in Ti, Mo microalloyed ferritic steels is insignificant and reaches a maximum value of  $\text{Ti}_{0.43}\text{Mo}_{0.08}\text{C}_{0.49}$  at the temperature of the  $\gamma \rightarrow \alpha$  transformation of steel. Therefore, the formed interphase precipitates have a composition close to TiC, and the role of molybdenum is in many respects associated with a decrease in the rate of phase transformation of the steel. The main contributions to the formation of strength properties are associated with obtaining a finely dispersed ferrite structure and dispersed carbide precipitates. The refinement of ferrite grain during the phase transformation is mainly influenced by carbide precipitates formed in austenite. Strengthening by nanoscale, especially interphase precipitates, is more effective with larger number and smaller sizes. It takes place when sizes of precipitates and distances between the resulting layers of precipitates are small (Fig. 2). All other conditions being equal, the amount of formed interphase precipitates increases with an increase in the content of phase-forming elements in the solid solution, the temperatures of finishing of rolling and coiling, as well as the rate of formation of small precipitates (1 – 2 nm) and phase transformation. On the other hand, an increase in the temperature of finishing of rolling and, as a result, the content of the phase-forming elements in the solid solution, can lead to a decrease in the amount of precipitates, which form in the austenite, and the dispersion of the resulting ferrite microstructure, reducing the contribution of this factor to the strength characteristics. The presented circumstances indicate that the numerical values of the metal treatment parameters and various types of phase precipitates must be coordinated. It will ensure the obtaining the maximum indicators of the complex of properties. In particular, this can be illustrated by a simple example. At close values of the treatment parameters and the content of the components in Ti, Mo, microalloyed ferritic steels increasing in the Ti concentration from 0.096 to 0.12 mass% led to an increase in the strength of the steel from 780 to almost 900 MPa. Under such conditions, the amount of austenite and interphase precipitations, which control the various strengthening mechanisms, grew practically proportionally. In particular, the average size of the interphase precipitates was 1 – 2 nm, the average distance between the layers is 5 – 8 nm (Fig. 2) [28].

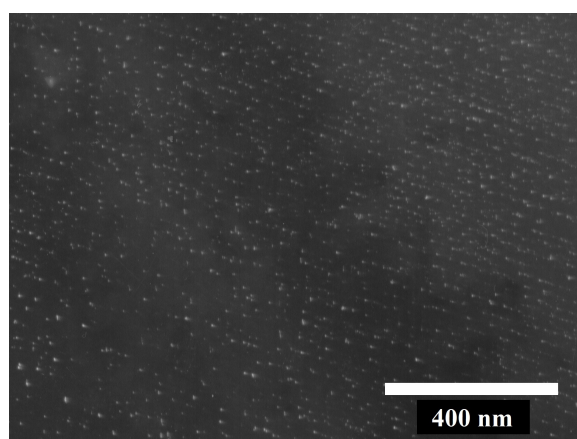


FIG. 2. Appearance of interphase carbide precipitates in Ti, Mo microalloyed ferritic steel, TEM [28]

## 5. Conclusion

The presented example demonstrates that only an adequate accounting of the influence of all the processing and treatment parameters of the metal, as well as of all the features of various mechanisms for the formation of the structural state and properties, allows us to increase the parameters of the complex of difficult to combine characteristics of steel essentially. The high efficiency of the formulated approach has now been confirmed in the development of a variety of new technical and technological solutions, technologies, and steel grades (see, for example, [28]). In particular, a significant increase in the homogeneity of the composition, structure, and properties of the metal has been achieved due to the formation of favorable silicate, complex, and other types of inclusions/precipitates. Efficient technologies have been developed for production of a wide range of structural, tube, automobile body sheet, clad, and other types of mass high-quality steels with a fundamentally improved complex of difficult to combine strengths, ductility, cold resistance, corrosion resistance, operational reliability, weldability, and other properties for transport, machine building, fuel and energy complex. New types of steels have been created. Among them, ferritic steels, which are hardened by thermally stable systems of nanoscale precipitates, and ferrite-cementite steels that are resistant to destruction in active carbon and hydrogen-containing gas media. At the same time, a significant reduction in costs and expansion of the raw material base has been achieved.

## Acknowledgement

This research was supported by the grant of the Russian Research Foundation (Project No. 18-19-00639) and was performed at the Bardin Central Research Institute of Ferrous Metallurgy.

## References

- [1] Zaitsev A.I. Prospective directions for development of metallurgy and materials science of steel. *Pure Appl. Chem.*, 2017, **89**(10), P. 1553–1565.
- [2] Zaitsev A.I., Kosyrev K.L., Rodionova I.G. Modern trends of development of metallurgical technology for achievement of a high complex of service properties and qualitative indicators of steel. *Probl. Chern. Met. Materialoved*, 2012, **3**, P. 5–13.
- [3] Shakhpazov E.Kh., Zaitsev A.I., Rodionova I.G., Semernin G.V. Key trends in the development of a metallurgical technology to meet the growing steel quality requirements. *Russ. Metall.*, 2011, **2011**(12), P. 1162–1170.
- [4] Zaitsev A.I., Kraposhin V.S., Rodionova I.G., Semernin G.V., Talis A.S. *Complex nonmetallic inclusions and steel properties*. Metallurgizdat, Moscow, 2015, 276 p.
- [5] Zaitsev A.I., Rodionova I.G., Baklanova O.N., Kryukova A.I., Udod K.A., Mishnev P.A., Mitrofanov A.V. Nonmetallic inclusions and promising principles for improving the set of properties and quality characteristics of steel. *Metallurgist*, 2015, **58**(11), P. 983–991.
- [6] Zaitsev A.I., Stepanov A.B., Karamysheva N.A., Rodionova I.G. Advancement of the properties of structural steels by creating an optimum form of existence of impurities and nonmetallic inclusions. *Met. Sci. Heat Treat.*, 2016, **57**(9), P. 531–538.
- [7] Shakhpazov E.Kh., Zaitsev A.I., Rodionova I.G., Shaposhnikov N.G. Nanotechnologies for the production of mass high-quality steels based on the management of nanosized precipitates of nonmetallic excess phases. *Probl. Chern. Met. Materialoved.*, 2008, **4**, P. 112–122.
- [8] Zaitsev A.I., Rodionova I.G., Semernin G.V., Shaposhnikov N.G., Kazankov A.Yu. New types of unfavorable nonmetallic inclusions based on MgO–Al<sub>2</sub>O<sub>3</sub> and metallurgical factors governing their content in metal. Part 1. Reasons and mechanisms for formation in steel of nonmetallic inclusions based on alumina magnesia spinel. *Metallurgist*, 2011, **55**(1-2), P. 107–115.
- [9] Zaitsev A.I., Rodionova I.G., Baklanova O.N., Udod K.A., Grishin A.V., Esiev T.S., Ryahovskikh I.V., Kohtev S.A., Lutsenko A.N., Nemtinov A.A., Mitrofanov A.V. Investigation of the influence of metallurgical factors on the resistance of modern tube steels against corrosion cracking. *Probl. Chern. Met. Materialoved.*, 2013, **1**, P. 54–69.
- [10] Rodionova I.G., Zaitsev A.I., Baklanova O.N., Golovanov A.V., Endel N.I., Shapovalov E.T., Semernin G.V. *Modern approaches to improve the corrosion resistance and operational reliability of steels for oilfield pipelines*. Metallurgizdat, Moscow, 2012, 172 p.
- [11] Zaitsev A.I., Rodionova I.G., Shaposhnikov N.G., Mogutnov B.M., Dunaev S.F., Mishnev P.A., Adigamov R.R. Development of scientific foundations for efficient technologies for the production of cold-rolled high-strength low-alloyed steels by controlling the type, quantity and morphology of precipitations of nonmetallic excess phases. *Probl. Chern. Met. Materialoved.*, 2012, **1**, P. 75–85.
- [12] Zaitsev A.I., Rodionova I.G., Yashchuk S.V., Mishnev P.A., Adigamov R.R., Bykova Yu.S., Efimova T.M. Development of scientific and technological fundamentals of production of automobile body sheet steels. *Chernaya Metallurgiya*, 2013, **3**, P. 89–109.
- [13] Fonstein N. *Advanced high strength sheet steels: physical metallurgy, design, processing and properties*. Springer International Publishing Switzerland, 2015, 396 p.
- [14] Frisk K., Borggren U. Precipitation in microalloyed steel by model alloy experiment and thermodynamic calculation. *Metall. and Mater. Trans. A*, 2016, **47**(10), P. 4806–4817.
- [15] Zaitsev A.I., Rodionova I.G., Pavlov A.A., Shaposhnikov N.G., Grishin A.V. Effect of composition, structural state, and manufacturing technology on service properties of high-strength low-carbon steel main bimetal layer. *Metallurgist*, 2015, **59**(7), P. 684–692.
- [16] Seto K., Funakawa Y., Kaneko S. Hot rolling high strength steels for suspension and chassis parts “NANOHITEN” and “BTH steels”. *JFE Techn. Report*, 2007, **10**, P. 19–25.
- [17] Funakawa Y., Shiozaki T., Tomita K., Yamamoto T., Maeda E. Development of high strength hot-rolled sheet steel consisting of ferrite and nanometer-sized carbides. *ISIJ Int.*, 2004, **44**(11), P. 1945–1951.
- [18] Deng X., Fu T., Wang Z., Liu G., Wang G., Misra R.D.K. Extending the boundaries of mechanical properties of Ti-Nb low-carbon steel via combination of ultrafast cooling and deformation during austenite-to-ferrite transformation. *Met. Mater. Int.*, 2017, **23**(1), P. 175–183.

- [19] Rijkenberg A., Blowey A., Bellina P., Wooffindin C. Advanced high stretch-flange formability steels for chassis & suspension applications. Proceedings of the Conference SCT2014 (4-th International Conference on Steels in Cars and Trucks), Braunschweig, Germany, 15-19 June 2014, P. 426–433.
- [20] Kosaka N., Funakawa Y. Work hardening in ferritic steel containing ultra-fine carbides. *ISIJ Int.*, 2016, **56**(2), P. 311–318.
- [21] Zhang K., Li Z.-D., Sun X.-J., Yong Q.-L., Yang J.-W., Li Y.-M., Zhao P.-L. Development of Ti-V-Mo complex microalloyed hot-rolled 900-MPa-grade high-strength steel. *Acta Metall. Sin. Engl.*, 2015, **28**(5), P. 641–648.
- [22] Wang Z., Sun X., Yang Z., Yong Q., Zhang C., Li Z., Weng Y. Carbide precipitation in austenite of a Ti-Mo-containing low-carbon steel during stress relaxation. *Mater. Sci. Engin. A*, 2013, **573**, P. 84–91.
- [23] Kim Y.W., Hong S.-G., Huh Y.-H., Lee C.S. Role of rolling temperature in the precipitation hardening characteristics of Ti-Mo microalloyed hot-rolled high strength steel. *Mater. Sci. Engin. A*, 2014, **615**, P. 255–261.
- [24] Bu F.Z., Wang X.M., Yang S.W., Shang C.J., Mirsa R.D.K. Contribution of interphase precipitation on yield strength in thermomechanically simulated Ti-Nb and Ti-Nb-Mo microalloyed steels. *Mater. Sci. Engin. A*, 2015, **620**, P. 22–29.
- [25] Zajac S. Precipitation of microalloy carbo-nitrides prior, during and after  $\gamma/\alpha$  transformation. *Mater. Sci. Forum.*, 2005, **500**, P. 75–86.
- [26] Cheng L., Caa Q.-W., Xie B.-S., Ning Z., Zhou X.-C., Li G.-S. Relationships among microstructure, precipitation and mechanical properties in different depths of Ti-Mo low carbon low alloy steel plate. *Mater. Sci. Engin. A*, 2016, **651**, P. 185–191.
- [27] Zaitsev A.I., Baklanova O.N., Koldaev A.V., Grishin A.V., Rodionova I.G., Yashchuk S.V., Lyasotskii I.V. Microstructure and property formation for high-strength low-carbon steels microalloyed with titanium and molybdenum. *Metallurgist*, 2016, **60**(5), P. 492–498.
- [28] Shaposhnikov N.G., Koldaev A.V., Zaitsev A.I., Rodionova I.G., D'yakonov D.L., Arutyunyan N.A. Regularities of titanium carbide precipitation in low carbon Ti-Mo-microalloyed high strength steels. *Metallurgist*, 2016, **60**(8), P. 810–816.
- [29] Wang Z., Yong Q., Sun X., Yang Z., Li Z., Zhang C., Weng Y. An analytical model for kinetics of stress-induced precipitation in titanium micro-alloyed steels. *ISIJ Int.*, 2012, **52**(9), P. 1661–1669.
- [30] Koldaev A.V., D'yakonov D.L., Zaitsev A.I., Arutyunyan N.A. Kinetics of the formation of nanosize niobium carbonitride precipitates in low-alloy structural steels. *Metallurgist*, 2017, **60**(9), P. 1032–1037.

## An effective nanostructured green phosphor $\text{Zn}_2\text{SiO}_4:\text{Mn}^{2+}$ prepared by sol-gel method

K. A. Sergeeva<sup>1</sup>, A. A. Sergeev<sup>2</sup>, A. A. Rempel<sup>1,3</sup>

<sup>1</sup>Ural Federal University, Mira, 19, Ekaterinburg, 620002, Russia

<sup>2</sup>Far-Eastern Federal University, Sukhanova, 8, Vladivostok, 690091, Russia

<sup>3</sup>Institute of Metallurgy, Ural Branch of the Russian Academy of Sciences, Amundsena, 101, Ekaterinburg, 620016, Russia

kspetrovyh@mail.ru

PACS 78.55.-m, 81.20-n

DOI 10.17586/2220-8054-2018-9-4-507-512

A nanostructured willemite doped with manganese ( $\text{Zn}_2\text{SiO}_4:\text{Mn}^{2+}$ ) was synthesized by sol-gel method followed by high-temperature annealing. Prepared  $\text{Zn}_2\text{SiO}_4:\text{Mn}^{2+}$  is characterized by average particle size of 100 nm, narrow particle size distribution, and high crystallinity. Under UV-excitation nanostructured willemite shows an intensive photoluminescence at 520 nm corresponded to activator  $\text{Mn}^{2+}$  emission. It was found that the emission decay curves of willemite becomes non-exponential with increasing of manganese content.  $\text{Zn}_2\text{SiO}_4:\text{Mn}^{2+}$  reveals long-lasting phosphorescence up to 45 ms. Absolute quantum yield of  $\text{Zn}_2\text{SiO}_4:\text{Mn}^{2+}$  reaches 47 % at 0.1 at. % of  $\text{Mn}^{2+}$ . The luminescence concentration quenching effect at  $\text{Mn}^{2+}$  concentration higher than 1 at % is observed.

**Keywords:** willemite, manganese, photoluminescence, quantum yield.

*Received: 10 July 2018*

### 1. Introduction

Wide band gap semiconductor oxide phosphors doped with ions of transition and/or rare-earth metals are used extensively to create optical and luminescent instruments for various purposes. At the same time, the field of application is not limited to bulk microcrystalline materials, but includes nanostructured powders, thin films and multilayer coatings consisting of nanoparticles from 1 to 100 nm. The main benefits of nanostructured phosphors are increase of luminescence brightness, higher adhesion to the substrate, large specific surface, etc. [1].

Willemite, activated by manganese, or  $\text{Zn}_2\text{SiO}_4:\text{Mn}^{2+}$ , is one of the brightest representatives of oxide phosphors. Manganese ions, embedded in the crystal lattice of zinc orthosilicate, form a solid substitutional solution, which leads to a change in the optical and photoluminescent (PL) properties of the material [2]. Since the band gap of willemite is 5.0 – 6.2 eV, under UV-excitation (3 – 5 eV) the intracenter absorption and emission of photons within the  $3d^5$  electron shell of  $\text{Mn}^{2+}$  ions is the dominant process [3]. To date, the mechanisms of energy transfer in  $\text{Zn}_2\text{SiO}_4:\text{Mn}^{2+}$  under interband excitation, as well as competition between the interband and intracenter relaxation, the nature of the intrinsic defects of the matrix and their interaction with activator ions remain insufficiently studied. The effect of the nanostructured state and the activator concentration on the spectral and kinetic characteristics of the willemite is of great importance for practical applications.

The aim of this work was the analysis of the spectral and kinetic parameters of photoluminescence of nanostructured  $\text{Zn}_2\text{SiO}_4:\text{Mn}^{2+}$ , prepared by sol-gel method, depending on the crystallinity degree of the structure, the particle size and the concentration of the  $\text{Mn}^{2+}$  activator.

### 2. Experimental

#### 2.1. Synthesis

Nanostructured  $\alpha\text{-Zn}_2\text{SiO}_4:\text{Mn}^{2+}$  was prepared by sol-gel method followed by high-temperature annealing. Zinc nitride  $\text{Zn}(\text{NO}_3)_2$ , manganese acetate  $\text{Mn}(\text{CH}_3\text{COO})_2$ , and tetraethylorthosilicate (TEOS)  $\text{Si}(\text{OC}_2\text{H}_5)_4$  were used as sources of zinc, manganese and silicon, respectively. The stoichiometric ratio of mixture components was  $\text{Zn}_{2-x}\text{SiO}_4:\text{Mn}_x$ , where x varies from 0 to 0.35. Appropriate amounts of metal salts were diluted in ethanol, and then TEOS was added. The mixture was stirred for 3 h. The pH of the mixture was adjusted to approximately 2 by dropwise addition of  $\text{HNO}_3$ . To initiate hydrolysis, water was added in the volume ratio of  $V_{\text{EtOH}}:V_{\text{H}_2\text{O}} = 10:1$ . Prepared sol was transparent and sediment-free. The gelation process was initiated by subjecting of sols in boiled water bath within 1 h. After that, the gels were dried in a drying oven at 300 °C for 5 h. To form the  $\alpha\text{-Zn}_2\text{SiO}_4$  crystalline modification the dried powders were annealed in air at temperatures ranging from 500 – 1000 °C for 5 h.

## 2.2. Characterization

The crystal structure and phase composition of prepared  $\text{Zn}_2\text{SiO}_4:\text{Mn}^{2+}$  was investigated by X-ray diffraction (Shimadzu XRD MAXIMA) in the Bragg-Brentano geometry. The crystallinity degree was determined as the ratio of  $\alpha\text{-Zn}_2\text{SiO}_4$  diffraction peak intensity to intensity of diffusive halo in the willemite diffraction pattern. The average particle size in  $\text{Zn}_2\text{SiO}_4:\text{Mn}^{2+}$  was calculated by Williamson–Hall method [4] as:

$$\langle D_{CSR} \rangle = 1/\beta^*(2\theta = 0), \quad (1)$$

where  $\beta^* = \cos \theta \cdot \beta(2\theta)$  is normalized diffraction peak broadening,  $1/\text{nm}^{-1}$ ;  $2\theta$  is X-Ray scattering angle.

The particle size distribution in nanostructured  $\text{Zn}_2\text{SiO}_4:\text{Mn}^{2+}$  was investigated by dynamic light scattering (Malvern Zetasizer Nano ZS). The 633 nm laser light scattering angle was  $13^\circ$ . The nanopowders were preliminary dispersed in ethanol-water solution and stirred by SONOPULS ultrasonic homogenizer (Bandelin).

The diffuse reflection spectra of  $\text{Zn}_2\text{SiO}_4:\text{Mn}^{2+}$  nanopowders in the range from 220 to 800 nm was recorded by Cary Varian 5000 spectrometer using an integrated sphere. The optical band gap was determined by Tauc method [5]:

$$(h\nu F(r))^{\frac{1}{n}} = A(h\nu - E_g), \quad (2)$$

where  $E_g$  is fundamental band gap, eV;  $h$  is Plank constant, J·s;  $\nu$  is electromagnetic wave oscillation frequency, Hz;  $F(r) = (1 - r_\infty)^2/2r_\infty$  is Kubelka–Munc function;  $A$  is a constant. For the willemite exponent,  $n$  is equal to  $1/2$  corresponding to direct transition.

The photoluminescence emission and excitation (PLE) spectra of nanostructured willemite were recorded using Horiba Fluorolog 3 spectrometer. PLE spectra was normalized to xenon lamp emission specter. PL decay measurements were performed in the range of 0 to 150 ms and initial delay of 0.05 ms with the same equipment.

The PL decay curves were fitted using superposition of stretched and simple exponential functions:

$$I(t) = I_1 \exp \left[ - \left( \frac{t}{t_1} \right)^\beta \right] + I_2 \exp \left[ - \frac{t}{t_2} \right], \quad (3)$$

where  $\beta$  is the degree of nonexponentiality.

The absolute quantum yield (AQY) was calculated as the ratio of emitted photons to absorbed ones:

$$\varphi_{abc} = \frac{E_c - E_a}{L_a - L_c}, \quad (4)$$

where  $E_c$  is integrated PL intensity of the sample;  $E_a$  is integrated PL intensity of the integrated sphere;  $L_c$  is integrated PLE intensity of the sample;  $L_a$  is integrated PLE intensity of the integrated sphere.

## 3. Results and discussion

Figure 1 shows the XRD patterns of  $\text{Zn}_2\text{SiO}_4:\text{Mn}^{2+}$  in dependence on the annealing temperature and manganese content. After annealing at  $1000^\circ\text{C}$ , all the samples are characterized with 100 % of  $\alpha\text{-Zn}_2\text{SiO}_4$  crystal phase (Fig. 1a). One should note that the crystallinity of obtained willemite is higher than in case of  $\text{ZnCl}_2$  precursor used in previous study [6]. The amount of manganese (in the chosen range from 0.1 to 5 at.%) does not affect the crystallinity degree of  $\alpha\text{-Zn}_2\text{SiO}_4:\text{Mn}^{2+}$  (Fig. 1b). The absence of other willemite modifications and manganese-related crystal phases indicates the formation of homogeneity activator-matrix solid solution. The average particle size of  $\text{Zn}_2\text{SiO}_4:\text{Mn}^{2+}$  rises from 60 to 100 nm with  $\text{Mn}^{2+}$  content increasing.

Fig. 2 shows the particle size distribution of nanostructured willemite in ethanol-water solution. It was found that the distribution function is bimodal and indicates the particles of 130 nm and about 700 nm. The smaller particle size is in good correlation with the XRD data. The fact that the particles of 700 nm are observed can be explained as both nonsolubility of  $\text{Zn}_2\text{SiO}_4:\text{Mn}^{2+}$  and a tendency of smaller particles to agglomerate. The particle size distribution function is independent of manganese concentration.

The diffusive reflection and PLE spectra of nanostructured willemite are shown in Fig. 3. Independent of manganese content, there is an absorption in the region of 5 eV and higher. That corresponded to fundamental absorption edge of  $\text{Zn}_2\text{SiO}_4$ , which is close to 5.8 eV according to different estimates [7, 8]. Willemite doped with  $\text{Mn}^{2+}$  are characterized by an additional absorption edge at 3.5 eV. That value is well-correlated with PLE bands in the same region related to excitation within  $3d^5$  electron shell of  $\text{Mn}^{2+}$ . One can add that the absorption in 3.5 eV is observed also for undoped willemite. That is possible due to uncontrollable manganese impurity in precursors (<0.005 at.%). The optical band gap estimated by Tauc method varies from 5.6 to 4.0 eV for undoped willemite and the sample with 5 at.% of  $\text{Mn}^{2+}$ , respectively.

It was found that even low-crystalline willemite (30 % –  $600^\circ\text{C}$ ) under excitation at 5.0 eV exhibits a broad PL band with maximum at 515 nm (Fig. 4). The PL maximum and structure correspond to  ${}^4T_1 \rightarrow {}^6A_1$  transition

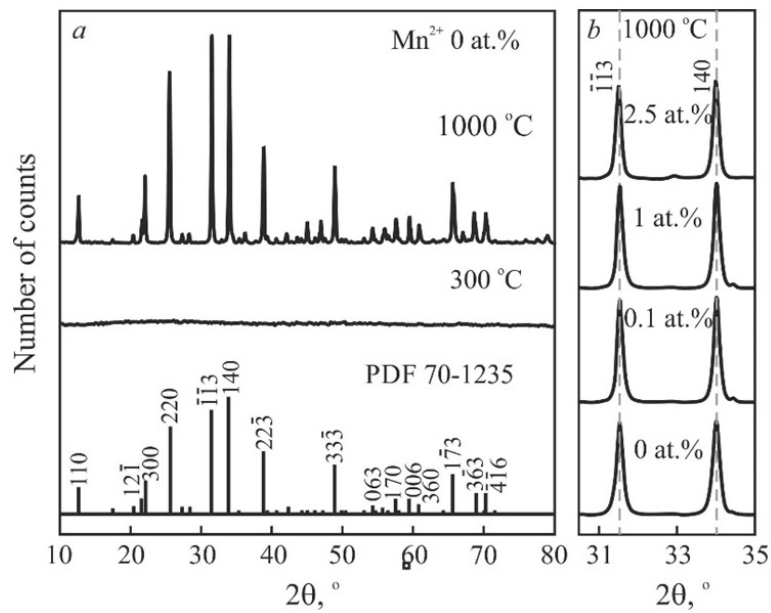


FIG. 1. X-ray diffraction patterns of nanostructured  $\text{Zn}_2\text{SiO}_4:\text{Mn}^{2+}$  depending on the annealing temperature (a) and manganese content (b)

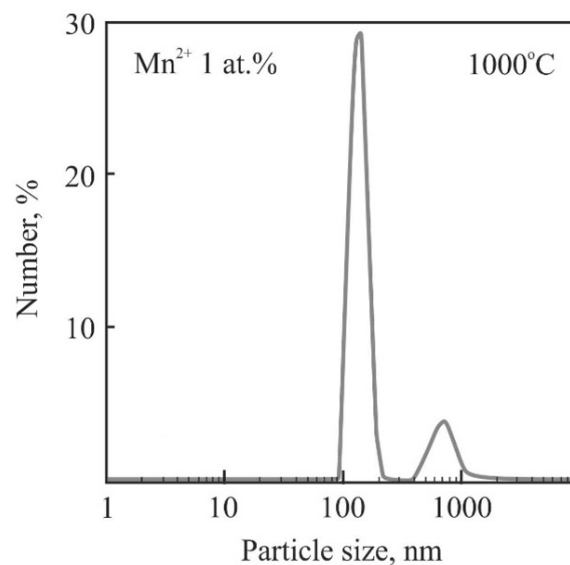


FIG. 2. Particle size distribution in willemit dispersed in ethanol-water solution

within  $3d^5$  electron shell of  $\text{Mn}^{2+}$ . Increasing the annealing temperature to 1000 °C leads to PL band rising while its maximum shifts to 525 nm. The observed PL intensity rising is due to crystallinity improvement, residual OH group elimination, and increasing of the nanoparticle surface roughness [9].

The PL decay curves of  $\text{Zn}_2\text{SiO}_4:\text{Mn}^{2+}$  at low manganese concentrations (<0.1 at. %) has an exponential form since all the activator ions are single (has no nearest neighbors of the same type) (Fig. 5a). As  $\text{Mn}^{2+}$  content is increased, the decay becomes stretched exponential due to the presence of different types of luminescence centers ( $\text{Mn}^{2+}$  pairs and next nearest neighbors) and energy transfer from isolated  $\text{Mn}^{2+}$  ions to the pairs. All the centers could be excited both directly and by nonradiative energy transfer that causes the range of charge carrier recombination time [10]. The non-exponentiality degree  $\beta$  varies from 0.55 to 0.9. Long-lasting phosphorescence of the nanostructured willemit (average decay time  $\tau_{1/e}$  is up to 45 ms) is caused by the release of the electrons from deep traps. The PL rising stage for 2 ms also indicates the process of interaction between the traps and activator ions. It was supposed that the oxygen vacancies may act as the traps in  $\text{Zn}_2\text{SiO}_4$  crystal lattice [11].

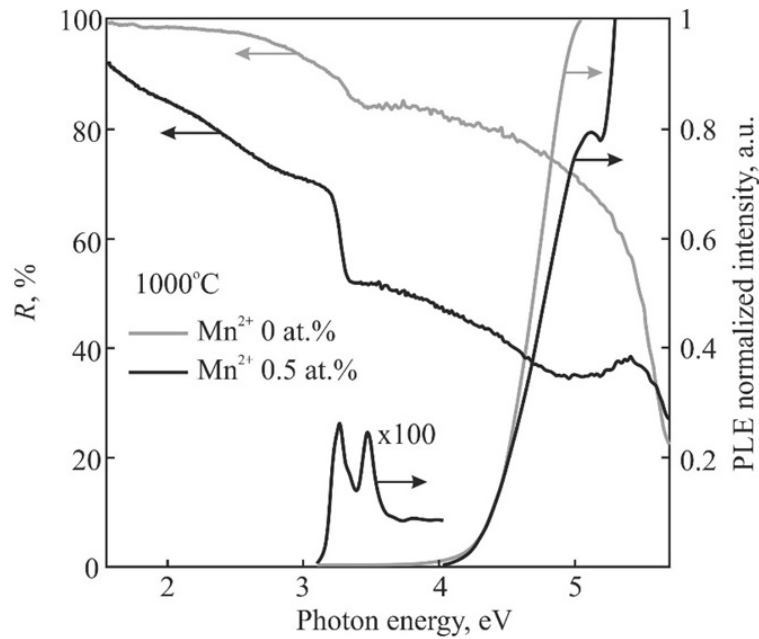


FIG. 3. The diffusive reflection and PLE spectra of nanostructured  $\text{Zn}_2\text{SiO}_4:\text{Mn}^{2+}$  in dependence of manganese concentration

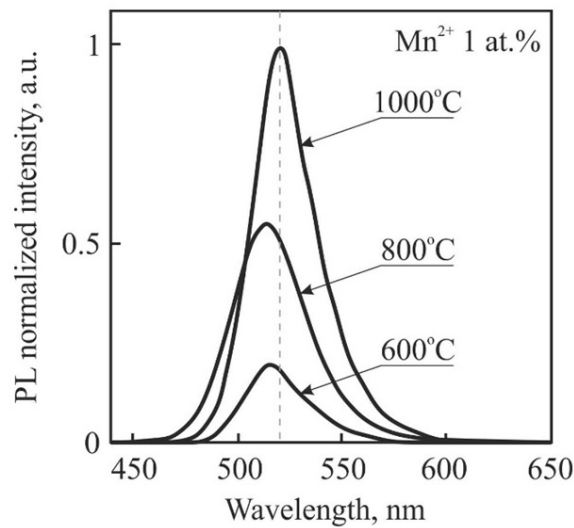


FIG. 4. PL spectra of nanostructured  $\text{Zn}_2\text{SiO}_4:\text{Mn}^{2+}$  (1 at. %) depending on the annealing temperature

The threshold concentration of manganese in the obtained nanostructured  $\text{Zn}_2\text{SiO}_4:\text{Mn}^{2+}$  is found to be equal to 1 at. % (Fig. 5b). After reaching the threshold concentration, the possibility of radiation-free energy transfer between nearest  $\text{Mn}^{2+}$  ions becomes higher than the possibility of radiative recombination in single  $\text{Mn}^{2+}$ . That leads to the significant PL quenching at high manganese content. As a result of exchange coupling between  $\text{Mn}^{2+}$  pairs, the average decay time is shortening from 45 to 1 ms (5 at. %  $\text{Mn}^{2+}$ ).

Sol-gel, prepared  $\text{Zn}_2\text{SiO}_4:\text{Mn}^{2+}$  nanopowder and nanostructured willemite ceramics, obtained earlier by solid state sintering of nanopowders [12], show almost four times higher PL efficiency comparing with commercial microcrystalline powder (Fig. 6). It is caused by large specific surface of nanostructured phosphor that provides significant adoption of activator ions. In addition, sol-gel method provides willemite with high crystallinity, homogeneity, and better manganese incorporation in  $\text{Zn}_2\text{SiO}_4$  crystal lattice than conventional solid-state reaction. Along with high AQY nanostructured willemite is characterized by PL decay time in wide range of 6 – 45 ms.

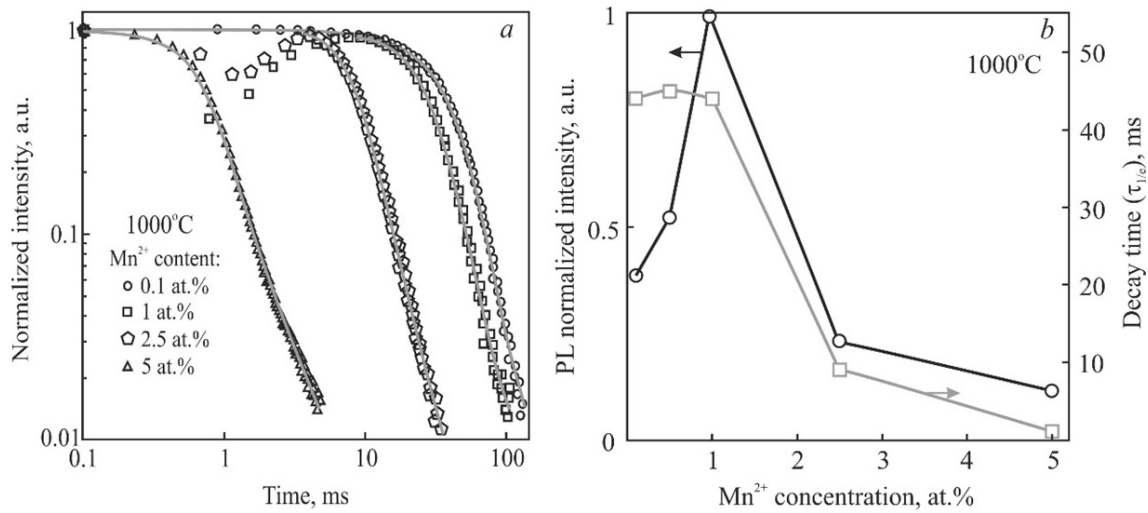


FIG. 5. PL decay curves (a); PL intensity and average decay time (b) depending on manganese content in  $\text{Zn}_2\text{SiO}_4:\text{Mn}^{2+}$

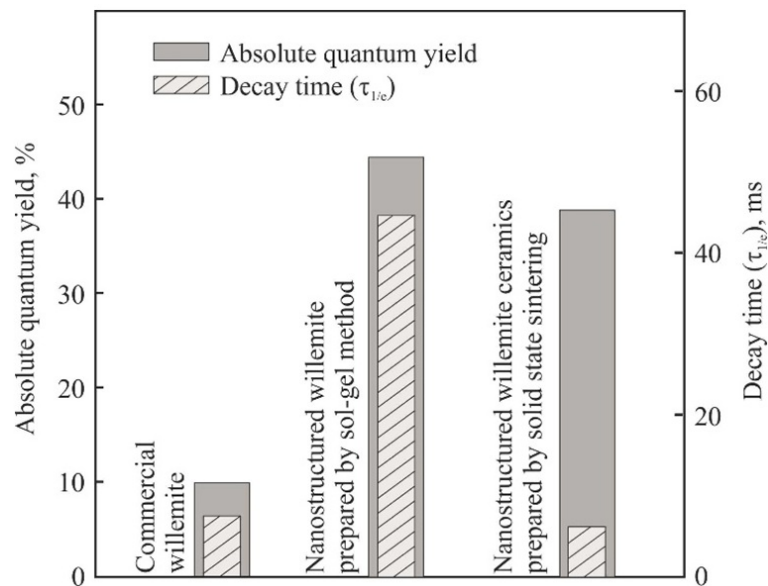


FIG. 6. Absolute quantum yield and PL decay time of microcrystalline willemite (FGI-520),  $\text{Zn}_2\text{SiO}_4:\text{Mn}^{2+}$  nanopowders obtained by sol-gel method and nanostructured willemite ceramics

#### 4. Conclusions

Nanostructured monodispersed  $\text{Zn}_2\text{SiO}_4:\text{Mn}^{2+}$  with a particle size of 100 nm, high crystallinity and homogeneity was prepared by sol-gel method. The structure and maximum position of PL spectra confirmed the formation of  $\text{Mn}-\text{Zn}_2\text{SiO}_4$  solid solution. The absolute quantum yield of luminescence of the obtained willemite is four times higher than of commercial one. Long decay time (45 ms) makes it possible to use  $\text{Zn}_2\text{SiO}_4:\text{Mn}^{2+}$  as a phosphor in medical and radar devices. While the nanostructured willemite ceramics characterized by high efficiency and rather short decay time of 6 ms is promising material for plasma display panels and optical devices in which short response time is required.

#### Acknowledgement

This work was supported by Act 211 Government of the Russian Federation, contract No 02.A03.21.0006. The authors are grateful to Minobrnauki initiative project No 16.5186.2017/8.9.

## References

- [1] Suzdalev I.P. *Nanotechnology: Physics and Chemistry of nanoclusters, nanostructures and nanomaterials*. Kom.Kniga, Moscow, 2006, 592 p.
- [2] Stevels A.L.N. Recent developments in the application of phosphors. *Journal of Luminescence*, 1976, **12**, P. 97–107.
- [3] Ilmas E.R., Savikhina T.I. Investigation of luminescence excitation processes in some oxygen-dominated compounds by 3 to 21 eV photons. *Journal of Luminescence*, 1970, **1**, P. 702–715.
- [4] Williamson G.K., Hall W.H. X-ray line broadening from field Aluminium and Wolfram. *Acta Metallurgica*, 1953, **1**, P. 22–31.
- [5] Kortyum G., Braun V., Gertsog G. Principles and methods of registration in diffusive reflectance spectroscopy. *Physics-Uspokhi (Advances in Physical Sciences)*, 1965, **85**(2), P. 365–380.
- [6] Petrovykh K.A., Rempel A.A., Kortov V.S., Buntov E.A. Sol-gel synthesis and Photoluminescence of nanosized  $\text{Zn}_2\text{SiO}_4\text{:Mn}$ . *Inorganic materials*, 2015, **51**(2), P. 152–157.
- [7] Karazhanov S.Z., Ravindran P., Fjellvåg H., Svensson B.G. Electronic structure and optical properties of  $\text{ZnSiO}_3$  and  $\text{Zn}_2\text{SiO}_4$ . *Journal of Applied Physics*, 2009, **106**, P. 123701.
- [8] El Ghoul J., El Mir L. Sol-gel synthesis and luminescence of undoped and Mn-doped zinc orthosilicate phosphor nanocomposites. *Journal of Luminescence*, 2014, **148**, P. 82–88.
- [9] Tsai M.T., Lin Y.H., Yang J.R. Characterization of Manganese-doped Willemite Green Phosphor Gel Powders. *IOP Conference Series: Materials Science and Engineering*, 2011, **18**, P. 32026.
- [10] Vink A.P., de Bruin M.A., Roke S., Peijzel P.S., Meijerink A. Luminescence of Exchange Coupled Pairs of Transition Metal Ions. *Journal of The Electrochemical Society*, 2001, **148**, P. E313–E320.
- [11] Dubey V., Tiwari R., Pradhan M., Rathore G., Sharma C., Tamrakar R. Photoluminescence and Thermoluminescence Behavior of  $\text{Zn}_2\text{SiO}_4\text{:Mn}^{2+}$ ,  $\text{Eu}^{2+}$  Phosphor. *Journal of Luminescence and Applications*, 2014, **1**, P. 30–39.
- [12] Kortov V.S., Sergeeva K.A., Pustovarov V.A., Rempel A.A. Photoluminescence of nanosized  $\text{Zn}_2\text{SiO}_4\text{:Mn}^{2+}$  ceramics under UV- and VUV-excitation. *Journal of Surface Investigation: X-Ray, Synchrotron and Neutron techniques*, 2017, **7**, P. 49–54.

## In-situ formation of carbon shells on the surface of Ni nanoparticles synthesized by the electric explosion of wire

I. V. Beketov<sup>1,2</sup>, A. P. Safronov<sup>1,2</sup>, A. I. Medvedev<sup>1,2</sup>, A. M. Murzakaev<sup>1,2</sup>,  
O. R. Timoshenkova<sup>1</sup>, T. M. Demina<sup>1</sup>

<sup>1</sup>Institute of Electrophysics UB of RAS, 620016, Yekaterinburg, Amundsen st., 106, Russia

<sup>2</sup>Ural Federal University, 620002, Yekaterinburg, Mira st., 19, Russia

beketov@iep.uran.ru

DOI 10.17586/2220-8054-2018-9-4-513-520

The controlled addition of butane to the inert working gas during the production of nickel nanoparticles by the electrical explosion of wire (EEW) method leads to the formation of carbon shells on the surface of particles. EEW provides formation of spherically shaped nanoparticles, with an average diameter that varies from 60 to 100 nm and depended on the energy introduced into the wire in the EEW process. The thickness and the structure of carbon layer deposited onto the surface of Ni nanoparticles as a function of butane addition was characterized by low-temperature adsorption of nitrogen, x-ray diffraction, complex thermoanalysis, transmission and scanning electron microscopy. It was shown that the thickness of carbon shell on the surface of nanoparticles varied from 2 to 6 nm and depended on the amount of energy introduced into the wire during the EEW process and on the amount of butane added. The crystalline structure of the carbon shell consisted of amorphous and graphite regions.

**Keywords:** nickel nanoparticles, electrical explosion of wire, core shell, carbon deposition.

*Received:* 12 July 2018

*Revised:* 27 July 2018

### 1. Introduction

Ultrafine metal powders have high chemical activity. As the particle size decreases, their reactivity at low temperatures increases, and it greatly complicates their further use. Usually, after the synthesis of the metal nanoparticles they are inactivated by a thin layer of oxide formed on the surface of the particles, which subsequently protects the metal from rapid oxidation. Given a high specific surface area of the powder, even if the oxide layer is thin, the oxide content in the powder is large. Additionally, some metals such as copper [1], do not form a gas-tight oxide shell during inactivation. In order to protect metal nanoparticles from oxidation, their surface can be covered with silicon carbide, polyethylene, and carbon [2], which are not active at low temperatures.

Deposition of the protective carbon layer is the most universal route for passivation. Metal nanoparticles coated with a protective carbon shell can be used in magnetic fluids, sensor devices, hydrogen sorbents, protective coatings, in some biomedical applications and others.

Different methods are used to create a carbon protective shell on the surface of the particles. In particular they are: encapsulation of particles during annealing of metal powder under a hydrocarbon (gasoline) atmosphere [3], filling of carbon tubes with metal [4], annealing of a mixture of metal particles with carbon [5]. All these technologies involve processing as the subsequent next step after the synthesis of nanoparticles. The formation of a carbon shell on the surface of the metal particles in-situ, in the process of their synthesis is, in our opinion, more preferable. One of these techniques is the method of microarc discharge under an inert atmosphere containing hydrocarbon [6] or in the atmosphere of pure hydrocarbon [7]. However, the disadvantage of the methods described in the literature, is their low productivity, often not exceeding 10 grams per hour.

The electric explosion of wire (EEW) is an efficient method of producing the weakly aggregated nanoparticles of metals, alloys and their chemical compounds [8,9]. The basic principle of the method is the evaporation of the metal wire between two working electrodes under the electric discharge. The electrical current of several kV passes through the wire and instantly overheats it in the explosion-type manner, which gives the name of the method. The cloud of metal vapor originated from the explosion of the wire is then expanding in the surrounding gas giving rise to the condensation of spherical nanoparticles. The process of the electrical explosion of portion by portion continuously fed wire goes up in the step-wise manner. The details of the method and a scheme of the EEW apparatus used are given elsewhere [8]. The production rate of this method ranges from 50 to 1000 g/hour depending on the material of the nanopowder. In addition, the method has low energy consumption, not exceeding 50 kW·h/kg, is environmentally friendly, and provides high purity of the produced nanoparticles. The EEW units implemented are compact and do not require special premises. The valuable advantage of EEW

is its flexibility, which provides the in-situ surface modification of synthesized nanoparticles. In particular, in our previous studies [10, 11] we had shown the opportunity of the in-situ carbon deposition on the surface of nickel nanoparticles by the addition of butane in the working gas of a EEW installation. Meanwhile, the effects of the nanoparticles' synthetic conditions on their characteristics have not yet been described.

The objective of the present study was to disclose how to control the deposition of carbon shell on the surface of nickel nanoparticles via varying the synthetic conditions in the process of EEW synthesis. We studied the effect of the excess of the electrical energy introduced in the wire in the EEW process and of the amount of butane added to the working gas on the degree of dispersity of the produced nanoparticles, on the thickness of the carbon shells on their surface, as well as on the morphology of the particles and their structure.

## 2. Experimental

The synthesis of nickel nanoparticles was carried out in the EEW installation described in detail in our previous works [8, 9]. In the present study, the discharge circuit of the installation had an inductance of  $0.4 \mu\text{H}$ . The capacitance of the capacitor bank was varied from 3.2 to  $4.8 \mu\text{F}$ , and the charging voltage – from 20 to 30 kV, which provided a variation of the overheating ratio  $K$  in the range 1 – 2.2 ( $K$  is the ratio of the electric energy introduced into the wire to the sublimation energy of the metal material of the wire). To obtain nanoparticles, a wire of nickel (grade NP2) with a diameter of 0.3 mm, with the length of the explosive wire segment of 88 mm was used. The wire was fed into the installation step-wise. The explosions were carried out at a frequency of 0.5 Hz.

The gas system of the installation consisted of an explosion chamber, two inertial traps with gas flow rotation by  $90^\circ$  and  $180^\circ$ , a mechanical (cloth) filter and a fan in serial connection and was filled by circulating argon at a pressure of 0.12 MPa. Inertial traps were used to separate large particles, including micron-sized; fine particles were collected in the filter. As it was shown by preliminary experiments, the amount of fine particles in the filter depended on the value of the electric energy introduced into the wire and averaged 85 % of the amount of all the powder produced by the EEW. Only nanoparticles from the filter are considered below as a potential product for further use.

To create carbon shells on the surface of the particles during nanoparticle synthesis, gaseous butane was continuously fed into the apparatus, where it was mixed with the working gas of the installation immediately before entering the explosion chamber. Butane flow rate was varied from  $0.3 - 20 \text{ cm}^3/\text{s}$  using an adjustable throttle flow. For the convenience of the characterization of nanoparticles obtained in different regimes, the amount of added butane will further be given in the weight ratio to the weight of the evaporated nickel wire ( $Q$ ). The value of  $Q$  was calculated from the ratio of the butane feed rate and the average feed rate of nickel wire. To find the limits of the efficient passivation of Ni nano, the collected nanoparticles were optionally passivated after the synthesis by an oxide layer on their surface, while oxygen was supplied to the unit at  $0.5 \text{ cm}^3/\text{s}$ . The passivation process was controlled by a sensor of partial pressure of oxygen. Passivation was terminated when the partial pressure of oxygen in the installation reached 2 kPa.

The energy introduced into the wire was determined by the oscillograms of the current pulse passing through the wire segment during EEW. The specific surface area of the produced nanoparticles was determined by low-temperature nitrogen adsorption (Brunauer–Emmett–Teller (BET) approach) using Micromeritics TriStar 3000 analyzer. X-ray phase analysis (XRD) was performed using Bruker D8 DISCOVER diffractometer in  $\text{Cu}_{k\alpha}$  radiation ( $\lambda = 1.54 \text{ \AA}$ ) with a graphite monochromator on a secondary beam. Diffractogram processing was performed using the built-in software TOPAS 3. High-resolution transmission electron microscopy (HRTEM) was performed using JEOL JEM2100 electron microscope at an accelerating voltage 200 kV. The amount of carbon deposited onto nickel nanoparticles was determined by complex thermal analysis using NETZSCH STA409 analyzer with mass-spectrometer. The carbon content in shells was calculated by integrating the peak of carbon dioxide release on a complex thermogram. The mass spectrometer was previously calibrated by introducing a metered amount of gaseous  $\text{CO}_2$  into the gas line. The error in determining the carbon content in the nanopowder was about 10 wt.%.

## 3. Results and discussion

Figure 1 shows the experimental dependence of the specific surface area of nickel nanoparticles (Ni NPs) collected in the filter setup on the consumption of butane at two values of overheating ratio  $K - 1.2$  and  $2$ . It can be noticed that the increase in butane flow rate led to a linear increase in the specific surface area of Ni NPs. The increase in the specific surface area is significant at  $K = 2$  and less significant at  $K = 1.2$ .

For any value of butane/Ni ratio, the specific surface area of the particles obtained at the overheating ratio  $K = 2$  are approximately 1.5 – 2 times higher than the specific surface area of the particles obtained at the degree

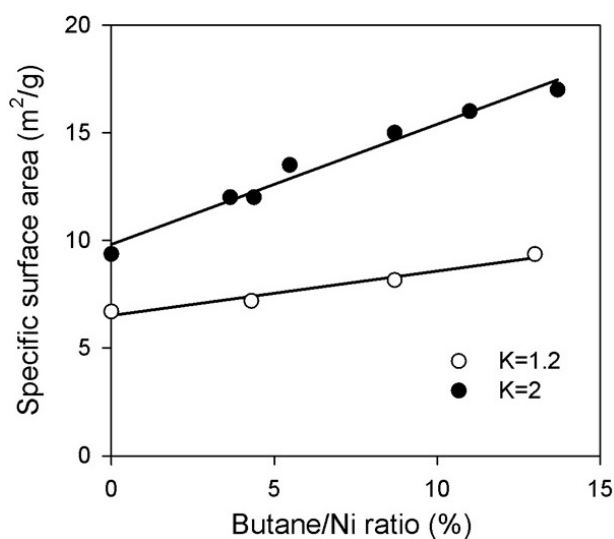


FIG. 1. Dependence of the specific surface area of Ni NPs on butane/Ni ratio ( $Q$ ) at different overheating ratios ( $K$ )

of overheating  $K = 1.2$ . This effect is consistent with the literature data [12], which indicate that with an increase in overheating  $K$ , the size of the obtained particles decreases due to an increase in the expansion rates of the explosion products. As the size of the particles decreases their specific surface area enlarges.

The energy that is released in an electrical explosion is sufficient to decompose the hydrocarbon (butane) into atomic carbon and hydrogen. The temperature of the explosion products at the initial moments of their expansion reaches  $10^4$  K by an order of magnitude. At such temperatures carbon is in a gaseous state. According to the diagram of the state starting from 4000 K (at normal pressure), carbon condense into graphite [13]. The temperature of graphite formation is higher than the temperature of formation (condensation) of Ni NPs. Thus, the process of formation of the graphite shell can begin from the moment of formation of liquid nickel nanosized droplets. The graphite shell prevents their coagulation and aggregation of metal particles during cooling, and eventually leads to a decrease in their final size and to an increase of the specific surface area of the produced powder.

At high levels of the consumption of hydrocarbon added to the working gas, carbon accumulation as a separate phase is not excluded. The carbon content of the powder samples was determined using a mass spectrometer for  $\text{CO}_2$  emission during TG analysis. The samples were heated in the air flow to a temperature of  $1000^\circ\text{C}$  at a heating rate of 10 K/min. A typical combined thermogram is shown in Fig. 2.

As it can be seen from Fig. 2 (TG curve) the oxidation of nickel (mass gain) starts at  $225^\circ\text{C}$ , ends at  $900^\circ\text{C}$ , and has a clear two-step character with the first step at  $225 - 500^\circ\text{C}$  and the second step at  $500 - 900^\circ\text{C}$ .

The process of Ni oxidation obscures the reduction of the sample mass due to carbon oxidation to  $\text{CO}_2$ . The use of mass spectrometer allows tracing the process of carbon oxidation contained in the sample. The thermogram shows the peak of the ion current of  $\text{CO}_2$  emission. Based on the area under the thermogram of ion current, the carbon content in the nanopowder samples obtained at different values of butane/Ni ratios was calculated. Differential scanning calorimetry (DSC) thermogram shows that the processes of oxidation of carbon and nickel are accompanied by exothermic effect. The shape of the thermogram repeats the shape of the mass spectrometric curve of  $\text{CO}_2$  release with an additional exothermic peak corresponding to the second (high-temperature) stage of nickel oxidation.

Based on the results of thermal analysis, the values of the carbon content in the Ni NPs obtained at different butane/Ni ratios were calculated. The dependence of carbon/Ni ratio in Ni NPs on the butane/Ni ratio in EEW process is reported in Fig. 3. For the sake of clarity, the x-axis, which stands for the butane/Ni ratio in EEW process was recalculated to carbon/Ni ratio.

As it can be seen from Fig. 3, the carbon content in the collected Ni NPs detected by the method of complex thermal analysis depends linearly on the amount of carbon introduced (as part of butane) during the EEW of Ni wire. The carbon content values obtained at different degrees of overheating  $K$ , lay on a common linear dependence within the experimental error. The tangent of the slope of the line is 1.16, which is fairly close to unity. This means that all of the carbon introduced into the working gas of the installation during EEW, is almost quantitatively transferred to the Ni NPs synthesized.

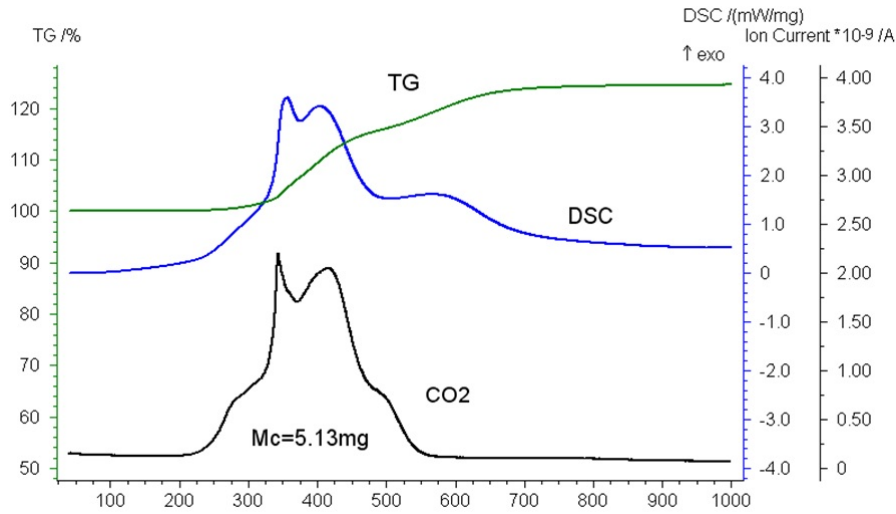


FIG. 2. Combined thermogram of heating in the air of Ni NPs obtained by the EEW at butane/Ni ratio  $Q = 8.7\%$ . Heating rate 10 K/min. TG – thermogravimetry curve, DSC – thermogram of differential scanning calorimetry,  $\text{CO}_2$  – mass-spectrometric signal of carbon dioxide release

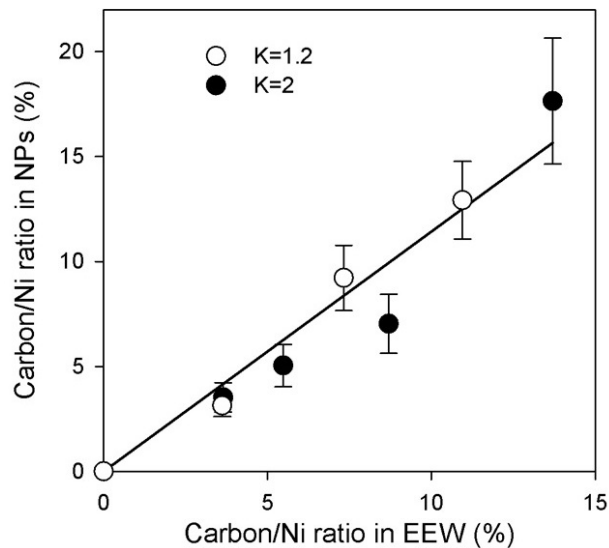


FIG. 3. Comparison of the introduced amount of carbon at EEW at different values of overheating  $K$  and the amount of carbon found in the nanopowder by combined thermal analysis

It is known [6] that the metal nanoparticles obtained by the EEW method have a spherical shape, which is a consequence of their condensation in the rarefied vapor phase. The value of the specific surface area for the ensemble of spherical particles, allows calculating their average diameter using the following equation [14]:

$$d = \frac{6}{S\rho}, \quad (1)$$

where  $S$  is the specific surface area,  $\rho$  – is the density of the particle material.

Figure 4 reports the calculated values of the average diameter of the particles obtained at different overheating ratios and different butane/Ni ratios. In the calculation, according to equation (1), the change in the average density of particles due to an increase in the carbon content in the sample was taken into account.

It is seen that the diameter of the particles obtained at the overheating ratio  $K = 1.2$  is substantially higher than the diameter of the particles obtained at a higher overheating ratio  $K = 2$ . In general, the average diameter of Ni NPs diminishes with the increase in the amount of carbon introduced into the system at EEW. Meanwhile at  $K = 1.2$  the change in particle size is insignificant, and at  $K = 2$  it becomes more pronounced.

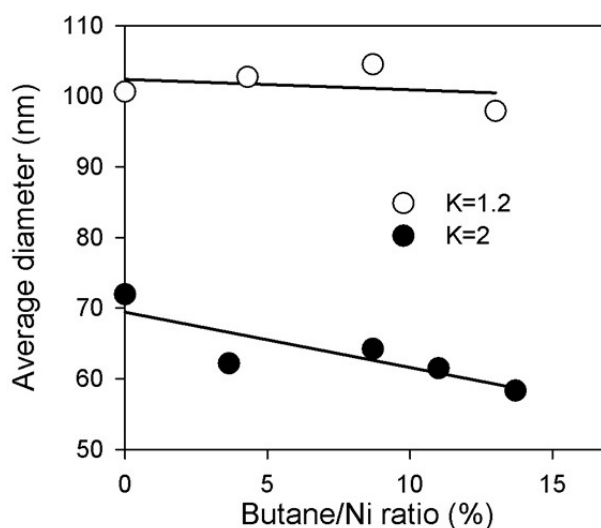


FIG. 4. Dependence of the average particle diameter on the butane/Ni ratio at different degrees of overheating  $K$

An XRD pattern of Ni NPs with deposited carbon shell is given in Fig. 5. Diffraction lines are clearly asymmetric and drawn towards small angles, which is possible in the presence of a composition gradient. It may reflect the fact of non-uniform dissolution of carbon in Ni NPs, for example, by the depth of the particle. The crystal lattice period  $a = 0.3533 (\pm 0.0003)$  nm which differs from the typical value for pure Ni ( $a = 0.35238$  nm, PDF No. 004-08550), also indicates the formation of a solid solution of carbon in Ni NPs. According to reference [15] the maximum solubility of carbon in solid nickel is 2.51 at.%. Taking into account the atomic weights of carbon and Ni this value gives 0.52 wt. % of carbon dissolved in Ni crystal lattice at maximum. This value is substantially lower than the overall carbon content found at Ni NPs at any butane/Ni ratio. Thus we may conclude that the dominating fraction of carbon is deposited on the surface of Ni NPs.

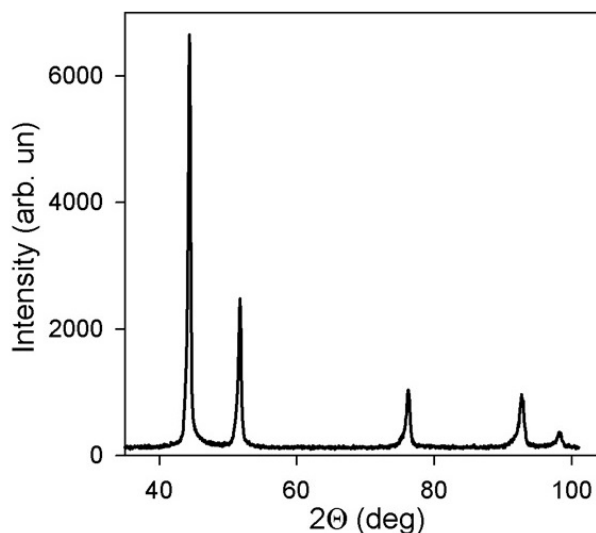


FIG. 5. The diffraction pattern of Ni NPs, obtained at butane/Ni ratio 13 wt.%.

If we assume that all of the particles are covered with a carbon shell of the same thickness, the carbon content in the powder, its specific surface area and the thickness of the shell will be related to each other by the equation:

$$W_C = S \cdot h \cdot \rho_C, \quad (2)$$

where  $W_C$  is the weight fraction of carbon in the Ni nanopowder;  $h$  is the thickness of the carbon shell;  $\rho_C$  is the density of carbon.

Based on the experimental values of  $C_c$  and  $S_s$ , the thickness of the carbon shell  $h$  on the surface of Ni NPs was calculated using equation (2). Fig. 6 shows the dependence of the calculated thickness of the deposited carbon shell on the value of butane/Ni ratio. It is seen that with the increase in the amount of butane supplied to the working gas of the installation, the thickness of the carbon shell on the nickel particles increases. At lower values of overheating ratio ( $K = 1.2$ ) the shells are thicker than carbon shells obtained at overheating ratio  $K = 2$ . Apparently, it is due to the fact that lower  $K$  values provide larger particles (see Fig. 4). Given the same overall mass, their number is less than the number of smaller particles obtained at high overheating ratio, so the same amount of carbon is deposited onto smaller surface making the shells on larger particles thicker.

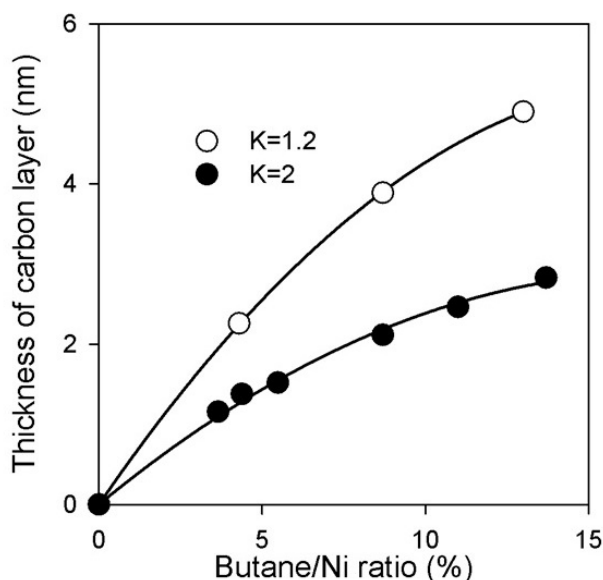


FIG. 6. The dependence of the calculated thickness of the carbon shell on Ni NPs on the butane/Ni ratio at different overheating ratios ( $K$ )

Figure 7 shows a TEM image of Ni NPs with carbon shells. Deposited carbon shells at the surface of particles are clearly noticeable and their thickness varies from particle to particle. The average thickness of the deposited carbon layer was estimated by the graphical analysis of TEM images. The values are given in Table 1 as a function of butane/Ni ratio and overheating ratio.

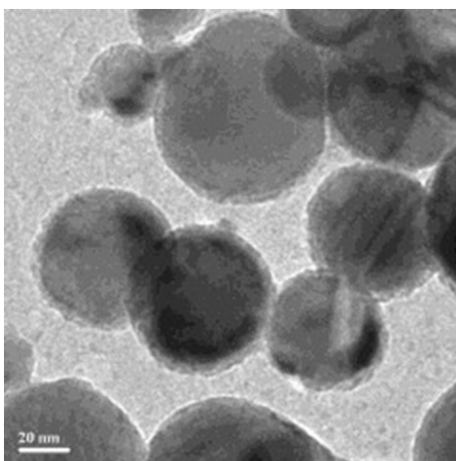


FIG. 7. TEM image of Ni NPs synthesized at butane/Ni ratio of 8.7 wt.% and overheating ratio  $K = 1.2$

As it can be seen from Table 1, the increase in butane/Ni ratio leads to an increase in the average thickness of the shell, and the increase in overheating ratio, on the contrary, lowers the average thickness of the shells. These

TABLE 1. The thickness of the carbon shells based on TEM images

Butane/Ni ratio, %	$K$	Average thickness of the shell, nm	Thickness range, nm
4.3	1.2	$3.0 \pm 0.3$	2 – 4
13.0	1.2	$4.2 \pm 0.7$	2 – 6
3.6	2	$2.7 \pm 0.3$	2 – 4
11.0	2	$3.5 \pm 0.5$	2 – 5

trends and the values of the shell thickness on the surface of nanoparticles are consistent with the data presented above in Fig. 6.

Figure 8 shows the structure of carbon shells obtained by HRTEM. On some particles Fig. 8a presents the evidence of a layered crystalline fragments typical to graphite. The average lattice line spacing was  $3.5 \text{ \AA}$ . Meanwhile, the crystal structure is not visible on other particles (Fig. 8b) – possibly, in these cases carbon is in the amorphous state.

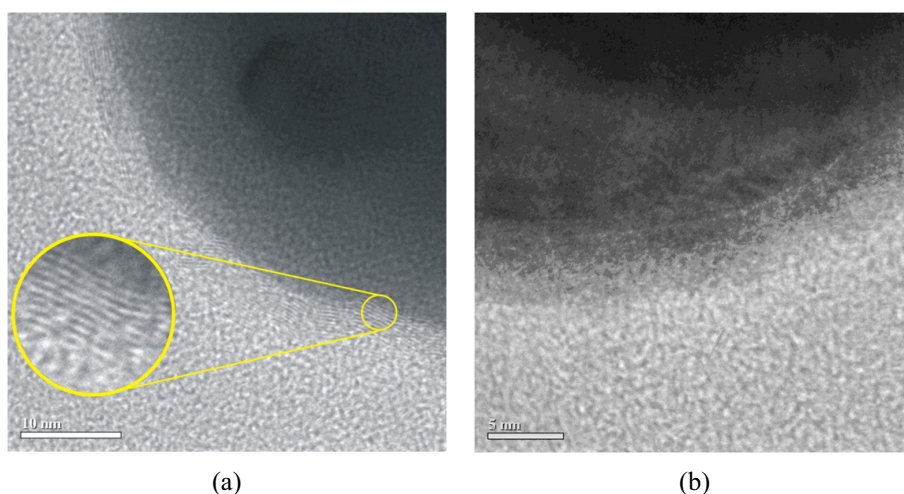


FIG. 8. The structure of carbon shells on the surface of Ni NPs: a) graphite domains; b) disordered amorphous structures

Judging from the TEM and HRTEM images (Figs. 7 and 8), the deposited carbon forms sufficiently dense shell on the surface of Ni NPs, the thickness of which is estimated as 4 – 6 nm. Such a shell provides protective coating layer, which prevents oxidation and reduces the pyrophoricity of the Ni nanopowder as a whole. It was determined experimentally that the minimal butane/Ni ratio, which provides efficient passivation of Ni NPs was 4 %. At this butane/Ni ratio the obtained Ni NPs with protective carbon layer can be safely exposed to air.

Meanwhile, if butane/Ni ratio was lower than 4 %, the synthesized Ni NPs could be extracted to the air only after passivation with oxygen. Otherwise the samples were flammable. Evidently, the amount of the deposited carbon was not sufficient to cover the total surface of particles in this case. If combined with carbon deposition at low butane/Ni ratio oxygen passivation results in formation of fragments of Ni oxide on the surface of Ni NPs. HRTEM image in Fig. 9 shows such Ni oxide inclusions in the deposited carbon layer. The lattice line spacing of these inclusions was found  $4.18 \text{ \AA}$ , which clearly distinguishes them from graphite fragments (Fig. 8a) Eventually, such inclusions operate as “patches” in the non-uniform carbon layer on the surface of Ni NPs.

#### 4. Conclusion

Controlled addition of butane  $C_4H_{10}$  to the inert working gas (argon) of the EEW installation during the synthesis of nickel nanoparticles by the electrical explosion of wire provides the deposition of 2 – 6 nm dense carbon shells on the surface of spherical nickel nanoparticles from the vapor phase during the condensation process. The energy that is released in an electrical explosion is sufficient to decompose the hydrocarbon (butane) into atomic carbon and hydrogen. Since the temperature of condensation of carbon (4000 K) is above the temperature

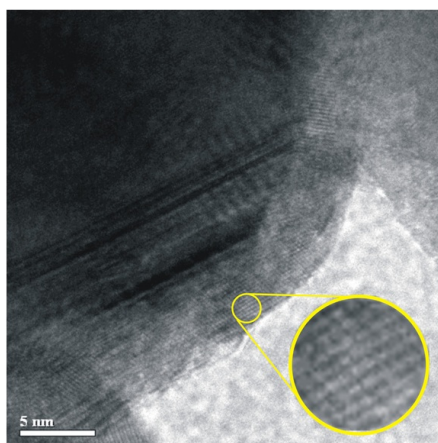


FIG. 9. HRTEM image of the shell on the surface of the Ni NPs synthesized at butane/Ni ratio 2 %. Inset – enlarged view of crystal fragment of Ni oxide

of condensation of Ni (3173 K), the process of formation of a graphite shell can begin with the formation of nickel particles. The deposited carbon layer prevents coalescence and aggregation of metal nanoparticles, which leads to a decrease in their size. The increase in butane consumption in the range of butane/Ni ratio 0 – 10 % results in an increase of the specific surface area of the nanopowder by 40 – 80 % and in a proportional increase in carbon content. All carbon introduced into the installation is eventually deposited on the nanoparticles. With the increase of the energy introduced into the wire at the EEW, both the diameter of the synthesized nickel nanoparticles and the thickness of the carbon shell on their surface decreases. The structure of the obtained carbon shells includes both fragments of the crystal structure of graphite and disordered carbon in the amorous state. At the same time, the shells are dense enough to prevent oxidation of nickel nanoparticles by aerobic oxygen.

## References

- [1] Kotov Yu.A., Rhee Ch.K., Beketov I.V., Bagazeev A.V., Demina T.M., Murzakayev A.M., Samatov O.M., Timoshenkova O.R., Medvedev A.I., Shtols A.K. Production of Copper Nanopowders by Electric Explosion of Wire-Study of Their Oxidation during Storage and Heating in Air. Proc. 9th ISMANAM-2002, *J. of Metastable and Nanocrystalline Materials*, 2003, **15-16**, P. 343–348.
- [2] Athanassiou E., Grass R., Stark W. Large-scale production of carbon-coated copper nanoparticles for sensor applications. *Nanotechnology*, 2006, **17**, P. 1668–1673.
- [3] Hayashi C. Ultrafine particles. *J. Vac. Sci. Technol. A5*, 1987, **4**, P. 1375
- [4] Tsang S.C., Chen Y.K., Harris P.J.F. Synthesis of carbon nanotubes with totally hollow channels and/or with totally copper filled nanowires. *Nature*, 1994, **372**, P. 159.
- [5] Tomita S., Hikita M., Fujii M. Formation of Co filled carbon nanocapsules by metal-template graphitization of diamond nanoparticles. *J. Appl. Phys.*, 2000, **88**, P. 5452.
- [6] Ermoline A., Schoenitz M., Dreizin E. and Nan Yao. Production of Carbon-Coated Aluminium Nanopowders in Pulsed Microarc Discharge. *Nanotechnology*, 2002, **13**, P. 638–643.
- [7] Zhang Z.D., Zheng J.G., Skorvanek I. Shell/core structure and magnetic properties of carbon-coated Fe-Co(C) nanocapsules. *J. Phys. Condens. Matter*, 2001, **13**, P. 1921.
- [8] Kotov Yu.A. The electrical explosion of wire: a method for the synthesis of weakly aggregated nanopowders. *Nanotechnologies in Russia*, 2009, **4(7-8)**, P. 415–424.
- [9] Kotov Yu.A. Electric explosion of wires as a method for preparation of nanopowders. *Journal of Nanoparticle Research* 5, 2003, P. 539–550.
- [10] Beketov I.V., Safronov A.P., Bagazeev A.V., Larranaga A., Kurlyandskaya G.V., Medvedev A.I. In situ modification of Fe and Ni magnetic nanopowders produced by the electrical explosion of wire. *Journal of Alloys and Compounds*, 2014, **586**, P. S483–S488
- [11] Safronov A.P., Kurlyandskaya G.V., Chlenova A.A., Kuznetsov M.V., Bazhin D.N., Beketov I.V., Sanchez-Ilarduya M. B., Martinez-Amesti A. Carbon deposition from aromatic solvents onto active intact 3d metal surface at ambient conditions. *Langmuir*, 2014, **30(11)**, P. 3243–3253.
- [12] Chace W.G. A brief survey of exploding wire research. In: Chace W.G. and More H.K. eds. Exploding Wires, Vol. 1. Proc. of 1-st Conf. on the Exploding Wire Phenomenon, Boston, USA, 24-27 March 1959, Plenum Press, New York, P. 7–13.
- [13] Properties of elements: Textbook/ under edition of M.E. Drutz. Moscow. Metallurgia. 1985.
- [14] Beketov I.V., Safronov A.P., Medvedev A.I., Alonso J., Kurlyandskaya G.V., Bhagat S. M. Iron oxide nanoparticles fabricated by electric explosion of wire: focus on magnetic nanofluids. *AIP Adv.*, 2012, **2**, P. 022154.
- [15] Gariel A., Chatillon C., and Ansara I. Thermohmial and Phase Diagram Analysis of th Ni-C, Co-C, and Co-Ni-C Systems. *High Temperature Science*, 1988, **25**, P. 17–53.

**Capillary filling of carbon nanotubes by BiCl<sub>3</sub>: TEM and MD insight**E. A. Anumol<sup>1</sup>, F. L. Deepak<sup>1</sup>, A. N. Enyashin<sup>2</sup><sup>1</sup>Nanostructured Materials Group, Department of Advanced Electron Microscopy, Imaging and Spectroscopy, International Iberian Nanotechnology Laboratory (INL), Braga, Portugal<sup>2</sup>Institute of Solid State Chemistry UB RAS, Ekaterinburg, Russia

leonard.francis@inl.int; enyashin@ihim.uran.ru

**PACS 34.30.+h, 34.35.+a, 05.70.Np****DOI 10.17586/2220-8054-2018-9-4-521-531**

Among numerous trichlorides, the melt of BiCl<sub>3</sub> is a distinctly molecular liquid with a relatively low melting point, yet, with a high surface tension. Therefore, the attractiveness of a simple capillary filling technique for fabrication of nanosized BiCl<sub>3</sub> by dispersion within a nanocapillary needs a special investigation. Here, we report the successful synthesis and the transmission electron microscopy characterization of the hybrids consisting of multi-walled carbon nanotubes and endohedral BiCl<sub>3</sub> crystallites. The main peculiarities of imbibition into carbon nanotubes and an intricate internal organization of molten BiCl<sub>3</sub> are established using the developed 4-site force-field model of BiCl<sub>3</sub> and consequent molecular dynamics simulations at nanosecond time scale.

**Keywords:** Bismuth trichloride, carbon nanotubes, capillary, TEM characterization, MD simulations.

*Received: 18 July 2018*

**1. Introduction**

The main attribute of Carbon nanotubes – the cavity – suggests their capillary activity, assigning their role as proper templates for the growth of other one-dimensional nanostructures in its interior or serve as containers for nanocargos. Open-ended carbon nanotubes, soon after their discovery, were theoretically characterized as “molecular straws” capable of capturing molecules from a vapor or a fluid due to the interactions akin to those in wetting and capillary action [1]. This prediction was successfully proved by the first experiment on filling of multi-walled carbon nanotubes with molten lead in air [2].

Nowadays, the capillary filling technique is routinely employed for encapsulation of fusible metals and compounds into carbon nanotubes, forming endohedral hybrids subsequent to annealing at temperatures above the melting points and followed by cooling. Considerable progress has been attained in both the production and the TEM characterization of ultra-thin halide, oxide and sulfide nanowires encapsulated in single- and multi-walled nanotubes [3–6].

The wetting of the nanotubular interior by the melt of a quasi-two-dimensional inorganic compound can yield the single-walled inorganic nanotubes, too. Hence, the properties of conventional inorganic compounds confined within carbon nanotubes can be modified not only at the level of simple size scaling, but as well at the level of structural organization. Currently, it is the only way to obtain the nanotubes of halides (PbI<sub>2</sub> [7], ZnI<sub>2</sub>, CeI<sub>3</sub>, CeCl<sub>3</sub>, TbCl<sub>3</sub> [8], GdI<sub>3</sub> [9], BiI<sub>3</sub> [10]) in large and stable amounts, since the walls of carbon hosts are excellent protectors from environmental moisture.

Being active intermediators or accumulators of charge carriers, the walls of metallic carbon nanotubes can act as nanoreactors, forcing the encapsulated compounds to undergo a further polymorphic or chemical transformation. Particularly, the crystal lattices of many halides, when confined in the one-dimensional space, tend to adopt an unusual ionic coordination [11], whereas LaI<sub>3</sub> transforms formally into a different stoichiometric composition LaI<sub>2</sub> [12], which may lead to the rise of materials with new electronic, luminescent and magnetic properties. The capillary filling of carbon nanotubes by HgCl<sub>2</sub> [13], NiI<sub>2</sub> [14] and GdI<sub>3</sub> [15] is accompanied by the metal reduction, which, in the case of iodides, manifests itself as the final product containing also the carbon nanotubes filled either by iodine or by metal nanowires.

Endohedral hybrids of inorganic compounds and carbon nanotubes fabricated using capillary filling technique are promising advanced materials for biomedical applications. As the locked vehicles the carbon nanotubes are capable of improving the long-term stability of encapsulated materials *in vivo*. They can convey within organisms such nanocargos like radionuclides serving as radiolabels [16] or anticancer agents [17]. Potentially, carbon nanotubes dispersing at their interior a heavy metal compound could become the components of radioprotective composites.

Bismuth trichloride BiCl<sub>3</sub> is a compound with a relatively low melting point ( $T_m = 507$  K) among other metal trichlorides [18]. Presumably, the application of this compound as an eco-friendly catalyst in organic

synthesis [19,20] and as a core-building component in antimicrobial complex agents [21] could be expanded at the nanoscale level, e.g. by nanodispersion using encapsulation into carbon nanotubes.

Here, we explore the abilities of capillary filling technique for fabrication of endohedral hybrids  $\text{BiCl}_3@MWCNT$  – encapsulates of crystalline  $\text{BiCl}_3$  in multi-walled carbon nanotubes (MWCNTs). Notwithstanding the low  $T_m$ , molten  $\text{BiCl}_3$  has the challengingly high values of surface tension ( $\sigma = 65 \text{ mJ/m}^2$  at  $T = 1.1T_m$ ) and viscosity ( $\eta = 26 \text{ mPa}\cdot\text{s}$  at  $T = 1.1T_m$ ) [22], which could suppress the capillary activity of carbon nanotubes. Compared to the other molten trichlorides, the compound also demonstrates anomalously high values of electrical conductivity [18] and has a tendency for disproportionation at elevated temperatures [23], not yet clarified in the presence of an extended carbon surface. However, despite all these challenges, our joint results from both the transmission electron microscopy (TEM)/scanning transmission electron microscopy (STEM) characterization and the molecular dynamics (MD) simulations confirm a successful capillary action of MWCNTs regarding the molten  $\text{BiCl}_3$ , yielding stoichiometric rod-like or tubular-like  $\text{BiCl}_3$  nanostructures shielded by the carbon shell.

## 2. Experimental part

### 2.1. Procedure of capillary filling

Bismuth(III) chloride, anhydrous, 99.999 % (metals basis) was purchased from Alfa Aesar and used without further purification. MWCNTs were purchased from Nanocyl SA, Belgium and US Research Nanomaterial, Inc, USA. The as-purchased nanotubes were open ended. The encapsulation of  $\text{BiCl}_3$  into MWCNTs was carried out by capillary filling. Bismuth trichloride along with MWCNTs, both sealed under vacuum in a quartz ampule, were annealed in a furnace above the melting point of  $\text{BiCl}_3$  and subsequently cooled to room temperature. The detailed conditions for the synthesis of  $\text{BiCl}_3@MWCNT$  hybrids are given in Table 1 and Fig. 1. The final synthetic products were not treated and were characterized as they have been obtained.

TABLE 1. Synthesis conditions for  $\text{BiCl}_3@MWCNT$  hybrids. The histograms for diameter distributions of parent MWCNTs are visualized in Fig. 1

Sample	CNT: $\text{BiCl}_3$ (mg)	Temperature ( $^{\circ}\text{C}$ )	Heating Rate ( $^{\circ}\text{C}/\text{min}$ )	Duration (h)
$\text{BiCl}_3$ MWCNT 1	13:300	350	2	72
$\text{BiCl}_3$ MWCNT 2	10:300	350	2	72
$\text{BiCl}_3$ MWCNT 2A	15:300	500	2	168
$\text{BiCl}_3$ MWCNT 3	11:300	350	2	72
$\text{BiCl}_3$ MWCNT 4	10:300	350	2	72

### 2.2. Microscopy characterization

Samples for TEM/STEM analysis were prepared on porous carbon film 300 mesh Cu grids. An FEI Titan Themis 60 – 300 kV electron microscope, operated at 80 kV, equipped with probe and image correctors and a monochromator, was used for TEM and STEM imaging. EDX spectra were obtained using a Super-X detector and acquired and analyzed using Bruker Esprit software. Crystal models were constructed using Crystal maker software and diffraction patterns were simulated using Single crystal software.

### 2.3. Computational details

Capillary filling of carbon nanotubes was simulated using MD and was considered as an imbibition of a finite drop-like amount of melt. The starting model for drop of molten  $\text{BiCl}_3$  was designed as a fragment of crystalline  $\text{BiCl}_3$  consisting of 250 or 500 stoichiometric units and annealed in series at MD temperatures  $T = 300 \text{ K}$ ,  $533 \text{ K}$ ,  $623 \text{ K}$  as well as  $693 \text{ K}$  and  $773 \text{ K}$ . The drop  $(\text{BiCl}_3)_{500}$  was employed for validation of the force-field as described below. The final structure of the drop  $(\text{BiCl}_3)_{250}$  equilibrated at  $T = 623 \text{ K}$  was used further as the starting model to study the imbibition at the same temperature. MWCNT model was designed as a rigid cluster of double-walled (20,20)@(25,25) carbon nanotube (DWCNT) composed of 75 unit cells (internal and external radii of 13.56 and 16.95 Å, 13500 atoms in total). The edge surface of the  $\text{BiCl}_3$  drop was installed initially at 3 Å from the apex of DWCNT.

MD simulations have been performed using in-house code as for canonical ensembles (NVT). In all simulations the temperature was controlled with the velocity scaling. Newton's equations of motion were integrated with the MD time step of 2.5 fs via the Verlet leapfrog algorithm during 500,000 steps for the annealing and during 1,380,000 steps for the imbibition.

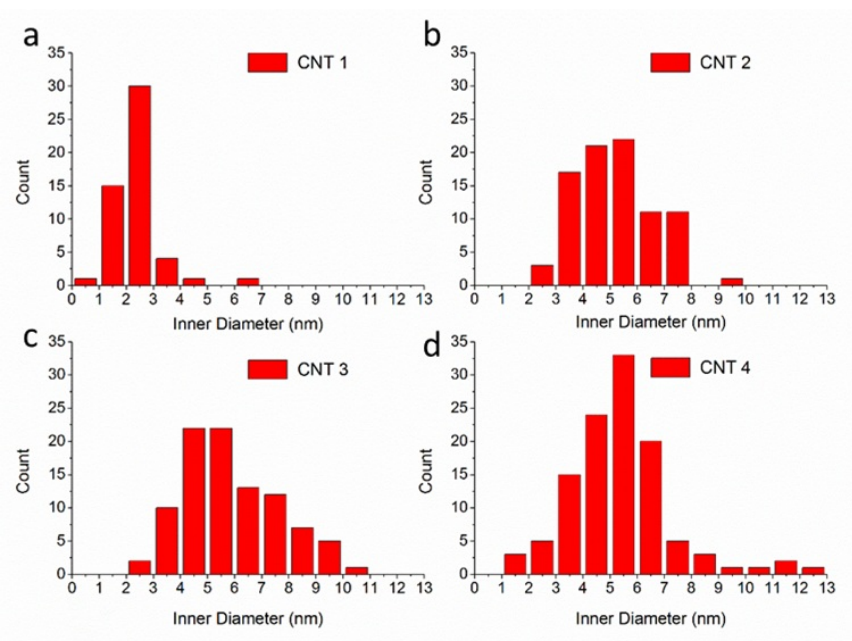


FIG. 1. Diameter distributions for multi-walled carbon nanotubes (MWCNT) in the samples employed for the synthesis of BiCl<sub>3</sub>@MWCNT composites (see Table 1)

The force-field level of theory was applied for these nanosecond MD simulations. The model of liquid BiCl<sub>3</sub> was represented as an ensemble of the rigid 4-site molecules with the geometry matching that within BiCl<sub>3</sub> crystal ( $r_{Bi-Cl} = 2.464 \text{ \AA}$ ,  $\varphi_{Cl-Bi-Cl} = 94.46^\circ$  [24]). Therefore, intramolecular interactions were not considered, while intermolecular BiCl<sub>3</sub> interactions were described using Coulomb and Lennard-Jones potentials as parametrized in framework of Universal Force Field (UFF) [25]. Atomic charges on Bi and Cl were taken to be equal +2.1 e and +0.7 e, which allow a tolerant reproduction of the sublimation enthalpy [26] and the specific electrical conductivity of molten BiCl<sub>3</sub> (*vide infra*) [ [27]. Interatomic interactions between BiCl<sub>3</sub> melt and DWCNT were described using Lennard-Jones potentials in UFF parametrization. The truncation at 25 Å for all short-range non-bonded interactions was used, while the long-range electrostatic interactions were computed without any restriction and approximation.

Visualization of atomic structure and MD trajectories was performed using VMD software [28].

### 3. Results and discussion

#### 3.1. Morphology and composition of BiCl<sub>3</sub>@MWCNT

Since a direct visualization of the melt imbibition by the nanotubes is not possible using current TEM characterization, we have focused on characterization of the final products. Extending the study to other molten halides, BiCl<sub>3</sub> was encapsulated within the MWCNTs by annealing of a mixture of BiCl<sub>3</sub> and MWCNT at typical temperature of 350 °C in vacuum sealed quartz ampules. Encapsulation was observed in all the samples of MWCNTs used. Fig. 2 shows the low magnification image of the composite BiCl<sub>3</sub>@MWCNT with tube-like and rod-like BiCl<sub>3</sub> nanostructures encapsulated within the cavities of MWCNTs.

Figure 3 shows the elemental map distribution of Bi and Cl within the cavity of an individual MWCNT along with the corresponding EDX spectrum, which on quantification gives Bi:Cl ratio consistent with that of BiCl<sub>3</sub>. The filling was predominantly amorphous in nature along with some crystalline BiCl<sub>3</sub>. The analysis of HRTEM image of the crystalline filling indicates the presence of orthorhombic BiCl<sub>3</sub> crystal (ICSD PDF Number: 00-024-1003) within MWCNT (Fig. 4). Both the tube- and rod-like morphologies of BiCl<sub>3</sub> were observed in the case of BiCl<sub>3</sub> encapsulation within MWCNTs.

Hence, all experiments with the capillary filling of MWCNTs by molten BiCl<sub>3</sub> have been successful irrespective of the peculiarities of the synthesis, especially, related to the diameter distribution of MWCNTs. All set of characterization techniques ensured that, the stoichiometric composition of the encapsulated BiCl<sub>3</sub> is preserved at the experimentally employed elevated temperatures.

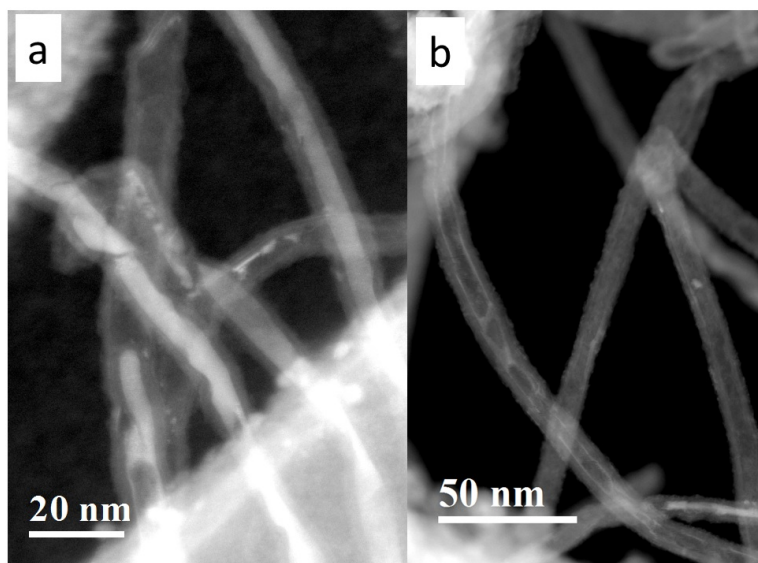


FIG. 2. The HAADF-STEM characterization of the composite  $\text{BiCl}_3$ @MWCNT, unveiling both a rod-like(a) and a tube-like (b) encapsulation of  $\text{BiCl}_3$  into MWCNTs

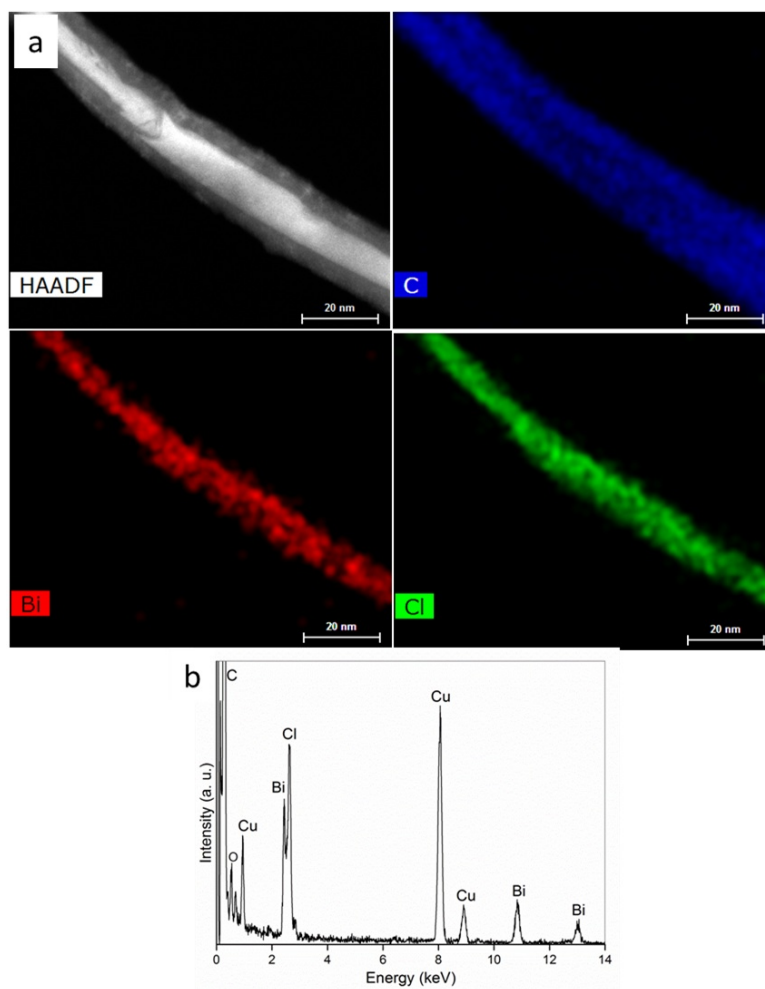


FIG. 3. Individual  $\text{BiCl}_3$ @MWCNT hybrid with a rod-like encapsulation of  $\text{BiCl}_3$ : a) HAADF-STEM image and EDX mappings of C, Bi and Cl elements; b) EDX spectrum corresponding to the panel (a)

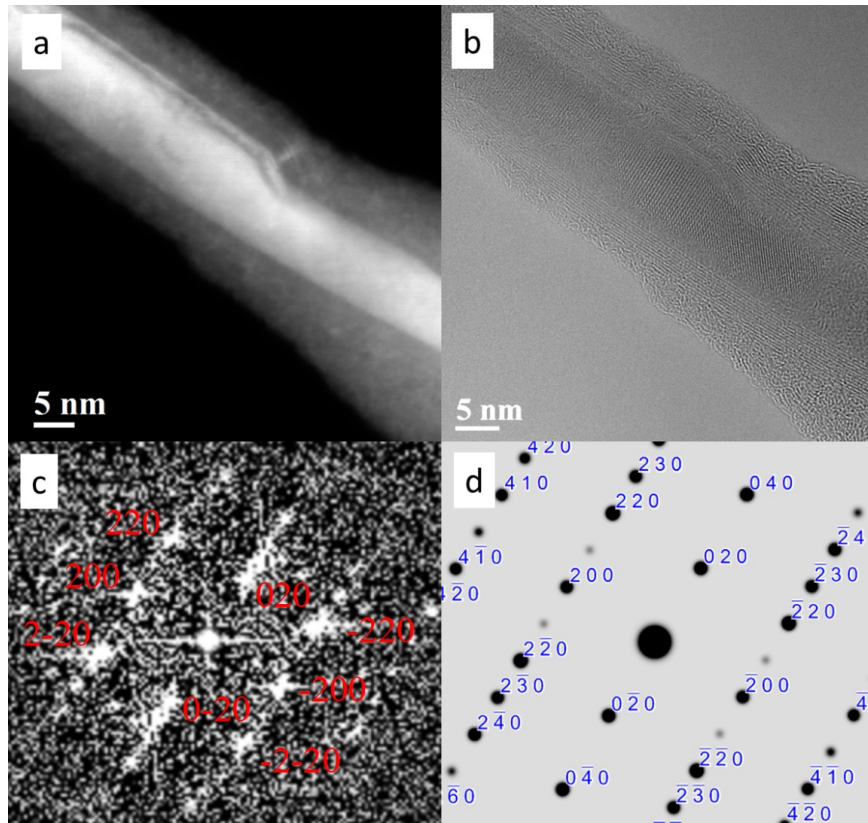


FIG. 4. Structural analysis of a BiCl<sub>3</sub> nanorod encapsulated within the MWCNT: a) HAADF-STEM image and b) AC-TEM image of a BiCl<sub>3</sub> crystal inside MWCNT; c) is the corresponding FFT which shows that the crystal orientation is [001]; d) the simulated diffraction pattern of the [001] zone axis of orthorhombic BiCl<sub>3</sub>, which matches with the FFT pattern in the panel (c)

### 3.2. Validation of force-field for liquid BiCl<sub>3</sub>

Notwithstanding a high surface tension of molten BiCl<sub>3</sub>, our TEM characterization testifies clearly that, the capillary activity of MWCNTs is sufficient enough to employ the capillary filling technique for fabrication of BiCl<sub>3</sub>@MWCNT hybrids. Yet, the filling process by such a tensed liquid might have some peculiarities at the nanoscopic level, which cannot be established experimentally. To gain insights into the mechanism of this process at the atomistic level, the force-field model was evaluated and approved for liquid BiCl<sub>3</sub>.

Both X-ray and neutron diffractions on the solid crystal unveil an anisotropy in Bi-Cl bond lengths, suggesting an aggregation of molecular-like BiCl<sub>3</sub> units [24], where a Bi atom is strongly bonded to three Cl atoms and less strongly to five more. Neutron diffraction on the melt of BiCl<sub>3</sub> [18] and electron diffraction on the vapor of BiCl<sub>3</sub> [29] indicate a Bi ion coordination of  $\sim 3$ , confirming that the BiCl<sub>3</sub> molecules are the building blocks for the solid BiCl<sub>3</sub>. Though, as a molecular liquid among trichlorides, this compound demonstrates anomalously high values of electrical conductivity and surface tension [18].

To strengthen the credibility of our empirical force-field and to testify the dominantly molecular organization of molten BiCl<sub>3</sub> (Fig. 5a,b), such quantitative proofs as the self-diffusion coefficients  $D$  for Bi and Cl atoms and the corresponding molar conductivity  $\Lambda_m$  have been received by analysis of obtained MD trajectories using Nernst-Einstein's equation:

$$\Lambda_m = \frac{F^2}{R_G T} (v_+ D_+ z_+^2 + v_- D_- z_-^2), \quad D = \lim_{t \rightarrow \infty} \frac{\langle |\vec{r}_i(t) - \vec{r}_i(0)|^2 \rangle}{6t},$$

where  $F$  is the Faraday constant,  $R_G$  is the gas constant,  $v_+$  and  $v_-$  are the number of cations and anions per formula unit of electrolyte,  $z_+$  and  $z_-$  are the ion charges,  $t$  is the MD time and  $r$  is the radius vector of an ion.

The data on  $D(\text{Bi})$ ,  $D(\text{Cl})$  and  $\Lambda_m$  collected at different temperatures  $T$  are listed in Table 2. They are found to be in fair agreement with available experimental data and, to some extent, exceeding the accuracy of another theoretical *ab initio* based MD study, which has considered the evolution of the Bi<sub>16</sub>Cl<sub>48</sub> supercell during 220

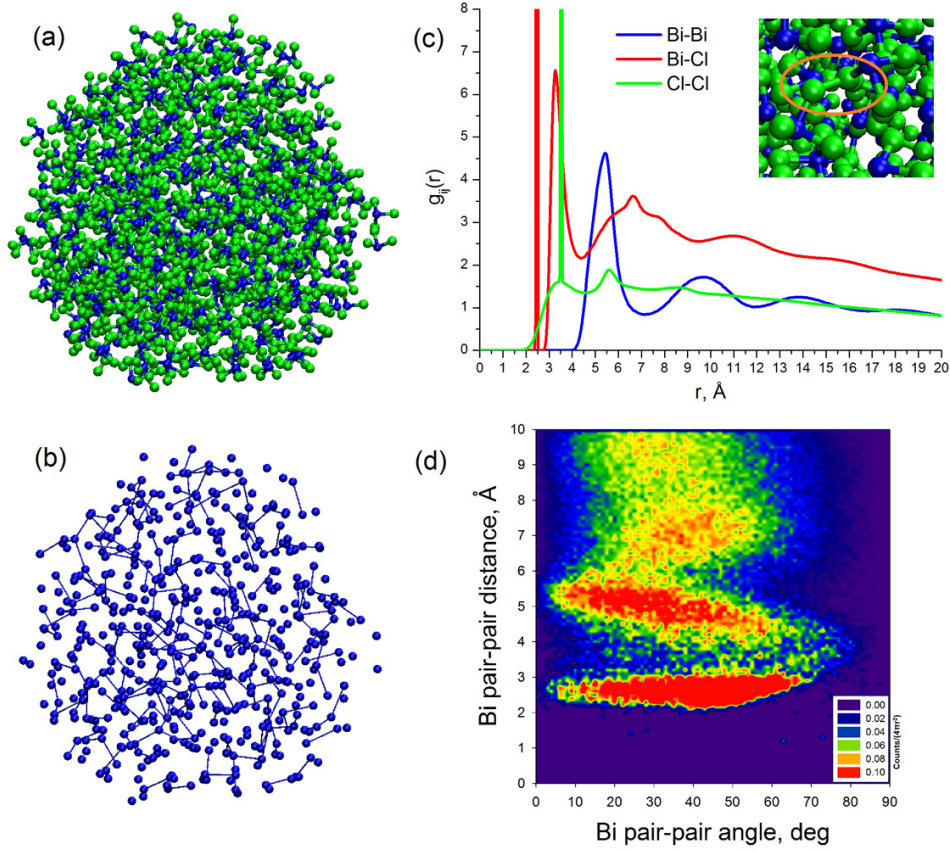


FIG. 5. Structural properties of molten  $\text{BiCl}_3$  obtained using MD annealing of a  $(\text{BiCl}_3)_{500}$  drop at  $T = 623$  K: (a) ball-and-stick rendering with Bi and Cl atoms painted in blue and green; (b) visualization of only Bi atoms within the drop; (c) radial distribution functions  $g_{ij}(r)$  for all types of atomic pairs within the drop, an ultra-short Cl-Cl pair is rendered in inset; (d) angle-resolved radial distribution function of the nearest-neighbor Bi-Bi pairs within the drop

ps [27]. Indeed, our approach might be more successful, since the much larger statistics can be collected for estimation of self-diffusion coefficients using the force-field based MD simulations. On the other hand, our model implies a tight relation between mobility of Bi and Cl atoms, since the rigidity of  $\text{BiCl}_3$  unit is assumed. Hence,  $D(\text{Bi})$  and  $D(\text{Cl})$  observed here at the same temperature share a close value, which is in contrast to the data from *ab initio* MD simulations suggesting a larger mobility of Cl atoms, comparing to that of Bi atoms [27].

TABLE 2. Self-diffusion coefficients  $D$  and molar conductivity  $\Lambda_m$  for molten  $\text{BiCl}_3$  at different temperatures obtained from our force-field MD simulations, from experimental data and from *ab initio* MD simulations after [27]

$T$ , K	our work			Exp. [27]	theor. [27]		
	$D(\text{Bi})10^{10}$ ( $\text{m}^2/\text{s}$ )	$D(\text{Cl})10^{10}$ ( $\text{m}^2/\text{s}$ )	$\Lambda_m$ ( $\Omega^{-1}\text{cm}^{-1}$ )	$\Lambda_m$ ( $\Omega^{-1}\text{cm}^{-1}$ )	$D(\text{Bi})10^{10}$ ( $\text{m}^2/\text{s}$ )	$D(\text{Cl})10^{10}$ ( $\text{m}^2/\text{s}$ )	$\Lambda_m$ ( $\Omega^{-1}\text{cm}^{-1}$ )
533	3.3	3.7	0.42	0.433	4.9	8.5	0.9
623	7.0	7.1	0.74	0.551	8.2	15.0	1.2
693	12.4	12.4	1.18	0.585	15.0	25.9	1.5
773	13.8	14.4	1.19	0.556	24.7	44.2	2.0

One should realize that, despite of all advantages, our model of the rigid  $\text{BiCl}_3$  molecules is valuable and may be employed for MD simulations at relatively low temperatures up to  $\sim 700$  K, since at elevated temperatures above  $\sim 733$  K the thermal dissociation of  $\text{BiCl}_3$  takes place, releasing possibly  $\text{BiCl}$  species in vapor and polynuclear

complex ions in liquid state [30]. Henceforth, our discussion is limited for  $T = 623$  K – a typical temperature used for the capillary filling of MWCNTs.

### 3.3. Structural organization of molten BiCl<sub>3</sub>

Expectedly, the radial distribution functions  $g_{ij}(r)$  plotted using MD trajectories demonstrate two artifacts – the narrow peaks at the distances  $r = 2.46$  Å and  $3.62$  Å corresponding to the rigid intramolecular Bi-Cl and Cl-Cl distances, respectively (Fig. 5c). Otherwise, the  $g_{ij}(r)$  profiles are characterized by several smoothed maxima. The latter are very pronounced for Bi-Bi and Bi-Cl pairs up to the distances of  $\sim 18$  Å, providing evidence for a possible ordered organization at intermediate range in the Bi part of the amorphous melt via the Bi-Cl-Bi bridging. Indeed, direct visualization of the Bi part with interatomic Bi-Bi distances up to  $5.5$  Å (first maximum of  $g_{BiBi}(r)$ ) unveils a confused network (Fig. 5b), consisting of dimer-, triplet-like clusters, zigzag or branched chains. The clustering degree within the melt can be viewed quantitatively, analyzing mutual orientation between all two nearest Bi-Bi neighbors – the pairs – using the map of their angle-resolved radial distribution function (Fig. 5d). In the absence of any positional correlation between the couple of such Bi-Bi pairs at short distances or in the case of total disorder the distribution function is equal to zero. However, the map for molten BiCl<sub>3</sub> demonstrates the distinct preferences in orientation of the Bi-Bi pairs, extending even beyond  $7$  Å. A wide angular distribution  $\sim 15 - 65^\circ$  in orientation of the Bi-Bi pairs agrees with the previously visualized stochastic chain-like organization of the Bi part.

Thus, our study uncovers unexpectedly a structural organization of the BiCl<sub>3</sub> molecules at intermediate range order. This phenomenon relates the molecular melt of BiCl<sub>3</sub> to the melts of clearly expressed ionic nature. Noteworthy, the map of angle-resolved radial distribution function for Bi-Bi pairs in BiCl<sub>3</sub> is reminiscent of the relative maps for Pb<sup>2+</sup>-Pb<sup>2+</sup> cationic pairs in molten PbI<sub>2</sub>, assembling the V-shaped triplets, and Gd<sup>3+</sup>-Gd<sup>3+</sup> cationic pairs in molten GdCl<sub>3</sub>, assembling an amorphous 3D network [31]. Therefore, the internal structure of BiCl<sub>3</sub> may impose a significant kinetic obstacle for capillary activity of a nanotube like it was observed during imbibition of molten PbI<sub>2</sub> by carbon and BN nanotubes [32] or molten GdCl<sub>3</sub> by WS<sub>2</sub> nanotubes [33].

Meanwhile, the  $g_{ij}(r)$  profile for Cl-Cl pair demonstrates another interesting peculiarity as a shoulder from  $\sim 2$  Å to  $3.62$  Å (Fig. 5c and inset). This means that a part of Cl atoms can be found closer to each other than the intramolecular Cl-Cl distance in BiCl<sub>3</sub> molecule, and almost approaching the bond length  $2.00$  Å in molecular chlorine. Therefore, our simple force-field model points to a structural predisposition of molten BiCl<sub>3</sub> for partial dissociation with gassing of Cl<sub>2</sub> at higher temperatures [30].

### 3.4. Imbibition of molten BiCl<sub>3</sub> by MWCNT

MD simulations of imbibition of molten BiCl<sub>3</sub> by DWCNT confirm a slow dynamics of capillary filling, obstructed by two factors: poor wettability of carbon surface and internal organization of the melt (Fig. 6). The melt penetration proceeds very slowly during the first MD period until  $\sim 2500$  ps. At the initial stage of imbibition, the convex meniscus is formed, which is preserved during all MD simulation. Molecules of BiCl<sub>3</sub> exclusively enter the cavity and none are adsorbed at the external surface of nanotube. During this period, only a half of the drop is imbibed (Fig. 7a). In contrast, the second MD period is very rapid, and the other half of the drop is imbibed during  $\sim 300$  ps. It starts, when the diameter of outer segment of the drop becomes comparable to the diameter of the absorbed part, i.e. becomes slightly smaller, than the inner diameter of nanotube. At this stage the exponential acceleration of imbibition can be observed, which is not essentially constrained by the friction due to the high smoothness of the graphene-like surface. Such slippage causes a rapid cruise of the drop. Obviously, it would continue far away from the entrance point along the channel of a semi-infinite nanotube. Yet, in our model the drop slows down, reaching the opposite open end of nanotube, and then returns to the entrance point. Here, its cruise is oscillating in a dampened manner. Noteworthy, the once entered drop does not leave the cavity of nanotube anymore.

Analyzing the kinetics of imbibition, the invalidity of the Lucas and Washburn theory for a capillary flow is registered (Fig. 7a). The classical theory establishes the dependence of penetrated atoms  $\langle N \rangle$  on the time of capillary action  $t$  as  $\langle N \rangle \sim \sqrt{t}$  for the case of a non-compressible Newtonian liquid, while for molten BiCl<sub>3</sub> the relation between  $\langle N \rangle$  and  $t$  is nearly linear. Such dependence is observed for the liquids with a specific internal structure [31], which coincides with our discussion on the structure of molten BiCl<sub>3</sub>.

The penetration kinetics can be also traced numerically using the axial (along nanotube) velocity of the drop (Fig. 7b). The variation in axial velocity of the drop's barycenter during the MD simulation amply illustrates two basic stages distinguished above: more or less slack invasion of the melt at a near-zero in average velocity and, finally, exponential growth of velocity to  $\sim 70$  m/s.

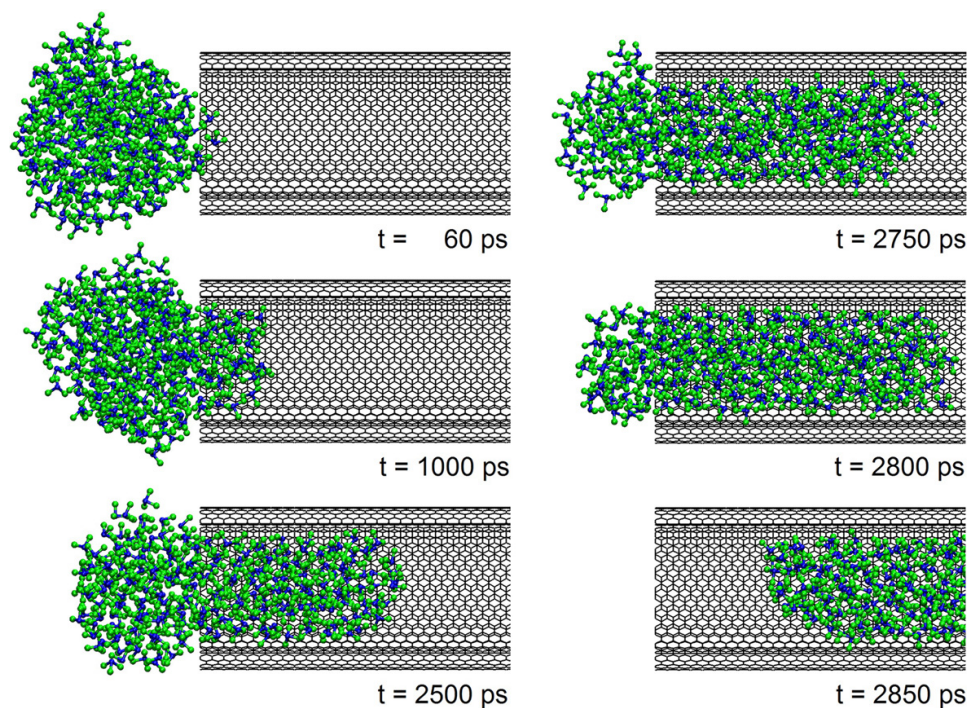


FIG. 6. Snapshots of MD simulation at  $T = 623$  K for imbibition of the  $(\text{BiCl}_3)_{250}$  drop into a  $(20,20)@(25,25)$  DWCNT. Bi and Cl atoms are painted in blue and green, while the network of C–C bonds is in black. Frontal part of the nanotube wall is removed for clearness. Full MD movie is accessible via link <https://youtu.be/CLMNa9gBMmg> or on request to the authors

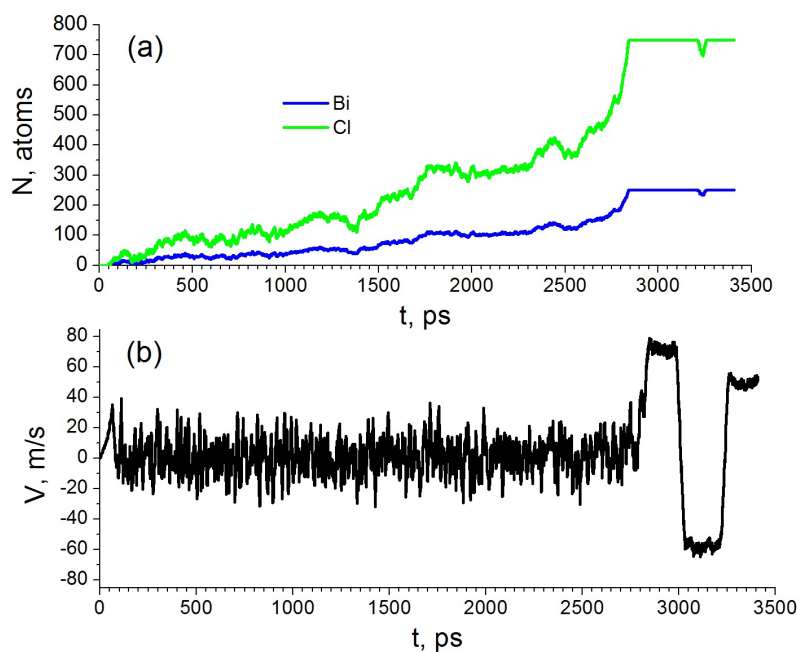


FIG. 7. Kinetics for imbibition of the  $(\text{BiCl}_3)_{250}$  drop into a  $(20,20)@(25,25)$  DWCNT at  $T = 623$  K: the number of atoms  $N$  penetrated into the cavity (a) and the velocity of the drop barycenter  $V$  (b) as functions of time  $t$

Obviously, the long time required for penetration of a  $\text{BiCl}_3$  drop into the narrow cavity of a DWCNT can be explained by a reorganization of internal structure of the melt. The comparison of the  $g_{ij}(r)$  profiles for the melt within a nanotube and for the melt as free drop does not establish their essential difference. The structure of molten  $\text{BiCl}_3$  preserves an amorphous character and is not affected by the nanotube wall. However, the mapping of angle-resolved radial distribution function unveils that, a Bi network within such  $\text{BiCl}_3$  becomes more disorganized: a correlation between the Bi pairs disappears at distances more, than 7 Å, and is suppressed essentially at distance of 5 Å (Fig. 8a). Therefore, the structural reorganization of the melt is manifested through the progressive destruction of its chain-like Bi network during imbibition. Indeed, the size of a coiled or branched chain within the melt confined in a nanotube cavity is limited in one dimension by the inner diameter of the nanotube. The one-dimensional character of a nanotube imposes constraint on conformational variety for the labile chain-like structures of the melt, restricting their conformations allowed for imbibition to the mostly one-dimensional ones. Together with the destruction of chain-like Bi network in the drop outside of nanotube some time is required for the alignment of new chain-like Bi network in the drop inside the nanotube.

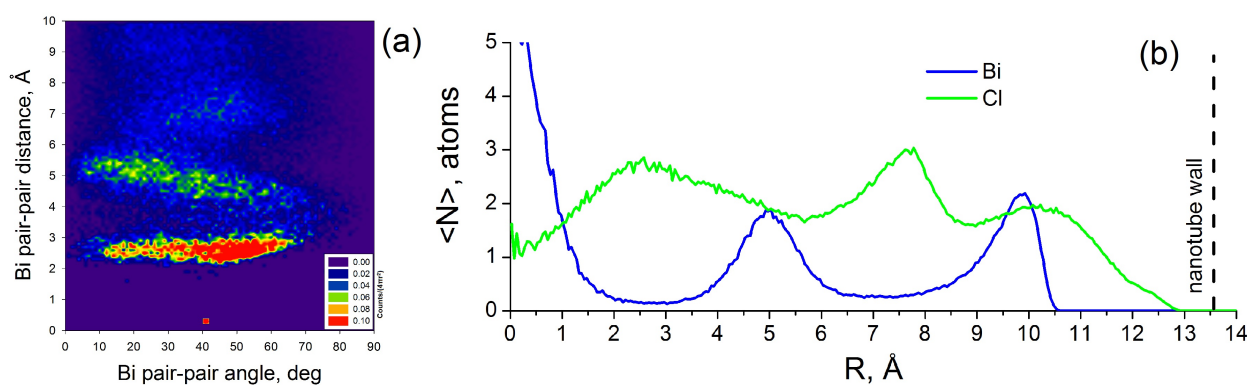


FIG. 8. Structural properties of the drop  $(\text{BiCl}_3)_{250}$  embedded fully in the cavity of a  $(20,20)@(25,25)$  DWCNT after MD simulation at  $T = 623$  K: (a) angle-resolved radial distribution function of the nearest-neighbor Bi–Bi pairs within the drop; (b) distribution of atoms along the radial direction of nanotube ( $R$  – the distance from the tube axis)

A view on the cross-section of final structure of the fully injected  $\text{BiCl}_3$  melt along the DWCNT axis uncovers also a shell-like statistical distribution of the Bi and Cl atoms along radial direction (Fig. 8b). A clear alternation of the shells can be seen. At least in our model case, the core of the melt would mostly consist of Bi atoms, while the external part of the melt would consist of Cl atoms. A similar shell-like particles' distribution within a nanotube is typical also for other liquids assembled of either ions or non-polar molecules [31, 32, 34].

#### 4. Summary

In summary, a facile capillary filling technique was tested for the fabrication of hybrid nanostructures  $\text{BiCl}_3@MWCNT$  – multi-walled carbon nanotubes filled with  $\text{BiCl}_3$ . Notwithstanding a relatively high surface tension of molten  $\text{BiCl}_3$ , the filling proceeds successfully at an elevated temperature of  $350^\circ\text{C}$  ( $\sim 115^\circ\text{C}$  above the melting point of  $\text{BiCl}_3$ ) and irrespective of the diameter distribution of MWCNTs. The encapsulated phase possesses a rod- or a tube-like morphology and is constituted by the pure and stoichiometric phase of orthorhombic  $\text{BiCl}_3$ .

The mechanism of imbibition of  $\text{BiCl}_3$  by MWCNTs is considered at atomistic level and nanosecond time scale by means of molecular dynamics simulations, employing a force-field especially evaluated and approved for molten  $\text{BiCl}_3$ . The internal chain-like organization of molten  $\text{BiCl}_3$  is recognized at an intermediate range order due to the correlation in dynamics of Bi–Bi pairs bridged via Cl atoms. In this sense, the  $\text{BiCl}_3$  melt behaves very similar to an ionic melt with polyvalent cations, despite its molecular-like constitution. Such organization of molten  $\text{BiCl}_3$  explains possibly its high surface tension as well the violation of the Lucas–Washburn rule for capillary filling into such narrow diameter capillaries like MWCNT. The imbibition of a  $\text{BiCl}_3$  drop with the diameter larger, than the diameter of MWCNT host, requires a long induction period until diameters' equalization. Thereafter, the imbibition accelerates exponentially, finalizing in a frictionless cruise of the melt along the nanotubular channel and far away the entrance point.

The success of our study points to the opportunity of scalable production of  $\text{BiCl}_3@ \text{MWCNT}$  hybrids as functional components of some eco-friendly catalysts for organic synthesis and as materials for nanodispersed radioprotective shielding.

### Acknowledgement

E. A. A. and F. L. D. acknowledge the financial support by the N2020: Nanotechnology Based Functional Solutions (NORTE-01-0145-FEDER-000019), supported by Norte Portugal Regional Operational Program (NORTE2020), under the PORTUGAL 2020 Partnership Agreement, through the European Regional Development Fund (ERDF). A. E. recognizes the support from the Ural Branch of Russian Academy of Sciences via the multi-purpose program 18-10-3-32.

### References

- [1] Pederson M.R., Broughton J.Q. Nanocapillarity in Fullerene Tubules. *Physical Review Letters*, 1992, **69**, P. 2689–2692.
- [2] Ajayan P.M., Iijima S. Capillarity-induced filling of carbon nanotubes. *Nature*, 1993, **361**, P. 333–334.
- [3] Sloan J., Luzzi D.E., Kirkland A.I., Hutchison J.L., Green M.L. Imaging and Characterization of Molecules and One-Dimensional Crystals Formed within Carbon Nanotubes. *MRS Bulletin*, 2004, **29**, P. 265–271.
- [4] Eliseev A.A., Kharlamova M.V., Chernysheva M.V., Lukashin A.V., Tretyakov Yu.D., Kumskov A.S., Kiselev N.A. Preparation and properties of single-walled nanotubes filled with inorganic compounds. *Russian Chemical Reviews*, 2009, **78**, P. 833–854.
- [5] Gautam U.K., Costa P.M.F.J., Bando Y., Fang X., Li L., Imura M., Golberg D. Recent developments in inorganically filled carbon nanotubes: successes and challenges. *Sci. Technol. Adv. Mater.*, 2010, **11**, P. 054501.
- [6] Hong S.Y., Kreizman R., Rosentsveig R., Zak A., Sloan J., Enyashin A.N., Seifert G., Green M.L.H., Tenne R. One- and Two-Dimensional Inorganic Crystals inside Inorganic Nanotubes. *European Journal of Inorganic Chemistry*, 2010, P. 4233–4243.
- [7] Cabana L., Ballesteros B., Batista E., Magen C., Arenal R., Oro-Sole J., Rurali R., Tobias G. Synthesis of  $\text{PbI}_2$  Single-Layered Inorganic Nanotubes Encapsulated Within Carbon Nanotubes. *Advanced Materials*, 2014, **26**, P. 2016–2021.
- [8] Sandoval S., Pach E., Ballesteros B., Tobias G. Encapsulation of two-dimensional materials inside carbon nanotubes: Towards an enhanced synthesis of single-layered metal halides. *Carbon*, 2017, **123**, P. 129–134.
- [9] Fidiani E., Costa P.M.F.J., Wolter A.U.B., Maier D., Buechner B., Hampel S. Magnetically Active and Coated Gadolinium-Filled Carbon Nanotubes. *The Journal of Physical Chemistry C*, 2013, **117**, P. 16725–16733.
- [10] Anumol E.A., Enyashin A.N., Deepak F.L. Single Walled  $\text{BiI}_3$  Nanotubes Encapsulated within Carbon Nanotubes. *Scientific Reports*, 2018, **8**, P. 10133.
- [11] Sloan J., Kirkland A.I., Hutchison J.L., Green M.L.H. Integral atomic layer architectures of 1D crystals inserted into single walled carbon nanotubes. *Chemical Communications*, 2002, P. 1319–1332.
- [12] Friedrichs S., Falke U., Green M.L.H. Phase Separation of  $\text{LaI}_3$  inside Single-Walled Carbon Nanotubes. *ChemPhysChem*, 2005, **6**, P. 300–305.
- [13] Fedoseeva Y.V., Orekhov A.S., Chekhova G.N., Koroteev V.O., Kanygin M.A., Senkovskiy B.V., Chuvilin A., Pontiroli D., Ricco M., Bulusheva L.G., Okotrub A.V. Single-Walled Carbon Nanotube Reactor for Redox Transformation of Mercury Dichloride. *ACS Nano*, 2017, **11**, P. 8643–8649.
- [14] Nie C., Galibert A.-M., Soula B., Datas L., Sloan J., Flahaut E., Monthiox M. The unexpected complexity of filling double-wall carbon nanotubes with nickel (and iodine) 1D nanocrystals. *IEEE Transactions on Nanotechnology*, 2017, **16**, P. 759–766.
- [15] Batra N., Anumol E.A., Smajic J., Enyashin A.N., Deepak F.L., Costa P.M.F.J. Morphological Phase Diagram of a Metal Halide Encapsulated in Carbon Nanotubes. *The Journal of Physical Chemistry C*, 2018 (submitted).
- [16] Hong S.Y., Tobias G., Al-Jamal K.T., Ballesteros B., Ali-Boucetta H., Lozano-Perez S., Nellist P.D., Sim R.B., Finucane C., Mather S.J., Green M.L.H., Kostarelos K., Davis B.G. Filled and glycosylated carbon nanotubes for *in vivo* radioemitter localization and imaging. *Nature Materials*, 2010, **9**, P. 485–490.
- [17] Spinato C., de Garibay A.P.R., Kierkowicz M., Pach E., Martincic M., Klippstein R., Bourgoignon M., Wang J.T.-W., Menard-Moyon C., Al-Jamal K.T., Ballesteros B., Tobias G., Bianco A. Design of antibody-functionalized carbon nanotubes filled with radioactivable metals towards a targeted anticancer therapy. *Nanoscale*, 2016, **8**, P. 12626–12638.
- [18] Adya A.K., Takagi R., Gaune-Escard M. Unravelling the Internal Complexities of Molten Salts. *Zeitschrift für Naturforschung A*, 1998, **53**, P. 1037–1048.
- [19] Ravi K., Krishnakumar B., Swaminathan M.  $\text{BiCl}_3$ -loaded montmorillonite K10: a new solid acid catalyst for solvent-free synthesis of bis(indolyl)methanes. *Research on Chemical Intermediates*, 2015, **41**, P. 5353–5364.
- [20] Patil V.D., Sutar N.R., Patil K.P., Giddh P.  $\text{BiCl}_3$  - an eco-friendly catalyst for an efficient synthesis of benzoxazoles at room temperature. *Chemistry of Heterocyclic Compounds*, 2015, **51**, P. 1019–1022.
- [21] Diemer R., Dittes U., Nuber B., Seifried V., Opferkuch W., Keppler B.K. Synthesis, Characterization and Molecular Structures of some Bismuth(III) Complexes with Thiosemicarbazones and Dithiocarbazonic Acid Methylene Derivatives with Activity against *Helicobacter Pylori*. *Metal-Based Drugs*, 1995, **2**, P. 271–292.
- [22] Marcus Y. *Ionic Liquid Properties: From Molten Salts to RTILs*. Springer International Publishing, 2016, 244 p. ISBN 978-3-319-30313-0
- [23] Friedman R.M., Corbett J.D. On the Synthesis and Crystal Structure of Dodecabismuth Tetrachloride,  $\text{Bi}_{12}\text{Cl}_{14}$ . *Inorganica Chimica Acta*, 1973, **7**, P. 525–527.
- [24] Bartl H. Meßzeitersparnis durch Profilauswertung bei der Registrierung von Neutroneneinkristallreflexen. Die Kristallstruktur von Wismuttrichlorid,  $\text{BiCl}_3$ . *Fresenius' Zeitschrift für analytische Chemie*, 1982, **312**, P. 17–18.
- [25] Rappé A.K., Casewit C.J., Colwell K., Goddard III W., Skiff W., UFF, a Full Periodic Table Force Field for Molecular Mechanics and Molecular Dynamics Simulations. *Journal of American Chemical Society*, 1992, **114**, P. 10024–10035.

- [26] Imperatori P., Ferro D., Piacente V. Sublimation study of  $\text{BiCl}_3$  and of  $\text{BiBr}_3$ . *The Journal of Chemical Thermodynamics*, 1982, **14**, P. 461–472.
- [27] Clay A.T., Kuntz C.M., Johnson K.E., East A.L.L. The origin of the conductivity maximum in molten salts. I. Bismuth chloride. *Journal of Chemical Physics*, 2012, **136**, P. 124504.
- [28] Humphrey W., Dalke A., Schulten K. VMD: Visual molecular dynamics. *Journal of Molecular Graphics*, 1996, **14**, P. 33–38.
- [29] Töke O., Hargittai M. Molecular Structure of Bismuth Trichloride from Combined Electron Diffraction and Vibrational Spectroscopic Study. *Structural Chemistry*, 1995, **6**, P. 127–130.
- [30] Denchik E., Nyburg S.C., Ozin G.A., Szymanski J.T. Raman Spectra of Gaseous, Liquid, and Solid Bismuth Trichloride: Resonance Fluorescence Spectra of gaseous  $\text{BiCl}$  and  $\text{BiBr}$ . *Journal of the Chemical Society A*, 1971, **0**, P. 3157–3159.
- [31] Deepak F.L., Enyashin A.N. Capillary Imbibition of Gadolinium Halides into  $\text{WS}_2$  Nanotubes: a Molecular Dynamics View. *Israel Journal of Chemistry*, 2017, **57**, P. 501–508.
- [32] Enyashin A.N., Kreizman R., Seifert G. Capillary Imbibition of  $\text{PbI}_2$  Melt by Inorganic and Carbon Nanotubes. *The Journal of Physical Chemistry C*, 2009, **113**, P. 13664–13669.
- [33] Anumol E.A., Enyashin A.N., Batra N.M., Costa P.M.F.J., Deepak F.L. Structural and chemical analysis of gadolinium halides within  $\text{WS}_2$  nanotubes. *Nanoscale*, 2016, **8**, P. 12170.
- [34] Goldbart O., Cohen S.R., Kaplan-Ashiri I., Glazyrina P., Daniel Wagner H., Enyashin A., Tenne R. Diameter-dependent wetting of tungsten disulfide nanotubes. *Proceedings of the National Academy of Sciences*, 2016, **113**, P. 13624–13629.

## Laboratory facility for working with supercritical fluids

A. I. Izotov, G. V. Kilman, R. V. Shalaev, A. M. Prudnikov

Donetsk Institute for Physics and Engineering named after A. A. Galkin,

R. Luxembourg str. 72, 83114, Donetsk, Ukraine

sharos@donfti.ru

DOI 10.17586/2220-8054-2018-9-4-532-536

An apparatus for working with supercritical fluids has been developed, and results have been obtained on purification of the diamond blend by supercritical isopropanol, as well as by selective etching of  $CN_x$  films. It is shown that the proposed method for purifying diamond blend in supercritical isopropanol is not only effective, but also quite simple to use.

**Keywords:** supercritical fluids, diamond blend, carbon nitride.

*Received:* 14 December 2017

*Revised:* 24 December 2017

### 1. Introduction

Supercritical fluid (SCF) is a form of the aggregate state into which many organic and inorganic substances are able to pass when a certain temperature and pressure are reached. The SCF is a phase that exists somewhere between gas and liquid. It can compress like a gas and, at the same time, is capable of dissolving solids, which is not peculiar to gases. In this case, the dissolution capacity of SCF is very sensitive to changes in temperature and pressure, which makes the process completely controllable [1]. A combination of low viscosity and high diffusion coefficient with negligible interfacial tension allows supercritical fluids to penetrate relatively easily into porous media [2]. Not surprisingly, these interesting properties have attracted the attention of a wide range of researchers.

However, supercritical fluids began to be widely used only in the late 1980s, when the general level of industrial development made it possible to make installations for obtaining SCF relatively affordable. Then the intensive development of supercritical technologies began.

The pharmaceutical industry was one of the first to apply the new technology, because SCF allows the most complete extraction of biologically active substances from plant raw materials, keeping their composition unchanged [1,2]. In perfumery and cosmetics, SCF is used to extract essential oils, vitamins, phytoncides from plant and animal products. At the same time, there are no traces of solvent in the extracted substances, and the soft extraction method allows preservation of their biological activity [1]. In the food industry, the new technology makes it possible to extract delicately various flavoring and aromatic components from vegetable raw materials [2]. Radiochemistry uses SCF to solve environmental problems [1]. The previously mentioned property of fluids – to change the dissolving power with increasing pressure – is widely used in polymer chemistry.

Given all of the above, and the fact that SCF-technologies are often cheaper to use than traditional ones, it is not difficult to understand why interest in supercritical fluids has increased over the last few decades. Substances in the supercritical state find new applications, and plants for their production are constantly being improved.

In this paper, we describe the construction and operation principle of a laboratory apparatus for working with SCF that we developed. This apparatus is designed to carry out experiments with relatively small volumes of working substance and is characterized by sufficient accuracy, reliability and safety. Some experimental results for the purification of a diamond blend and processing of thin carbon films, obtained with the help of this device are also presented in the work.

### 2. Description of the installation and experimental procedure

The scheme of the developed apparatus is shown in Fig. 1. A similar apparatus (with some differences that will be described below) and the method of operating it are also considered in [3].

The apparatus consists of a high-pressure chamber with a heater and thermal insulation. The temperature is monitored and automatically maintained within a given range by the controller 4 (“Termotest-04/2”) having an accuracy of  $\pm 1$  °C and a range of 0 – 1000 °C. The pressure is controlled by a MTI type pressure gauge 7 with a range of 0 – 250 kgf/cm<sup>2</sup>.

Preliminary setting of the voltage on the heater is carried out by an adjustable autotransformer 6. The fine adjustment valve serves to relieve the excess pressure 10. The presence of this valve is the main difference of our

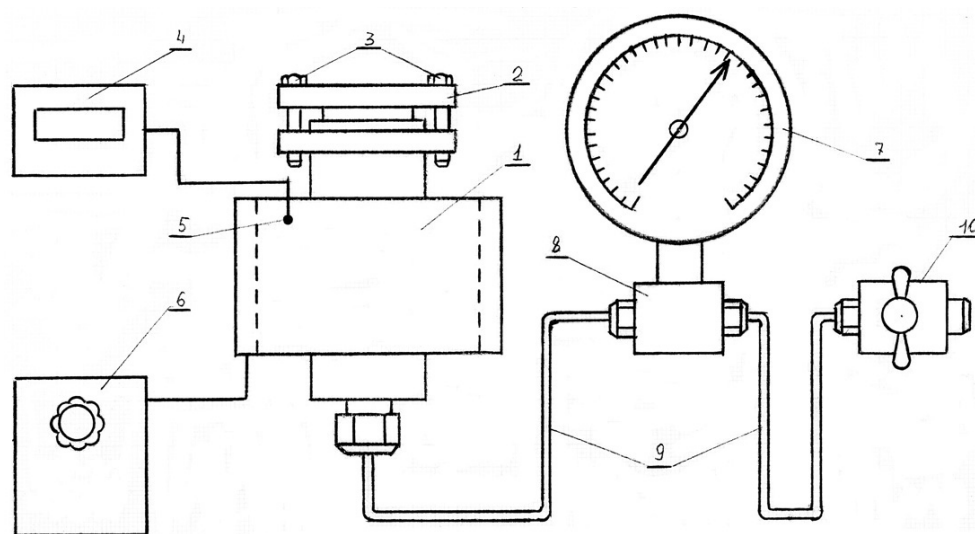


FIG. 1. Scheme of installation for working with supercritical fluids: 1 – high pressure chamber with heater and thermal insulation; 2 – the camera cover; 3 – cover fixing bolts; 4 – temperature controller; 5 – thermocouple; 6 – adjustable autotransformer; 7 – manometer; 8 – T-piece; 9 – high pressure tubes; 10 – fine adjustment valve

apparatus from that described in [3]. It permits more accurate entry into the operating mode, without interrupting the experiment, and maintain the desired pressure value for the entire specified time period.

The high-pressure chamber is shown in detail in Fig. 2.

Chamber 1 is made of heat-resistant stainless steel. On top of the camera is a heater 2 with thermal insulation. A supporting beaker 3 is inserted into the chamber, also made of heat-resistant stainless steel, with a glass tube 4 in which the sample being processed in the experiment. The beaker is designed to preserve the sample in the event of a breakdown of the tube during heating.

The chamber is hermetically sealed with a cover 5. The hermetic integrity of the cover and the outlet tube is provided by copper gaskets 6 and 7.

The method of operating the apparatus is quite simple. The experiment is carried out as follows. A sample to be processed is loaded into the glass tube 4. The tube and chamber 1 are filled with a working substance (we used isopropanol), the amount of which is determined experimentally, in the same way as in [3], but with a small margin, to further be able to more accurately adjust the pressure, dosing it with a fine adjustment valve 10.

Then the chamber is closed by the cover 5 and the heater is turned on. The heating speed is controlled by a step-by-step voltage supply to the heater. With constant pressure monitoring, the temperature is brought to the set value, after which it is automatically supported by the controller 4.

The specified temperature and pressure are maintained for the required period of time; then the heater is turned off and the sample is cooled. After cooling, the cover of the chamber is opened, the tube is removed, and the sample is transferred for further investigation.

The camera allows operation at temperatures up to 300 °C and pressures up to 200 kgf/cm<sup>2</sup>.

### 3. Results and discussion

The diamond blend with the characteristic nanocrystallite size of about 4 – 5 nm in a glass tube was placed in a high-pressure chamber, as described above. Samples were processed in supercritical isopropanol at the temperature of 240 °C and the pressure of 55 atm for 6 hours.

IR absorption spectra of samples obtained before and after treatment are shown in Fig. 3. The spectra demonstrate the presence of various absorption bands characteristic of the C–H, N–H, O–H bonds, etc., from which the shell of diamond nanocrystallites consists [4, 5]. It can be seen from the figure that after treatment with SCF, a noticeable decrease in the intensity of IR absorption bands of oxygen-containing bonds is observed. This indicates an effective etching of the crystallite shell during processing.

Typical Raman spectra of samples in the wave number range 1100 – 1800 cm<sup>-1</sup> are shown in Fig. 4. The spectrum consists of at least four components with maxima of approximately 1220 cm<sup>-1</sup> (TPA-transpolyacetylene chains), 1322 cm<sup>-1</sup> (diamond phase), 1500 cm<sup>-1</sup> and 1620 cm<sup>-1</sup> (sp<sup>2</sup>-hybridized carbon), which characterize the

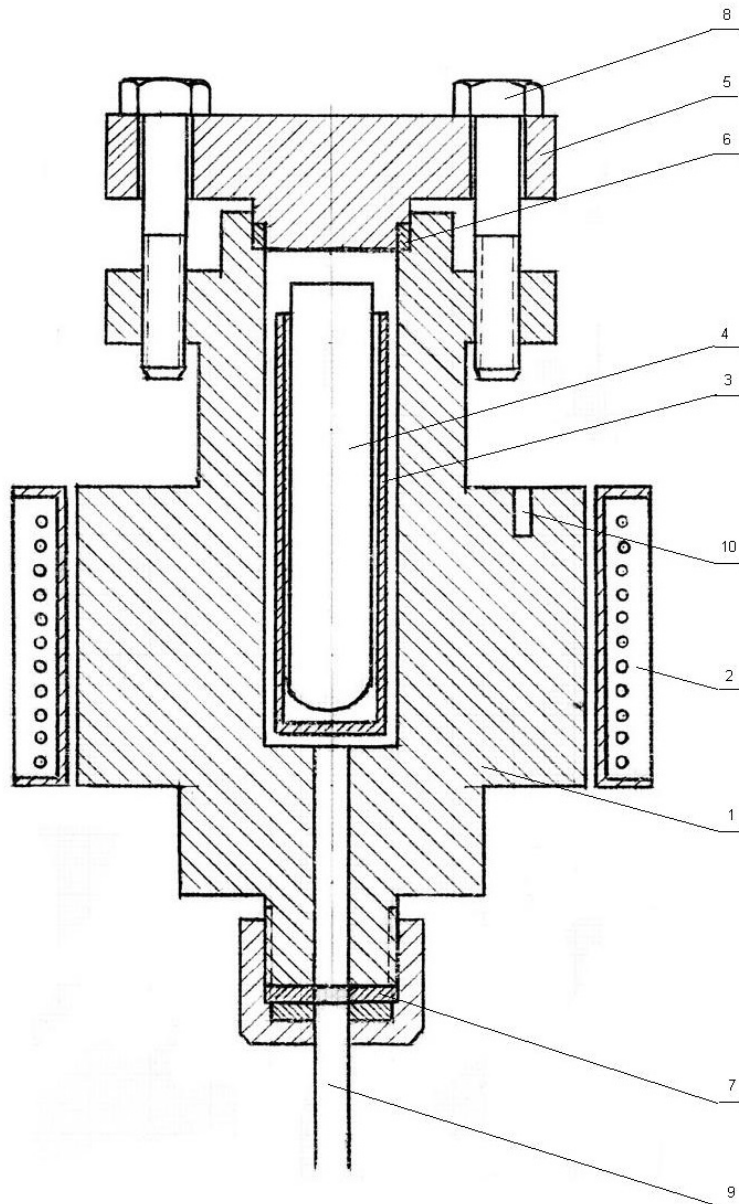


FIG. 2. High pressure chamber: 1 – housing; 2 – heater with thermal insulation; 3 – steel beaker; 4 – glass tube; 5 – cover; 6, 7 – copper gasket; 8 – cover fixing bolts; 9 – outlet tube

volume and surface of diamond crystallites [4,6]. In Fig. 4b, a noticeable increase in the half-width of the diamond line is observed after processing the sample in supercritical isopropanol. This is associated with a decrease in the size of the diamond nanocrystallites by removing the surface defect layer.

Carbon nitride films  $CN_x$  were grown by the magnetron sputtering of a graphite target in a nitrogen atmosphere on a cover glass substrate. Films with graphite-like properties were selected for the experiment. They are characterized by low hardness and weak adhesion. The obtained samples were processed in supercritical isopropanol at a temperature of 240 °C and a pressure of 55 atm for 20 min.

The transmittance spectra of the  $CN_x$  film studied before and after the treatment are shown in Fig. 5. It can be seen that as a result of the processing, the transparency of the sample as a whole increased, although in the visible region, this increase is not that large. On the spectrum of the sample after treatment, the displacement of the absorption edge toward higher energies is also well marked, which indicates an increase in the optical band gap of the investigated sample. Further calculations carried out graphically showed that the band gap width of the film actually increased by approximately 15 % (from the initial 1.7 eV to 1.95 eV).

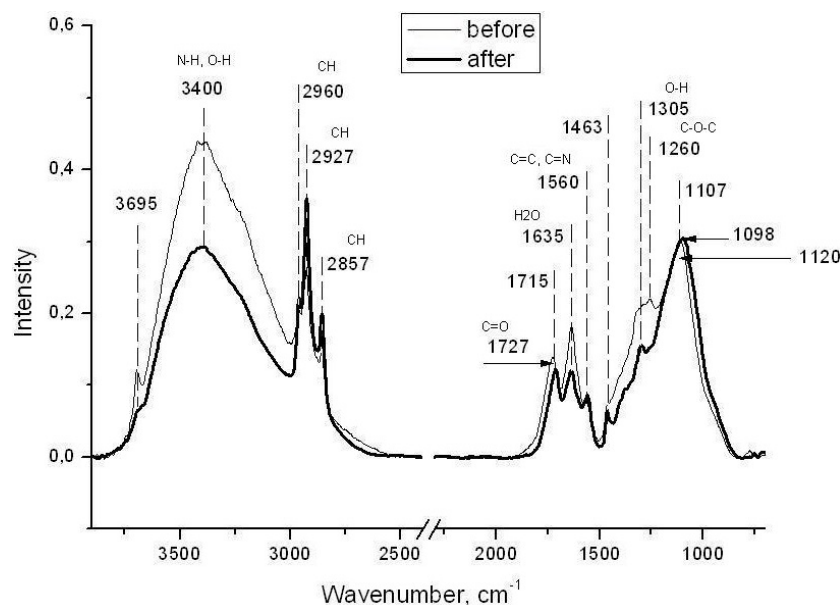


FIG. 3. Infrared absorption spectra of diamond blend before and after treatment

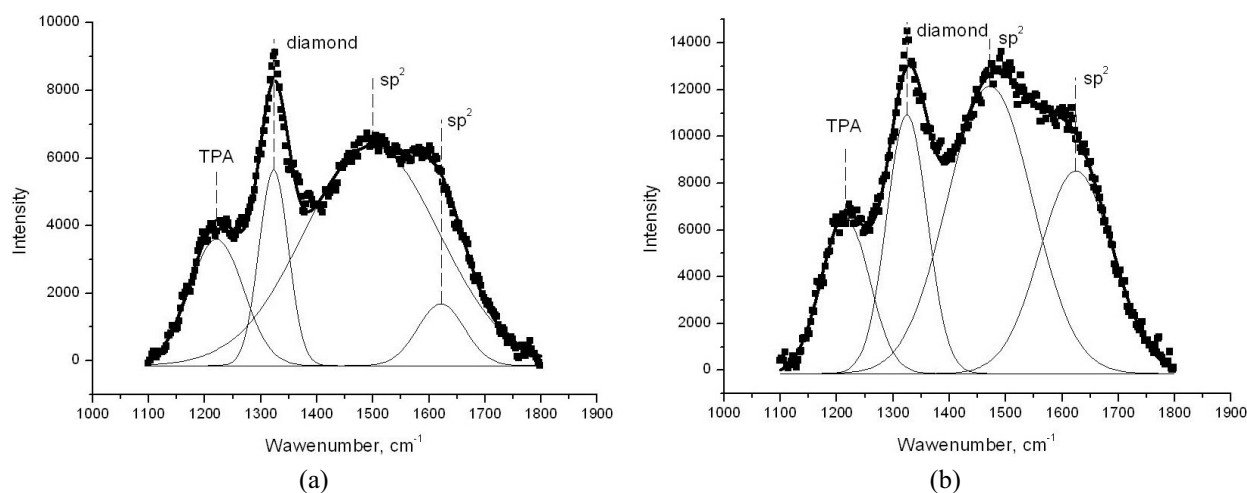


FIG. 4. Raman spectra of diamond blend before treatment (a) and after treatment (b)

It is known that this material is an inhomogeneous metastable structure consisting of two different phases [7]. This structure contains in the amorphous medium elements formed by  $sp^3$ -hybridized C and N atoms, as well as clusters of trigonal  $sp^2$ -hybridized C and N atoms. The physical properties of the resulting film coatings depend, to a considerable extent, on the amount and ratio of the above structural components. In particular, the inverse relationship between the fraction of atoms with  $sp^2$ -hybridization and the band gap width is indicated in [8]. Taking this into account, it can be assumed that an increase in the optical band gap width of carbon nitride films is the result of selective etching of functional groups in the  $sp^2$  state under the influence of supercritical isopropanol.

#### 4. Conclusions

Thus, the efficiency of the developed installation to work with SCF is shown. It is shown that, as a result of the treatment, the transparency of carbon nitride films has increased, and the band gap width has been increased, presumably as a result of selective etching of  $sp^2$ -hybridized carbon. Also, based on the results of the experiment, it can be concluded that the proposed method for purifying diamond blend in supercritical isopropanol with the help of this apparatus is not only effective but also quite simple to use. Obviously, the described method has obvious advantages in comparison with the use of aggressive hot acid media for prolonged periods [9, 10].

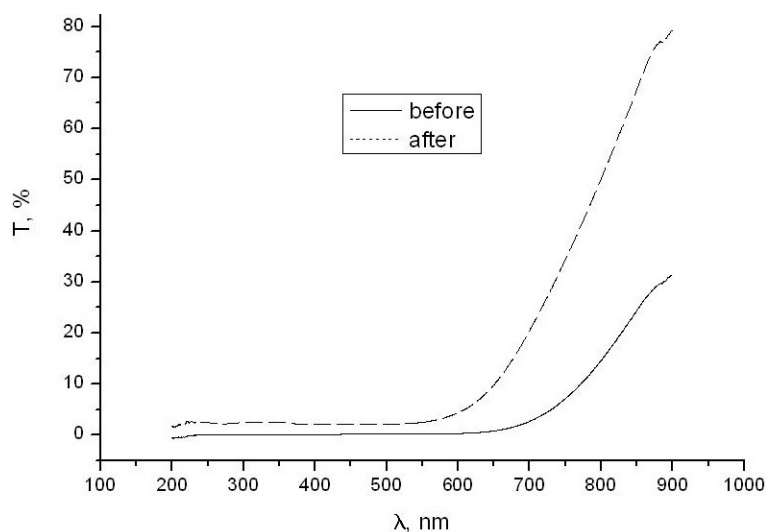


FIG. 5. The transmission spectra of the  $CN_x$  film before and after treatment

## References

- [1] Beketova A.B., Kasenova Zh.M. State of the art of progress Supercritical fluid technologies. *Bulletin of the L. N. Gumilyov Eurasian National University*, 2012, **4**, P. 249–255.
- [2] Zalepugin D.Yu., Tilkunova N., Chernyshova I.V., Polyakov V.S. Development of technologies based on supercritical fluids. *Supercritical fluids: theory and practice*, 2006, **1** (1), P. 27–51.
- [3] Buslaeva E.Yu., Gubin S.P. Supercritical isopropanol as a reducing agent for inorganic oxides. *Supercritical fluids: theory and practice*, 2009, **4** (4), P. 73–96.
- [4] Uglov V.V., Shimanski V.I., Rusalsky D.P., Samtsov M.P. Spectral analysis of the structure of ultradispersed diamonds. *Journal of Applied Spectroscopy*, 2008, **75** (4), P. 546–549.
- [5] Baidakova M.V., Kukushkina Yu.A., Sitnikova A.A., Yagovkina M.A. et al. Structure of nanodiamonds prepared by laser synthesis. *Physics of the Solid State*, 2013, **55** (8), P. 1747–1753.
- [6] Ferrari A.C., Robertson J. Origin of the  $1150\text{ cm}^{-1}$  Raman mode in nanocrystalline diamond. *Phys. Rev. B*, 2001, **63** (12), P. 121405-4.
- [7] Robertson J., O'Reilly E.P. Electronic and atomic structure of amorphous carbon. *Phys. Rev. B*, 1987, **35**, P. 2946–2957.
- [8] Kolpakov A.Ya., Sujanskaya I.V., Galkina M.E., et al. Effect of the degree of nitrogen doping and thickness on the electrical conductivity and morphology of nanoscale carbon coatings on silicon. *Russian nanotechnology*, 2011, **6** (3-4), P. 43–45.
- [9] Dolmatov V.Yu. Detonation-synthesis nanodiamonds: synthesis, structure, properties and applications. *Russ. Chem. Rev.*, 2007, **76** (4), P. 339–360.
- [10] Sushchev V.G., Dolmatov V.Yu., Marchukov V.A., and Veretennikova M.V. Principles of the chemical purification of detonation diamond-containing mixture by nitric acid. *Journal of Superhard Materials*, 2008, **5**, P. 16–25.

## Cerium oxide nanoparticles increase the cytotoxicity of TNF-alpha in vitro

O. Shydlovska<sup>1</sup>, E. Kharchenko<sup>2</sup>, N. Zholobak<sup>1</sup>, A. Shcherbakov<sup>1</sup>, A. Marynin<sup>2</sup>,  
O. Ivanova<sup>3</sup>, A. Baranchikov<sup>3</sup>, V. Ivanov<sup>3,4</sup>

<sup>1</sup>Zabolotny Institute of Microbiology and Virology NANU, Kyiv, Ukraine

<sup>2</sup>National University of Food Technologies, Kyiv, Ukraine

<sup>3</sup>Kurnakov Institute of General and Inorganic Chemistry, Moscow, Russia

<sup>4</sup>National Research Tomsk State University, Tomsk, Russia

olgashydlovska@gmail.com, yugin171094@gmail.com, n.zholobak2018@gmail.com, ceroform@gmail.com,  
andrii.marynin@ukr.net, runetta05@mail.ru, a.baranchikov@yandex.ru, van@igic.ras.ru

PACS 81.07.Bc, 81.16.Be, 87.14.ef

DOI 10.17586/2220-8054-2018-9-4-537-543

Cerium oxide nanoparticles (CeONP) were used as the modifying agent for the recombinant tumor necrosis factor- $\alpha$  and recombinant tumor necrosis factor- $\alpha$ -thymosin- $\alpha$ 1 (rhTNF and rhTNF-T). A notable increase of the biological activity of proteins with antitumor effect was demonstrated. It was established that the cytotoxicity of rTNF-T+CeONP composite increases with the duration of exposure to 7 days. Modification of rTNF-T with cerium oxide nanoparticles provides a stronger and more stable cytotoxic effect in Hep-2, L929, and A-549 tumor cell lines.

**Keywords:** cerium oxide nanoparticles, tumor necrosis factor, nano-biocomposite, biological activity, antitumor effect.

Received: 2 May 2018

Revised: 18 June 2018

### 1. Introduction

Improving the quality of medication typically relies on the use of totally new (or previously unknown) groups of biologically active substances. One such group includes different cytokines. Therapeutic attempts to use genetically-engineered cytokines in clinical practice have been performed for the last quarter of a century [1]. One of such promising therapeutic cytokines is tumor necrosis factor- $\alpha$  (TNF- $\alpha$ ).

It is well established that the biological effects of TNF depend on its concentration. At low concentrations, it acts as a para- and autocrine regulator of autoimmune reactions against injury or infection [2]. This cytokine is the major stimulator for neutrophils and endothelial cell adhesion and subsequent migration of leukocytes, fibroblasts and endothelial cell proliferation during the healing of wounds [3, 4]. Medium concentrations of TNF- $\alpha$  cause a pyrogenic effect, stimulating the formation of phagocytes, increased blood clotting, and reduced appetite. TNF- $\alpha$  is an important factor in the development of cachexia in such chronic diseases as tuberculosis and cancer [5, 6].

The use of tumor necrosis factor in the therapy of malignant tumors requires relatively high concentrations, which means that the native form of cytokine cannot be directly used. That is why there is a need to improve the biological properties, namely to increase the activity and to reduce the toxicity of TNF- $\alpha$ . Thus, further research aimed at modification and enhancement of the biological activity of TNF and other therapeutic proteins would be the basis for the elaboration of novel highly effective commercial medicines.

Recently, an interesting means of modifying therapeutic proteins was proposed, based on the use of gold or calcium carbonate nanoparticles [7, 8]. Complexes of TNF- $\alpha$  with gold nanoparticles (TNF-AuNPs) are formed by nonspecific binding. Interestingly, the formation of the TNF-AuNPs complexes protects TNF- $\alpha$  protein from adsorption by specific anti-TNF antibodies [7]. In turn, the layer-by-layer assembled TRAIL/ALG shells have been successfully coated on the surface of highly doxorubicin (DOX)-loaded calcium carbonate ( $\text{CaCO}_3$ ) nanoparticles as drug carriers. Scanning electron microscopy (SEM), transmission electron microscopy (TEM) and confocal laser scanning microscopy (CLSM) have shown that TRAIL/ALG coated DOX- $\text{CaCO}_3$  nanocomposites can be readily internalized by cancer cells [8].

In the last few years, cerium oxide nanoparticles (CeONP) have been proposed as a promising carrier for drug delivery and agent for protein modification. CeONP's have been shown to increase immunogenicity of the influenza vaccine [9]. CeONP causes enhanced interferon ( $\text{rIFN}\alpha\text{-}2\beta$ ) response in mice in comparison with the unmodified one [10]. Our preliminary *in vitro* study [11] also showed that CeONP-modified rhTNF- $\alpha$  is more active than the pristine rhTNF- $\alpha$ , that is probably due to adjuvant-mimic properties of CeONP.

Thus, the aim of our current study was to establish the possibility of modifying the tumor necrosis factor with cerium oxide nanoparticles and influence on TNF cytotoxicity of tumor cells.

## 2. Materials and methods

### 2.1. Cerium oxide nanoparticles and tumor necrosis factor

In this research, we used two different preparations of tumor necrosis factor (TNF) as model objects: Human Recombinant Tumor Necrosis Factor- $\alpha$  (rhTNF- $\alpha$ , Promega Corporation Part# 9PIG524, USA) and Recombinant Tumor Necrosis Factor- $\alpha$ -Thymosin- $\alpha$ 1 (rhTNF-T, Refnot-Pharm, LLC, series 020616, Russia).

RhTNF- $\alpha$  is a 17 kDa protein containing 157 amino acid residues; the concentration used was 3.8105 U/ml (10  $\mu$ g/ml). A rhTNF- $\alpha$  is supplied as a dried powder and contains no additives.

The rhTNF-T is a hybrid of tumor necrosis factor- $\alpha$  and thymosin- $\alpha$ 1. It consists of 185 amino acid residues, of which the last 28 at the C-terminus are the thymosin- $\alpha$ 1 sequence. The concentration of rhTNF-T was 106 U/ml (55  $\mu$ g/ml). The rhTNF- $\alpha$  is supplied as a dried powder and contains mannitol, sodium chloride, sodium phosphates (dihydrate and dodecahydrate) additives.

Cerium oxide nanoparticles (CeONP, size  $\sim$  5.8 nm,  $\zeta$ -potential  $\sim$  +12 mV) were synthesized as an aqueous 0.01 M sol [12].

### 2.2. Study of TNF+CeONP complex formation

The interaction of CeONP with TNF and the formation of the corresponding nano-biocomposite should lead to an increase in the peptide's hydrodynamic diameter (HD). HD was monitored by dynamic light scattering (DLS) method using a Zetasizer Nano ZS (Malvern, UK) analyzer. All measurements were performed at a constant temperature (25 °C) and neutral media (pH = 7.2).

### 2.3. Study of the biological activity of TNF+CeONP nano-biocomposite

The biological activity of tumor necrosis factor was analyzed on murine L929 fibrosarcoma cell line from R. E. Kavetsky Institute of Experimental Pathology, Oncology and Radiobiology, NASU, using Promega Corporation protocol [13]. L929 is commonly used to test the activity of TNF- $\alpha$  [14, 15]. The cells were cultured in 96-wells Sarstedt plates using 199 media (Sigma, USA) supplemented with 10 % fetal bovine serum (FBS, Sigma, USA), 100 units/ml gentamicin (Arterium, Ukraine) and 50 units/ml kanamycin (Arterium, Ukraine). Cells were maintained at 37 °C for 24 hours in TC-80M-2 thermostat with 5 % CO<sub>2</sub> under a humidified atmosphere.

CeONP was added to TNF (rhTNF- $\alpha$  or rhTNF-T) in the weight ratio of 1:3 respectively and the composite was analyzed for biological activity 15 minutes, 24 hours and 7 days after exposition. Samples of non-modified TNF (positive control) and TNF modified with CeONP (test sample) were titrated with two-fold step in 96-wells plates in four repetitions.

According to the standard method, in each well actinomycin-D was added in the concentration of 0.15 mg/ml.

The culture medium was removed after 24 hours of cultivating cells with samples. Cells were dyed and fixed by 0.5 % ethanol solution of crystal violet ("Sigma", USA). Dye absorbed by the cells was dissolved with 70 % ethanol solution. The same procedure was used when testing efficacy for unmodified and modified rhTNF-T.

The optical density was measured by a Thermo Labsystems Multiskan Ascent spectrophotometer at a wavelength of 540 nm. The degree of cytolysis was calculated in comparison with intact cells taken as 100 %. Activities of rhTNF- $\alpha$  and rhTNF-T (both unmodified and modified with CeONP) were analyzed using Area Under Curve (AUC) method [16], which is a simple technique for assessing the activity of biomolecules. The mathematical formula for calculating the AUC is:

$$AUC = \sum \frac{h(r_n + r_{n+1})}{2},$$

where  $r_n$  and  $r_{n+1}$  – the percentage of lysis in two nearby dilutions and  $h = 1$ , because the dilutions are the part of the continuous logarithmic series.

Also, two different cultures of tumor cells were used to test the antitumor activity of TNF+CeONP complexes: A549 (human alveolar adenocarcinoma) and Hep-2 (HeLa contaminant, human carcinoma) from the collection of Kavetsky Institute of Experimental Pathology, Oncology and Radiobiology, NASU. To determine the biological activity of TNF and TNF+CeONP complexes on cell cultures the above mentioned method was used.

## 2.4. Statistical study

All obtained data are presented as the median and interquartile range Me (LQ–UQ) of AUC, where Me = median (50 % percentiles), LQ = 25 % percentiles, and UQ = 75 % percentiles. Validity check for the null hypothesis was performed using a nonparametric Wilcoxon matched pairs test (WMP-test). The difference between groups was judged to be statistically significant at  $p < 0.05$ . Statistical calculations were conducted in a Stat Plus Pro 5.9.8. software and STATISTICA data analysis software system, version 10 (StatSoft, Inc. 2011).

## 2.5. Analysis of cell viability of L929 treated with rhTNF-T and rhTNF-T+CeONP

In this study, murine fibrosarcoma cells (L929) were cultured in 24-wells plates (TPP, Switzerland) on Sarstedt plastic coverslips (Sigma, USA) using 199 media (Sigma, USA) supplemented with 10 % fetal bovine serum, 100 units/ml gentamicin and 50 units/ml kanamycin. L929 cells were maintained at 37 °C for 24 hours in TC-80M-2 thermostat with 5 % CO<sub>2</sub> in a humidified atmosphere.

RhTNF-T and rhTNF-T+CeONP were taken in a concentration of 102 U/ml. The following experimental groups were prepared: CeONP (0.5  $\mu$ M), rhTNF-T, rhTNF-T+CeONP, actinomycin D (0.15  $\mu$ g), cells control. The incubation time after the application of the preparations was 24 hours. Following a standard procedure, actinomycin D was added to experimental groups rhTNF-T and rhTNF-T+CeONP.

Propidium iodide (PI, Sigma-Aldrich, USA) and bis-benzimide H 33342 (Hoechst, Sigma-Aldrich, Germany) dyes were used for cell viability analysis. Before dye application, the culture medium was removed from the plate wells. 850  $\mu$ l of 199 media with 2 % FBS was added to each well. 50  $\mu$ l of HOE was added to each well and cells were incubated for 30 minutes at room temperature in the dark. After that, 100  $\mu$ l of PI was added and cells were incubated at room temperature for 15 minutes in the dark. The samples were then analyzed with LOMO MICMED-2 fluorescent microscope equipped with a 480 nm dichroic filter, 450 nm long-pass filter (for Hoechst dye fluorescence measurements), 480 nm dichroic filter, 515 nm long-pass filter (for PI dye fluorescence measurements), and HBO 103 W/2 Mercury lamp (OSRAM, Germany).

## 3. Results

### 3.1. The study of TNF+CeONP complex formation

The particle size distributions of the samples are presented in Table 1. DLS data indicate that cerium oxide nanoparticles cause the increase of both rhTNF- $\alpha$  and rhTNF-T hydrodynamic diameters.

### 3.2. Study of the biological activity of TNF+CeONP preparations

The biological activity of TNF and TNF+CeONP nanocomposites were tested by the standard method on L929 cell culture. The exposure time was varied from 15 minutes to 7 days. The AUC calculation results and the percentage of increased activity are presented in Table 2.

The most effective exposition time for rhTNF- $\alpha$  was 15 minutes – biological activity increased by 23.9 % for rhTNF- $\alpha$ +CeONP in comparison with rhTNF- $\alpha$ . Validity check for the null hypothesis (evidence of the statistically significant difference between two compared groups) was performed using nonparametric Wilcoxon matched pairs test (WMP-test). Since the  $p$ -value was equal to 0.0051 upon rhTNF- $\alpha$  and rhTNF- $\alpha$ +CeONP comparison, the null hypothesis was rejected. The difference between unmodified and CeONP-modified rhTNF- $\alpha$  exposition (24 hours or 7 days) was less pronounced – 6.1 % ( $p = 0.0077$ ) and 9.2 % ( $p = 0.0051$ ) of cytotoxicity increase, respectively.

It should be noted, that for rhTNF-T the most effective exposition time was 7 days – biological activity increases by 15 % for rhTNF-T+CeONP in comparison with pristine rhTNF-T ( $p = 0.0077$ ). The increase in cytotoxicity of rhTNF-T+CeONP upon 15 min or 24 h exposition wasn't as high – 1.7 % ( $p = 0.8590$ ) and 2.8 % ( $p = 0.3743$ ), respectively. Different behavior of TNF preparations upon modification with ceria nanoparticles can be related with the differences in the structure of tumor necrosis factor molecules.

Since the most notable effect of rhTNF-T modification with CeONP was registered upon 7-day exposure, these conditions were also chosen for confirmation experiment with other cultures of tumor cells – A549 and Hep-2. Results of these studies are presented in Table 3.

Determination of biological activity of nano-biocomposites on A-549 and Hep-2-cells has confirmed the efficiency of rhTNF-T modification with ceria nanoparticles. The increase in the biological activity of rhTNF-T+CeONP composite compared to the unmodified rhTNF-T is more pronounced in A-549 cells (29.3 %) than in Hep-2 cells (12.0 %). The  $p$ -value for both cultures according to WMP-test was 0.0277, thus the null hypothesis was rejected.

TABLE 1. The study of TNF+CeONP composites formation by DLS

	Size distribution by intensity, nm (median [interquartile range])		
	Peak 1	Peak 2	Peak 3
rhTNF- $\alpha$	499.4 [441.2–572.3]	75.4 [64.4–79.9]	5352.5 [0.0–5560.0]
Area.%	66.6 [56.7–70.3]	31.4 [24.3–40.3]	2.5 [0.0–3.8]
Z-Average	508.3 [452.2–676.1]		
PdI*	0.6 [0.5–0.7]		
rhTNF- $\alpha$ +CeONP	898.3 [817.4–990.8]	0.0 [0.0–0.0]	0.0 [0.0–0.0]
Area.%	100.0 [100.0–100.0]	0.0 [0.0–0.0]	0.0 [0.0–0.0]
Z-Average	1510.0 [1356.0–1604.5]		
PdI*	0.7 [0.3–0.8]		
rhTNF-T	125.3 [112.8–142.0]	20.2 [10.1–29.1]	0.0 [0.0–0.0]
Area.%	94.9 [93.2–97.5]	5.1 [2.6–6.8]	0.0 [0.0–0.0]
Z-Average	315.1 [269.8–397.8]		
PdI*	0.4 [0.3–0.5]		
rhTNF-T+CeONP	2832.5 [2168.8–3212.5]	220.3 [165.9–536.8]	0.0 [0.0–215.9]
Area.%	91.8 [88.1–93.9]	7.0 [5.5–8.5]	0.0 [0.0–3.7]
Z-Average	2320.5 [2110.3–2506.3]		
PdI*	0.5 [0.4–0.5]		

\*PdI – Polydispersity Index

TABLE 2. Biological activity (AUC) of TNF and TNF+CeONP composites depending on the exposure time

Preparation name	Exposure time of pure TNF and TNF+CeONP composites		
	15 min	24 h	7 days
rhTNF- $\alpha$	646.7* [641.4–651.9]	1778.0* [1752.2–1815.4]	1244.2* [1238.0–1250.4]
rhTNF- $\alpha$ +CDN	800.9* [782.1–819.9]	1886.6* [1856.7–1905.7]	1358.0* [1348.7–1367.4]
Increase in activity, %	23.9 [20.1–27.8]	6.1 [2.3–8.8]	9.2 [7.9–10.5]
rhTNF-T	1479.1* [1475.6–1496.3]	1027.6* [1018.0–1087.0]	996.4* [996.1–998.7]
rhTNF-T+CeONP	1504.0* [1479.2–1504.9]	1056.7* [996.3–1097.0]	1146.3* [1135.2–1161.4]
Increase in activity, %	1.7 [0.2–2.0]	2.8 [7.7–7.9]	15.0 [13.7–16.6]

\*The table shows the values of the area under the curve (AUC) for the medians of the experimentally obtained values

TABLE 3. Cytotoxicity (AUC) of TNF and TNF+CeONP composites to A-549 and Hep-2 cell cultures

	A-549	Hep-2
rhTNF-T	290.0* [285.8–291.9]	1317.4*[1315.3–1388.0]
rhTNF-T+CeONP	375.1* [370.4–378.1]	1475.6* [1473.4–1532.1]
increase in activity, %	29.3 [26.9–32.3]	12.0 [6.2–16.5]

\*The table shows the values of the area under the curve (AUC) for the medians of the experimentally obtained values

### 3.3. Analysis of cell viability of L929 treated with rhTNF-T and rhTNF-T+CeONP

Analysis of viability of L929 cells treated with rhTNF-T and rhTNF-T+CeONP was performed using fluorescent dyes. After staining with fluorescent dyes, the cells were studied with a fluorescent microscope using relevant filters (480 nm dichroic filter, 450 nm long-pass filter for Hoechst dye fluorescence; 480 nm dichroic filter, 515 nm long-pass filter for PI dye fluorescence).

Figure 1 shows that under the action of rhTNF-T (B1) and rhTNF-T+CeONP (A1) complexes L929 cells lose their natural morphology (as compared to the control cells – E1), with those for rhTNF-T were observed the single cells, which kept natural morphology. Analysis of groups A and B and their comparison with the control (E), allows to conclude that the intensity of cells coloration with Hoechst dye in these groups is rather small, which may indicate the inhibition of active transport across cell membranes. It should be noted that the intensity of coloration in Group A is the lowest. In comparison with E3 image, A3 and B3 images demonstrate an intense staining of the cells with fluorescent PI dye, which may indicate an integrity violation of cell membranes and the development of necrosis.

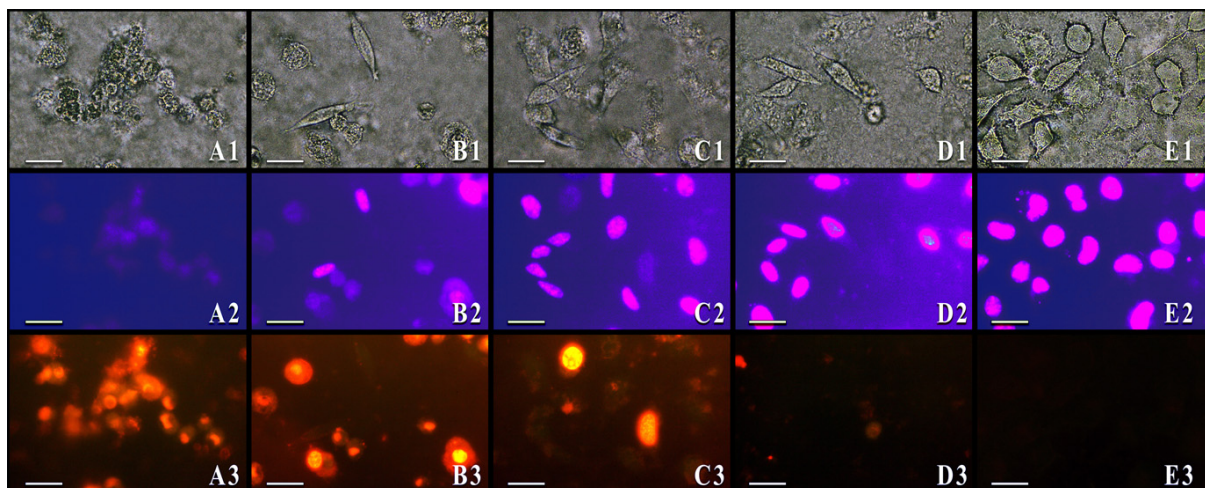


FIG. 1. Bright field (1) and fluorescent (2 – Hoechst dye, 3 – PI dye) micrographs of L929 cells treated with rhTNF-T and rhTNF-T+CeONP. L929 cells treated with rhTNF-T+CeONP – A1-A3; rhTNF-T – B1-B3; CeONP – C1-C3; actinomycin D – D1-D3; cell control – E1-E3. Scale Bar = 30  $\mu$ m

It should be mentioned that the treatment of cells with bare CeONP (Group C) results in quite intense coloration of Hoechst dye, which indicates good cell viability and active membrane transport. Nevertheless, a few cells intensely colored with PI dye were found, indicating the presence of necrotic cells in this experimental group. Cell groups treated with actinomycin D (Group D) shows virtually no PI coloration, which indicates that the experimental groups treated with antibiotic show no signs of cell death, and their intense coloration with Hoechst dye indicates cell viability.

#### 4. Discussion

Several proteins belonging to a tumor necrosis factor superfamily were investigated in this study: rhTNF- $\alpha$  (a natural form of TNF- $\alpha$ ) and rhTNF- $\alpha$  (a hybrid form of TNF and thymosin- $\alpha$ 1). Based on the results of preclinical and clinical studies of *Refnot*, a commercial drug, whose major active substance is rhTNF-T, it can be stated that rhTNF-T has up to 100 times less toxicity to normal cells in comparison with the natural form – rhTNF- $\alpha$  [17, 18].

In this study, the formation of nano-biocomposites of TNF and CeONP was revealed. It should be noted that according to previously published results hydrodynamic diameter of TNF measured by DLS is  $\sim 4.5$  nm [19]. In our experiments, the hydrodynamic diameter for pure TNF samples was in 130 – 500 nm range. This can be explained by the ability of nanoparticles and macromolecules to form large agglomerates in buffer solutions like serum or PBS [20]. Previously published results for the formation of TNF complexes with its antagonists were based on DLS data collected also using PBS solution, but the samples were filtered through 0.2  $\mu$ m syringe filter prior to the measurements that could be the reason for different results obtained by us [21].

Investigation of the dependence of the biological activity of TNF and TNF+CeONP composites on the exposure time showed that the modification of therapeutic proteins with cerium oxide nanoparticles efficiently increase the biological activity of TNF- $\alpha$  at various exposure times, with the most pronounced effect registered at 15 min exposure. The rhTNF-T+CeONP nano-biocomposite demonstrate the inverse trend in the biological activity changes: with exposure time increasing the rhTNF-T+CeONP complex activity increases. At 7-days exposure, the biological activity increased by 15 %. This result suggests that CeONP has a positive effect on the biological activity of rhTNF-T and proves that CeONP is not only a stabilizer and a substance that prevents the loss of biological activity of TNF, but it actually forms a promising therapeutic rhTNF-T+CeONP nano-biocomposite with enhanced activity. One important thing is that the natural form of rhTNF, even modified with the CeONP, eventually loses its biological activity, whereas the presence of thymosin fragment in rhTNF-T causes increased biological activity of rhTNF-T+CeONP composite and preserves it over time.

To confirm the positive effect of ceria nanoparticles on rhTNF-T protein, the study of cytotoxicity was carried out on two tumor cell cultures, A549 and Hep-2. The results obtained showed that the biological activity of the rhTNF-T+CeONP nano-biocomposite is higher by 29.3 % compared to the pristine rhTNF-T on the A-549 cell culture. An increase of 12.0 % in biological activity was noted for the Hep-2 cell culture.

The results obtained using different cell cultures allowed us to state that the rhTNF-T+CeONP composite definitely has a higher biological activity in comparison with the native form of the rhTNF-T therapeutic protein. It should be noted that the cytotoxicity of the rhTNF-T+CeONP composite depends strongly on the cell culture. This allows us to suppose that human lung carcinoma can be regarded as a good target for rhTNF-T+CeONP nano-biocomposite anticancer therapy.

Data obtained indicate that rhTNF-T preparation causes necrosis of tumor cells. When CeONP is used to modify rhTNF-T, the necrotic effect of the therapeutic protein increased.

In recent years, information about the mechanisms for the formation of nanoparticle-therapeutic protein complexes appeared in the scientific literature. It has been established that nanoparticles, entering the protein-containing medium (a solution of therapeutic cytokines), are covered with a kind of a “crown” – a layer of proteins, which are adsorbed on the surface of the particles [22]. As a result of a mutual influence of the components, the properties of the nanoparticles change under the influence of the “crown”, and the proteins that contact the particles are prone to modification. We believe that the presence of the thymosin domain in the structure of the rhTNF-T molecule is the factor facilitating the formation of such a “crown” structure, which leads to a greater biological activity of the rhTNF-T+CeONP composite in comparison with rhTNF+CeONP.

#### 5. Conclusions

In this study, we demonstrated that cerium oxide nanoparticles can be used as an effective modifying agent for therapeutic proteins such as rhTNF and rhTNF-T. The obtained rhTNF+CeONP and rhTNF-T+CeONP nano-biocomposites have a stronger cytotoxic effect to malignant tumor cells than pristine proteins. Modified rhTNF-T+CeONP demonstrated greater efficacy and stability over time compared to other samples. The enhanced cytotoxic effect of this composite was confirmed by fluorescent microscopy study of stained cells.

Our study allows consideration of nanocomposites of rhTNF+T with CeONP as a promising therapeutic agents with direct antitumor action.

## References

- [1] Goh C.R. Tumour necrosis factors in clinical practice. *Ann Acad Med Singapore*, 1990, **19** (2), P. 235–239.
- [2] Oberholzer A., Oberholzer C., Moldawer L.L. Cytokine signaling-regulation of the immune response in normal and critically ill states. *Crit Care Med.*, 2000, **28** (4), P. 3–12.
- [3] Klebanoff S.J., Vadas M.A., et al. Stimulation of neutrophils by tumor necrosis factor. *J. Immunol.*, 1986, **136** (11), P. 4220–4225.
- [4] Yan C., Grimm W.A., et al. Epithelial to mesenchymal transition in human skin wound healing is induced by tumor necrosis factor- $\alpha$  through bone morphogenic protein-2. *Am. J. Pathol.*, 2010, **176** (5), P. 2247–2258.
- [5] VanCreveld R., Karyadi E., et al. Decreased plasma leptin concentrations in tuberculosis patients are associated with wasting and inflammation. *J. Clin. Endocrinol. Metab.*, 2002, **87** (2), P. 758–763.
- [6] Gelin J., Moldawer L.L., Lönnroth C., Sherry B. Role of endogenous tumor necrosis factor- $\alpha$  and interleukin-1 for experimental tumor growth and the development of cancer cachexia. *Cancer Res.*, 1991, **51**, P. 415–421.
- [7] Tsai D.-H., Elzey S., et al. Tumor necrosis factor interaction with gold nanoparticles. *Nanoscale*, 2012, **4** (10), P. 3208.
- [8] Cui W., Cui Y., Zhao J., Li J. Fabrication of tumor necrosis factor-related apoptosis inducing ligand (TRAIL)/ALG modified CaCO<sub>3</sub> as drug carriers with the function of tumor selective recognition. *J. Mater. Chem.*, 2013, **1** (9), P. 1326–1332.
- [9] Zholobak N.M., Mironenko A.P., et al. Cerium dioxide nanoparticles increase immunogenicity of the influenza vaccine. *Antiviral research*, 2016, **127**, P. 1–9.
- [10] Shydlovska O., Zholobak N., et al. Response of interferon system to introduction of recombinant interferon modified with cerium dioxide nanoparticles. Proceedings of VIII International conference “Bioresources and viruses”, Kyiv, September 12–14, 2015, P. 51–54.
- [11] Shydlovska O., Spivak M., et al. Nanoparticles of cerium dioxide increase activity of recombinant tumor necrosis factor- $\alpha$ . Proceedings of XIV International Scientific Conference of Students, PhD Students & Young Scientists “Shevchenkivska Vesna: Biology”. Kyiv, April 23–24, 2016.
- [12] Ivanov V.K., Polezhaeva O.S., et al. Microwave-hydrothermal synthesis of stable nanocrystalline ceria sols for biomedical uses. *Russ. J. Inorg. Chem.*, 2010, **55** (1), P. 1–5.
- [13] Tumor Necrosis Factor- $\alpha$ , Human, Recombinant: Certificate of Analysis. Promega Corporation Protocol <https://www.promega.com/-/media/files/resources/protocols/product-information-sheets/g/tumor-necrosis-factor-alpha-human-recombinant-protocol.pdf?la=en>.
- [14] Wang H.J., He W.Q., et al. Type I collagen gel protects murine fibrosarcoma L929 cells from TNF $\alpha$ -induced cell death. *Biochem. Biophys. Res. Commun.*, 2015, **457** (4), P. 693–699.
- [15] Ye Y.C., Wang H.J., et al. RIP1-mediated mitochondrial dysfunction and ROS production contributed to tumor necrosis factor alpha-induced L929 cell necroptosis and autophagy. *Int. Immunopharmacol.*, 2012, **14** (4), P. 674–682.
- [16] Myerson J., Green L., Warusawitharana M. Area under the curve as a measure of discounting. *J. Exp. Anal. Behav.*, 2001, **76** (2), P. 235–243.
- [17] Shmelev V.A., Bunina Z.F., et al. Isolation of a group of hybrid proteins consisting of tumor necrosis factor alpha and thymosin alpha 1. *Mol Gen Mikrobiol Virusol*, 1995, **1**, P. 9–14.
- [18] Shmelev V.A., Grigorev B.V., Mozharova T.I., Popov S.G. Thymosin alpha-1 and hybrid proteins consisting of tumor necrosis factor-alpha and thymosin alpha-1 enhance the efficacy of vaccination against the causative agent of plague. *Zh. Mikrobiol. Epidemiol. Immunobiol.*, 1994, **4**, P. 85–89.
- [19] Tsai D.-H., Elzey S., et al. Tumor necrosis factor interaction with gold nanoparticles. *Nanoscale*, 2012, **4** (10), 3208.
- [20] Flaherty N.L., Chandrasekaran A., et al. Comparative analysis of redox and inflammatory properties of pristine nanomaterials and commonly used semiconductor manufacturing nano-abrasives. *Toxicol Lett.*, 2015, **239** (3), P. 205–215.
- [21] Kim M.S., Lee S.H., et al. Comparative Analyses of Complex Formation and Binding Sites between Human Tumor Necrosis Factor-alpha and its Three Antagonists Elucidate their Different Neutralizing Mechanisms. *J. Mol. Biol.*, 2007, **374** (5), P. 1374–1388.
- [22] Nguyen V.H., Lee B.J. Protein corona: A new approach for nanomedicine design. *Int. J. Nanomedicine*, 2017, **12**, P. 3137–3151.

## Effect of high pressures and high temperatures on the structure of nanostructured titanium monoxide

A. A. Valeeva<sup>1,2</sup>, M. G. Kostenko<sup>1</sup>, A. Pfitzner<sup>3</sup>, A. A. Rempel<sup>1,2</sup>

<sup>1</sup>Institute of Solid State Chemistry UB RAS, 91, Pervomaiskaya st., Ekaterinburg, 620990, Russia

<sup>2</sup>Ural Federal University named after the first President of Russia B. N. Eltsin,  
91, Mira st., Ekaterinburg, 620002, Russia

<sup>3</sup>Institute of Inorganic Chemistry, Regensburg University, Regensburg, Germany

anibla\_v@mail.ru

PACS 61.72.Dd, 61.72.Bb, 64.70.Nd, 71.20.Ps

DOI 10.17586/2220-8054-2018-9-4-544-548

The structure of nanostructured titanium monoxide  $\text{TiO}_{0.98}$  containing structural vacancies in two sublattices simultaneously has been modified via thermobaric annealing. Analysis of the experimental data on thermobaric synthesis of nanostructured  $\text{TiO}_{0.98}$  with cubic  $B1$  type structure at temperatures 573 – 2273 K and pressure 6 GPa revealed that a transition from the cubic  $B1$  (sp. gr.  $Fm\bar{3}m$ ) phase to the trigonal  $\text{Ti}_2\text{O}_3$  (sp. gr.  $R\bar{3}c$ ) phase takes place in the nanostructured monoxide as a result of high pressures and high temperatures. The first-principle calculations of the cohesive energy and electronic structure show that the trigonal phase with space group  $R\bar{3}c$  is energetically favorable compared to the cubic phase of the same composition  $\text{TiO}_{3/2}$  and the orthorhombic ordered  $\text{Ti}_2\text{O}_3$  (sp. gr.  $Immm$ ) phase.

**Keywords:** nanostructured titanium monoxide, structural vacancy, nonstoichiometry, high pressure, high temperature, phase transition, electronic structure.

Received: 25 May 2018

Revised: 12 July 2018

### 1. Introduction

Oxides, carbides and nitrides of transition metals of IV – V groups of the periodic table having  $B1$  type crystal structure feature wide homogeneity regions due to an anomalously high concentration of structural vacancies – crystal lattice sites which are not occupied by atoms [1,2]. Vacancies are associated not only with nonstoichiometry, but also with short- and long-range order effects allowing a great number of various phases and structural modifications of a compound to be obtained while retaining the type of its basis crystal structure [3–8]. This peculiarity is of importance in terms of the topical problem of designing materials with pre-defined properties.

Titanium monoxide is a unique compound with a wide homogeneity region ( $\text{TiO}_{0.7}$  –  $\text{TiO}_{1.3}$ ) and an anomalously high (to 30 at. %) concentration of vacancies simultaneously in the metal and nonmetal sublattices of  $B1$  structure [8–13]. The experimental works performed earlier on samples of microcrystalline titanium monoxide showed that electron irradiation [14,15] and the treatment by pressure [16–19] or heat [8–12] lead to the modification of the structure and properties by changing the concentration of the vacancies or the way of their arrangement in the structure. In the nanostate, in addition to point defects (structural vacancies), two-dimensional defects (crystal surface) should also be taken into consideration. The interference of these two types of defects extends the variety of possible structural modifications and the range of controllable properties [20–23]. In particular, while high-temperature annealing of microcrystalline titanium monoxide gives rise to the monoclinic phase  $\text{Ti}_5\text{O}_5$  [10–12], in the experiment on nanostructured samples a  $\text{Ti}_9\text{O}_{10}$  phase was observed whose structure is not typical of microcrystalline state [24]. The aim of this work is to study the behavior of the structure of nanostructured titanium monoxide under high pressure and high temperature.

### 2. Experimental

The microcrystals of titanium monoxide  $\text{TiO}_y$  with the average size of  $\sim 25 \mu\text{m}$  have been synthesized by the solid phase sintering from a mixture of titanium Ti and titanium dioxide  $\text{TiO}_2$  powders in vacuum  $10^{-3}$  Pa at 1770 K. In order to achieve a disordered state of titanium dioxide, the evacuated ( $10^{-3}$  Pa) quartz ampoules with samples were annealed for 3 h at 1330 K, whereupon they were dropped into the water, the quenching rate was  $\sim 200$  K/s. According to the XRD data, the microcrystalline powder contained reflections only of the cubic phase with  $B1$  structure (sp. gr.  $Fm\bar{3}m$ ) with a disordered arrangement of vacancies in sublattices. A multi-parameter certification of the samples was carried out with the use of chemical, spectral, pycnometer, X-ray diffraction and

X-ray structure analysis methods. The heat treatment method for obtaining the disordered and ordered states and the results of attestation of the synthesized samples are described in detail in work [12].

Nanocrystals of titanium monoxide were produced by high-energy milling in a Retsch PM 200 planetary ball mill using  $Y_2O_3$ -stabilized  $ZrO_2$  grinding media and vials. The ball-to-powder weight ratio in our experiments was 10:1. The milling liquid used was isopropanol. The high-energy milling conditions were as follows: milling time of 15, 30, 60, 120, 240, and 480 min; rotation direction reversed every 15 min; interval between direction reversals, 5 s; rotation speed of the disk supporting the grinding vials, 500 rpm [22].

The XRD studies of  $TiO_y$  were carried out with a STOE STADI P transmission diffractometer equipped with a linear PSD, a Ge-monochromator, and a Mythen 1 K detector at 293 K. The measurements were performed using  $CuK\alpha_1$  radiation, the  $2\theta$  range was  $10 - 116^\circ$  with a step-width of  $0.015^\circ$ . Polycrystalline silicon ( $a = 543.07$  pm) was used as external standard. The XRD patterns were measured both in a short run and a longer run with better statistics. Four XRD powder patterns were summed up for better statistics and were used for a full profile analysis. The error of the lattice constant determination was about 1 pm. The phase analysis of the XRD pattern was performed using the Powder Cell 2.4 program. For phase identification the powder standards database ICDD PDF2 (ICDD, USA, Release 2009) was used. There are small crystalline peaks around  $2\theta = 36.7, 41.5$  and  $54.2$  degree in the initial sample. According to phase analysis, the impurity lines on the XRD pattern are from an unidentified compound.

In addition to reducing particle size, that is, comminuting, milling produces internal lattice strain in the resulting nanoparticles. The diameter of nanocrystals  $D$  was determined from the broadening of X-ray diffraction reflections by the Williamson–Hall method [25,26]. Owing to the fragmentation of ordered titanium monoxides with near-stoichiometric compositions, we obtained nanoparticles  $20 \pm 10$  nm in size, with the lowest lattice strain at a level of 0.3 %. The fragmentation of disordered titanium monoxides with both substoichiometric and superstoichiometric compositions resulted in roughly the same particle size, about  $40 \pm 10$  nm, but the lattice strain was three times higher. Analysis of X-ray diffraction patterns showed that high-energy milling led to disordering and reduced the degree of long-range order. The techniques used to prepare nanocrystals by high-energy milling, analysis of X-ray diffraction patterns, SEM and TEM pictures, calculation of the coherent scattering region sizes were described elsewhere [22,24].

High-pressure experiments were performed on a modified high-pressure plant (Sack & Kiesselbach 1041, Germany). The nanostructured titanium monoxide powder was placed into a cylindrical boron nitride capsule; then the capsule was covered with pyrophyllite  $Al_2(OH)_2(Si_2O_5)_2$  serving as a medium for pressure transfer. After that, the upper and lower parts of the capsule were covered with graphite lids. Initially, the pressure was increased to 6 GPa over 60 sec, and then the temperature was raised, also over 60 sec. In this study, the experiments were carried out at 573, 773, 1273, 1773 and 2273 K. The pressure and temperature were held constant for 60 min, then the temperature in the cell was rapidly decreased to ambient temperature at the rate of  $\sim 200$  K/sec at approximately constant pressure, and after that, the pressure was released to atmospheric pressure during several seconds. The experiments were repeated 2-3 times under the same conditions, and according to the XRD data, the reproducibility of the results was observed.

### 3. Results and discussion

The results of X-ray diffraction experiments on samples subjected to thermobaric annealing are presented in Table 1 and Fig. 1. The microcrystalline state, according to [16–19], is characterized by large lattice period values, 418 – 421 pm. The temperature dependence of the lattice period for the nanostructured state is not monotonic: in the temperature interval from 298 to 773 K the lattice period increases from 417.6 to 417.82 pm. At 1273 K, the lattice period decreases to 417.5 pm and at 1773 K it reaches the value of 416.07 pm. At 2273 K, the lattice period increases to 417.54 pm, which is somewhat smaller than that observed at 298 K. The temperature range, over which the lattice period of the basis structure increases monotonously, corresponds to the sole initial disordered cubic phase. At temperatures above 1273 K, the system becomes two-phase. A trigonal phase  $Ti_2O_3$  (sp. gr.  $R\bar{3}c$ ) is formed, whose structure is not a  $B1$  derivative and contains no vacancies.

The first-principle calculations of the cohesion energy and electronic structure, performed by the technique described in [24] with the use of code [27], reveal that the trigonal phase with the  $R\bar{3}c$  space group is energetically advantageous compared with the disordered cubic phase of the same  $TiO_{3/2}$  composition and with the orthorhombic ordered phase  $Ti_2O_3$  (sp. gr.  $Immm$ ) [28] having a  $B1$ -derived structure. The calculated cohesive energy of the phase with  $R\bar{3}c$  space group is  $-17.76$  eV vs.  $-16.21 \pm 0.04$  eV for the disordered cubic phase and  $-17.25$  eV for the orthorhombic ordered phase with space group  $Immm$ . Fig. 2 displays the density of electronic states calculated for three alternative structures of the  $TiO_{3/2}$  composition. All of them possess metallic conduction; the largest density of states at the Fermi level was observed for the orthorhombic model [28]. The trigonal phase observed

TABLE 1. The conditions of thermobaric treatment of nanostructured titanium monoxide  $\text{TiO}_{0.98}$  and the XPD results after treatment

$T, P$	$\text{TiO}_y$ (sp. gr. $Fm\bar{3}m$ )			$\text{Ti}_2\text{O}_3$ (sp.gr. $R\bar{3}c$ )		
	Lattice period $a_{B1}$ , pm	$C_{\text{TiO}_y}$ , mass.%	Crystal size $D$ , nm	Lattice period $a_{B1}$ , pm	$C_{\text{Ti}_2\text{O}_3}$ , mass. %	Crystal size $D$ , nm
298 K	417.60	100	40	–	–	–
573 K, 6 GPa	417.63	100	42	–	–	–
773 K, 6 GPa	417.82	100	50	–	–	–
1273 K, 6 GPa	417.05	70	50	511.4, 1379.0	30	75
1773 K, 6 GPa	416.07	60	50	511.7, 1379.9	40	80
2273 K, 6 GPa	417.54	30	50	512.3, 1378.7	70	80

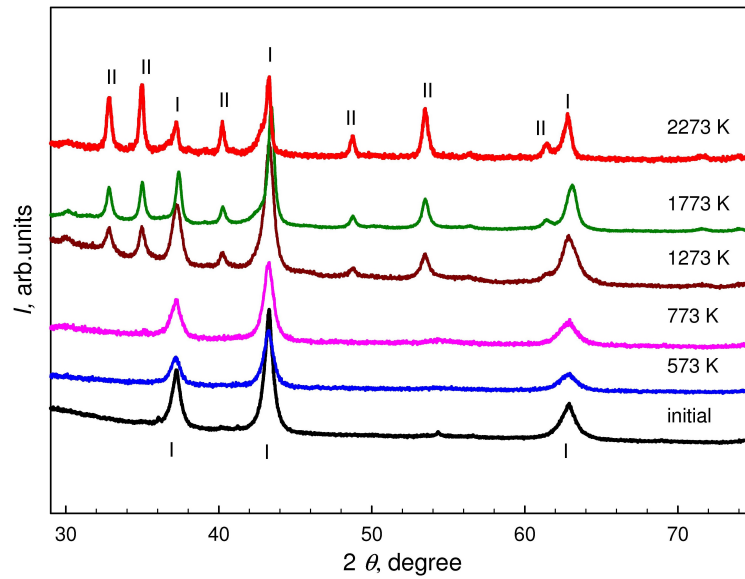


FIG. 1. The experimental X-ray diffraction patterns of  $\text{TiO}_{0.98}$  powders: initial nanostructured powder; after thermobaric treatment at 6 GPa and 573, 773, 1273, 1773, 2273 K (phases: I –  $\text{TiO}_y$  (sp. gr.  $Fm\bar{3}m$ ), II –  $\text{Ti}_2\text{O}_3$  (sp. gr.  $R\bar{3}c$ ))

in the experiment was characterized by a much wider  $p$ - $d$  gap between the valence band and the conduction band compared with the  $p$ - $d$  gap of  $B1$  derived structures.

The nonmonotonic character of the temperature dependence of the lattice period observed in the experiment is likely to be due to the isolation of the trigonal phase  $\text{Ti}_2\text{O}_3$ , whose composition ( $\text{TiO}_{3/2}$ ) differs from the composition of the initial disordered cubic phase  $\text{TiO}_{0.98}$ . In order to retain the initial ratio of components in the two-phase system, the composition of the disordered cubic phase should be shifted into the substoichiometric region. However, for the microcrystalline phase under atmospheric pressure this would mean a lattice period enhancement [29], whereas in our case the lattice period decreases. This suggests a different mechanism of variation in the composition and vacancy concentration compared with the microcrystalline state under atmospheric pressure. Note also that the nanostate features smaller lattice period values compared with the microcrystalline state, which agrees with the predictions of theoretical calculations [30].

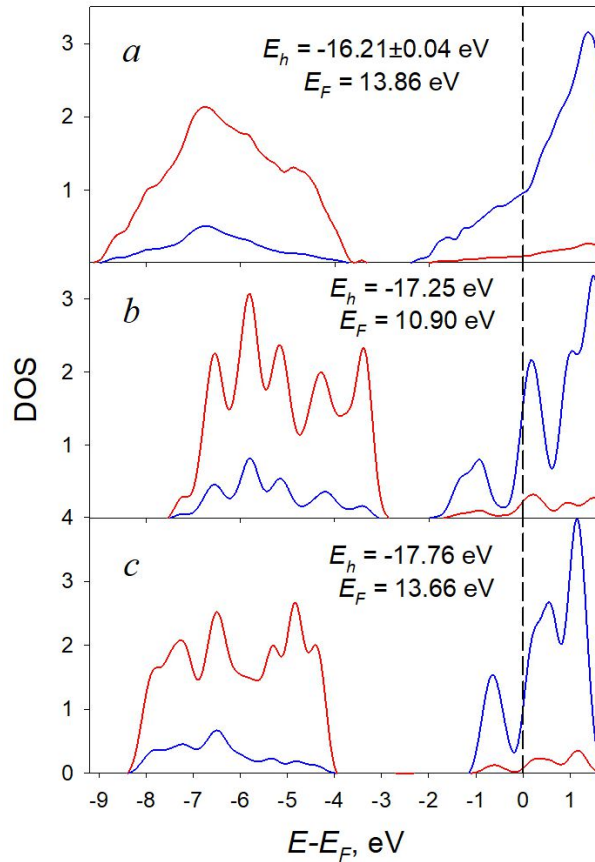


FIG. 2. The density of O 2*p* (red lines) and Ti 3*d* (blue lines) electronic states calculated for the disordered cubic phase TiO<sub>3/2</sub> (sp. gr. *Fm* $\bar{3}$ *m*), the orthorhombic ordered phase Ti<sub>2</sub>O<sub>3</sub> (sp. gr. *Immm*), as well as for the trigonal phase Ti<sub>2</sub>O<sub>3</sub> (sp. gr. *R* $\bar{3}$ *c*) observed in the experiment

#### 4. Conclusion

In the present work, the nanostructured TiO<sub>0.98</sub> powder, which contained structural vacancies in two sublattices simultaneously, was subjected to high pressures up to 60 kbar and high temperatures up to 2273 K. The X-ray powder diffraction revealed a change of the structure from cubic TiO<sub>*y*</sub> phase (sp. gr. *Fm* $\bar{3}$ *m*) to the trigonal phase Ti<sub>2</sub>O<sub>3</sub> (sp. gr. *R* $\bar{3}$ *c*) after applying the high pressure in combination with the high temperature. According to first-principle calculations, the trigonal Ti<sub>2</sub>O<sub>3</sub> (sp. gr. *R* $\bar{3}$ *c*) phase observed in the experiment is energetically favorable compared to the cubic phase of the same TiO<sub>3/2</sub> composition and the orthorhombic-ordered Ti<sub>2</sub>O<sub>3</sub> (sp. gr. *Immm*) phase and is characterized by a much wider *p*-*d* gap between the valence band and the conduction band compared with the *p*-*d* gap of structures derived from *B1* structure. The purposeful synthesis of materials based on particles of various stoichiometry, crystal size and dimension with pre-defined properties and structure gives enhanced functionality and provides comprehensive control of the settings.

#### Acknowledgements

We are grateful to Dr. M. Andratschke, F. Rau, and U. Schiessl (Institute of Inorganic Chemistry, Regensburg University) for their help during the experiments.

The work was carried out at the Institute of Solid State Chemistry UB RAS with financial support from the Russian Science Foundation (project 14-23-00025). The electronic structure calculations were performed on “Uran” supercomputer at the IMM UB RAS.

## References

- [1] Gusev A.I., Rempel A.A., Magerl A.J. *Disorder and Order in Strongly Nonstoichiometric Compounds: Transition Metal Carbides, Nitrides and Oxides*. Springer: Berlin-Heidelberg-New York, 2001.
- [2] Rempel A.A., Valeeva A.A. Thermodynamics of atomic ordering in nonstoichiometric transition metal monoxides. *Mend. Communication*, 2010, **20**, P. 101–103.
- [3] Kostenko M.G., Valeeva A.A., Rempel A.A. Relationship between short- and long-range orders in nonstoichiometric titanium monoxide  $\text{TiO}_y$ . *JETP*, 2010, **111**, P. 786–795.
- [4] Kostenko M.G., Rempel A.A., Lukoyanov A.V. Internal energy and parameters of the order–disorder phase transition in titanium monoxide  $\text{TiO}_y$ . *JETP*, 2013, **116**, P. 945–951.
- [5] Kostenko M.G., Rempel A.A. Electrostatic stabilization of an ordered phase in titanium monoxide. *Phys. Sol. St.*, 2010, **52**, P. 776–780.
- [6] Kostenko M.G., Rempel A.A. Probabilities of octahedral clusters depending on long-range order parameters and composition in nonstoichiometric titanium monoxide  $\text{TiO}_y$ . *JETP*, 2012, **115**, P. 99–107.
- [7] Kostenko M.G., Valeeva A.A., Rempel A.A. Octahedral clusters in various phases of nonstoichiometric titanium monoxide. *Mend. Communication*, 2012, **22**, P. 245–247.
- [8] Valeeva A.A., Rempel S.V., Schroettner H., Rempel A.A. Influence of the degree of order and nonstoichiometry on the microstructure and microhardness of titanium monoxide. *Inorganic materials*, 2017, **53**, P. 1174–1179.
- [9] Andersson S., Collen B., Kuylentierna U., Magneli A. Phase-analysis studies on the titanium-oxygen system. *Acta Chem. Scand.*, 1957, **11**, P. 1641–1652.
- [10] Watanabe D., Castles J.R., Jostsons A., Marlin A.S. Ordered structure of titanium oxide. *Nature*, 1966, **210**, P. 934–936.
- [11] Banus M.D., Reed T.B. Structural, electrical and magnetic properties of vacancy stabilized cubic TiO and VO, in: L. Eyring, M.O. Keefe (Eds.), *The Chemistry of Extended Defects in Non-Metallic Solids*, Amsterdam-London: North-Holland Publ., 1970, P. 488–521.
- [12] Valeeva A.A., Rempel A.A., Gusev A.I. Ordering of cubic titanium monoxide into monoclinic  $\text{Ti}_5\text{O}_5$ . *Inorganic materials*, 2001, **37**, P. 603–612.
- [13] Gusev A.I., Valeeva A.A. Diffraction of electrons in the Cubic  $\text{Ti}_5\text{O}_5$  superstructure of titanium monoxide. *JETP Letters*, 2012, **96**, P. 364–369.
- [14] Rempel A.A., Renterghem W.V., et al. In situ disordering of monoclinic titanium monoxide  $\text{Ti}_5\text{O}_5$  studied by transmission electron microscope TEM. *Scientific reports*, 2017, **7**, 10769.
- [15] Guo C., Jia S., et al. Orientation domains in vacancy-ordered titanium monoxide. *Acta Cryst. B*, 2013, **69**, P. 589–594.
- [16] Kostenko M.G., Valeeva A.A., Rempel A.A. Effect of high pressure on the period of the b-axis lattice and concentration of vacancies in titanium monoxide TiO. *JETP Lett.*, 2017, **106**, P. 354–357.
- [17] Valeeva A.A., Rempel A.A., Pfitzner A. Elimination of vacancies in titanium monoxide under high pressure in combination with high temperature. *Journal of Monatshefte für Chemie – Chemical Monthly*, 2015, **146**, P. 1205–1209.
- [18] Taylor A., Doyle N.G. Vacancy filling in titanium monoxide and similar semi-metals, in: *The chemistry of extended defects in non-metallic solids*, Eds by L. Eyring, M. O'Keefe. Amsterdam–London: North-Holland Publ., 1970, P. 523–540.
- [19] Fujimura T., Iwasaki H., et al. Structure changes in vacancy-rich titanium monoxide at high pressures and high temperatures. *High pressure research*, 1989, **1**, P. 213–224.
- [20] Valeeva A.A., Nazarova S.Z., Rempel A.A. Influence of Particle Size, Stoichiometry, and Degree of Long-Range Order on Magnetic Susceptibility of Titanium Monoxide. *Physics of the Solid State*, 2015, **58**, P. 771–778.
- [21] Rempel A.A. Hybrid nanoparticles based on sulfides, oxides, and carbides. *Russ. Chem. Bull.*, 2013, **4**, P. 857–868.
- [22] Valeeva A.A., Petrovykh K.A., Schroettner H., Rempel A.A. Effect of stoichiometry on the size of titanium monoxide nanoparticles produced by fragmentation. *Inorganic Materials*, 2015, **51**, P. 1132–1137.
- [23] Rempel S.V., Valeeva A.A., et al. Vacuum-made nanocomposite of low-temperature hydroxyapatite and hard nonstoichiometric titanium monoxide with enhanced mechanical properties. *Mend. Communication*, 2016, **26**, P. 543–545.
- [24] Valeeva A.A., Kostenko M.G., et al. A new  $\text{Ti}_9\text{O}_{10}$  nanophase prepared by heat-treating nonstoichiometric milled  $\text{TiO}_y$  nanopowder. *Inorganic Materials*, 2018, **54**, P. 568–574.
- [25] Hall W.H. X-ray line broadening in metals. *Proc. Phys. Soc. London. Sect. A*, 1949, **62**, P. 741–743.
- [26] Hall W.H., Williamson G.K. The diffraction pattern of cold worked metals: I. The nature of extinction. *Proc. Phys. Soc. London B*, 1954, **64**, P. 937–946.
- [27] Giannozzi P., Baroni S., et al. Quantum Espresso: a modular and open-source software project for quantum simulations of materials. *Journal of Physics. Condensed Matter*, 2009, **21**, 395502 (19 pp.)
- [28] Gusev A.I. Ordered orthorhombic phases of titanium monoxide. *JETP Letters*, 2001, **74**, P. 91–95.
- [29] Banus M.D., Reed T.B., Strauss A.J. Electrical and magnetic properties of TiO and VO. *Physical Review B*, 1972, **5**, P. 2775–2784.
- [30] Popov I.S., Enyashin A.N., Rempel A.A. Size dependent content of structural vacancies within TiO nanoparticles: Quantum-chemical DFTB study, *Superlattices and Microstructures*, 2018, **113**, P. 459–465.

## Effect of nonstoichiometry and amount of additives on the structure of HAp-TiO<sub>y</sub> mixtures produced by high-energy fragmentation

S. V. Rempel<sup>1,2</sup>, K. A. Sergeeva<sup>3</sup>, H. Schroettner<sup>4</sup>, A. A. Valeeva<sup>1,2</sup>

<sup>1</sup>Institute of Solid State Chemistry UB RAS, 91, Pervomaiskaya st., 620990, Ekaterinburg, Russia

<sup>2</sup>Ural Federal University named after the first President of Russia B. N. Eltsin, 19, Mira st., 620002, Ekaterinburg, Russia

<sup>3</sup>Far-Eastern Federal University, 8, Sukhanova st., 690090, Vladivostok, Russia

<sup>4</sup>Institute for Electron Microscopy and Nanoanalysis, Graz University of Technology, Steyrergasse 17/III, A-8010 Graz, Austria

svetlana\_rempel@ihim.uran.ru

PACS 81.20.n

DOI 10.17586/2220-8054-2018-9-4-549-557

The nanoparticle sizes in hydroxyapatite (HAp), titanium monoxide (TiO<sub>y</sub>) and HAp-TiO<sub>y</sub> mixtures ( $y = 0.92; 1.23$ ) have been studied by XRD and HRTEM techniques as a function of milling time. It was established that the high-energy milling does not lead to a considerable decrease in the particle size and to a variation in the HAp crystal lattice parameters, but it promotes 4-fold reduction of microstrains. It was shown that the dependence of the average size of crystal and structural parameters on the milling time for the HAp-TiO<sub>y</sub> mixtures is similar to that of initial HAp. The coherent scattering region of HAp does not depend on stoichiometry and TiO<sub>y</sub> content in the mixture and is  $\sim 15 \pm 5$  nm after milling for 480 min.

**Keywords:** titanium monoxide, hydroxyapatite, milling, mixtures, crystal structure, microstructure, phase composition.

*Received:* 28 May 2018

*Revised:* 13 July 2018

### 1. Introduction

High-energy milling in a planetary ball mill is a common technique of producing nanomaterials [1]. This technique can be also used for creating of composite materials for medicine since nanoceramics and mixtures have some advantages over macro- and microcrystalline materials. For example, HAp ceramics exhibits an enhanced ability to osteosynthesis and adhesion of osteoblasts compared with microstructured ceramics [2–6]. The shape and aspect ratio of nanoparticles are also of much importance for creating favorable conditions for adhesion [2]. In recent years, the nanostructured calcium orthophosphates, in particular, HAp become an active research field in materials synthesis [7–11]. High-energy milling can be a convenient method of unification of nanoparticles of different shape obtained by different techniques. However, the processes occurring during fragmentation and mixing of materials having essentially different properties require a detailed study. So, the Vickers microhardness of the initial components of the composite nanomaterial HAp/TiO [12] differs on several times and is 138 and 992 MPa for HAp and TiO, respectively. In that case, mechanosynthesis, destruction of a softer material by a harder material, and the appearance of excess microstrains that can affect the properties of the final material etc. may take place. The aim of this work is to study in detail the effect of high-energy fragmentation on the microstructure, phase composition, and microstresses of materials and initial components of HAp/TiO<sub>y</sub> mixture, as well as the effect of nonstoichiometry of TiO<sub>y</sub> additives on these properties.

### 2. Experimental

Stoichiometric HAp and microcrystalline TiO<sub>y</sub> were produced using the techniques described in works [13–15]. Nanocrystalline HAp, TiO<sub>y</sub> powders ( $y = 0.92$  and  $1.23$ ) and their mixtures were produced by high-energy milling in a Retsch PM 200 planetary ball mill using Y<sub>2</sub>O<sub>3</sub>-stabilized ZrO<sub>2</sub> grinding media and vials. The ball-to-powder weight ratio was 10 : 1. The high-energy milling conditions were as follows: milling time of 15, 30, 60, 120, 240, and 480 min; rotation direction reversed every 15 min; interval between direction reversals, 5 s; rotation speed of the disk supporting the grinding vials, 500 rpm. Note that the milled nanopowders contain impurities of Y<sub>2</sub>O<sub>3</sub>-stabilized ZrO<sub>2</sub> ( $\sim 2 - 3$  %) and carbon since milling was performed in Y<sub>2</sub>O<sub>3</sub>-stabilized ZrO<sub>2</sub> grinding media and vials with the use of isopropanol [16].

The morphology of the initial microcrystalline powders and mixtures after milling was studied by high-resolution scanning electron microscopy (SEM) on a ZEISS Ultra 55 microscope. The lens-to-sample distance and

the accelerating voltage were 3.4 – 4.0 mm and 5 keV, respectively. The beam width varied from 1 to 115  $\mu\text{m}$  depending on magnification.

The structure and microstructure of HAp was determined using high-resolution transmission electron microscopy (HRTEM) on a JEM 2010 electron microscope (JEOL, Japan) with accelerating voltage 200 kV. To perform electron microscopy studies, the particles were placed into alcohol and were applied on carbon substrates (biological adhesive) (diameter of holes  $\sim 1 \mu\text{m}$ ) fixed on copper or molybdenum networks. The particles were applied by means of ultrasonic disperser providing a uniform distribution of particles on the substrate surface. After the particles on the carbon substrate and network were removed from the alcohol, it was evaporated.

The X-ray diffraction (XRD) studies of the powders were performed in  $\text{CuK}\alpha_1$ -radiation on a STADI-P automatic diffractometer (STOE, Germany) in the Bragg–Brentano geometry by stepwise scanning with  $\Delta(2\theta) = 0.02^\circ$  in the angle interval from 10 to  $120^\circ$  with a high degree of statistics. Polycrystalline silicon ( $a = 543.07 \text{ pm}$ ) was used as external standard. Phase analysis of the XRD pattern was performed using Powder Cell 2.4 program. For phase identification the powder standards database ICDD PDF2 (ICDD, USA, Release 2009) was used.

Diffraction line profiles were analyzed by fitting with pseudo-Voigt functions of the form:

$$V(\theta) = ca \left[ 1 + \frac{(\theta - \theta_0)^2}{\theta_L^2} \right]^{-1} + (1 - c)a \exp \left[ -\frac{(\theta - \theta_0)^2}{2\theta_G^2} \right], \quad (1)$$

where  $c$  is the relative contribution of the Lorentzian function to the total reflection intensity;  $\theta_L$  and  $\theta_G$  are the Lorentz and Gauss profile parameters, respectively;  $a$  is a normalizing intensity factor; and  $\theta_0$  is the function and reflection maximum position.

The numerical analysis of X-ray diffraction patterns was performed using the technique [11, 12, 17, 18]; it revealed that the powders are homogeneous and single-phase. Therefore, the average size of the coherent scattering regions was determined as [19, 20]:

$$D = K_{hkl} \cdot \frac{\lambda}{\cos \theta} \cdot \beta(2\theta) \equiv K_{hkl} \cdot \frac{\lambda}{2} \cdot \cos \theta \cdot \beta(\theta), \quad (2)$$

where  $K_{hkl}$  is the James coefficient, and  $\beta(2\theta)$  is the broadening. The diffraction reflection broadening  $\beta(2\theta) \equiv 2\beta(\theta)$  was determined as:

$$\beta(2\theta) = \sqrt{\text{FWHM}_{\text{exp}}^2 - \text{FWHM}_{\text{R}}^2}. \quad (3)$$

The instrumental broadening (the resolution function of the diffractometer) was determined in a special diffraction experiment with a standard powder of lanthanum hexaboride  $\text{LaB}_6$  (NIST Standard Reference Powder 660a) with cubic lattice spacing  $a_{\text{cub}} = 415.69 \text{ pm}$  and particle size of  $\sim 10 \mu\text{m}$ . The resolution function of the diffractometer, determined with lanthanum hexaboride, had the following parameters:  $u = 0.0058$ ,  $v = -0.0046$ ,  $w = 0.0101$ .

The particle size and microstrain contributions to the reflection broadening were determined by the Williamson–Hall technique [21, 22]. The reduced broadening was calculated by the formula

$$\beta^*(2\theta) = \beta(2\theta) \cos \theta / \lambda. \quad (4)$$

The experimental broadening  $\beta(2\theta)$  is a superposition of particle size  $\beta_s$  and strain  $\beta_d$  broadening:

$$\beta = \sqrt{\beta_s^2 + \beta_d^2}. \quad (5)$$

The size of nanoparticle coincides with the coherent scattering region (CSR). The CSR size was determined as:

$$\langle D \rangle = 1/\beta^*(2\theta = 0). \quad (6)$$

The size of nanoparticle was determined by extrapolating  $\beta^*(s)$  to  $s = 0$ , and the lattice microstrain was found from the slope of the resultant straight line. Lattice strain  $\varepsilon = \Delta d/d_0$ , where  $d_0$  is the average interplanar spacing and  $\Delta d$  is its deviation, leads to a strain-induced diffraction line broadening  $\beta d(2\theta) = 2\varepsilon \tan \theta$ .

The dependence of the CSR and the volume fraction of nanoparticles on the milling time were described by the relations proposed in [23]:

$$D(\tau) = \frac{D_0 - D_{\text{min}}}{1 + b\tau} + D_{\text{min}}, \quad (7)$$

$$V(\tau) = \frac{a}{1 - \exp(-\tau/\tau_0)}, \quad (8)$$

where  $D_0$  is the initial particle size before milling;  $D_{\text{min}}$  is the minimal particle size achieved by milling;  $b$  is the coefficient related to softness of material;  $a$  is the volume contribution of nanodimensional fraction; and  $\tau$  is the time of milling.

For more accurate determination of the compounds' crystal lattice parameters, the Nelson–Riley extrapolation function was used:

$$0.5 \left[ \frac{\cos^2 \theta}{\sin \theta} + \frac{\cos^2 \theta}{\theta} \right], \quad (9)$$

where  $\theta$  is the scattering angle.

### 3. Results and discussion

The analysis of the X-ray diffraction patterns of the initial and milled HAp showed that all powders are homogeneous and single-phase. The crystal structure of HAp belongs to the hexagonal system (sp. gr.  $P 63/m$ ). As the milling time increases, a small broadening of diffraction reflections occurs and their intensity lowers (Fig. 1). The position of reflections remains unchanged within the accuracy of the experiment. After milling, the type and crystal lattice symmetry of the HAp are retained. When 10 and 20 wt.% titanium monoxide are introduced into HAp, additional diffraction reflections corresponding to  $(111)_{B1}$ ,  $(200)_{B1}$  and  $(202)_{B1}$  reflections are observed on the HAp X-ray diffraction patterns (Fig. 1). These reflections exhibit a high intensity. The considerable widths of the  $(200)_{B1}$  and  $(202)_{B1}$  reflections are due to the overlapping with the HAp diffraction reflections.

According to analysis of X-ray patterns, the average CSR size of initial HAp is  $20 \pm 5$  nm. As a result of milling, the particle size was decreased to  $13 \pm 5$  nm (Fig. 2).

The parameters of the model curve (formula 7), which was used for data approximation, are  $D_0 = 20$  nm,  $b = 0.02$  and  $D_{\min} = 13$  nm. As the time of milling increases, the microstrain value decreases (Fig. 2) by hyperbolic function  $y = y_0 + a \exp(-kx)$  with parameters  $y_0 = 0.10$ ,  $a = 0.30$  and  $k = 0.04$ .

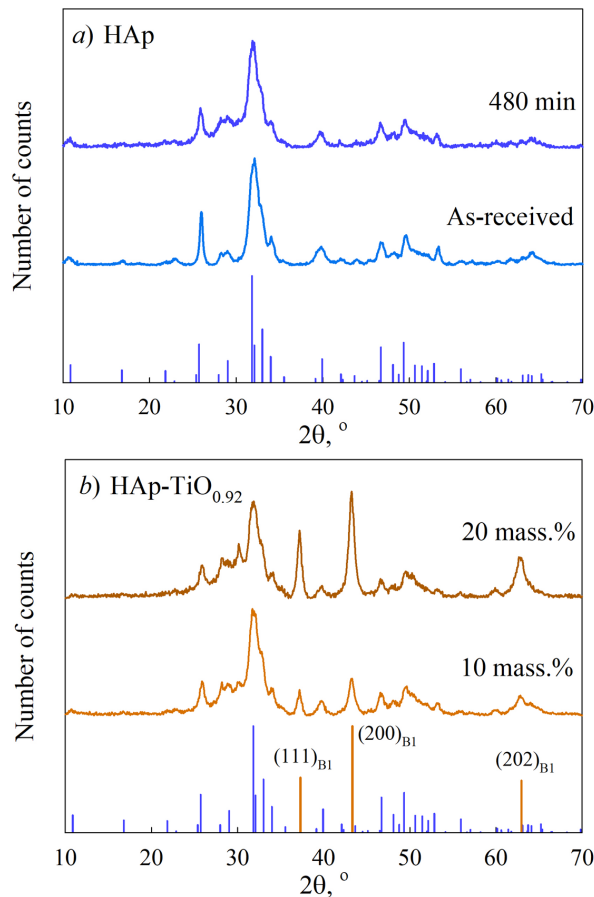


FIG. 1. The X-ray diffraction patterns of HAp powders (a) and HAp-TiO<sub>0.92</sub> mixture (b) vs. the milling time and the content of titanium monoxide. The position and intensity of diffraction peaks of hydroxyapatite with unit cell parameters  $a = 940.0$  pm and  $c = 693.0$  pm (card 98-008-6843) and titanium monoxide with the disordered cubic cell parameter  $a = 418.5$  pm are given below

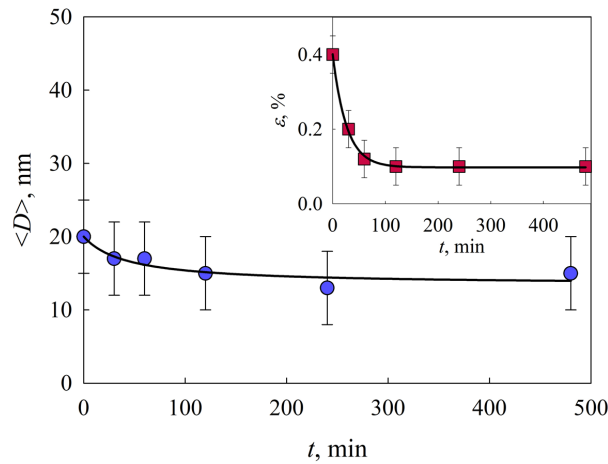


FIG. 2. The CSR size and the HAp crystal lattice microstrain value (inset) as functions of the milling time

The dependences of the CSR size and the volume fraction of nanoparticles on the time of milling for sub- and superstoichiometric compositions of titanium monoxide are shown in Fig. 3. Both materials are characterized by the presence of microparticles even after 480 min milling.

The performed calculations revealed that the unit cell parameters  $a$  and  $c$  of HAp powders change within the computational error as the milling duration increases. The parameter  $a$  changes insignificantly, and the parameter  $c$  increases monotonically. The lattice parameter of titanium monoxide changes little, if at all, and the cubic structure remains stable after milling for 480 min. More detailed data on the structural parameters of HAp and  $\text{TiO}_y$  powders are presented in Table 1.

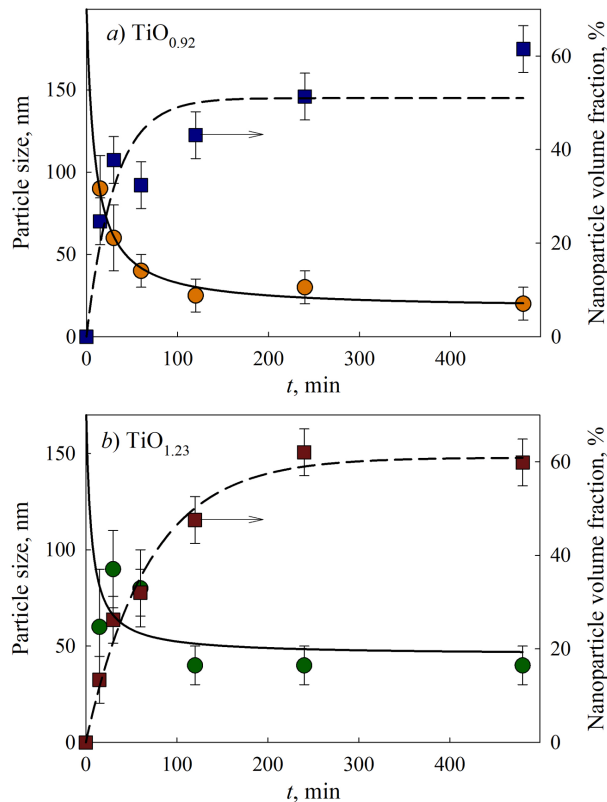


FIG. 3. The CSR size and the volume fraction of  $\text{TiO}_y$  ( $y = 0.92$  (a);  $1.23$  (b)) powder nanoparticles as functions of the milling time

TABLE 1. The properties of initial and milled HAp and titanium monoxide powders

Compound	Milling time, min	Lattice constant <i>a</i> and <i>c</i> , pm ( $\pm 1$ nm)	Crystal size $\langle D \rangle > \pm 5$ nm	Volume fraction of nanoparticles, %	Microstrains, %
Initial HAp	0	<i>a</i> = 941.5, <i>c</i> = 688.6	20	100	0.4
	30	<i>a</i> = 941.7, <i>c</i> = 689.0	17	100	0.2
	60	<i>a</i> = 941.7, <i>c</i> = 689.3	17	100	0.12
	120	<i>a</i> = 942.0, <i>c</i> = 689.4	15	100	0.1
	240	<i>a</i> = 941.5, <i>c</i> = 689.5	13	100	0.1
	480	<i>a</i> = 941.5, <i>c</i> = 691.1	15	100	0.1
Initial TiO <sub>0.92</sub>	0	<i>a</i> = 418.5	200	0	0.0013
	30	<i>a</i> = 418.5	60	37	0.27
	60	<i>a</i> = 418.5	40	32	0.39
	120	<i>a</i> = 418.5	25	43	0.41
	240	<i>a</i> = 418.6	30	51	0.65
	480	<i>a</i> = 418.5	20	61	0.73
Initial TiO <sub>1.23</sub>	0	<i>a</i> = 416.9	180	0	0.0015
	30	<i>a</i> = 416.9	90	16	0.27
	60	<i>a</i> = 416.9	80	32	0.41
	120	<i>a</i> = 416.9	40	47	0.47
	240	<i>a</i> = 416.8	40	62	0.59
	480	<i>a</i> = 416.9	40	60	0.85

Analysis of the X-ray diffraction patterns of HAp/TiO<sub>y</sub> mixtures demonstrated that the dependence of the average CSR size and structural parameters on the time of milling is similar to that for the initial HAp. Note that the size of CSR of mixture components corresponds within experimental error to the values for milled HAp and TiO<sub>y</sub> (Table 2). Moreover, the CSR size of HAp does not depend on stoichiometry and the content of TiO<sub>y</sub> in mixtures and is  $\sim 15 \pm 5$  nm.

TABLE 2. The properties of mixtures after 480 min milling

Mixture	HAp-TiO <sub>0.92</sub> (10 mass.%)		HAp-TiO <sub>0.92</sub> (20 mass.%)		HAp-TiO <sub>1.23</sub> (10 mass.%)		HAp-TiO <sub>1.23</sub> (20 mass.%)	
	HAp	TiO <sub>0.92</sub>	HAp	TiO <sub>0.92</sub>	HAp	TiO <sub>1.23</sub>	HAp	TiO <sub>1.23</sub>
Crystal size $\langle D \rangle \pm 5$ , nm	18	12	16	12	16	30	15	13
Microstrains, %	0.2	0.9	0.03	0.9	0.05	0.35	0.06	0.9
Lattice constant <i>a</i> and <i>c</i> , pm ( $\pm 1$ )	<i>a</i> = 941.6, <i>c</i> = 688.9	<i>a</i> = 417.8	<i>a</i> = 941.2, <i>c</i> = 690.5	<i>a</i> = 418.1	<i>a</i> = 941.2, <i>c</i> = 687.3	<i>a</i> = 416.7	<i>a</i> = 942.2, <i>c</i> = 692.5	<i>a</i> = 416.8

The lowest crystal lattice microstrain value of HAp in HAp-TiO<sub>y</sub> mixture corresponds to substoichiometric composition TiO<sub>0.92</sub> and amounts to 0.03 % (Table 2). When mixtures are milled in the presence of additives, the HAp crystal lattice parameters change nonmonotonically (Fig. 4). The changes depend on both the amount and nonstoichiometry of the additives.

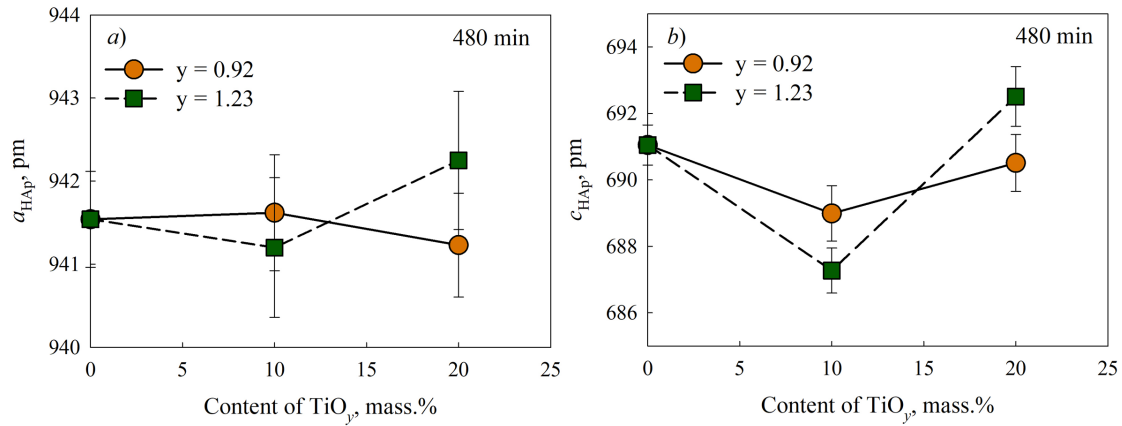


FIG. 4. The HAp crystal lattice parameters  $a$  and  $c$  as functions of the titanium monoxide  $\text{TiO}_y$  content ( $y = 0.92$  (a); 1.23 (b)) with different stoichiometry

According to the SEM data, the initial HAp contains mainly cylindrical nanoparticles (Fig. 5) to 250 nm in length and  $\sim 20$  nm in diameter. Analysis of the SEM data of milled HAp showed that such nanoparticles were not observed any longer. According to the HRTEM data, the sample consists of HAp particles (card# 98-008-6843); cylindrical particles of the length to 100 nm (Fig. 6) are observed on the surface of larger particles. The CSR size also decreases, but not so considerably. Taking into account the X-ray diffraction data, it can be supposed that the initial cylindrical HAp nanoparticles are polycrystals growing during synthesis mainly along the crystallographic direction  $c$ . During milling, both fragmentation of nanoparticles and reduction of their constituent blocks predominately along the  $a$  direction take place.

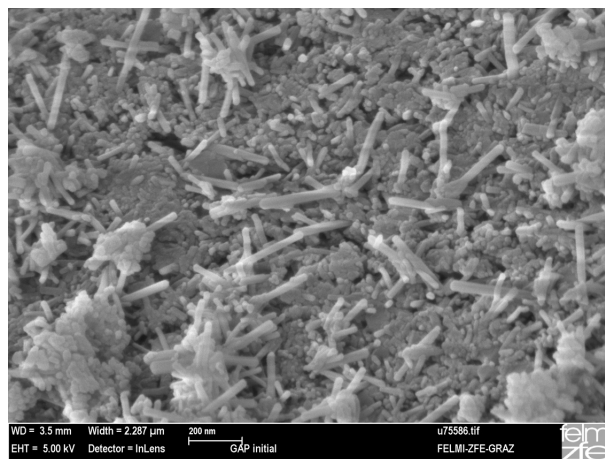


FIG. 5. The microphotographs of the initial HAp powder before fragmentation, SEM

Figures 7 and 8 display the microphotographs of microcrystalline monoxides (sub- and superstoichiometric) and nanocrystalline TiO<sub>y</sub> after milling for 480 min. After milling, the TiO<sub>y</sub> nanopowders are represented by agglomerates to 200 – 250 nm in size, consisting of bound together nanoparticles with a size of about 20 nm.

It is interesting that after milling of HAp and TiO<sub>y</sub> nanoparticles in a planetary ball mill for 480 min, the morphology of the mixture becomes similar to the morphology of nanocrystalline TiO<sub>y</sub> [18,23] (Fig. 9). Owing to additives, the particles of the mixture acquire a flattened shape that facilitates the compaction and promotes the adhesion of cells. The morphology of the powders does not depend on the stoichiometry of additives.

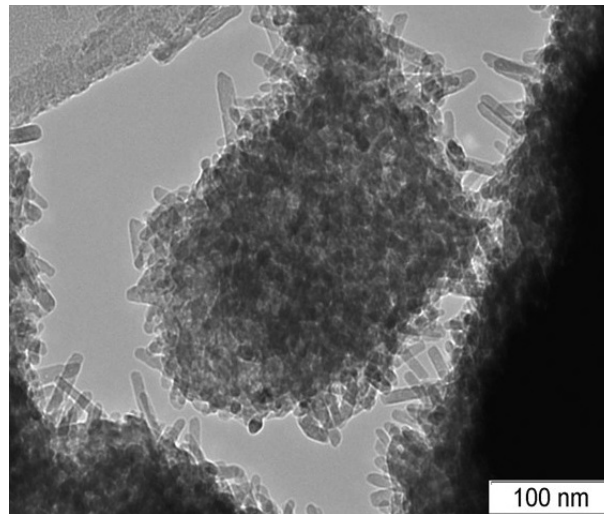


FIG. 6. The microphotograph of HAp powder nanoparticles after 480 min milling, HRTEM

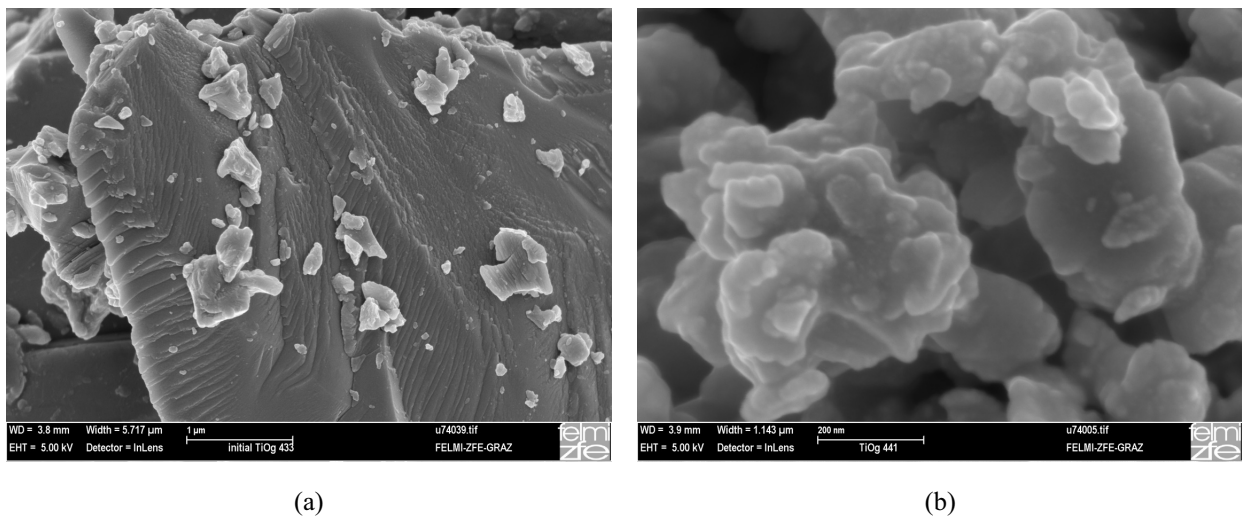


FIG. 7. The microphotographs of substoichiometric titanium monoxide TiO<sub>0.92</sub>: a) initial, microcrystalline; b) after 480 min high-energy milling, SEM

#### 4. Conclusion

The structural and morphological studies of HAp, TiO<sub>y</sub> ( $y = 0.92; 1.23$ ) nanopowders and their mixtures produced by high-energy milling have been carried out. It was established that after the fragmentation the crystal structure of HAp is retained. The high-energy milling does not lead to a variation in the HAp crystal lattice parameters, promoting however a 4-fold reduction in microstrain. The dependence of the CSR size on the HAp milling time is reliably described by the function proposed earlier for titanium monoxide. This hyperbolic function can be also applied to other nonstoichiometric oxides and carbides of transition metals.

It is shown that for HAp/TiO<sub>y</sub> mixtures ( $y = 0.92; 1.23$ ) the dependence of the average CSR size and structural parameters on the milling time is similar in many respects to that for initial HAp. The HAp CSR size does not depend on the stoichiometry and content of TiO<sub>y</sub> in mixtures and is  $\sim 15 \pm 5$  nm upon 480 min milling. The least microstrain value of HAp crystal lattice in HAp-TiO<sub>y</sub> nanocomposite corresponds to the substoichiometric composition TiO<sub>0.92</sub>.

After milling, the nanopowder mixtures acquire the morphology of TiO<sub>y</sub> nanopowders, which is favorable for compaction and adhesion of cells during further application.

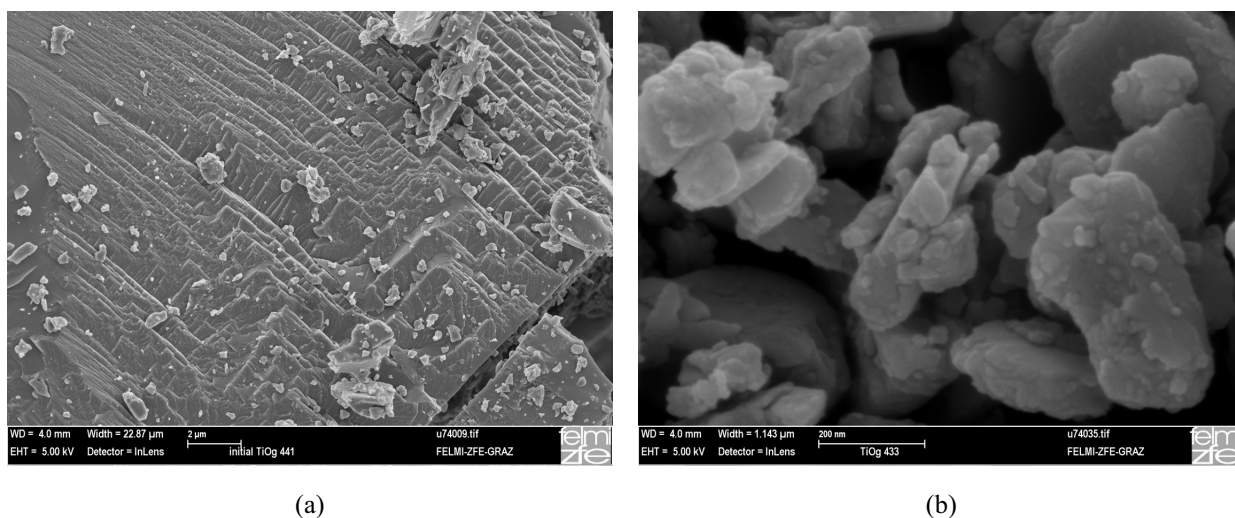


FIG. 8. The microphotographs of superstoichiometric titanium monoxide  $\text{TiO}_{1.23}$ : a) initial, microcrystalline; b) after 480 min high-energy milling, SEM

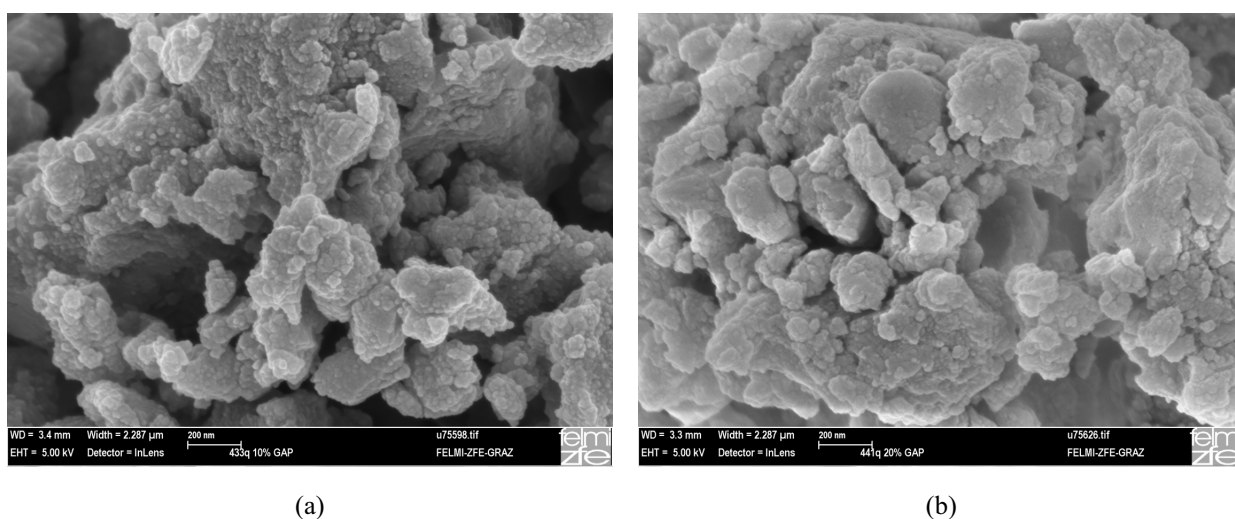


FIG. 9. The microphotographs of powder mixtures after 480 min high-energy milling: a) HAp/ $\text{TiO}_{0.92}$ ; b) HAp/ $\text{TiO}_{1.23}$ , SEM

Thus, the high-energy milling does not change the crystal structure of initial nanopowders, it decreases microstrains and unifies the morphology. The stoichiometry of  $\text{TiO}_y$  additives has no considerable effect on the CSR size of the mixtures.

### Acknowledgements

The work was carried out at the Institute of Solid State Chemistry UB RAS with financial support from the Russian Science Foundation (Project 14-23-00025). The authors are grateful to E. A. Bogdanova for the synthesis of HAp powders and E. Yu. Gerasimov for HRTEM experiment.

### References

- [1] Rempel A.A. Nanotechnologies. Properties and applications of nanostructured materials. *Russian Chemical Reviews*, 2007, **76**, P. 435–461.
- [2] Okada M., Matsumoto T. Japanese Synthesis and modification of apatite nanoparticles for use in dental and medical applications. *Dental Science Review*, 2015, **51**, P. 85–95.
- [3] Okada M., Furuzono T., Hydroxylapatite nanoparticles: fabrication methods and medical applications. *Sci. Technol. Adv. Mater.*, 2012, **13** (064103), P. 1–14.
- [4] Webster T.J., Ergun C., et al. Enhanced osteoclast-like cell functions on nanophase ceramics. *Biomaterials*, 2001, **22**, P. 1327–1333.

- [5] Balasundaram G., Sato M., Webster T.J. Using hydroxyapatite nanoparticles and decreased crystallinity to promote osteoblast adhesion similar to functionalizing with RGD. *Biomaterials*, 2006, **27**, P. 2798–2805.
- [6] Sun W., Chu C., Wang J., Zhao H. Comparison of periodontal ligament cells responses to dense and nanophase hydroxyapatite. *J. Mater. Sci. Mater. Med.*, 2007, **18**, P. 677–683.
- [7] Wen Z., Wang Z., et al. Manipulation of partially oriented hydroxyapatite building blocks to form flowerlike bundles without acid-base regulation. *Colloids and Surfaces B: Biointerfaces*, 2016, **142**, P. 74–80.
- [8] Terraschke H., Rothe M., et al. In situ luminescence analysis: a new light on monitoring calcium phosphate phase transitions. *Inorg. Chem. Front.*, 2017, **4**, P. 1157–1165.
- [9] Shkir M., Kilany M., Yahia I.S. Facile microwave-assisted synthesis of tungsten-doped hydroxyapatite nanorods: A systematic structural, morphological, dielectric, radiation and microbial activity studies. *Ceramics International*, 2017, **43**, P. 14923–14931.
- [10] Abutalib M.M., Yahia I.S. Novel and facile microwave-assisted synthesis of Mo-doped hydroxyapatite nanorods: Characterization, gamma absorption coefficient, and bioactivity. *Materials Science and Engineering C*, 2017, **78**, P. 1093–1100.
- [11] Hu S., Jia F., et al. Ferroelectric polarization of hydroxyapatite from density functional theory. *RSC Adv.*, 2017, **7**, P. 21375–21379.
- [12] Rempel S.V., Valeeva A., et al. Vacuum-made nanocomposite of low-temperature hydroxyapatite and hard nonstoichiometric titanium monoxide with enhanced mechanical properties. *Mendeleev Commun.*, 2016, **26**, P. 543–545.
- [13] Rempel S.V., Bogdanova E., et al. Microhardness and phase composition of TiO<sub>y</sub>/hydroxyapatite nanocomposites synthesized under low-temperature annealing conditions. *Inorganic Materials*, 2016, **52** (5), P. 476–482.
- [14] Valeeva A.A., Rempel A.A., Gusev A.I. Ordering of Cubic Titanium Monoxide into Monoclinic Ti<sub>5</sub>O<sub>5</sub>. *Inorganic Materials*, 2001, **37**, P. 603–613.
- [15] Valeeva A.A., Rempel S.V., Schroettner H., Rempel A.A. Influence of the degree of order and nonstoichiometry on the microstructure and microhardness of titanium monoxide. *Inorganic Materials*, 2017, **53**, P. 1174–1179.
- [16] Valeeva A.A., Petrovykh K.A., Schroettner H., Rempel A.A. Effect of stoichiometry on the size of titanium monoxide nanoparticles produced by fragmentation. *Inorganic Materials*, 2015, **51**, P. 1132–1137.
- [17] Rempel A.A., Rempel S.V., Gusev A.I. Quantitative assessment of homogeneity of nonstoichiometric compounds. *Doklady Physical Chemistry*, 1999, **369**, P. 321–325.
- [18] Rempel A.A., Gusev A.I. Preparation of disordered and ordered highly nonstoichiometric carbides and evaluation of their homogeneity. *Physics of the Solid State*, 2000, **42**, P. 1280–1286.
- [19] Warren B.E. *X-Ray Diffraction*. Dover Publications, New York, 1990. 381 p.
- [20] James R. *Optical principles of X-Ray diffraction*. Foreign Literature Publishing House, Moscow, 1950, 574 p.
- [21] Hall W.H. X-ray line broadening in metals. *Proc. Phys. Soc. A*, 1949, **62**, P. 741–743.
- [22] Hall W.H., Williamson G.K. The diffraction pattern of cold worked metals: I. The nature of extinction. *Proc. Phys. Soc. B*, 1951, **64**, P. 937–946.
- [23] Valeeva A.A., Schroettner H., Rempel A.A. Fragmentation of disordered titanium monoxide of stoichiometric composition TiO. *Russian Chemical Bulletin*, 2014, **63**, P. 2729–2732.

## High-temperature synthesis of finely dispersed oxide materials and C12A7:e electrides in carbon nanoreactor conditions

A. M. Volodin, A. F. Bedilo, V. O. Stoyanovskii, V. I. Zaikovskii

Boreskov Institute of Catalysis, Prospekt Lavrentieva, 5, Novosibirsk, 630090, Russia  
volodin@catalysis.ru

DOI 10.17586/2220-8054-2018-9-4-558-567

Solid-state transformations of the oxide core in core-shell structures Oxide@C consisting of oxide nanoparticles covered with a carbon coating were studied at temperatures of up to 1500 °C. It is shown that such coating can stabilize the size of the oxide core nanoparticles for alumina, zirconia, calcium and lanthanum aluminates and act as a shell of a nanoreactor where phase and chemical transformation can take place. For ZrO<sub>2</sub>@C and Al<sub>2</sub>O<sub>3</sub>@C it is demonstrated that it is the preservation of the small particle size that accounts for the preservation of cubic ZrO<sub>2</sub> and δ-Al<sub>2</sub>O<sub>3</sub> until the carbothermal reduction temperatures of the corresponding oxides (above 1400 °C for Al<sub>2</sub>O<sub>3</sub>). The electride state C12A7:e is shown to be formed in C12A7@C material at temperatures above its melting point. The surface of activated C12A7 was found to have a significant concentration of active OH radicals capable of converting diphenylamine into stable nitroxyl radicals.

**Keywords:** Core-shell, nanocrystalline oxide, electride, ZrO<sub>2</sub>, Al<sub>2</sub>O<sub>3</sub>, carbon nanoreactor.

*Received:* 9 June 2018

*Revised:* 10 July 2018

### 1. Introduction

Core-shell structures with different chemical composition are widely used as nanoreactors in modern chemical studies [1–6]. The main goals for design of such materials are the formation of optimal conditions for operation of the core materials that do not depend on the external conditions, preservation of the core composition and size, performing selective chemical reactions with participation of the core using reagents penetrating through the shell, etc. It is obvious that the choice of the core and shell materials depends on their role and the range of operation conditions. In most cases, such systems are used either for reactions carried out in the liquid phase or in catalytic reactions taking place in the gas phase at moderate temperatures. The shells for catalysts operating at relatively high temperatures are commonly made of either SiO<sub>2</sub> [1, 2, 6] or carbon [3–5].

Carbon-coated nanocrystalline MgO was shown to preserve the small particle size and have superior reactivity in decomposition of chlorinated compounds [7, 8]. In our recent papers [9–12] it was demonstrated that the carbon coating in Oxide@C core-shell structures can function as a relatively solid nanoreactor shell, which is permeable to molecules from the gas phase and stabilizes the size of the oxide core at high temperatures.

A natural condition that limits this temperature range is the temperature of the oxide core carbothermal reduction, which depends on its composition. For aluminum-containing oxide systems studied by us (Al<sub>2</sub>O<sub>3</sub>, calcium and lanthanum aluminates) this temperature exceeds 1400 °C. So, the synthesis of core-shell particles makes it possible to study the effect of the nanoparticle oxide core size on solid state reactions in a wide temperature range. Meanwhile, for TiO<sub>2</sub>, carbothermal reduction starts already at 800 °C. Above this temperature, the TiO<sub>2</sub>@C core-shell structure is destroyed, and non-stoichiometric titanium oxide phases are formed.

High-temperature treatment of aluminum-containing oxide systems Oxide@C (above 1100 – 1200 °C) gives a unique possibility to synthesize relatively dispersed oxide materials that do not contain structural water. Synthesis of such materials under conventional conditions is practically impossible because intense sintering of the samples and the accompanying phase transformations take place in this temperature range.

Electron paramagnetic resonance (EPR) is an excellent method for characterization of various active sites present on the surface of oxides, which can generate radical or ion-radical species after adsorption of suitable spin probes [13–16]. Electron-donor sites on such oxide supports as Al<sub>2</sub>O<sub>3</sub>, MgO, ZrO<sub>2</sub>, etc. can be studied using aromatic nitro compounds due to their pronounced electron-acceptor properties, leading to the formation of stable radical anions [17, 18]. Various aromatic donor molecules can be used to characterize electron-acceptor sites on the surface of a great variety of oxide materials, which can generate radical cations by abstracting a single electron from them [15, 16, 19]. The strength of the surface acceptor sites can be qualitatively characterized by selecting probe molecules with different ionization potentials [16].

The goal of this study was to compare high-temperature transformations of several oxide and core-shell structures based on them and determine the effect of the oxide nanoparticles size on their chemical transformations.

Special attention was paid to characterization of the active sites on the surface of  $\text{Al}_2\text{O}_3$  and C12A7 materials that are important for their application as supports for catalyst synthesis.

## 2. Experimental

The following materials were used as the main objects in this study. Nanocrystalline alumina (AP- $\text{Al}_2\text{O}_3$ ) was prepared using the aerogel technique described in detail elsewhere [20,21]. A  $\gamma$ - $\text{Al}_2\text{O}_3$  sample (SB1- $\text{Al}_2\text{O}_3$ ) prepared by decomposition of Condea Pural SB1 pseudoboehmite was studied for comparison. Before deposition of the carbon coating, the samples were calcined in a muffle furnace in air at 720 °C for 6 h. The specific surface area of the used samples was  $\sim 200 \text{ m}^2/\text{g}$ .

Hydrated zirconia samples with the surface area  $\sim 300 \text{ m}^2/\text{g}$  were prepared by traditional precipitation from a  $\text{ZrOCl}_2$  solution with ammonia at pH = 10.6. The precipitate was washed with a water excess until neutral pH. The obtained sample was dried at 110 °C for 12 h and was not subjected to any heat treatment before deposition of the carbon coating.

A mixture of aluminum hydroxide (Condea Pural SB1 pseudoboehmite) and calcium hydroxide with the required stoichiometric ratio was used as a precursor for C12A7 synthesis. The mixture was thoroughly stirred in distilled water for 10 h, filtered and dried at 110 °C. Then it was calcined in a muffle furnace in air at 550 °C for 6 h. The obtained C12A7-550 sample was used as a starting material for further synthesis.

Core-shell materials were prepared by mixing each oxide powder with polyvinylalcohol (PVA) in the weight ratio 7 : 3 followed by calcination of the obtained mixture in argon at desired temperature typically for 6 h. The carbon-coated samples will be hereafter denoted as Oxide@C- $T$ , where Oxide is the type of the oxide core, and  $T$  is the final calcination temperature in °C.

$\text{LaAl}_{11}\text{O}_{18}$  and  $\text{LaAlO}_3$  samples were synthesized by a modified Pechini route from ethylene glycol – citric ester polyester precursors [22]. After aerobic decomposition of the polymeric precursors 400 °C, further calcination of the samples with preservation of the carbon shell was carried out under argon at 700 – 1300 °C. So, the procedure used for synthesis of core-shell samples was different for this material. The samples without the carbon coating were calcined in air.

The EPR spectra were recorded at room temperature using an ERS-221 EPR spectrometer working in the X-band. The experimental installation was described in detail elsewhere [23]. 1,3,5-Trinitrobenzene (TNB), anthracene, phenothiazine and diphenylamine probes used to characterize various surface active sites were adsorbed from 20 mM solutions in toluene. Prior to adsorption of the probe molecules, the samples were activated in air at 500 °C for 3 h. The probe adsorption and spectrum recording procedure was reported in detail in our earlier publications [16,18].

Specific surface areas determined by the BET method were calculated from the data obtained by low-temperature argon adsorption using an ASAP-2400 instrument. XRD analysis was performed using a Bruker D8 diffractometer with  $\text{Co K}\alpha$  irradiation. High-resolution transmission electron microscopy images were obtained using a JEM-2010CX microscope with 1.4 Å line resolution.

## 3. Results and discussion

### 3.1. $\text{Al}_2\text{O}_3$ @C

$\gamma$ - $\text{Al}_2\text{O}_3$  is widely used in chemical technology as a sorbent and a catalyst support. This compound preserves its phase composition and relatively high surface area (200 – 300  $\text{m}^2/\text{g}$ ) up to 700 – 800 °C. At higher temperatures, it is subjected to dehydration and sintering of nanoparticles to form  $\delta$ - $\text{Al}_2\text{O}_3$  phase with typical surface area 100 – 120  $\text{m}^2/\text{g}$ . Further temperature increase is accompanied by the surface area drop to 1 – 5  $\text{m}^2/\text{g}$  with the formation of corundum ( $\alpha$ - $\text{Al}_2\text{O}_3$ ) phase. Usually, this corresponds to complete alumina dehydration. It has been demonstrated that size effects play an important role in the phase transformations of this oxide [24–26]. The  $\gamma$ - $\text{Al}_2\text{O}_3$  phase is thermodynamically stable for samples with high specific surface area and the corresponding small particles size. Meanwhile,  $\alpha$ - $\text{Al}_2\text{O}_3$  is formed only after substantial growth of the oxide nanoparticles due to their sintering caused by the presence of direct contacts between the nanoparticles. Deposition of any shell eliminating such contacts favors the particle size stabilization and, as result, prevents the corundum phase formation and dehydration of catalytic materials. Earlier, we demonstrated that the size of the oxide core can be stabilized for various oxide nanoparticles in core-shell structures Oxide@C after deposition of the carbon coating on the surface. It is evident that the size of the starting oxide core, its morphology and the properties of the deposited carbon shell may have a significant effect on the thermal stability of such materials.

Data for the surface areas and the phase composition of AP- $\text{Al}_2\text{O}_3$  and the oxide core in AP- $\text{Al}_2\text{O}_3$ @C system at high temperatures are shown in Figs 1 and 2. The presented data clearly demonstrate that complete conversion

to corundum is not observed for AP- $\text{Al}_2\text{O}_3@\text{C}$ , even at temperatures as high as 1400 °C. Meanwhile, the thermal stability of the low-temperature alumina phases in SB1- $\text{Al}_2\text{O}_3@\text{C}$  is substantially lower [10, 12].

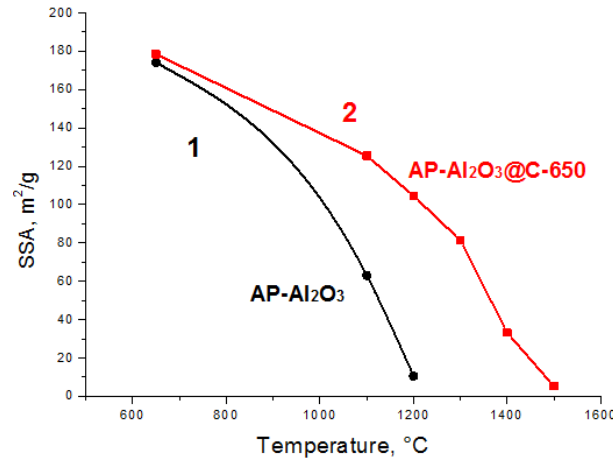


FIG. 1. Effect of calcination temperature on the surface area of AP- $\text{Al}_2\text{O}_3$  (1) and AP- $\text{Al}_2\text{O}_3@\text{C}$  sample after burning its carbon shell by calcination in air at (2)

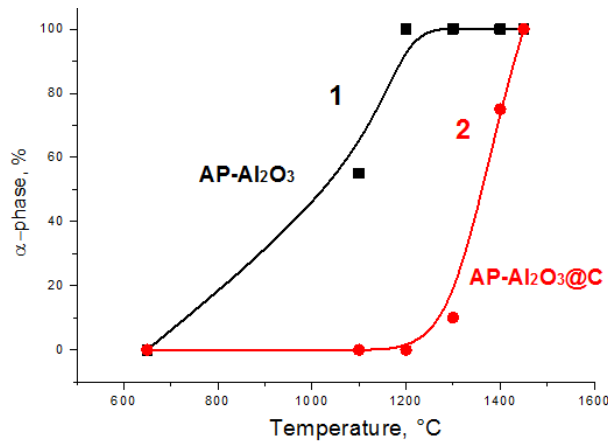


FIG. 2. Effect of calcination temperature on the corundum concentration in AP- $\text{Al}_2\text{O}_3$  (1) and AP- $\text{Al}_2\text{O}_3@\text{C}$  (2)

The evolution of Raman spectra of the carbon shell in AP- $\text{Al}_2\text{O}_3@\text{C}$  at different calcination temperatures is presented in Fig. 3. Intense  $G$  lines at  $\sim 1590\text{ cm}^{-1}$  corresponding to allowed  $E_{2g}$  vibrations of the graphite hexagonal lattice and disorder-induced  $D$  lines attributed to activated  $A_{1g}$  mode due to the finite crystal size [27,28] at  $\sim 1340\text{ cm}^{-1}$  were observed in the first-order scattering spectra of all AP- $\text{Al}_2\text{O}_3@\text{C}$  samples. As the temperature increases, the  $I_D/I_G$  ratio increases from 0.83 to 1.47, and a second-order 2D line appears in the spectrum. A line at  $\sim 864\text{ cm}^{-1}$ , corresponding to the most intense  $A_{1g}$  line of  $\text{Al}_4\text{C}_4$  appears in the spectrum of the sample calcined at 1500 °C [29]. Its appearance corresponds to the start of the oxide core carbothermal reduction to aluminum carbide.

As was noted above, a natural restriction on the highest temperature at which the oxide core size can be preserved for Oxide@C materials is the temperature of the chemical reaction between the shell and the core materials. Based on the presented data, we managed to approach this maximum temperature for  $\text{Al}_2\text{O}_3@\text{C}$  using the AP- $\text{Al}_2\text{O}_3$  core and our carbon shell deposition technique.

Alumina is a popular catalyst support. The presence of certain types of active sites on its surface is crucial for this application. So, we compared the concentrations of different active sites on the  $\text{Al}_2\text{O}_3$  surface and on the surface of the  $\text{Al}_2\text{O}_3$  core of  $\text{Al}_2\text{O}_3@\text{C}$  calcined at high temperature after removing the carbon shell from them by calcination in air. 1,3,5-Trinitrobenzene adsorption was used for characterization of electron-donor sites [18].

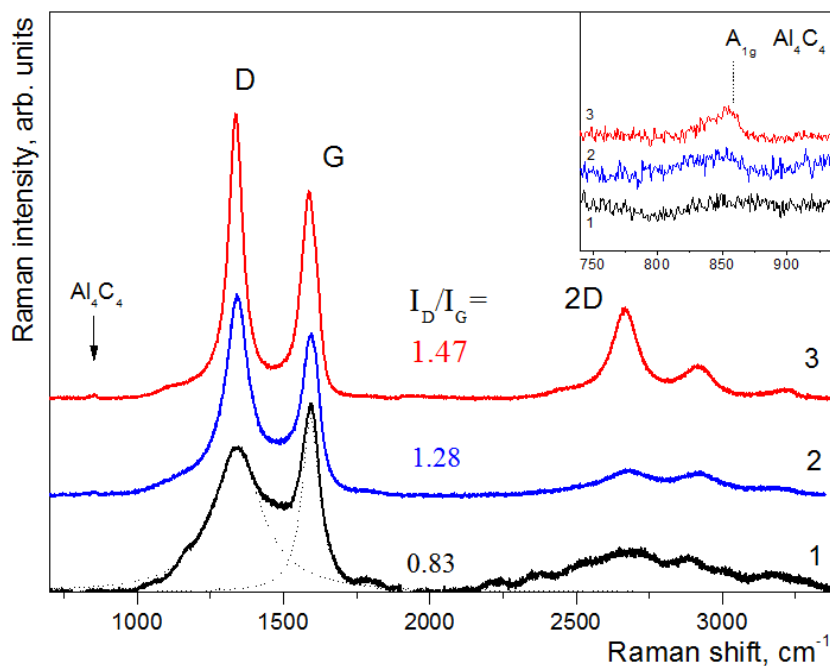


FIG. 3. Raman spectra of AP- $\text{Al}_2\text{O}_3$ @C samples calcined in Ar at 650 °C (1), 1200 °C (2) and 1500 °C (3). Inset shows the section of the spectrum where the  $\text{A}_{1g}$  line of  $\text{Al}_4\text{C}_4$  is observed

Electron-acceptor sites were characterized using anthracene adsorption [30]. A  $\delta$ - $\text{Al}_2\text{O}_3$  sample obtained by aerobic calcination of SB1- $\text{Al}_2\text{O}_3$  sample at 1000 °C for 6 h was used as a reference.

Typical EPR spectra observed after adsorption of the probe molecules on the studied samples are shown in Fig. 4. The relative intensity of the signals reflects relative concentrations of electron-donor (Fig. 4A) and electron-acceptor (Fig. 4B) sites. The presented results indicate that the properties of the active sites on the oxide core in  $\text{Al}_2\text{O}_3$ @C are preserved, even after calcination at 1250 °C, and their concentration correlates with the surface of the sample obtained after this treatment.

### 3.2. $\text{ZrO}_2$ @C

$\text{ZrO}_2$  is another frequently used catalyst support. Depending on synthesis conditions and temperature, it can consist of cubic or monoclinic phase, or mixture of the two phases. The surface area dependence on the heat-treatment temperature for samples  $\text{ZrO}_2$ ,  $\text{ZrO}_2$ @C and  $\text{ZrO}_2$ @C-600 where the carbon coating was removed by 6 h calcination in air at 600 °C are shown in Fig. 5. The obtained results demonstrate a significant effect of the carbon coating on stabilization of the oxide core in  $\text{ZrO}_2$ @C system, similar to that observed for  $\text{Al}_2\text{O}_3$ @C. Comparison of the surface area of  $\text{ZrO}_2$ @C samples with that of the samples obtained after burning of the carbon shell in air (series  $\text{ZrO}_2$ @C and  $\text{ZrO}_2$ @C-600) indicates a substantial contribution of the carbon coating to the surface area measured for  $\text{ZrO}_2$ @C samples. Still, preservation of the oxide core surface area ( $\sim 20 \text{ m}^2/\text{g}$  after calcination of the core-shell material at 1400 °C) proves that the carbon coating assists in stabilization of the oxide core size. As in the case of alumina, the temperature range over which the cubic phase originally formed after synthesis is more stable in  $\text{ZrO}_2$ @C core-shell materials than in pure  $\text{ZrO}_2$  (Fig. 6). It correlates with the temperature range where relatively high surface area of the oxide is preserved.

### 3.3. $\text{LaAlO}_3$ @C

Lanthanum monoaluminate and hexaluminate are used as high-temperature catalyst supports. As the required phases of these materials are formed at high temperatures, synthesis of these materials with high specific surface area is quite complicated. Depending on the stoichiometry of the  $\text{La}_2\text{O}_3$ - $\text{Al}_2\text{O}_3$  system, either  $\beta$ -alumina structure  $\text{LaAl}_{11}\text{O}_{18}$  is formed at  $\text{La}/\text{Al} = 8.3 \%$  or  $\text{LaAlO}_3$  with a perovskite structure at  $\text{La}/\text{Al} = 50 \%$ . These phases have different temperature ranges of thermodynamic particle stability.

The formation of the  $\text{LaAlO}_3$  phases by the Pechini route takes place at 700 °C (Fig. 7). No other phases appear after the temperature increase. Only an amorphous phase containing residual carbon is observed in the  $\text{LaAlO}_3$ @C sample at the same temperature (Fig. 7).

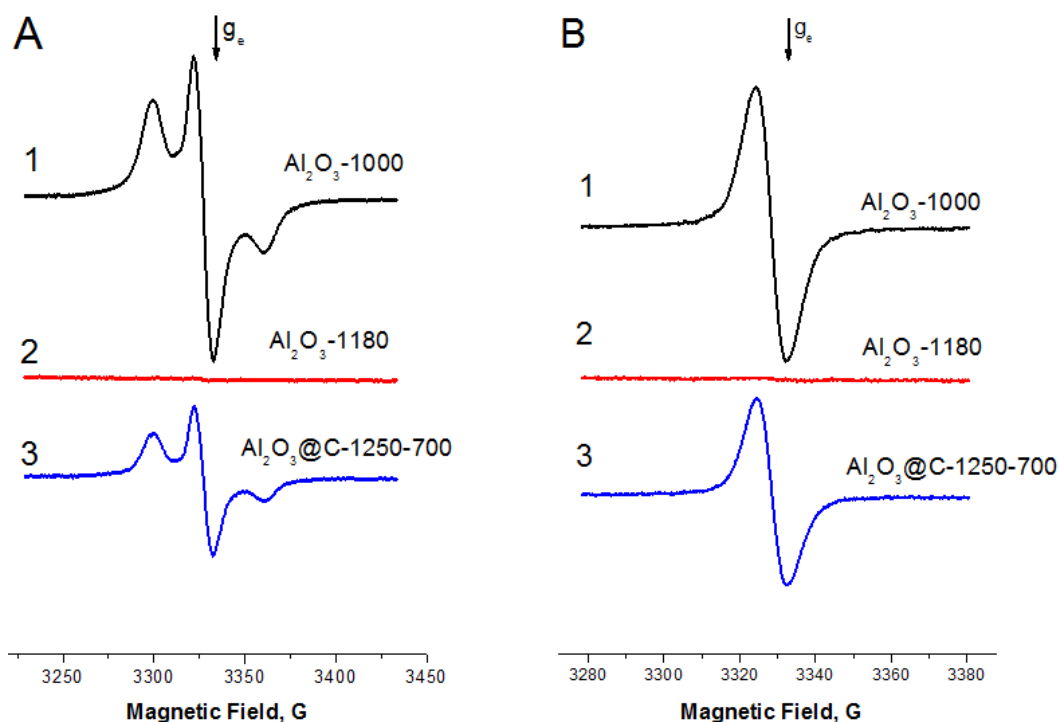


FIG. 4. EPR spectra of radicals registered after 1,3,5-trinitrobenzene (A) and anthracene (B) adsorption from toluene solution on SB1- $\text{Al}_2\text{O}_3$ -1000 and SB1- $\text{Al}_2\text{O}_3$ -1180 samples, and on the carbon-coated SB1- $\text{Al}_2\text{O}_3$ @C-1250 sample after aerobic calcination at 700 °C

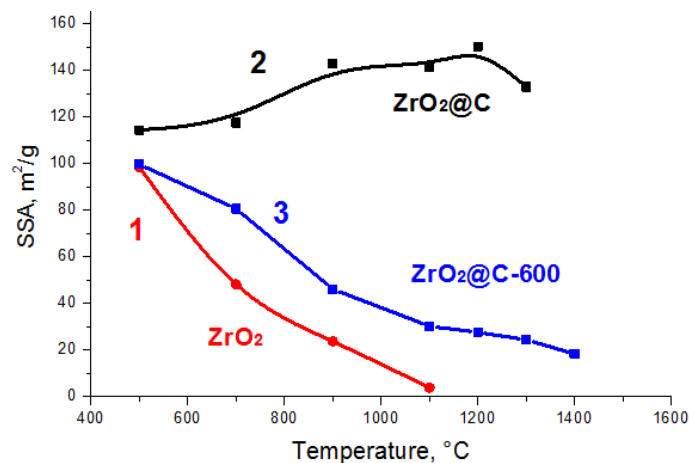


FIG. 5. Effect of calcination temperature on the surface area of  $\text{ZrO}_2$  (1),  $\text{ZrO}_2$ @C (2) and  $\text{ZrO}_2$ @C-600 sample obtained by burning of the carbon coating in air at 600 °C (3)

Preliminary experiments indicate that the presence of the carbon coating favors the formation of lanthanum hexaaluminate phase at temperatures above 1300 °C. The most likely reason for this result is the preservation of relatively small oxide core particles in the presence of carbon introduced into the material during its synthesis via the Pechini route.

### 3.4. C12A7@C

Calcium aluminate materials with different stoichiometry have been well known for some time and thus extensively studied. They are essential constituents of various cements and are sometimes used as catalyst supports. The explosive growth of interest in one such material – calcium aluminate with  $12\text{CaO}_7\text{Al}_2\text{O}_3$  composition, commonly denoted as C12A7, was inspired by the revelation of their unique chemical and electrophysical properties,

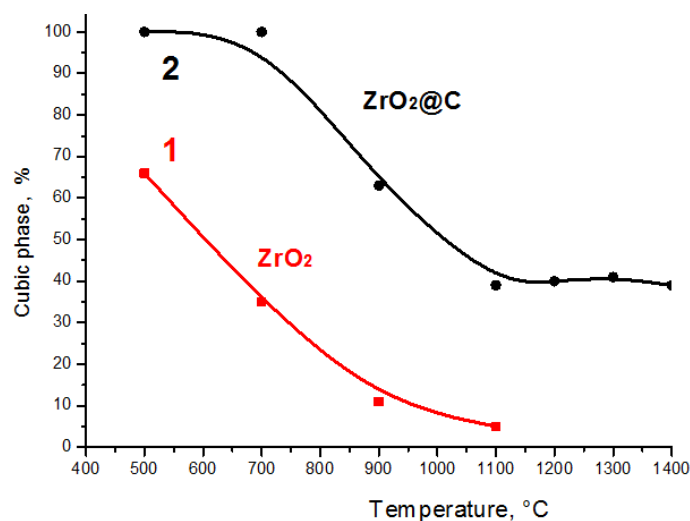


FIG. 6. Effect of calcination temperature cubic phase fraction in ZrO<sub>2</sub> (1) and ZrO<sub>2</sub>@C (2)

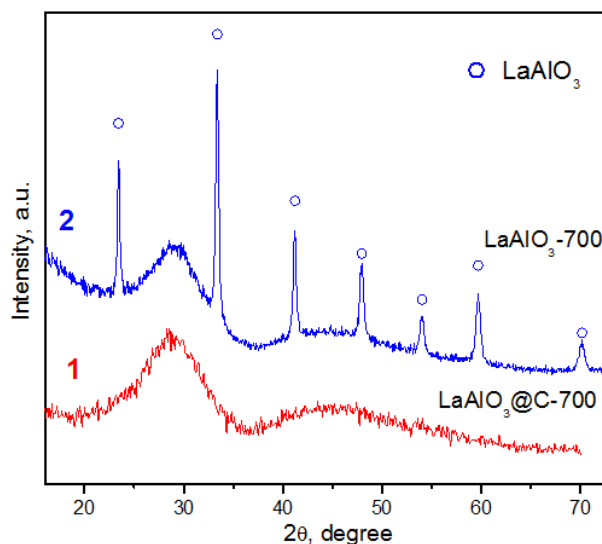


FIG. 7. XRD patterns of the LaAlO<sub>3</sub>@C-700 samples calcined at 700 °C in argon (1) and in air (2)

discovered and thoroughly investigated by Hosono et al. [31–34]. They contain a stable cationic framework  $[\text{Ca}_{24}\text{Al}_{28}\text{O}_{64}]^{4+}$  and relatively mobile anionic sublattice  $4\text{X}^-$ . The chemical and electrophysical properties of such materials can be varied over a wide range by altering the  $\text{X}^-$  anions. Their elementary cell can be written by the following formula:

$$1 \text{ unit cell} = [\text{Ca}_{24}\text{Al}_{28}\text{O}_{64}]^{4+} \cdot 4\text{X}^-, \quad \text{where } \text{X}^- = \text{H}^-, \text{O}^-, \text{O}_2^-, \text{O}^{2-}, \text{OH}^-, \text{Cl}^-, \text{F}^-, \text{e}^-.$$

Especially interesting among this list are electrified – materials with  $\text{X}^- = \text{e}^-$ . These materials have metal conductivity, unique emission, optical and chemical properties. However, their synthesis requires temperatures as high as 1600 °C, making it very difficult to prepare these materials in a finely dispersed form. Note that C12A7:e is the only bulk inorganic electrified known to date.

Structural and electrophysical features of the electrified phase formation in the carbon nanoreactor conditions in C12A7@C system have been described in detail in one of our recent publications [11, 35, 36]. One of the main obtained results is that we managed to stabilize the size of the oxide core in C12A7@C at ~ 100 nm, even at temperatures substantially exceeding the C12A7 melting point (1415 °C). The small particle size substantially facilitates diffusion process in this material making it possible to decrease the temperatures required for migration of anions and electrified formation.

The XRD data presented in Fig. 8 demonstrate that dispersed C12A7 phase can be synthesized in C12A7@C using the procedure described in the Experimental section starting from temperatures as low as 500 – 600 °C.

However, even after the formation of the electride state at 1380 °C, the size of the oxide core in such material is preserved in the range of 100 – 150 nm. Fig. 9 presents an HRTEM image of a typical particle of such material. Several graphene layers can be observed on the particle surface.

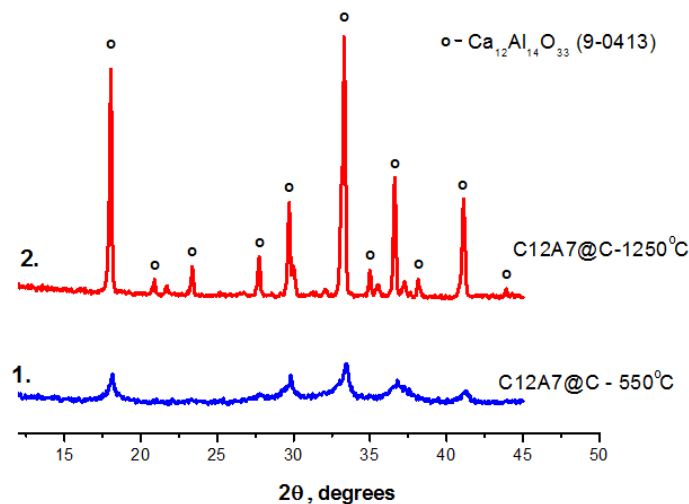


FIG. 8. XRD patterns of C12A7@C samples after calcination at different temperatures in argon flow

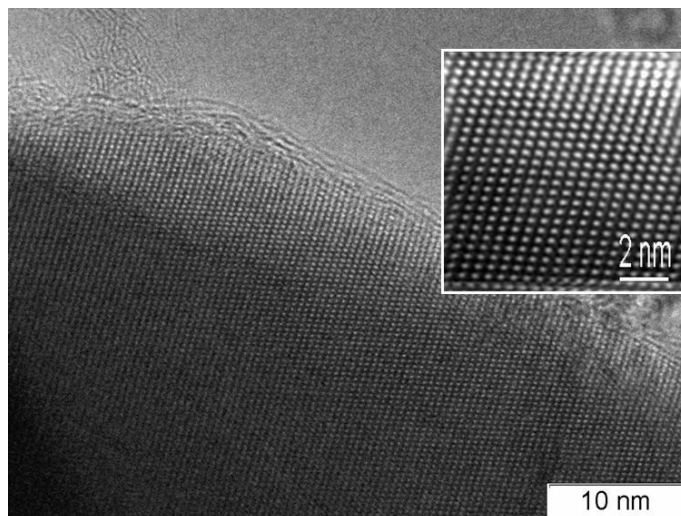


FIG. 9. HRTEM image of C12A7@C sample after calcination at 1380 °C under argon. The inset shows a section of the image after Fourier filtration

One possible application for finely dispersed C12A7 materials is their use in catalytic and adsorption technologies. Therefore, it was important to incorporate various active sites on their surface. No such information was available in the literature before this study.

EPR spectra observed after adsorption of TNB, phenothiazine and diphenylamine from toluene solutions on C12A7-600 (A) and Al<sub>2</sub>O<sub>3</sub>-720 (B) samples activated at 500 °C are presented in Fig. 10. The alumina sample prepared using the same precursor was chosen as a reference sample because C12A7 contains a substantial amount of alumina, whereas electron-donor and electron-sites on the alumina surface have been extensively characterized previously [16,18,30]. Although the surface area of C12A7-600 was lower than that of the alumina sample (80 vs. 200 m<sup>2</sup>/g), it is sufficiently high for its application as a catalyst support.

All the used probe molecules have nitrogen atoms, and their EPR spectra feature 3-component signals due to hyperfine splitting on a nitrogen atom with  $S = 1$  with frozen rotation. The spectrum observed after TNB

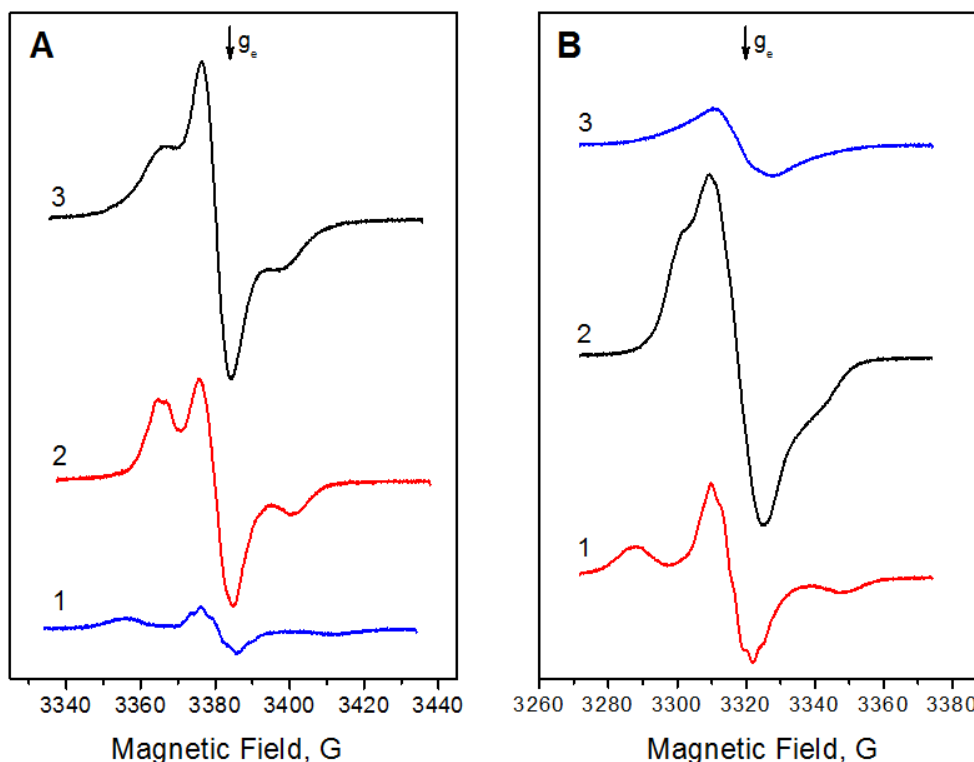


FIG. 10. EPR spectra observed on the surface of C12A7-600 (A) and Al<sub>2</sub>O<sub>3</sub>-720 (B) activated at 500 °C after adsorption of 1,3,5-trinitrobenzene (1), phenothiazine (2) and diphenylamine (3) from toluene solutions

adsorption on C12A7-600 is similar to the one observed after TNB adsorption on alumina with somewhat smaller  $A_{zz}$  (27 G vs. 30 G on Al<sub>2</sub>O<sub>3</sub>). It was previously attributed to TNB radical anion forming an ion pair with an aluminum cation [18]. This means that the studied C12A7-600 also has electron-donor sites of the same type as those present on the Al<sub>2</sub>O<sub>3</sub> surface. However, their concentration was ca. 8.5-fold lower than on the reference alumina sample when normalized to the sample weight or about 3.5-fold lower when normalized to the surface area.

Phenothiazine has very low ionization potential of approximately 6.8 eV; as a result, it can be used for characterization of very weak electron-acceptor sites. Its adsorption on Al<sub>2</sub>O<sub>3</sub> results in the appearance of a poorly-resolved three-component spectrum with  $A_{zz} = 20$  G attributable to its radical cations. On C12A7-600, the spectrum resolution was much better, with slightly smaller hyperfine constant (18 G), whereas the spectrum intensity, when normalized to the surface area, was approximately the same. So, C12A7-600 has weak electron-acceptor sites on its surface, and their concentration is approximately the same as on the Al<sub>2</sub>O<sub>3</sub> surface.

Diphenylamine also has low ionization potential, equal to 7.2 eV and can be ionized to its radical cations on the surface of many acidic materials that have electron-acceptor sites. Apparently, this is what happens after its adsorption on Al<sub>2</sub>O<sub>3</sub>-720, where a wide unresolved spectrum is observed. It resembles the one earlier reported after diphenylamine on H-ZSM-5 zeolite [37] where it was attributed to a mixture of primary diphenylamine radical cations and products of their transformations.

However, in solution, diphenylamine is well known to form quite stable diphenyloxyl nitroxyl radicals in the presence of peroxides, apparently, due to reaction with hydroxyls resulting from their decomposition. The spectrum observed after diphenylamine adsorption on the surface of C12A7-600 is a triplet with  $A_{zz} = 16$  G, which can be attributed to diphenyloxyl nitroxyl radicals adsorbed onto its surface. Remarkably, their concentration normalized to the surface area exceeded the concentration of radical species observed on the Al<sub>2</sub>O<sub>3</sub>-720 sample by roughly 3-fold. This means that the surface of activated C12A7 has a significant concentration of active OH radicals. It seems to be a specific feature of this material related to its unique structure that merits further investigation, as we did not observe similar signals on other oxide materials that we studied.

#### 4. Conclusion

It has been demonstrated that it is possible to stabilize dimensions of oxide nanoparticles with different chemical composition and prevent their sintering at high temperatures by depositing a carbon coating on their surface. Such approach appears to be fairly universal and can be used for various oxide materials in a wide temperature range below the temperature of the oxide core carbothermal reduction. The carbon coating prevents direct contact between the oxide nanoparticles, thus, preventing their sintering. Before our studies, possible effects of the particle size on the thermodynamic stability of different phases of  $\text{TiO}_2$  (anatase-rutile) and  $\text{Al}_2\text{O}_3$  (gamma, delta and alpha phases) were known. For  $\text{TiO}_2@\text{C}$  and  $\text{Al}_2\text{O}_3@\text{C}$ , the low-temperature phases of the oxide core could be preserved up to the temperature where they reacted with their carbon shell. So, for  $\text{TiO}_2@\text{C}$  the anatase phase is stable to 800 °C. Above this temperature, the carbon shell is destroyed, and non-stoichiometric titanium oxide phases are formed. For  $\text{Al}_2\text{O}_3@\text{C}$  the corundum phase is formed only at temperatures above 1400 °C, when decomposition of the carbon shell due to its interaction with the oxide core material begins. Based on the results obtained in this study for zirconium oxide and lanthanum aluminate, the carbon shell also can stabilize both the size and phase composition.

The data presented for the C12A7@C material exemplify the possibility of stabilizing the size of the oxide core, even above its melting temperature. Apparently the carbon shell prevents interaction between the droplets of the melted oxide core. Meanwhile, the carbon coating synthesized using the reported procedure appears to be permeable for molecules of the gas phase. This makes it possible to perform synthesis of new solid products by reaction of the oxide core material with gaseous reagents.

Carbon coating is only one of several possible variations of a nanoreactor shell for oxide nanoparticles. Such shell is not always inert, as is shown in carbothermal reduction processes. Also it is absolutely inapplicable for reactions at high temperatures in the presence of oxygen. The search of other materials that could function as such nanoreactor where similar processes could be carried out in the presence of air is important for many practical applications. One possible approach to creating air-stable materials with an oxide core is the synthesis of core-shell structures with an oxide shell. The first results we obtained using such shells as  $\text{SiO}_2$  and  $\text{MgO}$  for this purpose seemed to be promising.

#### Acknowledgements

This study was supported by Russian Science Foundation, Project 16-13-10168.

#### References

- [1] Park J.C., Bang J.U., et al. Ni@ $\text{SiO}_2$  yolk-shell nanoreactor catalysts: High temperature stability and recyclability. *J. Mater. Chem.*, 2010, **20** (7), P. 1239–1246.
- [2] Chaudhuri R.G., Paria S. Core/Shell Nanoparticles: Classes, Properties, Synthesis Mechanisms, Characterization, and Applications. *Chem. Rev.*, 2012, **112** (4), P. 2373–2433.
- [3] Yang W.L., Wang Y.R., et al. Carbon nanocoating: an effective nanoreactor towards well-defined carbon-coated GaN hollow nanospindles. *Nanoscale*, 2014, **6** (6), P. 3051–3054.
- [4] Plumejeau S., Alauzun J.G., Boury B. Hybrid metal oxide@biopolymer materials precursors of metal oxides and metal oxide-carbon composites. *J. Ceram. Soc. Jpn.*, 2015, **123** (1441), P. 695–708.
- [5] Li B., Nam H., et al. Nanoreactor of Nickel-Containing Carbon-Shells as Oxygen Reduction Catalyst. *Adv. Mater.*, 2017, **29** (7), 1605083.
- [6] Lee J., Kim S.M., Lee I.S. Functionalization of hollow nanoparticles for nanoreactor applications. *Nano Today*, 2014, **9** (5), P. 631–667.
- [7] Bedilo A.F., Sigel M.J., et al. Synthesis of carbon-coated MgO nanoparticles. *J. Mater. Chem.*, 2002, **12** (12), P. 3599–3604.
- [8] Bedilo A.F., Shuvarakova E.I., et al. Effect of Modification with Vanadium or Carbon on Destructive Sorption of Halocarbons over Nanocrystalline MgO: The Role of Active Sites in Initiation of the Solid-State Reaction. *J. Phys. Chem. C*, 2014, **118** (25), P. 13715–13725.
- [9] Yakovlev I.V., Volodin A.M., et al. Stabilizing effect of the carbon shell on phase transformation of the nanocrystalline alumina particles. *Ceram. Int.*, 2018, **44** (5), P. 4801–4806.
- [10] Volodin A., Bedilo A.F., et al. Nanocrystalline carbon coated alumina with enhanced phase stability at high temperatures. *RSC Adv.*, 2017, **7** (86), P. 54852–54860.
- [11] Volodin A.M., Zaikovskii V.I., et al. Synthesis of nanocrystalline calcium aluminate C12A7 under carbon nanoreactor conditions. *Mater. Lett.*, 2017, **189**, P. 210–212.
- [12] Volodin A.M., Bedilo A.F., et al. Carbon nanoreactor for the synthesis of nanocrystalline high-temperature oxide materials. *Nanotechnologies in Russia*, 2014, **9** (11), P. 700–706.
- [13] Flockhart B.D., Leith I.R., Pink R.C. Evidence for the redox nature of the surface of catalytic aluminas. *J. Catal.*, 1967, **9** (1), P. 45–50.
- [14] Garcia H., Roth H.D. Generation and reactions of organic radical cations in zeolites. *Chem. Rev.*, 2002, **102** (11), P. 3947–4007.
- [15] Bedilo A.F., Volodin A.M. Radical cations of aromatic molecules with high ionization potentials on the surfaces of oxide catalysts: Formation, properties, and reactivity. *Kinet. Catal.*, 2009, **50** (2), P. 314–324.
- [16] Bedilo A.F., Shuvarakova E.I., Rybinskaya A.A., Medvedev D.A. Characterization of Electron-Donor and Electron-Acceptor Sites on the Surface of Sulfated Alumina Using Spin Probes. *J. Phys. Chem. C*, 2014, **118** (29), P. 15779–15794.

- [17] Flockhart B.D., Leith I.R., Pink R.C. Electron-transfer at alumina surfaces. Part 3 – Reduction of aromatic nitro-compounds. *Trans. Faraday Soc.*, 1970, **66**, P. 469–476.
- [18] Medvedev D.A., Rybinskaya A.A., et al. Characterization of electron donor sites on Al<sub>2</sub>O<sub>3</sub> surface. *Phys. Chem. Chem. Phys.*, 2012, **14** (8), P. 2587–2598.
- [19] Shuvarakova E.I., Bedilo A.F., Chesnokov V.V., Kenzhin R.M. Dehydrochlorination of 1-Chlorobutane Over Nanocrystalline MgO: The Role of Electron-Acceptor Sites. *Top Catal.*, 2018, In Press, DOI: 10.1007/s11244-018-1000-8.
- [20] Khaleel A.A., Klabunde K.J. Characterization of aerogel prepared high-surface-area alumina: In situ FTIR study of dehydroxylation and pyridine adsorption. *Chem. Eur. J.*, 2002, **8** (17), P. 3991–3998.
- [21] Carnes C.L., Kapoor P.N., Klabunde K.J., Bonevich J. Synthesis, characterization, and adsorption studies of nanocrystalline aluminum oxide and a bimetallic nanocrystalline aluminum oxide/magnesium oxide. *Chem. Mater.*, 2002, **14** (7), P. 2922–2929.
- [22] Sadykov V., Usoltsev V., et al. Functional nanoceramics for intermediate temperature solid oxide fuel cells and oxygen separation membranes. *J. Eur. Ceram. Soc.*, 2013, **33** (12), P. 2241–2248.
- [23] Bolshov V.A., Volodin A.M., et al. Radical Intermediates in the Photoinduced Formation of Benzene Cation-Radicals Over H-Zsm-5 Zeolites. *J. Phys. Chem.*, 1994, **98** (31), P. 7551–7554.
- [24] Mchale J.M., Auroux A., Perrotta A.J., Navrotsky A. Surface energies and thermodynamic phase stability in nanocrystalline aluminas. *Science*, 1997, **277** (5327), P. 788–791.
- [25] Castro R.H.R., Ushakov S.V., et al. Surface energy and thermodynamic stability of gamma-alumina: Effect of dopants and water. *Chem. Mater.*, 2006, **18** (7), P. 1867–1872.
- [26] Castro R.H.R. On the thermodynamic stability of nanocrystalline ceramics. *Mater. Lett.*, 2013, **96**, P. 45–56.
- [27] Ferrari A.C., Robertson J. Interpretation of Raman spectra of disordered and amorphous carbon. *Phys. Rev. B*, 2000, **61** (20), P. 14095–14107.
- [28] Tuinstra F., Koenig J.L. Raman Spectrum of Graphite. *J. Chem. Phys.*, 1970, **53** (3), P. 1126–1130.
- [29] Kennedy J.L., Drysdale T.D., Gregory D.H. Rapid, energy-efficient synthesis of the layered carbide, Al<sub>4</sub>C<sub>3</sub>. *Green Chem.*, 2015, **17** (1), P. 285–290.
- [30] Zotov R.A., Molchanov V.V., Volodin A.M., Bedilo A.F. Characterization of the active sites on the surface of Al<sub>2</sub>O<sub>3</sub> ethanol dehydration catalysts by EPR using spin probes. *J. Catal.*, 2011, **278** (1), P. 71–77.
- [31] Hayashi K., Matsuishi S., Kamiya T., Hirano M. Light-induced conversion of an insulating refractory oxide into a persistent electronic conductor. *Nature*, 2002, **419** (6906), P. 462–465.
- [32] Matsuishi S., Toda Y., et al. High-density electron anions in a nanoporous single crystal, [Ca<sub>24</sub>Al<sub>28</sub>O<sub>64</sub>]<sup>4+</sup>4e<sup>-</sup>. *Science*, 2003, **301** (5633), P. 626–629.
- [33] Kitano M., Inoue Y., et al. Ammonia synthesis using a stable electrified as an electron donor and reversible hydrogen store. *Nature Chem.*, 2012, **4** (11), P. 934–940.
- [34] Kim S.W., Hosono H. Synthesis and properties of 12CaO 7Al<sub>2</sub>O<sub>3</sub> electrified: review of single crystal and thin film growth. *Philosophical Magazine*, 2012, **92** (19–21), P. 2596–2628.
- [35] Yakovlev I.V., Volodin A.M., et al. Structure of Carbon-Coated C12A7 Electrified via Solid-State NMR and DFT Calculations. *J. Phys. Chem. C*, 2017, **121** (40), P. 22268–22273.
- [36] Zaikovskii V.I., Volodin A.M., et al. Effect of carbon coating on spontaneous C12A7 whisker formation. *Appl. Surf. Sci.*, 2018, **444**, P. 336–338.
- [37] Garcia H., Marti V., et al. Generation and conversions of aromatic amine radical cations in acid zeolites. *Phys. Chem. Chem. Phys.*, 2001, **3** (14), P. 2955–2960.

## Formation mechanism of core-shell nanocrystals obtained via dehydration of coprecipitated hydroxides at hydrothermal conditions

O. V. Almjashaeva<sup>1,2</sup>, A. A. Krasilin<sup>2</sup>, V. V. Gusarov<sup>2</sup>

<sup>1</sup>Saint-Petersburg Electrotechnical University “LETI”, Saint-Petersburg, 197376 Russia

<sup>2</sup>Ioffe Institute, Saint-Petersburg, 194021, Russia

almjashaeva@mail.ru, ikrasilin@mail.ioffe.ru, victor.v.gusarov@gmail.com

DOI 10.17586/2220-8054-2018-9-4-568-572

Here, we propose a formation mechanism for core-shell nanoparticles by self-organization in coprecipitated mixed hydroxides under hydrothermal conditions. A thermodynamic reason for this process is because of a decrease in the components' solubilities together with an increase of structure's dimension. As a particular example of such type of behavior, we investigate core-shell nanoparticle formation in the  $ZrO_2$ - $Y_2O_3$ - $H_2O$  system.

**Keywords:** core-shell nanoparticles, hydrothermal synthesis, multi-component systems, solid solution, zirconia, formation mechanism.

*Received: 16 August 2018*

### 1. Introduction

Core-shell nanoparticles have garnered substantial interest due to the potential of their application in the field of biomedicine [1–3], catalysis [4, 5], sensorics [6, 7], luminophores [8], and materials for optics [9, 10]. A large number of papers [1–12], that have been published recently, cover aspects of chemical synthesis, structure and properties investigation of the nanoparticles.

There are two means of core-shell nanoparticle synthesis. The first one includes various types of application of the nanosized layers on the initial nanoparticle surface. This can be done by precipitation from a gaseous phase, for example, by CVD, PVD, ALD (ML) methods [12–17]; or by precipitation from a liquid phase by SILD and LbL methods [18, 19]. Layers and shells can be obtained by transport from one particle to another [20–23] as a result of non-autonomous (surface) phase movement [23]. However, this group of methods is not limited to the aforementioned techniques.

Another group relies on the effect of substance segregation inside the particle with redistribution of the components between the volume and the surface [24–26]. Despite the fact that the thermodynamic theory describing the component redistribution between autonomous (volume) and non-autonomous (surface) phase is well-developed [27], in certain cases there is a dramatic discrepancy between experimentally observed effects and their thermodynamic predictions. Among these problems, there is a case of substantial difference between the measured shell thickness, obtained after the segregation, and the equilibrium thickness of the non-autonomous phase [28]. In particular, this feature was observed for oxide nanoparticles in  $ZrO_2$ - $Y_2O_3$ - $H_2O$  ( $M=Y, In, Gd$ ) system [25, 26], produced by the hydrothermal treatment of coprecipitated hydroxides.

The aim of this work is to model processes which lead to the formation of core-shell structures through decomposition of initial substances and formation of nanoparticles – nuclei for the new nanostructured phase.

### 2. Model

Let us consider the case, in which initial substance forms quasi-2D layers of variable composition situated some substantial distance from each other and randomly oriented. In such a manner, chemical composition, structure, and properties do not depend on the layers' relative position. Distancing of quasi-2D layers owes to adsorption of molecules on their surface and their immersion into an isotropic medium, for example, water. Removal of adsorbates or liquid environment between the layers initiates distance decrease in between them. In turn, this leads to the layers' rearrangement, correlation in their structural changes and, as a consequence, their properties. In such a manner, 3D particles can be formed involving oriented attachment mechanism [29–32]. Fig. 1 shows the transformations described above. Let us assume that quasi-2D layers are of nanometer or sub-nanometer thick, and the width of layers is at least in order of magnitude larger than the thickness. At the same time, the width stays in nanometer scale, so the particles formed in oriented attachment process can be considered as nanoparticles. For the sake of simplicity, but without loss of generality of principle derivations, present research focuses on transformations occurring in binary solid solutions.

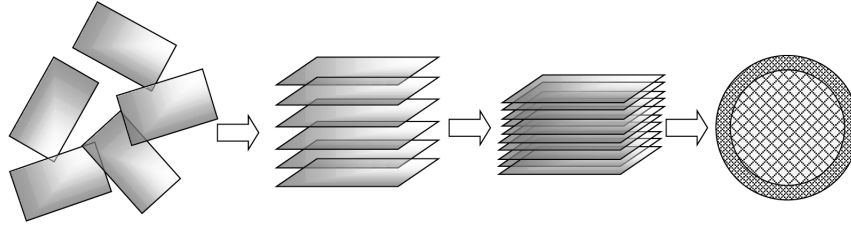


FIG. 1. Scheme of formation of c-ZrO<sub>2</sub>(Y<sub>2</sub>O<sub>3</sub>) nanoparticles during dehydration of coprecipitated hydroxides under hydrothermal conditions

For the case of two-component phases of variable composition and different dimension, the Gibbs energy of mixing is:

$$G^{(\nu)M} = G^{(\nu)EX}(x_1, x_2; \{a_i\}) - TS^{(\nu)ID}(x_1, x_2), \quad (1)$$

where  $x_1, x_2 = 1 - x_1$  are molar contents of components **1** and **2** in phases of variable composition; upper index  $\nu = 1, 2, 3$  shows dimension of corresponding phases:  $\nu = 1$  is for quasi-1D,  $\nu = 2$  is for quasi-2D, and  $\nu = 3$  is for 3D one (in general,  $\nu$  can be non-integer denoting structures with certain fractal dimension);  $T$  is temperature, K;  $S^{(\nu)ID}$  is configuration entropy of ideal state [33];  $G^{(\nu)EX}(x_1, x_2; \{a_i\})$  is the excess Gibbs energy of mixing determined by configuration entropy of ideal state; and  $\{a_i\}$  is a number of parameters included in model equations [33]. For the most basic case of ideal mixture of components **1** and **2**  $S^{ID} \equiv S^I = -R(x_1 \ln x_1 + x_2 \ln x_2)$ . For the case  $S^{ID} \equiv S^I$   $G^{EX} \equiv G^E$ , i.e. the equation (1) coincides with the commonly used equation for the excess Gibbs energy of mixing:  $G^E = G^M + TS^I$ .

It can be further simplified by assuming that  $S^{ID} = S^I$ . In making this assumption, the difference between the ideal entropy ( $S^I$ ) and configuration entropy of the proposed idealized state, which would, probably, better reflect the state of variable composition ( $S^{ID}$ ), transfers to the value  $G^E = G^{EX} + T(S^I - S^{ID})$ . One should expect to see the highest difference between the  $S^I$  and  $S^{ID}$  ( $G^E$  and  $G^{EX}$ , correspondingly) values in case the phase of variable composition is formed by components with different oxidation states [33, 34], because this leads to formation of defects like vacancies or ions in the interstitial space of the crystal lattice.

The 1D solid solution ( $\nu = 1$ ), as it was shown in [35], withholds from segregation at any temperature: this means that  $G^E = 0$ . Urusov [34] noted that the  $G^{(2)E}$  value for quasi-2D structures is several times smaller than the  $G^{(3)E}$  value for the 3D ones. One can conclude that the solid solution components solubility decreases with increase of the structure dimension (1D to 3D). There is a probability that, during the nanoparticle growth, the substance separated out of solid solution will form the shell on the particle surface. Next, we consider the possibility of the core-shell structure formation involving the proposed mechanism during dehydration in ZrO<sub>2</sub>-Y<sub>2</sub>O<sub>3</sub>-H<sub>2</sub>O system.

### 3. Results

Degtyarev and Voronin [36] calculated the thermodynamic parameters of coexisting phases in the ZrO<sub>2</sub>-Y<sub>2</sub>O<sub>3</sub> system. Dehydration of coprecipitated zirconium and yttrium hydroxides yields oxide nanoparticles with fluorite structure, which is characteristic for the high-temperature area of the ZrO<sub>2</sub>-Y<sub>2</sub>O<sub>3</sub> phase diagram. Thus, we used high-temperature data for thermodynamic analysis of low-temperature area of the phase diagram according to adopted equations proposed by Degtyarev and Voronin in [36]:

$$G^{EX} = x_1(1 - x_1)C(A_0 + A_1T + B_0x_1), \quad (2)$$

$$S^{ID} = -R[2(1 - x_1) \ln(1 - x_1) + 3x_1 \ln x_1 + (4 - x_1) \ln(4 - x_1) - 4(1 - x_1) \ln 4 - 3x_1 \ln x_3], \quad (3)$$

where  $x_1$  is molar content of YO<sub>1.5</sub>;  $R = 8.31$  is the gas constant, J/(mol·K);  $A_0 = -13273R$ ,  $A_1 = 5.324R$ , and  $B_0 = 12383R$  are numerical parameters;  $C^{(\nu)} = 0..1$  is a structure dimension depended coefficient.

Extrapolation of these data to the low-temperature area allows one to predict phase separation limits in cubic metastable phases in the ZrO<sub>2</sub>-Y<sub>2</sub>O<sub>3</sub> system (Fig. 2a, curves 1). An over-estimation of the limits in comparison to the experimental results [25] can be related with the extrapolation error. Since the Zr<sub>1-x</sub>Y<sub>x</sub>O<sub>2-0.5x</sub> nanocrystals grow from quasi-2D fluorite-like layers [29] during the dehydration, the yttrium content in the initial quasi-2D layer should be substantially higher than that in the 3D phase. Fig. 2b shows curves of ZrO<sub>2</sub>-Y<sub>2</sub>O<sub>3</sub> solid solution decomposition calculated in accordance with the assumption of the Gibbs energy decrease with decrease of the phase dimension ( $\nu = 3 \rightarrow \nu = 2$ ), which is equal to decrease of the coefficient  $C^{(\nu)}$  in (2).

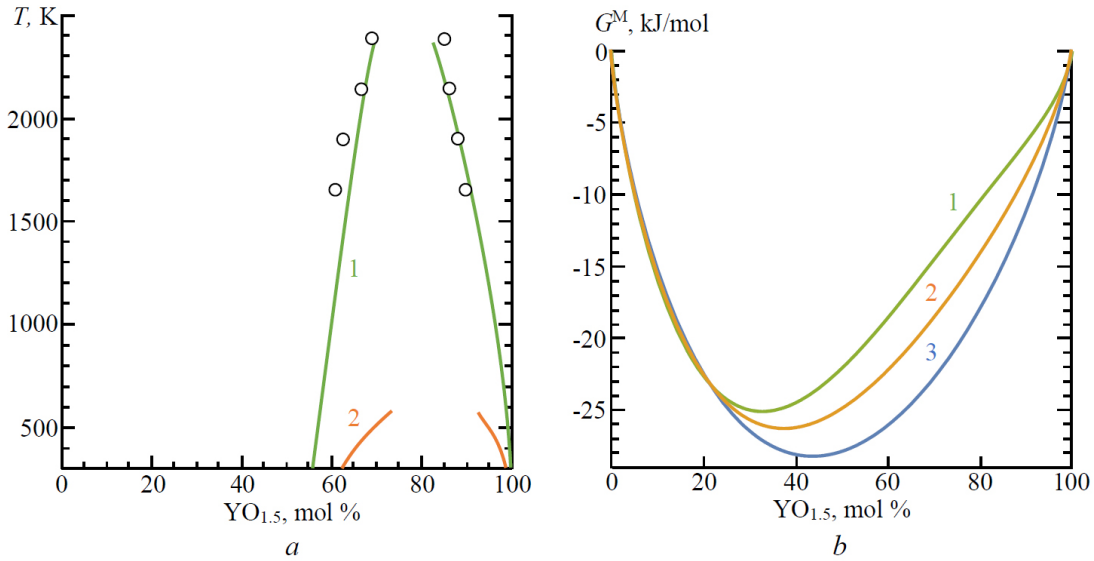


FIG. 2. a) Part of the  $ZrO_2$ - $YO_{1.5}$  calculated phase diagram. Points denote experimental data adopted from the paper [36]. Curve 1 was calculated at  $C^\nu = 1$ , curve 2 was calculated at  $C^\nu = 0.6$  (see equations (2) and (3)). b) The Gibbs energy of mixing  $G^M$  at 1 -  $C^\nu = 1$ , 2 -  $C^\nu = 0.6$ , 3 -  $C^\nu = 0.2$

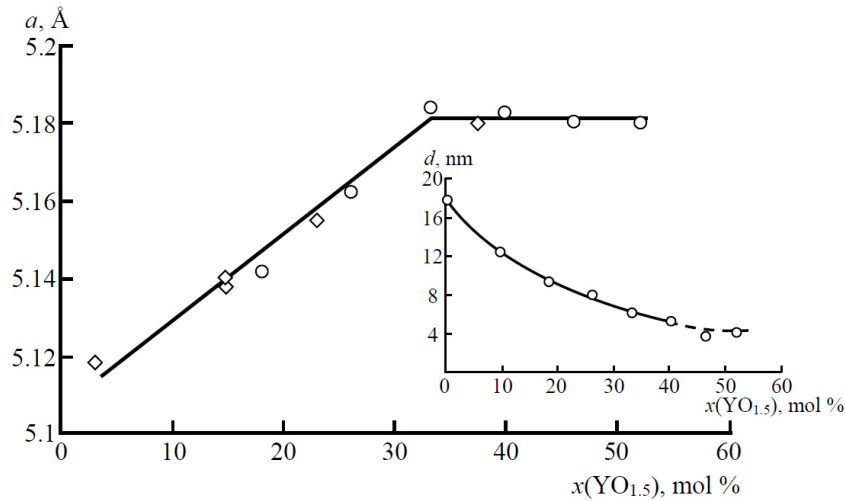


FIG. 3. Dependence of the parameters of the unit cell of the phase based on  $c$ - $ZrO_2$  with the fluorite structure on the content of  $YO_{1.5}$  in the system. The inset: the dependence of the crystallite size of  $c$ - $ZrO_2$  on the  $YO_{1.5}$  content

Summarizing the results for the thermodynamic analysis of the dimensions of the regions where solid solutions exist in quasi-2D and 3D phases, we conclude that, in the formation of nanocrystals based on phases of variable composition, by fusion of quasi-2D layers of variable composition, the solid solution can split into two coexisting phases. If the amount of matter released is not sufficient to form a crystalline nucleus of a new phase, it is possible to form core-shell structures, as shown on Fig. 1. Almjashaeva et al. [25] showed that the “crystal  $c$ - $ZrO_2/YO_{1.5}$  fluorite solid solution core – amorphous  $Y_2O_3$  shell” particles were formed in the  $ZrO_2$ - $Y_2O_3$ - $H_2O$  system under hydrothermal conditions. The results of the nanoparticles’ composition and size parameters analysis (Fig. 3,4) demonstrate qualitative correlation with the thermodynamic data on the change in the solubility of components during the transition from quasi-2D to 3D structures. It should be noted that this explanation is, most likely, also applicable for the case of core-shell nanoparticles formation in another  $ZrO_2$ - $M_2O_3$ - $H_2O$  systems  $M$  – In, Gd) [25,26].

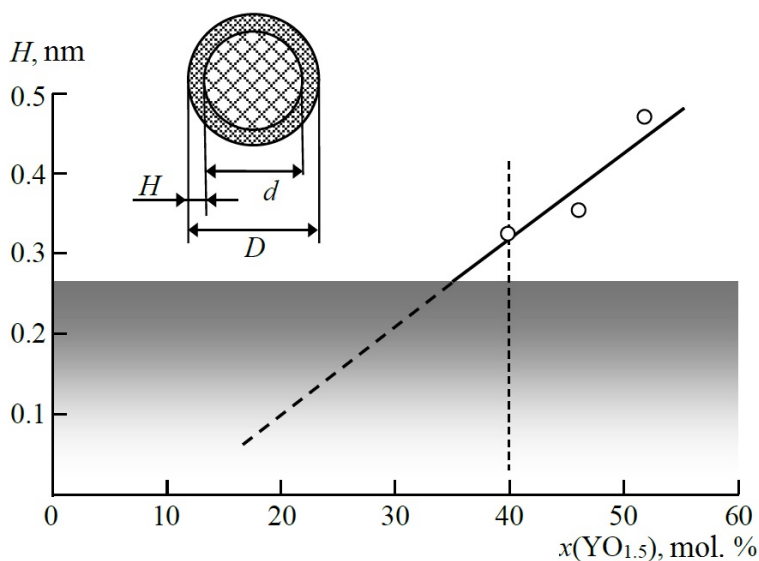


FIG. 4. Dependence of the thickness of the amorphous shell on the content of  $\text{YO}_{1.5}$  in the system

Thus, the mechanism for the formation of core-shell nanostructures (Fig. 1) by decreasing the mutual solubility of the components with increase of the structure dimension can be considered as one of the more promising means of such nanoparticle design.

#### Acknowledgement

The research was supported by Russian Science Foundation grant 16-13-10252.

#### References

- [1] Chatterjee K., Sarkar S., Rao K.J., Paria S. Core/shell nanoparticles in biomedical applications. *Adv. Colloid Interface Sci.*, 2014, **209**, P. 8–39.
- [2] Almjashveva O.V., Garabadzhiu A.V., Kozina Yu.V., Litvinchuk L.F., Dobritsa V.P. Biological effect of zirconium dioxide-based nanoparticles. *Nanosyst.: Phys. Chem. Math.*, 2017, **8**(3), P. 391–396.
- [3] Rosenholm J.M., Zhang J., Sun W., H. Gu Large-pore mesoporous silica-coated magnetite core-shell nanocomposites and their relevance for biomedical applications. *Microp. Mesop. Mater.*, 2011, **145**(1-3), P. 14–20.
- [4] Lee C., Shin K., Lee Y.J. Jung C. Lee H.M. Effects of shell thickness on Ag-Cu<sub>2</sub>O core-shell nanoparticles with bumpy structures for enhancing photocatalytic activity and stability. *Catalysis Today*, 2017, **303**, P. 313–319.
- [5] Gawande M.B., Goswami A., Asefa T., Guo H., Biradar A.V., Peng D.-L., Zboril R., Varma R.S. Core-shell nanoparticles: synthesis and applications in catalysis and electrocatalysis. *Chem. Soc. Rev.*, 2015, **44**(21), P. 7540–7590.
- [6] Khoshroo A., Hosseinzadeh L., Sobhani-Nasab A., Rahimi-Nasrabadi M., Ehrlich H. Development of electrochemical sensor for sensitive determination of oxazepam based on silver-platinum core-shell nanoparticles supported on graphene. *J. Electroanal. Chem.*, 2018, **823**, P. 61–66.
- [7] Majhi S.M., Naik G.K., Lee H.-J., Song H.-G., Lee C.-R., Lee I.-H., Yu Y.-T. Au@NiO core-shell nanoparticles as a p-type gas sensor: Novel synthesis, characterization, and their gas sensing properties with sensing mechanism. *Sens. Actuators B: Chem.*, 2018, **268**, P. 223–231.
- [8] Bugrov A.N., Smyslov R.Yu., Zavialova A.Yu., Kirilenko D.A., Pankin D.V. Phase composition and photoluminescence correlations in nanocrystalline  $\text{ZrO}_2:\text{Eu}^{3+}$  phosphors synthesized under hydrothermal conditions. *Nanosyst.: Phys. Chem. Math.*, 2018, **9**(3), P. 378–388.
- [9] Astafyeva L.G., Pustovalov V.K., Fritzsche W. Tuning light concentration inside plasmonic core-shell nanoparticles during laser irradiation. *Photonics Nanostruct.*, 2017, **26**, P. 35–40.
- [10] Li Y., Shao L., Zhong F., Ding P., Chu B. Luo F., Xu K., Zeng F., Du Y. Light control based on unidirectional scattering in metal-dielectric core-shell nanoparticles. *Opt. Commun.*, 2018, **426**, P. 483–489.
- [11] Klekotka U., Piotrowska B., Satu-la D, Kalska-Szostko B. Modified ferrite core-shell nanoparticles magneto-structural characterization. *Appl. Surf. Sci.*, 2018, **444**, P. 161–167.
- [12] Chaudhuri R.G., Paria S. Core/Shell nanoparticles: classes, properties, synthesis mechanisms, characterization, and applications. *Chem. Rev.*, 2012, **112**(4), P. 2373–2433.
- [13] Srdić V.V.; Mojić B., Nikolić M., Ognjanović S. Recent progress on synthesis of ceramics core/shell nanostructures. *Process. Appl. Ceram.*, 2013, **7**(2), P. 45–62.
- [14] Nomoev A.V., Bardakhanov S.P., Schreiber M., Bazarova D.G., Romanov N.A., Baldanov B.B., Radnaev B.R., Syzrantsev V.V. Structure and mechanism of the formation of core-shell nanoparticles obtained through a one-step gas-phase synthesis by electron beam evaporation. *Beilstein J. Nanotechnol.*, 2015, **6**, P. 874–880.

- [15] Gusarov V.V., Malkov A.A., Malygin A.A., Suvorov S.A. Thermally activated transformations of 2d nonautonomous phases and contraction of polycrystalline oxide materials. *Inorg. Mater.*, 1995, **31**(3), P. 320–323.
- [16] Gusarov V.V., Malkov A.A., Ishutina Z.N., Malygin A.A. Phase formation in a nanosize silicon oxide film on the surface of aluminum oxide. *Tech. Phys. Lett.*, 1998, **24**(1), P. 1–3.
- [17] Krasilin A.A., Bodalyov I.S., Malkov A.A., Khrapova E.K., Maslennikova T.P., Malygin A.A. On an adsorption/photocatalytic performance of nanotubular  $\text{Mg}_3\text{Si}_2\text{O}_5(\text{OH})_4/\text{TiO}_2$  composite. *Nanosyst.: Phys. Chem. Math.*, 2018, **9**(3), P. 410–416.
- [18] Korotcenkov G., Gulina L.B., Cho B.K., Han S.H., Tolstoy V.P.  $\text{SnO}_2$ -Au nanocomposite synthesized by successive ionic layer deposition method: Characterization and application in gas sensors. *Mater. Chem. Phys.*, 2011, **128**(3), P. 433–441.
- [19] Lee D.K., Song Y., Tran V.T., Kim J., Park E.Y., Lee J. Preparation of concave magnetoplasmonic core-shell supraparticles of gold-coated iron oxide via ion-reducible layer-by-layer method for surface enhanced Raman scattering. *J. Colloid Interface Sci.*, 2017, **499**, P. 54–61.
- [20] Gusarov V.V., Egorov F.K., Ekimov S.P., Suvorov S.A. Mossbauer study of kinetics of films state formation under the interaction of magnesium and iron oxides. *Zhurnal Fizicheskoi Khimii.*, 1987, **61**(6), P. 1652–1654 (in Russian).
- [21] Gusarov V.V. Fast solid-phase chemical reactions. *Russ. J. Gen. Chem.*, 1997, **67**(12), P. 1846–1851.
- [22] Gusarov V.V., Suvorov S.A. Transformations of nonautonomous phases and densification of polycrystalline systems. *J. of Appl. Chem. of the USSR*, 1992, **65**(7), P. 1227–1235.
- [23] Gusarov V.V., Popov I.Y. Flows in two-dimensional non-autonomous phases in polycrystalline systems. *Nuovo Cimento Della Societa Italiana Di Fisica D*, 1996, **18**(7), P. 799–805.
- [24] Almjashaeva O.V., Gusarov V.V. The role of non-autonomous state in the formation of nanomaterials structure and properties. Ch. 13 in *Nanomaterials: Properties and Potential Applications*. Nauchnyi Mir, Moscow, 2014. P. 384–409 (in Russian).
- [25] Almjashaeva O.V., Smirnov A.V., Fedorov B.A., Tomkovich M.V., Gusarov V.V. Structural features of  $\text{ZrO}_2$ - $\text{Y}_2\text{O}_3$  and  $\text{ZrO}_2$ - $\text{Gd}_2\text{O}_3$  nanoparticles formed under hydrothermal conditions. *Russ. J. Gen. Chem.*, 2014, **84**(5), P. 804–809.
- [26] Smirnov A.V., Fedorov B.A., Tomkovich M.V., Almjashaeva O.V., Gusarov V.V. Core-shell nanoparticles forming in the  $\text{ZrO}_2$ - $\text{Gd}_2\text{O}_3$ - $\text{H}_2\text{O}$  system under hydrothermal conditions. *Dokl. Phys. Chem.*, 2014, **456**(1), P. 71–73.
- [27] Rusanov A.I. *Phase equilibria and surface phenomena*. Khimiya, Leningrad, 1967. 388 p. (in Russian).
- [28] Gusarov V.V., Suvorov S.A. Thickness of 2-dimensional nonautonomous phases in local equilibrium polycrystalline systems based on a single bulk phase. *Russ. J. Appl. Chem.*, 1993, **66**(7), P. 1212–1216.
- [29] Pozhidaeva O.V., Korytkova E.N., Romanov D.P., Gusarov V.V. Formation of  $\text{ZrO}_2$  nanocrystals in hydrothermal media of various chemical compositions. *Russ. J. Gen. Chem.*, 2002, **72**(6), P. 849–853.
- [30] Almjashaeva O.V. Formation and structural transformations of nanoparticles in the  $\text{TiO}_2$ - $\text{H}_2\text{O}$  system. *Nanosyst.: Phys. Chem. Math.*, 2016, **7**(6), P. 1031–1049.
- [31] Ivanov V.K., Fedorov P.P., Baranchikov A.Y., Osiko V.V. Oriented attachment of particles: 100 years of investigations of non-classical crystal growth. *Russ. Chem. Rev.*, 2014, **83**(12), P. 1204–1222.
- [32] Fedorov P.P., Ivanov V.K. Cooperative Formation of Crystals by Aggregation and Intergrowth of Nanoparticles. *Dokl. Phys.*, **56**(4), P. 205–207.
- [33] Suvorov S.A., Semin E.G., Gusarov V.V. *Phase Diagrams and Thermodynamics of Oxide Solid Solutions*. Leningrad University, Leningrad, 1986. 140 p. (in Russian).
- [34] Urusov V.S. *Theory of Isomorphic Mixing*. Science, Moscow, 1977, 251 p. (in Russian).
- [35] Landau L.D., Lifshitz E.M. *Theoretical Physics. Statistical Physics*. (vol. V). Part I. 3-rd ed., Rev. M.: Science. Ch. Ed. Fiz.-Mat. Lit, 1976, 584 p. (in Russian).
- [36] Degtyarev S.A., Voronin G.F. Solution of ill-posed problems in thermodynamics of phase equilibria. The  $\text{ZrO}_2$ - $\text{Y}_2\text{O}_3$  system. *Calphad*, 1988, **12**(1), P. 73–82.



# ***NANOSYSTEMS:***

## ***PHYSICS, CHEMISTRY, MATHEMATICS***

### **INFORMATION FOR AUTHORS**

The journal publishes research articles and reviews, and also short scientific papers (letters) which are unpublished and have not been accepted for publication in other magazines. Articles should be submitted in English. All articles are reviewed, then if necessary come back to the author to completion.

The journal is indexed in Web of Science Core Collection (Emerging Sources Citation Index), Chemical Abstract Service of the American Chemical Society, Zentralblatt MATH and in Russian Scientific Citation Index.

#### **Author should submit the following materials:**

1. Article file in English, containing article title, the initials and the surname of the authors, Institute (University), postal address, the electronic address, the summary, keywords, MSC or PACS index, article text, the list of references.
2. Files with illustrations, files with tables.
3. The covering letter in English containing the article information (article name, MSC or PACS index, keywords, the summary, the literature) and about all authors (the surname, names, the full name of places of work, the mailing address with the postal code, contact phone number with a city code, the electronic address).
4. The expert judgement on possibility of publication of the article in open press (for authors from Russia).

Authors can submit a paper and the corresponding files to the following addresses: nanojournal.ifmo@gmail.com, popov1955@gmail.com.

#### **Text requirements**

Articles should be prepared with using of text editors MS Word or LaTeX (preferable). It is necessary to submit source file (LaTeX) and a pdf copy. In the name of files the English alphabet is used. The recommended size of short communications (letters) is 4-6 pages, research articles– 6-15 pages, reviews – 30 pages.

##### Recommendations for text in MS Word:

Formulas should be written using Math Type. Figures and tables with captions should be inserted in the text. Additionally, authors present separate files for all figures and Word files of tables.

**Recommendations for text in LaTeX:**

Please, use standard LaTeX without macros and additional style files. The list of references should be included in the main LaTeX file. Source LaTeX file of the paper with the corresponding pdf file and files of figures should be submitted.

References in the article text are given in square brackets. The list of references should be prepared in accordance with the following samples:

- [1] Surname N. *Book Title*. Nauka Publishing House, Saint Petersburg, 2000, 281 pp.
- [2] Surname N., Surname N. Paper title. *Journal Name*, 2010, **1** (5), P. 17-23.
- [3] Surname N., Surname N. Lecture title. In: Abstracts/Proceedings of the Conference, Place and Date, 2000, P. 17-23.
- [4] Surname N., Surname N. Paper title, 2000, URL: <http://books.ifmo.ru/ntv>.
- [5] Surname N., Surname N. Patent Name. Patent No. 11111, 2010, Bul. No. 33, 5 pp.
- [6] Surname N., Surname N. Thesis Title. Thesis for full doctor degree in math. and physics, Saint Petersburg, 2000, 105 pp.

**Requirements to illustrations**

Illustrations should be submitted as separate black-and-white files. Formats of files – jpeg, eps, tiff.



# ***NANOSYSTEMS:***

***PHYSICS, CHEMISTRY, MATHEMATICS***

## **Журнал зарегистрирован**

Федеральной службой по надзору в сфере связи, информационных технологий и массовых коммуникаций

(свидетельство ПИ № ФС 77 - 49048 от 22.03.2012 г.)

ISSN 2220-8054

**Учредитель:** федеральное государственное автономное образовательное учреждение высшего образования

«Санкт-Петербургский национальный исследовательский университет информационных технологий, механики и оптики»

**Издатель:** федеральное государственное автономное образовательное учреждение высшего образования

«Санкт-Петербургский национальный исследовательский университет информационных технологий, механики и оптики»

**Отпечатано** в Учреждении «Университетские телекоммуникации»

Адрес: 197101, Санкт-Петербург, Кронверкский пр., 49

## **Подписка на журнал НФХМ**

На первое полугодие 2019 года подписка осуществляется через

ОАО Агентство «Роспечать»

Подписной индекс 57385 в каталоге «Издания органов научно-технической информации»